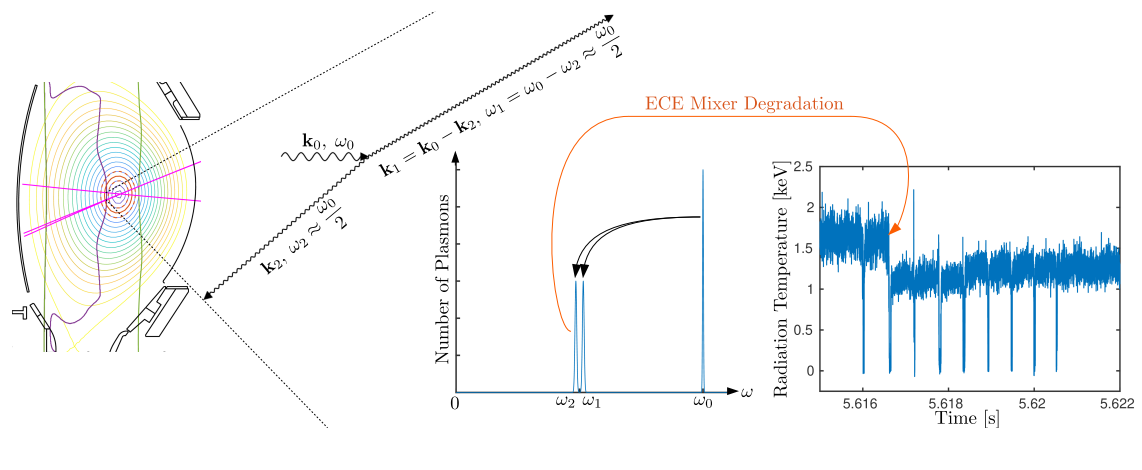


PhD Thesis

Parametric Decay Instabilities in the Electron Cyclotron Resonance Heating Beams at ASDEX Upgrade

Søren Kjer Hansen



Supervisors: Stefan Kragh Nielsen & Jörg Stober

Section for Plasma Physics and Fusion Energy
Department of Physics
Technical University of Denmark
&
Max-Planck-Institut für Plasmaphysik

31 August 2019

Abstract

In this Thesis we explore parametric decay instabilities (PDIs) in the electron cyclotron resonance heating (ECRH) beams at the ASDEX Upgrade tokamak. PDIs are nonlinear phenomena leading to decay of a strong quasi-monochromatic pump wave to two daughter waves once the amplitude of the pump wave exceeds a threshold determined by the interaction strength between the three waves. Due to their reliance on large wave amplitudes, PDIs are found in applications involving high-power wave heating, for instance in connection with ECRH of the plasmas at ASDEX Upgrade to temperatures relevant for fusion of hydrogen isotopes (~ 100 MK) by means millimeter-waves generated by gyrotron sources. Conservation of energy in the three-wave process underlying PDIs requires the daughter waves excited by the instability to have a different frequency from the pump wave used to excite them. This is a serious issue, as the ECRH beams at ASDEX Upgrade contain up to 1 MW of power, while the millimeter-wave diagnostics used to determine the plasma properties accept powers in the range of μW or lower. Even the conversion of a minuscule part of the ECRH power to millimeter-waves in the frequency range outside the protective filters around the ECRH frequency can thus have disastrous consequences for the millimeter-wave diagnostics, and this problem will be further amplified in a fusion power plant, which will rely heavily on millimeter-wave diagnostics due to their relative resistance to neutron damage. A further concern is that current theories suggest that a non-negligible part of the ECRH power can be converted to power in the daughter wave modes under certain circumstances, resulting in different heating and current drive characteristics than those expected from linear ECRH theories, potentially jeopardizing more than the just the diagnostics of a fusion power plant.

The studies at ASDEX Upgrade described in this work have been devised to assess the actual impact of PDIs in ECRH beams under fusion-relevant conditions, to avoid the above-mentioned deleterious effects, as well as to explore the possibility of utilizing such PDIs in novel diagnostic schemes. Our approach has been both theoretical and experimental in nature. We provide a detailed description of the theory behind PDIs, deriving some new and number of known results. With the developed theory and the ASDEX Upgrade ECRH system, we proceed to investigate PDIs experimentally. Our focus is on PDIs near the upper hybrid resonance (UHR) and its second-harmonic.

The PDIs near the UHR occur in connection with injection of 105 GHz radiation for collective Thomson scattering (CTS). Using analog modulation of the ECRH power, a sweep of the toroidal magnetic field strength, and the ASDEX Upgrade CTS system, we

are able to demonstrate agreement between the experimental PDI threshold and the PDI threshold expected theoretically. Additionally, we are for the first time able to characterize secondary and tertiary PDIs near the UHR in a controlled laboratory setting. A simple increase of the toroidal injection angle of the gyrotron beam is found to suppress these instabilities in usual cases.

The PDIs near the second-harmonic UHR are investigated in the standard 140 GHz ECRH scenarios at ASDEX Upgrade. These instabilities require the daughter waves to be trapped near the PDI region in order to be accessible at the power levels available with ECRH gyrotrons. They therefore occur when the second-harmonic UHR is located near a local density maximum, e.g., the center of an edge localized mode (ELM) filament, the O-point of a magnetic island, or the plasma center. PDIs in connection with ELMs are investigated in standard second-harmonic ECRH scenarios and found to be of limited concern to millimeter-wave diagnostics, but of potential diagnostic value. The PDI threshold during the passage of an ELM filament expected theoretically is found to be in reasonable agreement with the experimental PDI threshold observed during ELM crashes, and the duration of the microwave spikes during an ELM crash are additionally found to be in agreement with the passage time of an ELM filament through an ECRH beam according to a nonlinear magnetohydrodynamics simulation. The PDIs in connection with magnetic islands and near the plasma center are of more concern, as they have been found to damage mixers of the electron cyclotron emission (ECE) system due to the generation of strong millimeter-wave signals near half the ECRH frequency. For the PDIs in connection with magnetic islands, we have reproduced the original results from the TEXTOR tokamak and additionally shown the occurrence of such PDIs in third-harmonic ECRH experiments for the first time; we have also made the first observations of PDIs near the plasma center in third-harmonic ECRH experiments. The mere vicinity of an island to the overlap of an ECRH beam and the second-harmonic UHR is, however, found to be insufficient for the generation of strong millimeter-wave signals, highlighting the need for a more detailed characterization of the electron density profile associated with magnetic islands. The PDIs in third-harmonic ECRH scenarios are a potential risk to the ECE system in the early operation phase of ITER. They can, however, be mitigated by minimizing the ability of the ECE radiometers to pick up signals generated in the ECRH beams.

Dansk Resumé

Denne afhandling omhandler parametriske henfaldsinstabiliteter (PDI'er) i elektron-cyklotron-opvarmnings-strålerne ved ASDEX Upgrade-tokamakken. PDI'er er ikke-lineære fænomener, der fører til henfald af en stærk kvasi-monokromatisk pumpebølge til to datterbølger, når dens amplitude overstiger en tærskelværdi bestemt af interaktionsstyrken imellem de tre bølger. Da de afhænger af store bølgeamplituder, optræder PDI'er i anvendelser, der involverer bølgeopvarmning med høj effekt, f.eks. i forbindelse med elektron-cyklotron-resonans-opvarmning (ECRH) af plasmaer i ASDEX Upgrade, til temperaturer der er relevante for fusion af hydrogen-isotoper (~ 100 MK), vha. millimeterbølger genereret af gyrotron-kilder. Energibevarelse for den underliggende tre-bølge-proces kræver, at datterbølgerne, der eksiteres i instabiliteten, har en anden frekvens end pumpebølgen, der eksiterer dem. Dette er et alvorligt problem, da ECRH-strålerne ved ASDEX Upgrade kan indeholde en effekt op til 1 MW, mens millimeterbølge-diagnostikkerne, der bruges til at måle plasmaets opførelse, opererer med effekter af størrelsesordenen $1 \mu\text{W}$ eller mindre. Konvertering af selv en lille del af ECRH-effekten til millimeterbølger uden for frekvensområdet, der er beskyttet af filtre omkring ECRH-frekvensen, kan således have katastrofale konsekvenser for millimeterbølge-diagnostikkerne, og dette problem bliver forstærket i et fusionskraftværk, der vil være stærkt afhængigt af millimeterbølge-diagnostikker, pga. deres evne til at modstå neutron-skader. En yderligere grund til bekymring er, at nuværende teorier indikerer, at en ikke ubetydelig del af ECRH-effekten kan blive konverteret til effekt i datterbølgerne under bestemte omstændigheder, hvilket fører til andre opvarmningskarakteristika end de forventede, og kan have alvorligere konsekvenser for et fusionskraftværk end skadede måleinstrumenter.

Studierne ved ASDEX Upgrade, der beskrives i denne afhandling, er blevet formuleret med henblik på at undersøge konsekvenserne af PDI'er i ECRH-stråler under fusionsrelevante betingelser for at kunne undgå de ovennævnte negative følgevirkninger og desuden undersøge muligheden for nye diagnostikker baseret på PDI'er. Vores tilgang har været både teoretisk og eksperimentel. Vi giver en detaljeret beskrivelse af teorien bag PDI'er, i hvilken vi udleder nogle nye og mængde kendte resultater. Med den udledte teori og ASDEX Upgrade ECRH-systemet kan vi gå videre til den eksperimentelle undersøgelse af PDI'er. Vi fokuserer på PDI'er ved den øvre hybrid-resonans (UHR) og dens 2. harmoniske.

PDI'erne ved UHR'en sker i forbindelse med indsendelse af 105 GHz stråling brugt til kollektiv Thomson-spredning (CTS). Vha. analog modulation af ECRH-effekten, et skan af det toroidale magnetfelt og ASDEX Upgrade CTS-systemet er vi i stand til at vise ov-

erensstemmelse imellem teoretiske og eksperimentelle PDI-tærskelværdier. Vi kan desuden for første gang karakterisere sekundære og tertiære PDI'er ved UHR'en i et kontrolleret laboratorie-eksperiment. En simpel forøgelse af den toroidale indsendelsesvinkel er normalt nok til at undgå disse instabiliteter.

PDI'erne ved den 2. harmoniske UHR blev undersøgt i standard 140 GHz ECRH-scenarier ved ASDEX Upgrade. Disse instabiliteter kræver datterbølger, der er fangede i PDI-området, for at have en lav nok tærskelværdi til at kunne eksiteres med ECRH-gyrotroener. De finder derfor sted, når den 2. harmoniske UHR optræder ved et lokalt tæthedsmaksimum, f.eks. ved midten af et kant-lokaliseret filament (ELM), O-punktet i en magnetisk \emptyset eller plasma-centret. PDI'er i forbindelse med ELM's blev undersøgt i standard 2. harmoniske ECRH-scenarier, og lader ikke til at være noget problem for millimeterbølge-diagnostikker, men kan potentielt selv bruges som en diagnostik. Den teoretiske PDI-tærskelværdi, når en ELM passerer igennem en ECRH-stråle er i rimelig overensstemmelse med de eksperimentelle observationer, og varigheden af millimeterbølge-toppene er også i overensstemmelse med magnetohydrodynamiske simuleringer. PDI'erne i forbindelse med magnetiske øer og nær plasma-centret er mere bekymrende, da de har skadet elektron-cyklotron-emissions-systemets mikserer igennem stærke millimeterbølge-signaler nær den halve ECRH-frekvens. Vi har reproduceret de oprindelige resultater fra TEXTOR-tokamakken i forbindelse med magnetiske øer og desuden vist, at PDI'er sker i 3. harmoniske ECRH-scenarier for første gang både for øer og nær plasma-centret. Den blotte tilstedeværelse af en \emptyset nær den 2. harmoniske UHR er dog ikke tilstrækkelig til at generere stærke millimeterbølge-signaler, hvilket viser behovet for en bedre karakterisering af elektron-tæthedsprofilerne forbundet med magnetiske øer. PDI'er i 3. harmoniske ECRH-scenarier er en potentiel risiko for elektron-cyklotron-emissions-systemet i den tidlige operationsfase for ITER. Denne risiko kan dog reduceres ved at minimere elektron-cyklotron-radiometrets evne til at opfange signaler genereret i ECRH-strålerne.

Preface

The present Thesis is submitted as fulfillment of the prerequisites for obtaining the PhD degree at the Technical University of Denmark (DTU). The work has been carried out at the Department of Physics with the Section for Plasma Physics and Fusion Energy in Kgs. Lyngby, Denmark, and the Max-Planck-Institut für Plasmaphysik (IPP) in Garching b. München, Germany, from 1 September 2016 to 31 August 2019. This work was supported by a research grant (15483) from VILLUM FONDEN. This work has been carried out within the framework of the EUROfusion Consortium and has received funding from the Euratom research and training programme 2014–2018 and 2019–2020 under grant agreement No 633053. The views and opinions expressed herein do not necessarily reflect those of the European Commission.

There are number of people whom I shall like to thank for their involvement in the PhD project. First, I shall like to thank my supervisors, Dr. Stefan Kragh Nielsen (DTU) and Dr. Jörg Stober (IPP), for their patience with me during the PhD project in general and during the writing of the Thesis in particular. I shall also like to thank Dr. Matthias Hoelzl (IPP) for providing JOREK simulation output and Dr. Matthias Willensdorfer (IPP) for directing my attention toward microwave bursts observed by the electron cyclotron emission system at ASDEX Upgrade. On a less academic note, I shall like to thank the beer drinking delinquents of Club 47, particularly my co-founders Kristoffer "Kakao" Bitsch Joanesarson and Mads "Langfinger Røver" Givskov Senstius, for providing a welcome distraction from the PhD work while at DTU; at IPP, I shall like to thank my office mates and fellow PhD students, along with Dr. Asger Schou Jacobsen, Dr. Filip Janky, Dr. Ondrej Kudlacek, and Dr. Mikhail Zibrov, for playing a similar role. Finally, I shall like to thank my family for their love and support during the PhD project and my life in general.

Søren Kjer Hansen
Section for Plasma Physics and Fusion Energy
Department of Physics
Technical University of Denmark
&
Max-Planck-Institut für Plasmaphysik
31 August 2019

Contents

List of Figures	ix
List of Acronyms	x
1 Introduction	1
1.1 Plasma Physics and Fusion Energy	2
1.2 ASDEX Upgrade and Tokamak Physics	6
1.3 Wave and Electron Cyclotron Resonance Heating	10
1.4 Plasma (Wave) Diagnostics	13
1.4.1 Passive Plasma Diagnostics	13
1.4.2 Active Plasma Diagnostics	14
1.5 Three-Wave Interactions and Parametric Decay Instabilities	16
2 Plasma Wave Theory	20
2.1 Cold Electromagnetic Waves	22
2.2 Electrostatic Waves and Electron Bernstein Waves	27
2.3 Ion Bernstein and Warm Lower Hybrid Waves	33
3 Semi-Classical Wave Theory	37
3.1 Geometrical Optics as a Generalization of Classical Mechanics	38
3.2 Generalized WKBJ Methods	40
3.3 X-Mode Amplification from the Uniform Approximation	44
3.3.1 The Uniform Approximation	44
3.3.2 Field Enhancement near the Upper Hybrid Resonance	46

4	Parametric Decay Theory	50
4.1	Calculation of Nonlinear Charge Densities	51
4.2	Onset of Parametric Decay Instabilities with Free Daughter Waves	55
4.2.1	Onset of Parametric Decay Instabilities in Homogeneous Media	56
4.2.2	Onset of Parametric Decay Instabilities in Monotonic, Inhomogeneous Media	57
4.3	Onset of Parametric Decay Instabilities with Trapped Daughter Waves	60
4.3.1	Algorithm for Computing the Power Threshold of Parametric Decay Instabilities Involving Trapped Waves	70
4.4	Saturation of Parametric Decay Instabilities	70
5	Parametric Decay Instabilities near the Second-Harmonic Upper Hybrid Resonance	74
5.1	Parametric Decay Instabilities in Connection with Edge Localized Modes	76
5.2	Parametric Decay Instabilities in Connection with Rotating Magnetic Islands	84
5.3	Parametric Decay Instabilities in Connection with Pellet Injection	89
5.4	Parametric Decay Instabilities near the Plasma Center	91
6	Parametric Decay Instabilities near the Upper Hybrid Resonance	94
	Paper: Parametric Decay Instability near the Upper Hybrid Resonance in Magnetically Confined Fusion Plasmas	97
	Paper: Power Threshold and Saturation of Parametric Decay Instabilities near the Upper Hybrid Resonance in Plasmas	118
7	Conclusion	125
	Bibliography	129

List of Figures

1.1	Cross section of ASDEX Upgrade	6
1.2	Mixing of ECRH and ICRH waves in ASDEX Upgrade #34195	18
1.3	Visual representation of the PDI selection rules	19
1.4	Theoretical PDI spectrum with cascading	19
2.1	CMA diagram	26
2.2	Electron Bernstein wave CMA-like diagram	33
4.1	Amplification in a monotonic, inhomogeneous medium	59
4.2	Dispersion curves of a trapped wave	60
5.1	n_e^c at different B_t for a 140 GHz pump wave in ASDEX Upgrade	75
5.2	Plasma scenarios with PDIs during ELMs in ASDEX Upgrade	77
5.3	Slow CTS signal during ELMs in ASDEX Upgrade #35676 and #36583	78
5.4	P_0 pulses with analog modulations and CTS signal in ASDEX Upgrade #36583	79
5.5	P_0 modulations to determine P_0^{th} in ASDEX Upgrade #36583	79
5.6	Maximum CTS signal during ELMs in ASDEX Upgrade #35676 and #36583	80
5.7	IDA n_e - and T_e -profiles during ELMs in ASDEX Upgrade #35676	81
5.8	ELM signals during an ELM at low n_e and one at high n_e in ASDEX Upgrade #35676	82
5.9	Histogram of spike duration in during ELMs in ASDEX Upgrade #35676 and #36583	83
5.10	Evolution of n_e in the JOEREK simulation of ASDEX Upgrade #33616	83
5.11	Plasma and wave parameters in the trapping region at $t = 55.4 \mu\text{s}$ in the JOEREK simulation of ASDEX Upgrade #33616	84
5.12	Plasma scenarios with rotating islands near the warm 70 GHz UHR in ASDEX Upgrade	86

5.13 Degradation of ECE mixer during a rotating magnetic island in ASDEX Upgrade #35939	87
5.14 Fast CTS signal during rotating mode in ASDEX Upgrade #35186	87
5.15 Fast CTS signal during rotating mode in ASDEX Upgrade #35527	87
5.16 Spectrogram of the CTS channel from 139.0–139.1 GHz during the rotating island in ASDEX Upgrade #35186	88
5.17 Spectrogram of the CTS channel from 139.4–139.5 GHz during the rotating island in ASDEX Upgrade #35527	88
5.18 Observations of PDIs during rotating magnetic islands in ASDEX Upgrade	89
5.19 Strong CTS signal during edge density spikes in ASDEX Upgrade #35554 .	90
5.20 Plasma scenario with PDIs during edge density spike in ASDEX Upgrade #35554	90
5.21 Plasma and wave parameters in the trapping region of ASDEX Upgrade #35554	91
5.22 P_0^{th} during the edge density spike in ASDEX Upgrade #35554	91
5.23 Fast CTS signal during central PDI in ASDEX Upgrade #35527	92
5.24 Plasma scenario with central PDIs in ASDEX Upgrade #36149	92
5.25 Degradation of ECE mixer during central PDI in ASDEX Upgrade #36149	93

List of Acronyms

Acronym	Full name
ADC	Analog to digital converter
ASDEX	Axially Symmetric Divertor Experiment
CMA	Clemmow–Mullaly–Allis
CTS	Collective Thomson scattering
D–T	Deuterium–tritium
EBW	Electron Bernstein wave
EC	Electron cyclotron
ECE	Electron cyclotron emission
ECR	Electron cyclotron resonance
ECRH	Electron cyclotron resonance heating
ELM	Edge localized mode
IBW	Ion Bernstein wave
ICRH	Ion cyclotron resonance heating
IDA	Integrated data analysis
JET	Joint European Torus
LCFS	Last closed flux surface
LH	Lower hybrid
LO	Local oscillator
MHD	Magnetohydrodynamics
NBI	Neutral beam injection
NTM	Neoclassical tearing mode
PDI	Parametric decay instability
TEXTOR	Tokamak Experiment for Technology Oriented Research
UH	Upper hybrid
UHR	Upper hybrid resonance
WKBJ	Wentzel–Kramers–Brillouin–Jeffreys

Chapter 1

Introduction

The title of this Thesis includes the terms parametric decay instabilities (PDIs), electron cyclotron resonance heating (ECRH), and ASDEX (Axially Symmetric Divertor Experiment) Upgrade which are all related to plasma physics, and magnetic confinement fusion research in particular. PDIs are, however, ubiquitous in media with quadratic nonlinearities, including optical crystals [1], mechanical systems [2], fluids [3], ionospheric plasmas [4, 5, 6], and inertial confinement fusion plasmas [7], which has prompted us to approach the subject matter from a rather basic physics angle. When discussing the experiments at ASDEX Upgrade, we shall, nevertheless, investigate and apply many concepts that are mostly familiar to magnetic confinement fusion specialists, so in order to provide a coherent presentation that is accessible to an audience with a more general background, this Introduction Chapter is essential.

Before delving into the world of PDIs, ECRH, and ASDEX Upgrade, some remarks on the scope and style of presentation in the present work are in order. We have placed a rather heavy emphasis on the basic theoretical Chapters 2–4, which provide descriptions of linear plasma waves, semi-classical wave theory, and PDI theory, respectively. This is done in order to provide a more gentle introduction to PDIs than what can be provided in journal articles, which we hope will prove useful to researchers entering the field of PDIs in the ECRH frequency range. Our approach to PDIs in these Chapters is heavily based on PDI framework developed in [8, 9, 10, 11, 12], although our results are in some cases different from those of these works; when there is a non-negligible difference, we shall point out this difference, as well as the reason for the difference. The experimental Chapter 5 utilizes the theory developed in Chapters 2–4, particularly Section 4.3, which allows most of the experimental results to be explained satisfactorily. Chapter 6 is based on a rather different PDI framework than the previous chapters and somewhat special as a result. The theory and experiments discussed in Chapter 6 are presented in detail in [13, 14], which are so far the main articles published as a result of the PhD project associated with this Thesis. Chapter 6 therefore simply consists of an introduction, along with [13] and [14] in their entirety. We further note that a number of other works associated with the Author have been published during the course of the PhD project: two journal articles as a co-author

[15, 16] (plus one recently accepted journal article [17]), three conference contributions as a main author [18, 19, 20], two conference contributions as a co-author [21, 22], and two journal articles as part of a scientific collaboration [23, 24]; [20] forms a partial basis for Section 5.1 of the present work. Finally, Chapter 7 presents the conclusions based on the results of the entire Thesis.

Returning to the present Chapter, Section 1.1 discusses the basic properties of, and the motivation for studying, plasma physics, particularly focusing on fusion energy. Section 1.2 concerns the ASDEX Upgrade device and tokamaks (of which ASDEX Upgrade is one) in general. Section 1.3 addresses wave heating of magnetically confined plasmas, with a particular focus on ECRH. Section 1.4 presents the plasma diagnostics used in the experimental part of this work, focusing on wave-based diagnostics. Finally, Section 1.5 discusses three-wave interactions and PDIs in more detail.

1.1 Plasma Physics and Fusion Energy

The plasmas considered in this work are fairly close to the original definition by Langmuir [25], namely quasi-neutral collections of non-degenerate electrons, positive ions, and neutral particles. We do, however, note that plasma physics can also describe properties of non-neutral and pair plasmas [26, 27], electrolytes [28], metals [29], and warm dense matter [30] when appropriately modified. Although somewhat removed from everyday experience, classical plasmas make up the vast majority of the known matter in the universe, as they constitute the bulk of matter in stars and the interstellar medium. Classical plasmas are further capable opening up reaction pathways that are inaccessible in gases and condensed matter, making them essential for chemical processing and surface treatment/modification. In this work, we consider an application which combines the astrophysical and reaction technological aspects of classical plasmas: energy production by controlled fusion.

It is well-known that fusion of light nuclei, particularly isotopes of hydrogen, in stars is the principal source of free energy in the universe, and if fusion of heavy nuclei in supernovae is included, one can argue that all energy sources available to humanity at present are derived from fusion in some way. Based on this, it is natural to consider the feasibility and potential benefits of removing the intermediate steps, whether they be conversion of the kinetic energy of the fusion products to photons, chemical potential energy, nuclear potential energy, or kinetic energy of a fluid (wind/mechanical waves), and creating fusion power plants. Essentially, a fusion power plant should enable nuclei to come into close enough proximity for the fusion reaction to occur at a sufficient rate and with sufficiently low auxiliary power for the process to produce a significant amount of energy at a competitive price. Due to the short range of the attractive nuclear forces ($\sim 10^{-15}$ m) and the long range of the repulsive electrical forces, the power plant must allow the nuclei to overcome a rather large potential barrier in order for fusion to occur; the proximity to which the nuclei must be brought is, however, not quite as small as the nuclear scale length $\sim 10^{-15}$ m, but rather on the order of the de Broglie wavelength [31], as the nuclei may tunnel through the potential barrier with significant probability at this

point. In order to achieve fusion, the power plant must thus either heat the nuclei to be fused to an extremely high temperature, optimally around 174 MK (15 keV in energy units, obtained by multiplying the usual temperature by the Boltzmann constant, which will be used from this point onward) for the deuterium–tritium (D–T) reaction and higher for all other reactions [32], or have some mechanism for catalyzing the fusion reactions at a lower temperature.

The latter concept, known as "cold" fusion, has been the subject a considerable amount of pseudoscience, but is in principle just the nuclear equivalent of chemical catalysis. The most well known laboratory fusion catalyst is the muon, which is capable of forming hydrogen molecular ions where the distance between the nuclei is reduced by a factor of approximately 200 relative to electronic hydrogen molecular ions, owing to the muon mass being roughly 200 times that of the electron. The nuclei of the muonic hydrogen molecular ion are sufficiently close together for the nuclei to tunnel through the electric potential barrier and fuse within a time on the order of 250 fs for the D–T reaction [33]. This releases the muon, allowing it to catalyze another fusion reaction. It is, however, not feasible to extract energy from muon catalyzed fusion since a muon can only catalyze ~ 100 D–T reactions within its lifetime (and fewer of any other reaction) and the generation of muons requires high-energy particles which cannot be generated with high energy efficiency [33]. Unless some revolutionary catalytic process is found, it thus seems that a fusion power plant will have to achieve temperatures ~ 10 keV in order for the fusion reactions to occur at an appreciable rate; this requirement is the basic reason for the close connection between fusion energy research and high-temperature plasma physics. Before discussing "hot" fusion, we do, however, note that proton–proton fusion catalyzed by carbon, nitrogen, and oxygen (in the so-called CNO cycle) is the main energy producing process in large stars [34], but since proton–proton fusion must necessarily include decay of a proton to a neutron, which is mediated by the weak interaction, in order to produce isotopes within the proton drip line, such processes occur at a far slower rate than what is necessary to realize a non-astrophysical fusion power plant.

The main problem within "hot" fusion is to generate a plasma with temperatures ~ 10 keV and sustain it long enough for an appreciable number of fusion reactions to occur. Two rather different approaches to solving this problem, relying on different methods for confining the plasma, exist: magnetic confinement fusion and inertial confinement fusion.

Inertial confinement fusion relies on rapid compression of pellets of frozen hydrogen isotopes to create a short-lived high-density plasma (often its state is closer to warm dense matter than a classical plasma) which releases a large burst of fusion energy. The most well known example of inertial confinement fusion is the energy boost provided to a nuclear explosion in a hydrogen bomb, where the initial fission explosion provides the necessary compression of the hydrogen fuel to start fusion reactions. While this clearly illustrates the possibility of producing large amounts of energy from hydrogen fusion, it is not of much use in practical energy production. More recent developments in inertial confinement fusion have therefore focused on compression of much smaller hydrogen pellets with lasers. The current culmination of these efforts has been the report of net fusion energy gain from D–T pellets in the National Ignition Facility at the Lawrence Livermore National Laboratory, United

States of America [35]. It should, however, be noted that the energy gain only considers the energy coupled to the pellet, which is on the order of 1 % of the energy supplied to the lasers. An actual fusion power plant would further have to ignite pellets at a rate ~ 10 Hz in order to provide a significant power output. This rate will require the production time of the pellets and recharging time of the lasers to be reduced by several orders of magnitude; the cost of the pellets will likewise have to be reduced by several orders of magnitude. Inertial confinement fusion thus seems to provide the possibility of studying plasmas with a non-negligible number of fusion reactions, but several technological breakthroughs will have to take place in order for it provide a viable basis for a power plant.

Magnetic confinement fusion has more of the basic features desirable in a power plant and is, as previously stated, the main fusion concept considered in this work. Rather than the intense bursts of fusion energy produced due to compression in inertial confinement fusion, magnetic confinement fusion aims at creating a quasi-stationary low-density trapped fusion plasma; an exception is magnetized target fusion, which uses a magnetic field to compress a target plasma in order to achieve fusion. Due to the extremely high temperatures, the interaction of a trapped fusion plasma with the solid parts of a fusion power plant must be minimized. Since the plasma consists of charged particles, this can be achieved by a magnetic field (electrostatic fields cannot confine charged particles according to the Earnshaw theorem), generated, at least partially, by currents external to the plasma. A number of different magnetic confinement fusion concepts exist, the most promising at present being the toroidal tokamak and stellarator concepts [36]; toroidal geometries ensure that the magnetic field lines, to which the plasma is confined, form closed loops inside the plasma without terminating at solid surfaces. Stellarators generally produce the entire confining magnetic field externally, resulting in very stable, inherently steady-state plasmas (if the external field is generated by superconducting coils), but requiring rather complex geometries in order to cancel the drifts across the magnetic field lines introduced by the curvature and strength gradient of the magnetic field inherent in toroidal devices. Tokamaks have a simpler, almost axially symmetric, shape, but require a large plasma current (~ 1 MA in ASDEX Upgrade) to produce a magnetic field capable of canceling the drifts across the magnetic field and confining the plasma, resulting in plasmas that are more prone to disruptions and difficult to operate in steady-state than those of stellarators. The achievement of good plasma confinement in stellarators requires magnetic field coils of highly optimized shapes, which could only be found following the advent of high-performance computing, within very narrow tolerances. For these reasons, the development of stellarators was somewhat delayed relative to that of tokamaks, leaving the tokamak concept closer to a fusion power plant at the current stage. This is clearly illustrated when comparing the largest tokamak and stellarator presently in operation. The largest stellarator is Wendelstein 7-X at the Max-Planck-Institut für Plasmaphysik in Greifswald, Germany, which has a plasma volume of 30 m^3 , an energy confinement time around 0.2 s, and no D–T capability [37]. The largest tokamak is the Joint European Torus (JET) at the Culham Science Centre in Abingdon, United Kingdom, which has a plasma volume of 100 m^3 , an energy confinement time around 1.2 s, and D–T capability, with which it achieved a fusion power equivalent to 65 % of the auxiliary heating power in 1997 [38]. Wendelstein 7-X is capable sustaining

a plasma for much longer than JET, up to 30 minutes when its active cooling system is installed versus 10 s, owing to its superconducting coil system, but a similar plasma duration is possible in superconducting tokamaks. The next step toward a magnetic confinement fusion power plant, ITER, is therefore a superconducting tokamak with a plasma volume of 840 m^3 , an energy confinement time around 3.7 s, and D–T capability, with which it is predicted to produce a fusion power 10 larger than the auxiliary heating power; ITER is scheduled to start operation in 2025, although the D–T experiments will not take place until 2035 [39]. Provided that ITER is able to demonstrate the above features, the next step will be an actual demonstration power plant, DEMO, which may be a tokamak, a stellarator, or a hybrid of the two concepts, depending on the outcome of the various branches of current research.

Now that the feasibility of a magnetic confinement fusion power plant has been established, we briefly discuss the operation of such a power plant and its advantages over the energy sources presently known to humanity. As alluded to above, the D–T reaction, in which a deuteron and a triton collide to produce an alpha particle and a neutron with 3.5 MeV and 14.1 MeV of kinetic energy in the center of momentum frame, respectively, is the least demanding fusion reaction in terms of the required temperatures and hence the primary candidate for the first generation of fusion power plants [36]. Deuterium makes up approximately 0.0115 % of natural hydrogen, which is sufficient to cover present levels of energy consumption with fusion for billions of years [32], owing to the large amount of energy released in a fusion reaction. Since tritium is a radioactive element with a half-life of about 12 years [36], it is not found in naturally occurring hydrogen. Tritium can, however, be bred by neutron bombardment of lithium-6 and -7 [36]. A fusion power plant will therefore be equipped with a lithium breeder blanket (different concepts are to be tested in ITER [39]) where tritium will be bred by the neutrons generated by the D–T reactions; the neutrons are not confined by the magnetic field and therefore enter the breeder blanket almost immediately after their creation. This constantly replenishes the tritium consumed in the D–T reactions without the creation of a large tritium inventory which would be a potential safety hazard. While this method of tritium generation can only cover around twenty thousand years of energy consumption at current levels [32], this should still provide ample time to develop more advanced fusion power plants capable of deuterium–deuterium fusion, which would extend the currently known resources to billions of years. Apart from providing a virtually inexhaustible source of energy, a fusion power plant is expected to provide cost-effective electricity by driving turbines through the heat absorbed in the breeder blanket [32]. It is also clear that the operation of a fusion power plant will not be associated with the emission of any greenhouse gases or other atmospheric pollutants, the only product of the combined D–T and breeder reactions will be a small amount of inert helium-4. The neutrons released by the D–T process will invariably generate secondary radioactive isotopes, but by careful selection of the fusion reactor materials, none of these isotopes will be long-lived, allowing the fusion reactor materials to be recycled within a time on the order of 100 years after the plant ceases operation [32]. A fusion power plant is further inherently safe since it only contains a small inventory of tritium and deuterium fuel, and additionally relies on a high-temperature combustion process, which

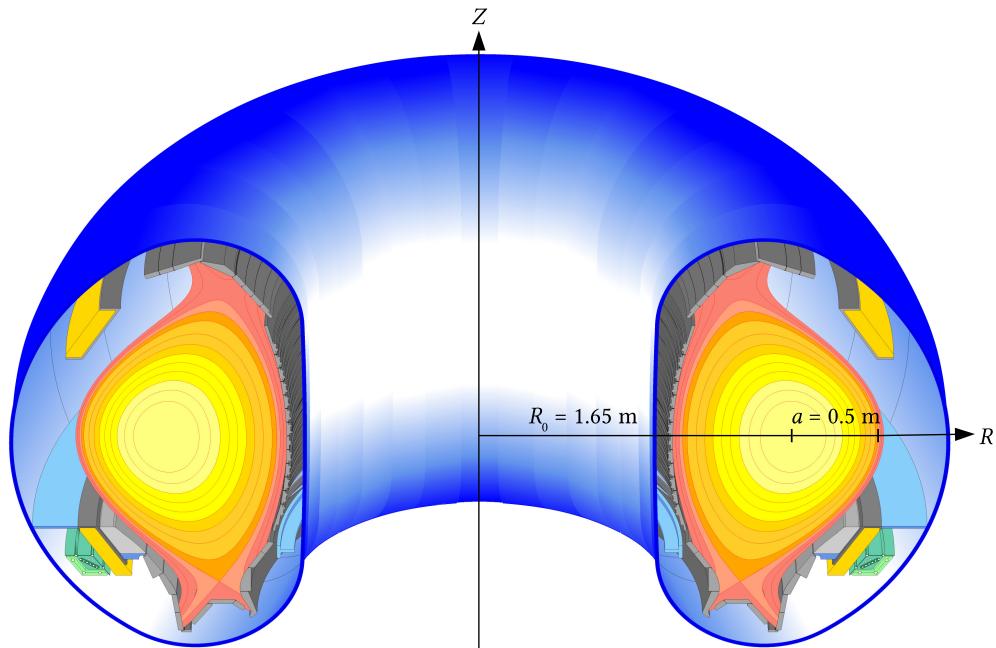


Figure 1.1 – Schematic cross section of ASDEX Upgrade illustrating the main parameters and plasma shape in the divertor configuration. Picture is adapted from the ASDEX Upgrade drawing gallery [40].

can be terminated by reducing the plasma fueling externally, rather than a potentially unstable chain reaction. Besides the attractive features listed above, the output of a fusion power plant will not depend on factors beyond human control, such as wind or cloud cover, and a fusion power plant will not require any specific natural features or change its local environment in any significant way, unlike a hydroelectric power plant. A fusion power plant would thus be complementary to renewable energy sources and enable controllable, virtually inexhaustible, carbon dioxide-free, cost-effective generation of electricity without the safety and waste issues of a fission power plant.

1.2 ASDEX Upgrade and Tokamak Physics

Having motivated plasma physics and magnetic confinement fusion research, we now turn to the specific device of interest in this work, ASDEX Upgrade. ASDEX Upgrade is a medium-sized tokamak with a plasma volume of 14 m^3 located at the Max-Planck-Institut für Plasmaphysik in Garching b. München, Germany, which is mainly used to investigate the physics basis of ITER and DEMO [23]. A schematic cross section of an ASDEX Upgrade plasma, including its major and minor radii, $R_0 = 1.65 \text{ m}$ and $a = 0.5 \text{ m}$, and the cylindrical (R, Z) -coordinate system used when describing such plasmas under the assumption of axial symmetry, is seen in Fig. 1.1.

The physics of tokamaks is described in a number of textbooks, e.g., [32, 41, 42], so here

we shall only provide a brief overview of the concepts that will be of interest later in this work. The simplest magnetohydrodynamics (MHD) description of a tokamak equilibrium involves assuming an axially symmetric plasma with no electrical resistivity and no fluid velocity in the laboratory frame. This leads to the plasma pressure being constant on axially symmetric surfaces, seen as yellow, orange and red areas in Fig. 1.1, which enclose a particular amount of poloidal magnetic flux (generated by the plasma current), ψ , wherefore they are known as flux surfaces [42]; the flux surfaces in a tokamak may be calculated using the Grad–Shafranov equation. In addition to having constant plasma pressure, which usually translates to constant density and temperature, the flux surfaces also contain the equilibrium magnetic field and current density vectors, and since charged particles roughly follow the magnetic field lines, they also tend to remain near the same flux surface.

When discussing the stability properties of tokamaks, an important parameter is the so-called q -factor of a flux surface which characterizes the number of toroidal revolutions necessary for a magnetic field line (and hence a particle/fluid element) to return to the same poloidal position. For rational q -values, a perturbation at one poloidal location remains localized to a narrow band on the flux surface, making such flux surfaces more prone to instabilities. Instabilities at the rational surfaces can, in the basic MHD description, be driven by the plasma current, the plasma pressure gradient, or a combination of these factors. The current-driven (kink) instabilities impose the condition $q > 2$ near the plasma edge, limiting the total plasma current, since the poloidal magnetic field, which reduces q , is produced by the plasma current; if $q < 1$ at the plasma center, i.e., for large central current densities, the plasma will further experience, generally non-disruptive, sawtooth instabilities [42]. Pressure-driven instabilities, unsurprisingly, provide a limit of the maximum plasma pressure attainable for a given confining magnetic field strength, although the overall limit, known as the Troyon limit, is determined by a combination of current- and pressure-driven modes [42]. The introduction of finite plasma resistivity further allows tearing of the flux surfaces near rational surfaces, creating magnetic islands. The most common source of magnetic islands in ASDEX Upgrade are so-called neoclassical tearing modes (NTMs) which are caused by the bootstrap current due to the plasma pressure gradient in the presence of trapped (banana) particles [32, 41, 42]. While a single island will generally not cause the plasma to disrupt so long as it is rotating, the occurrence of NTMs may still provide an effective limit on the attainable plasma pressure. The magnetic islands may further be associated with non-monotonic density profiles, making them of interest in connection with PDIs.

Flux surfaces in tokamaks can be split into two types, closed flux surfaces on which the magnetic field does not intersect any solid surfaces (yellow and orange areas in Fig. 1.1) and open flux surfaces where the magnetic field, and thus the plasma particles, eventually intersect a solid surface (red areas in Fig. 1.1). Fusion-relevant plasmas can only exist on the closed flux surfaces, while the open flux surfaces form the so-called scrape-off layer where the heat and particle exhaust from the core fusion plasma must be guided to material surfaces in a controlled manner if stable tokamak operation is to be maintained. ASDEX Upgrade is a divertor tokamak, meaning that the flux surfaces have a separatrix, where

$q \rightarrow \infty$, which separates the open and closed flux surfaces. The open flux surfaces outside the separatrix guide the exhaust particles to a so-called divertor structure, visible in the bottom of the plasma vessel in Fig. 1.1, removing the plasma–surface interaction from the vicinity of the core plasma. This improves the plasma performance over the traditional limiter configuration where the open flux surfaces are formed by a solid limiter structure inside the separatrix; ASDEX Upgrade can also be operated in limiter mode with the inner (or high-field side, since the magnetic field is stronger near the cylindrical axis) vessel wall acting as the limiter. A magnetic island has a separatrix structure, similar to the overall shape of a tokamak divertor equilibrium, but with a periodicity determined by the rational surface near which it occurs; the center of a magnetic island is known as the O-point, while its narrowest point is known as the X-point.

The shape of an ASDEX Upgrade plasma cross section clearly deviates from a simple circle. This is partially due to the X-point formed by the separatrix, visible near the divertor in Fig. 1.1, but the elongated D-shape also allows the plasma to carry a larger current and obtain higher pressure without becoming unstable [42]. In order to characterize the flux surfaces despite their non-trivial shapes, it is convenient to introduce a normalized poloidal flux coordinate, ρ_{pol} , which is zero at the plasma center and 1 at the last closed flux surface (LCFS). This may be done by using ψ , particularly its value at the center, ψ_{center} , and the LCFS, ψ_{LCFS} ,

$$\rho_{\text{pol}} = \sqrt{\frac{\psi - \psi_{\text{center}}}{\psi_{\text{LCFS}} - \psi_{\text{center}}}}; \quad (1.1)$$

the square root is taken to make ρ_{pol} approximately proportional to the distance from the plasma center. In the plots of ASDEX Upgrade equilibria in this work, we show ρ_{pol} from 0 to 1 as background contours to indicate the location of the bulk plasma.

With the basic concepts of tokamak plasmas established, we now discuss some more phenomenological and machine specific points. Apart from the basic Ohmic heating system used to drive current, based the plasma acting as a secondary winding of a central transformer core, ASDEX Upgrade is equipped with three auxiliary heating systems to create fusion-relevant conditions in the plasma core, drive additional current, generate fast ions and electrons, etc: neutral beam injection (NBI), ion cyclotron resonance heating (ICRH), and ECRH. NBI works by injecting high-energy neutral particles (kinetic energies in the range 60 – 100 keV at ASDEX Upgrade) into the plasma core, where they are ionized and subsequently confined by the magnetic field. ICRH and ECRH are both based on the injection of electromagnetic waves for heating the plasma; they will be discussed in detail in Section 1.3. The NBI system is the main auxiliary heating system at ASDEX Upgrade, consisting of 8 beams capable of providing at total heating power up to 20 MW; the ICRH system consists of four antennae capable of delivering a total heating power up to 7 MW; the ECRH system consists of 8 gyrotron sources capable of delivering up to 6 MW of heating power [23]. All heating systems operate in pulses up to 10 s, as this is the maximum duration of an ASDEX Upgrade plasma discharge due to heating of the uncooled copper coils used to generate the toroidal magnetic field.

When a heating power threshold is exceeded, tokamak plasmas undergo a transition from a

state characterized by relatively low edge densities and temperatures, the so-called L-mode, to a state characterized by high edge densities and temperatures with a steep pedestal region just inside the LCFS, the so-called H-mode [43, 36]; other confinement modes exist, but are unimportant for the plasmas discussed in this work. The H-mode transition is caused by a suppression of edge turbulence due to an increased radial electric field shear at high heating powers, although the detailed mechanism is still a field of active research [44]. While the H-mode is crucial for allowing ITER to achieve significant fusion power, it is also accompanied by quasi-period ejection of energy and particles on a fast time scale (~ 1 ms), known as edge localized modes (ELMs) [45]. A number of phenomenologically different ELM types exist, principally depending on the proximity of the heating power to the L-H threshold and the plasma shape [45, 24]; in this work, we are mainly interested in type I ELMs, which are large ELMs occurring for heating powers well above the L-H threshold in plasmas without strong shaping. ELMs are useful in reducing the accumulation of impurities in the plasma core and providing quasi-stationary H-mode plasmas, but the occurrence of large ELMs will greatly reduce the lifetime of plasma-facing components, particularly the divertor, in a tokamak fusion reactor, making operation in an ELM-mitigated, and ideally ELM-free, stationary high-confinement scenario necessary in such devices. There exist several methods for mitigating ELMs in H-modes at ASDEX Upgrade, the one of most interest in this work being magnetic perturbations [46]. The magnetic perturbations, produced by non-axially symmetric coils, increase losses from the plasma edge, replacing the large ELMs with a more continuous form of energy transport. When magnetic perturbations are applied to discharges with reduced toroidal magnetic (1.8 T at the plasma center, rather than the usual value of 2.5 T), the structure of their magnetic field may become resonant with the edge q -profile at attainable plasma currents, resulting in an increased impact on the ELMs from what is known as resonant magnetic perturbations. In clean low-density plasmas, e.g., discharges performed shortly after coating the vessel walls with boron (a boronization) [47] or dropping boron/boron nitride into the plasma during a discharge [48], resonant magnetic perturbations can lead to completely ELM-free stationary H-mode discharges [49]. In these discharges, the resonant magnetic perturbations further lead to a reduction of the plasma density, so-called pump out [49], resulting in conditions where PDIs are expected at ASDEX Upgrade.

We finally note that tokamak plasmas may not only be driven unstable by the plasma current and pressure gradients, but also by exceeding the so-called Greenwald edge density limit [50, 51]. Current theories suggest that the Greenwald edge density limit is caused by greatly increased radiation losses due to recombination at the edge once the temperature drops below 10 eV, which occurs at high densities [42]. However, in order to obtain high fusion power, it is obviously beneficial to have high core densities. Such densities may be obtained without exceeding the Greenwald edge density limit by fueling the plasma with pellets of frozen deuterium (and tritium) [52]. Pellets may further be the only effective fueling method in a tokamak fusion power plant [53] and create inverted density profiles of interest in connection with PDIs [54].

1.3 Wave and Electron Cyclotron Resonance Heating

Now that an overall description of ASDEX Upgrade has been given, we are in a position to discuss the more specific topic of interest in this work, namely wave heating and ECRH in particular. Wave heating of particles in the high-temperature, low-collisionality conditions of a tokamak core plasma generally relies on the collisionless Landau and cyclotron damping mechanisms, which are outlined below.

In the absence of a magnetic field, the Hamiltonian of a particle with mass m_σ is $H = \sqrt{m_\sigma^2 c^4 + p^2 c^2}$, where p is the magnitude of the momentum of the particle and c is the speed of light. When a particle absorbs a wave quantum with angular frequency ω and wave vector \mathbf{k} , its Hamiltonian and momentum is modified to H' , \mathbf{p}' . Energy and momentum conservation impose the selection rules $H' = H + \hbar\omega$ and $\mathbf{p}' = \mathbf{p} + \hbar\mathbf{k}$, with \hbar being the reduced Planck constant. Squaring the momentum equation yields $(p')^2 = p^2 + \hbar^2 k^2 + 2\hbar\mathbf{k} \cdot \mathbf{p}$, and inserting this in the energy equation gives

$$\omega = \frac{H}{\hbar} \left(\sqrt{1 + \frac{2\hbar\mathbf{k} \cdot \mathbf{p}c^2 + \hbar^2 k^2 c^2}{H^2}} - 1 \right). \quad (1.2)$$

In the classical limit of wave–particle interaction the change in particle parameters from absorption of a single wave quantum small, so $p \gg \hbar k$ and $\hbar k p c^2 / H^2 \ll 1$. This allows the above expression to be Taylor expanded with the result that

$$\omega \approx \frac{\mathbf{k} \cdot \mathbf{p}c^2}{H} = \mathbf{k} \cdot \mathbf{v}, \quad (1.3)$$

where $\mathbf{v} = \mathbf{p}c^2/H$ is the (pre-interaction) velocity of the particle according to the first Hamiltonian equation. Eq. (1.3) is the well-known Landau resonance condition. The derivation made no reference to whether the particle is charged or not, indicating that the Landau resonance occurs whenever a particle is moving at the phase velocity of a wave. If the particle distribution function is a monotonically decreasing function of $|\mathbf{v}|$ in the plasma frame, as assumed in this work, the Landau resonance always results in wave damping, known as Landau damping [55]. The universality of the Landau resonance is confirmed by the observation of strong damping of sound waves, consistent with the values expected for Landau damping, in neutral gases at low pressures [55, 56, 57]; at higher pressures collisions become sufficiently frequent to render the Landau mechanism ineffective, allowing sound waves to propagate [56]. As noted in [57], the observation of Landau damping in neutral gases [56] actually predates the observation of Landau damping in plasmas [58].

When charged particles move in a constant, static magnetic field, \mathbf{B} , their kinetic energy perpendicular to \mathbf{B} becomes quantized, giving rise to so-called Landau levels. For a particle of mass m_σ and charge q_σ the Dirac equation gives the Hamiltonian, $H = \sqrt{m_\sigma^2 c^4 + p_\parallel^2 c^2 + 2n\hbar|q_\sigma|Bc^2}$ [59], where p_\parallel is the component of \mathbf{p} parallel to \mathbf{B} and $n \in \mathbb{N}_0$. Conservation of energy and momentum parallel to \mathbf{B} when a wave quantum is absorbed by a particle again yields $H' = H + \hbar\omega$ and $p'_\parallel = p_\parallel + \hbar k_\parallel$. Inserting the expression for p'_\parallel

into H' , and introducing the variable $\Delta n = n' - n$, we find

$$\omega = \frac{H}{\hbar} \left(\sqrt{1 + \frac{2\hbar k_{\parallel} p_{\parallel} c^2 + \hbar^2 k_{\parallel}^2 c^2 + 2\Delta n \hbar |q_{\sigma}| B c^2}{H^2}} - 1 \right). \quad (1.4)$$

In the classical limit of wave–particle interaction, where $p_{\parallel} \gg \hbar k_{\parallel}$ and $|(\hbar k_{\parallel} p_{\parallel} c^2 + \Delta n \hbar |q_{\sigma}| B c^2)|/H^2 \ll 1$, the above equation may be Taylor expanded in a similar way to the non-magnetic case, from which

$$\omega \approx k_{\parallel} \frac{p_{\parallel} c^2}{H} + \Delta n \frac{|q_{\sigma}| B c^2}{H} = k_{\parallel} v_{\parallel} + \Delta n \frac{|\omega_{c\sigma}|}{\Upsilon}, \quad (1.5)$$

where $v_{\parallel} = p_{\parallel} c^2/H$ is the (pre-interaction) component of \mathbf{v} parallel to \mathbf{B} , $|\omega_{c\sigma}| = |q_{\sigma}| B/m_{\sigma}$ is the cold cyclotron frequency, and $\Upsilon = H/(m_{\sigma} c^2)$ is the (pre-interaction) Lorentz factor. The above expression gives the well-known Landau ($\Delta n = 0$) and cyclotron ($\Delta n \geq 1$) resonance conditions a relativistic, magnetized plasma. Note that only the projections of \mathbf{v} and \mathbf{k} parallel to \mathbf{B} enter the Landau resonance condition in a magnetized plasma, whereas their full scalar product was involved in the non-magnetic case. In actuality there is a transition between these extreme cases at a particular value of B [55, 60, 61]: when the collision frequency or growth rate of an instability is much larger than $|\omega_{c\sigma}|$, that species will behave as though it is unmagnetized, since it will only be deflected a negligible amount by the magnetic field before being strongly deflected by other effects; if $|\omega_{c\sigma}|$ is much larger than the collision frequency and instability growth rates, the species will be magnetized.

As indicated by their names, ICRH and ECRH rely on cyclotron heating of ions and electrons, respectively; lower hybrid (LH) heating and current drive on the other hand relies on Landau damping. The ratio of the ion and electron cyclotron frequencies, $\omega_{ci}/|\omega_{ce}| = Z_i m_e/m_i \approx 2.724 \times 10^{-3}$ (for deuterons), where Z_i is the ion charge number, determines the order of magnitude of the ICRH frequency (30–55 MHz at ASDEX Upgrade) to the ECRH frequency (105 or 140 GHz at ASDEX Upgrade).

Since a magnetized plasma is an anisotropic medium, it generally allows the propagation of two distinct electromagnetic modes, discussed in detail for ECRH in Section 2.1. For propagation close to perpendicular to \mathbf{B} , which is approximately true for the waves used for ECRH in tokamaks, the two modes can be characterized as an ordinary (O) mode, whose propagation characteristics are relatively unaffected by \mathbf{B} , and an extraordinary (X) mode, whose propagation characteristics are strongly affected by \mathbf{B} . O- and X-mode radiation may be injected by matching the polarization of the injected radiation to that of O- or X-mode at the plasma edge. The efficiency of the cyclotron damping mechanism, and hence the overall efficiency of ECRH, depends on the injected mode, the cyclotron harmonic(s) where absorption takes place, and the plasma parameters around the cyclotron harmonics, particularly the electron temperature, T_e , and density, n_e . Detailed calculations [62, 63] show that the optical thickness is proportional to $[T_e/(m_e c^2)]^{\Delta n}$ for O-mode when $\Delta n \geq 1$ and $[T_e/(m_e c^2)]^{\Delta n - 1}$ for X-mode when $\Delta n \geq 2$; the case of $\Delta n = 1$ for X-mode is somewhat special and discussed in more detail in Chapter 6. Since $T_e/(m_e c^2)$ is a small number $\sim 1/50$ in the core of a tokamak plasma, indicating that the electrons are weakly

relativistic, the absorption decreases rapidly with increasing cyclotron harmonics. ECRH is thus generally performed with O-mode at the first-harmonic ($\Delta n = 1$) or X-mode at the second-harmonic ($\Delta n = 2$); second-harmonic O-mode and third-harmonic X-mode ECRH are also employed, but require more care to ensure absorption of the ECRH power.

As mentioned in Section 1.2, the ECRH system at ASDEX Upgrade consists of 8 gyrotron sources [64, 65]. A gyrotron generates microwaves by inverting the process of the electron cyclotron damping discussed above, leading to electron cyclotron emission (ECE). Essentially, a hollow beam of electrons is sent into the gyrotron cavity where a strong magnetic field, generated by superconducting coils, is present. The electrons have a significant kinetic energy perpendicular to the magnetic field which may be reduced by the emission of photons at the electron cyclotron resonance (ECR) frequencies, usually the first-harmonic for high-power gyrotrons. The gyrotron cavity is constructed to be resonant with the photons emitted at the chosen ECR frequency and the hollow shape of the electron beam further ensures that the emission pattern corresponds to the selected mode of the gyrotron cavity; the photons emitted by the electron beam are coherent due to the relativistic shift of the ECR frequency [66]. This results in a strong microwave field in the gyrotron cavity, part of which is coupled out and converted to a Gaussian beam that is guided to the tokamak plasma, where it is injected for ECRH. Gyrotrons allow a high ECRH power (~ 1 MW per beam) to be generated with high efficiency ($\sim 50\%$). Apart from ECRH, gyrotrons with lower power are used in electron spin resonance investigations of chemical substances [66, 67] and for enhancing nuclear magnetic resonance signals through the dynamic nuclear polarization effect [68].

The gyrotrons at ASDEX Upgrade operate near 105 or 140 GHz [64, 65, 69]. They are capable of delivering 10 s pulses of up to 1 MW at 140 GHz and up to 800 kW at 105 GHz, although they are usually operated at slightly lower power to improve reliability [69]. It is further possible to modulate the gyrotron power on a fast time scale in an analog fashion by modulating the cathode voltage. Analog modulations allow determination of the dependence of microwave signals on gyrotron power, which is a very useful tool for identifying and characterizing PDIs. The ports from which the Gaussian output beams of the gyrotrons are injected are located on the outer (low-field side) part of the torus. The ports of the older (ECRH2) system are located close together with two ports slightly above and two ports slightly below the mid-plane. The ports of the newer (ECRH3) system are all located on the mid-plane, but distributed around the torus; the original ECRH1 system used the same ports as the ECRH3 system. In connection with PDIs, it is particularly worth noting that one of the ECRH3 gyrotrons is located near the ECE diagnostic port. In the standard scenario, with a central toroidal magnetic field, $|B_t|$, of 2.5 T, second-harmonic X-mode at 140 GHz is used, since the resonance for perpendicular injection, $\omega = 2|\omega_{ce}|$, occurs at the plasma center at this field; high plasma densities may necessitate the use of second-harmonic O-mode ECRH instead. We also consider discharges with third-harmonic X-mode ECRH at 140 GHz, in which $|B_t| = 1.8$ T. 105 GHz operation is only used for ECRH in special scenarios and for diagnostic purposes, e.g., for the probe beam of the collective Thomson scattering (CTS) diagnostic discussed in Section 1.4. Discharges with 105 GHz gyrotron operation are considered in Chapter 6.

1.4 Plasma (Wave) Diagnostics

With the basic plasma properties and heating methods of tokamaks covered, we shall now consider the problem of actually determining the properties of a fusion-relevant plasma. It is rather obvious that probe-based diagnostics, e.g., Langmuir probes, can only be used in the scrape-off layer and the very edge of the confined plasma, due to erosion of the probe and impurity accumulation in the plasma caused by the bombardment of the probe by energetic particles. Fusion plasmas are therefore diagnosed by a number of remote techniques, which may be separated based on whether they involve active or passive probing of the plasma, as well as on type of signals they are sensitive to.

1.4.1 Passive Plasma Diagnostics

Passive techniques measure signals generated by the plasma itself, rather than its response to external perturbations. They include magnetic diagnostics, e.g., Mirnov coils, Rogowski coils, and B-dot probes, which essentially measure the time derivatives of various components of \mathbf{B} through voltages induced due to Faraday's law, allowing reconstruction of the magnetic equilibrium and the plasma current through time integration, as well as the detection of magnetic islands and waves in the ICRH frequency range [70, 71]. Other passive diagnostics are based on the detection of fast ions and neutrons escaping the plasma, or currents in the plasma facing components due to interactions with the plasma; we particularly utilize the divertor current to infer the occurrence of ELM crashes. The class of passive diagnostics of most direct interest in this work is, however, the diagnostics based on the detection of electromagnetic radiation. Apart from the use of coils to detect relatively low-frequency waves, there are microwave diagnostics, most notably ECE, detecting waves in the ECRH frequency range; visible light diagnostics, detecting light from recombination of the deuterons with electrons at the plasma edge; soft X-ray diagnostics, measuring changes in the bremsstrahlung levels, providing a second diagnostic for detecting magnetic islands; and even gamma ray diagnostics detecting characteristic lines due to neutron-generated radioactive isotopes [70]. The passive diagnostic of most explicit interest in this work is ECE, as it is capable of detecting the waves generated by PDIs in the ECRH beams, but we shall of course also make use of magnetic and soft X-ray diagnostics for reconstructing magnetic equilibria, detecting magnetic islands, etc.

The physical principle behind the ECE diagnostic relies on emission of radiation at the ECR harmonics, just as a gyrotron, but unlike the gyrotron, the ECE originates from plasma electrons and is far weaker. \mathbf{B} in a tokamak is chiefly determined by the toroidal field, which decreases as $1/R$ due to Ampère's law, so a particular value of ω detected by the ECE system can be linked to radiation emitted from a particular R for a given ECR harmonic. Provided that the ECR is optically thick and that the electrons have a thermal distribution, the amplitude of the ECE signal will be given by the Planck radiation law and thus proportional to T_e at the R -value corresponding to a particular ω (since $T_e \gg \hbar\omega$); the output of the ECE system is therefore often given as a radiation temperature, which is the temperature that would correspond to a given signal with the above assumptions.

Several factors, such as the lack of an optically thick ECE, the overlap of ECE from several ECR harmonics, ECE from non-thermal electrons, and the occurrence of PDIs may cause the radiation temperature to be rather different from T_e [72].

The ECE radiometer at ASDEX Upgrade is, like most other microwave diagnostics, based on the heterodyne detection technique [73]. This technique involves picking up the radiation emitted by the plasma using a microwave horn (which provides localization of the measurements perpendicular to R , allowing T_e to be mapped to ρ_{pol}), filtering it, and mixing the filtered signal with a quasi-monochromatic signal from a local oscillator (LO) of angular frequency ω_{LO} . The mixing stage is a three-process, which, as discussed in Section 1.5, maps an angular frequency component ω of the filtered signal near ω_{LO} to a down-converted beat frequency $|\omega - \omega_{\text{LO}}|$; as frequency components shifted by the same amount above and below the LO frequency are mapped to the same frequency upon mixing, it is necessary to filter out one of these regions before the mixer in order to have an unambiguous mapping of the original signal to the down-converted signal, which is also known as the intermediate frequency (IF) signal. Provided that the LO signal is much stronger than any component of the filtered signal, the IF signal amplitude will be proportional to that of the filtered signal. If this is not the case, e.g., due the occurrence of PDIs, the IF signal will saturate and the mixer itself can even be damaged, as shown in Chapter 5. The IF signal is typically in the frequency range of 0 – 20 GHz, while the filtered signal has frequencies ~ 100 GHz, at ASDEX Upgrade [73]. This permits the IF signal to be amplified, split, re-amplified, sent through various band pass filters, detected by diodes, re-amplified, and sampled by analog to digital converts (ADCs). The above concept is that of a filter bank, which has a frequency resolution determined by the bandwidth of the band pass filters and a sampling rate determined by the ADCs. In order to cover a broad frequency range, several receivers with filter banks using mixers operating at different LO frequencies may be operated in parallel. ASDEX Upgrade has a 60 channel ECE system, consisting of three filter banks operating in parallel, with frequency resolutions of 300 or 600 MHz, sampled at a rate of 1 MHz [74]. Assuming that the radiation temperature is roughly equal to T_e at the measurement location, ECE measurements with a sampling rate of 1 MHz may be used to identify magnetic island structures and other MHD phenomena [74, 75]. The LO frequencies employed depend on $|B_t|$ of the plasma discharge and are tuned to observe second-harmonic X-mode ECE; the X-mode fraction of the microwave signal is selected by a polarizer before the mixer.

1.4.2 Active Plasma Diagnostics

Active plasma diagnostics are separate from their passive counterparts in that they involve subjecting the plasma to a known external perturbation and using the response of the plasma to infer the plasma parameters. Active plasma diagnostics may involve the injection of particles, e.g., fast neutral particles from the NBI system, lithium from the lithium beam system, and helium from a beam or in the form of a gas puff. Characteristic atomic and ionic lines of the injected particles may then be observed and the Doppler shift of these lines may provide information about the fast particles, thermal particles, and n_e

through charge exchange and beam emission spectroscopy [70]. The lithium beam diagnostic is, for instance, particularly useful for determining n_e near the plasma edge [76]. Other diagnostics, e.g., the heavy ion beam probe, detect the injected particles themselves upon exiting the plasma. The active plasma diagnostics most directly impacting this work are, however, the ones relying on the injection of electromagnetic waves. These include interferometry, polarimetry, reflectometry, and scattering-based diagnostics. Interferometry uses the phase shift of a quasi-monochromatic wave traversing the plasma relative to that of a similar wave traversing free space to determine the line-averaged n_e ; polarimetry is similar, but uses the change of polarization rather than the phase shift. Reflectometry relies on the injection of (micro)waves encountering a cutoff, at which they are reflected, into the plasma. The phase shift accumulated by the reflected wave allows the determination of the cutoff location, which corresponds to a particular n_e at a particular \mathbf{B} for a given polarization of the injected wave with a known ω . Using waves at various ω thus allow the plasma density profile to be reconstructed, and other features such as plasma turbulence may also be investigated using reflectometry. The scattering-based fusion plasma diagnostics rely on scattering of electromagnetic waves by free electrons, known as Thomson scattering in the classical limit. ASDEX Upgrade has two Thomson scattering systems, a conventional non-collective Thomson scattering system using scattering of an NdYAG laser beam and the CTS system using scattering of the ECRH beams. The conventional Thomson scattering system operates in the small-wavelength limit where electrons can be considered individually, meaning that the scattered signal is essentially an image of the NdYAG laser line broadened by the Doppler shift due to the electron velocities, allowing determination of T_e , with an amplitude depending on n_e [77]. The CTS system operates in a regime of larger wavelengths where collective plasma effects, such as electrostatic screening of the plasma ions by the electrons and plasma waves, must be taken into account [78]. Scattering of the gyrotron radiation from the electrons turns out to yield information about the thermal and fast ions due to electrostatic screening, but since the CTS signal originates from the ECRH beams, the CTS receiver view is designed to overlap with the ECRH beams; the beam which overlaps with the CTS receiver view is referred to as the probe beam. This makes the CTS diagnostic much more sensitive to PDIs in the aforementioned beams than other microwaves diagnostics, such as ECE and reflectometry [15].

The CTS system at ASDEX Upgrade consists of two heterodyne radiometers, both of which include a filter bank system with a frequency resolution of 100 to 500 MHz, sampled at a rate of 100 kHz [79]. Both CTS radiometers are capable of operating with a 95.5 GHz LO, which permits the use of a 105 GHz probe gyrotron for CTS measurements, but one of the radiometers can also be operated with a 130.5 GHz LO, which allows the use of a standard 140 GHz ECRH probe beam [80, 21]; PDIs with 140 GHz probe beams are studied in Chapter 5 and PDIs with 105 GHz probe beams are studied in Chapter 6. The CTS radiometers are connected to the lower ports of the ECRH2 launching system in ASDEX Upgrade, meaning that the operation of one of these prevents the operation of the gyrotron connected to the same port, and the polarization of the radiation detected by the CTS system is controlled using a universal polarizer [22]. A necessary component of the CTS system is a notch filter in front of the mixer blocking the signals in the frequency

range around the unshifted gyrotron frequencies; ECE radiometers operating near the ECRH frequency have similar, albeit generally broader notch filters. Other CTS safety systems include a pin-switch blocking the full frequency range of the radiometer when a gyrotron is switched on and off, as well as various variable attenuators. The CTS system is further equipped with a fast acquisition system, inserted after the IF signal is split. The IF signal going to the fast acquisition system is sent through a relatively broad bandpass filter (bandwidth ≈ 3 GHz) and amplified. After this, the IF signal is mixed with a second LO, creating a down-converted signal with frequencies in the range $0 - 3$ GHz, which is amplified, passed through a low-pass filter, and finally digitized at rate up to 12.5 GHz by a fast ADC, although only rates up to 6.25 GHz are used in this work, since this is sufficient to stay below the Nyquist frequency of the down-converted signal [81]. The LO and filter pass frequencies are chosen such that the the fast acquisition system is sensitive to frequencies in the range of ± 1.5 GHz from the gyrotron frequencies. The signal recorded by the fast acquisition system is a time domain signal which can be transformed to the frequency domain using a fast Fourier transform with a particular time window length and shape, determining the frequency and time resolution of the final spectra, both of which tend to be far finer than those of the filter bank. However, due to memory limitations, the fast acquisition system can only operate in limited phases of an ASDEX Upgrade discharge, while the filter bank system can operate throughout a discharge. We shall often refer to the fast acquisition system and the filter bank system as the fast and slow CTS systems, respectively. As the fast acquisition system has two channels, one of these can be connected to other signal sources than the usual CTS system, e.g., a mixer with a 70 GHz LO, allowing signals with frequencies near half that of a 140 GHz probe gyrotron to be investigated, or a B-dot probe [71], allowing low-frequency signals to be investigated; both these systems are of interest for studying PDIs.

In order to characterize the overall properties of an ASDEX Upgrade plasma, it is often necessary to combine the results from multiple diagnostic systems measuring related quantities or even the same quantity by different methods. An example of the former is the CLISTE code [82], which is used to reconstruct the magnetic equilibria from the magnetic diagnostic data with a time resolution of 1 ms. Multiple diagnostics measuring the same quantity can be combined through integrated data analysis (IDA) [76], which utilizes a Bayesian combination of the diagnostic signals and their uncertainties, along with certain regularization requirements, to construct the most likely n_e and T_e profiles, as well as their confidence intervals, on the flux surfaces with the same time resolution as CLISTE (1 ms). Unless explicitly stated otherwise, the magnetic equilibria and plasma profiles used in this work are calculated using CLISTE and IDA.

1.5 Three-Wave Interactions and Parametric Decay Instabilities

After a thorough general discussion, we are now in a position to discuss three-wave interactions and PDIs.

When multiple waves interact, it is necessary that the sum of ω and \mathbf{k} be conserved for the incoming and outgoing quanta in order to conserve the total Hamiltonian and canonical momentum of the system. For three-wave interactions, we thus get the selection rules

$$\omega_0 = \omega_1 + \omega_2, \quad \mathbf{k}_0 = \mathbf{k}_1 + \mathbf{k}_2 \quad (1.6)$$

where a large-amplitude pump wave, characterized by subscript 0, decays to two daughter waves, characterized by subscripts 1 and 2. If the pump wave combines with daughter wave 1 to produce another daughter wave, characterized by subscript 3, the selection rules become

$$\omega_0 + \omega_1 = \omega_3, \quad \mathbf{k}_0 + \mathbf{k}_1 = \mathbf{k}_3. \quad (1.7)$$

We note that a real signal invariably contains both positive and negative frequency components, such that combination of two waves also leads to waves with frequencies $|\omega_0 - \omega_1|$, which creates the IF signal in a heterodyne radiometer.

As is evident from the example of heterodyne radiometers, three-wave interactions have many important applications. Some select examples are the generation of entangled photons for fundamental tests of quantum mechanics [83, 84], the generation of squeezed states of light for increased sensitivity of gravitational wave observatories [85, 86], conversion of light between telecom and visible frequencies [1], and studies of the ionospheric plasma [4, 5, 6].

Three-wave interactions are inherently nonlinear and particularly originate from quadratic nonlinear terms in the governing equations, which occur in plasma physics, fluid mechanics, nonlinear optics, etc. We note that three-wave interactions are only the lowest order nonlinear interactions, i.e., the ones relying on the lowest order of the wave amplitudes, but that higher order nonlinear interactions in quadratically nonlinear media can be split into a cascade of three-wave interactions [87]. An interesting example of such interactions between ECRH and ICRH waves recorded by the fast CTS system at ASDEX Upgrade is seen in Fig. 1.2. In the experiment, 105 GHz O-mode radiation with no ECR in the main plasma is injected for CTS alongside 55.1 MHz radiation for third-harmonic ICRH, which is also poorly absorbed. As a result of the large amount of unabsorbed wave power, interactions between the 105 GHz radiation and the 55.1 MHz radiation is observed when both systems are switched on. This is evident from the sides bands with a separation of 55 MHz observed around the gyrotron frequency by the CTS system in pane (b) of Fig. 1.2; the chirping of the gyrotron frequency is due to analog gyrotron power modulations.

The dependence of three-wave interactions on the wave amplitudes means that their character may change as the wave amplitudes increase. This is indeed what happens in a PDI: once the pump wave amplitude exceeds a certain threshold, the decay into two daughter waves, implied in Eq. (1.6) and visualized in Fig. 1.3, becomes unstable. Depending on the characteristics of the medium, such an instability may lead to an initial exponential growth of the daughter wave amplitudes in time (an absolute instability), which will only saturate once a non-negligible fraction of the pump wave energy has been converted to daughter wave energy, or to a convective instability, which only results in finite spatial amplification of the daughter waves and generally consumes less of the pump wave energy.

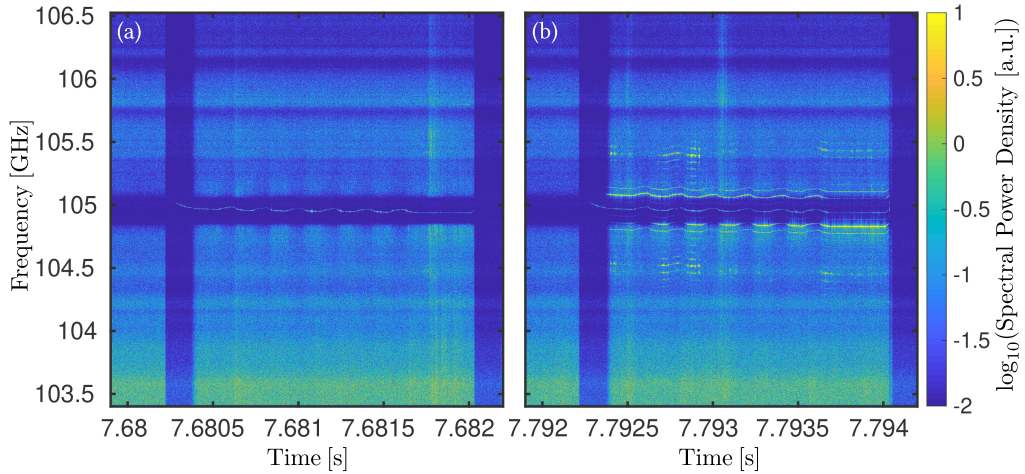


Figure 1.2 – Mixing of ECRH and ICRH waves in ASDEX Upgrade #34195. In pane (a), no ICRH power is injected, leading to a single line from the CTS gyrotron around 105 GHz. In pane (b), ICRH power with a frequency of 55.1 MHz is injected, leading to side bands separated by the ICRH frequency around the CTS gyrotron line. The low spectral power density around 105 GHz is due to the CTS notch filter; the overall low spectral power during switch on/off of the gyrotron is due to the CTS pin-switch.

Absolute PDIs occur in (almost) homogeneous plasmas, e.g., in the ionosphere [5, 6], and inhomogeneous plasmas if some mechanism by which the daughter wave energy may be continuously amplified exists, e.g., when the daughter waves are trapped around a region in which the PDI selection rules are satisfied [88, 8]. Convective PDIs generally require a higher pump wave amplitude threshold to be exceeded than absolute PDIs in order for their consequences to be observable and occur in inhomogeneous media when no localization of the daughter wave energy is possible [89, 90, 91]; the convective PDI threshold is well beyond the power of the ECRH beams in ASDEX Upgrade, except under special circumstances to be discussed in Chapters 2 and 6. Both PDI types are described theoretically in Chapter 4. Absolute PDIs in connection with daughter waves trapped in the non-monotonic n_e -profiles associated with ELMs, magnetic islands, edge density spikes, and near the plasma center are investigated experimentally in Chapter 5, while convective PDIs in the gyrotron beams used for CTS are investigated experimentally (and theoretically) in Chapter 6.

An idealized version of the spectrum generated in the presence of PDIs with trapped daughter waves is shown in Fig. 1.4. The original (primary) PDI generates waves near half the pump wave frequency, facilitating the trapping of both daughter waves, which results in the lowest PDI threshold. After the primary PDI, a secondary PDI, in which one of the daughter waves, taken to be daughter wave 2, decays to a secondary (still trapped) daughter wave near its own frequency, with angular frequency ω'_2 , and a low-frequency daughter wave, with angular frequency ω_{LF} , occurs; the frequency selection rule requires that $\omega_2 = \omega'_2 + \omega_{LF}$. The secondary PDI is involved in saturation of the instability, as will be shown in Section 4.4. The primary and secondary daughter waves

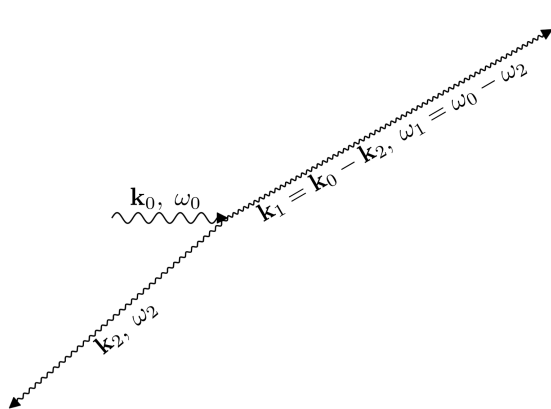


Figure 1.3 – Visual representation of the PDI selection rules.

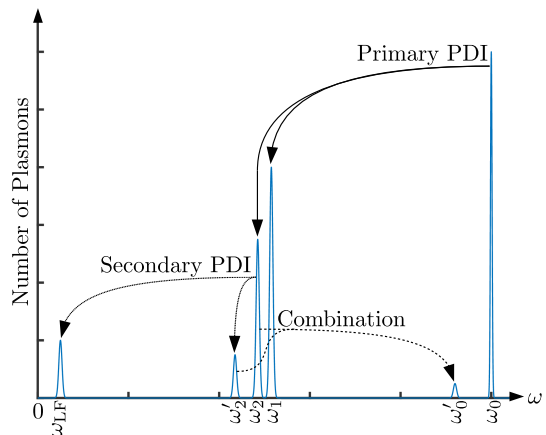


Figure 1.4 – Theoretical PDI spectrum with cascading.

additionally combine to produce radiation near the pump frequency with angular frequency $\omega'_0 = \omega_2 + \omega'_2 = 2\omega_2 - \omega_{LF} \approx \omega_0 - \omega_{LF}$. This radiation has the form of microwaves which may be picked up by the CTS system, and its theoretically expected amplitude has been shown to agree with experiments [9]. While the waves near half the pump frequency are nominally electrostatic, and thus not detectable by microwave diagnostics, they may give rise to strong electromagnetic signals, in agreement with the experiments in Chapter 5 [92].

We have already alluded to the consequences of PDIs, but for the sake of reference it is useful to have a detailed description here. First, the daughter waves generated by a PDI are shifted in frequency relative to the pump wave. In the case of an ECRH pump beam, the available power is ~ 1 MW, while microwave diagnostics are rated to receive wave powers $\lesssim 1 \mu\text{W}$. Even the conversion of a very small fraction of the ECRH power to microwaves in the frequency range detectable by microwave diagnostics can thus damage these diagnostics, as will be shown in Chapter 5. This problem will be further amplified in a fusion power plant which will rely heavily on microwave diagnostics due to their relative resistance to neutron damage compared with, e.g., optical diagnostics. It is therefore crucial to identify the situations in which PDI-generated microwaves may damage microwave diagnostics in order to mitigate or, ideally, avoid their deleterious consequences. Second, the occurrence of absolute PDIs with trapped daughter waves may lead to a significant fraction of the ECRH power being converted to power in the daughter wave modes; the fraction ranges from 6–60 % according to present theories [9, 10, 11, 12, 93] and values of 45 % have been found in recent low-temperature plasma experiments [94]. The alteration of ECRH power deposition and current drive characteristics caused by such drastic mode conversion would certainly have to be taken into account in ECRH applications like NTM suppression/stabilization and current profile tailoring. At present, there is, however, little experimental evidence of major deviations from the characteristics expected based on linear heating and current drive ECRH theories in tokamaks.

Chapter 2

Plasma Wave Theory

As PDIs involve coupling of different linear plasma wave modes, we provide a brief overview of linear plasma wave theory, focusing on the wave modes which enter in the instabilities treated in the latter part of this Thesis. Section 2.1 treats cold electromagnetic waves in the electron cyclotron frequency range, which are injected by gyrotrons at ASDEX Upgrade for ECRH and CTS. Section 2.2 discusses electrostatic waves in the electron cyclotron frequency range, particularly electron Bernstein waves (EBWs). Finally, Section 2.3 considers electrostatic waves with a significant ion response, specifically ion Bernstein waves (IBWs) and warm lower hybrid (LH) waves.

The most fundamental macroscopic, classical description of plasma waves is provided by kinetic theory. Kinetic theory describes the evolution of the distribution function of plasma species σ (characterized by its mass, m_σ , and charge, q_σ), f_σ , in phase space through a Boltzmann-like equation [95],

$$\frac{\partial f_\sigma(\mathbf{r}, \mathbf{p}, t)}{\partial t} + \mathbf{v} \cdot \frac{\partial f_\sigma(\mathbf{r}, \mathbf{p}, t)}{\partial \mathbf{r}} + q_\sigma [\mathbf{E}(\mathbf{r}, t) + \mathbf{v} \times \mathbf{B}(\mathbf{r}, t)] \cdot \frac{\partial f_\sigma(\mathbf{r}, \mathbf{p}, t)}{\partial \mathbf{p}} = \left[\frac{\partial f_\sigma(\mathbf{r}, \mathbf{p}, t)}{\partial t} \right]_{\text{col}}. \quad (2.1)$$

In Eq. (2.1), t is time, \mathbf{r} is the position vector, \mathbf{p} is the momentum vector ($\partial/\partial \mathbf{r}$ and $\partial/\partial \mathbf{p}$ denote gradients with respect to \mathbf{r} and \mathbf{p}), $\mathbf{v} = \mathbf{p}c^2/H$ is the velocity vector, $H = \sqrt{m_\sigma^2 c^4 + p^2 c^2}$ is the Hamiltonian, c is the vacuum speed of light, \mathbf{E} is the electric field vector, \mathbf{B} is the magnetic field vector, and $[\partial f_\sigma(\mathbf{r}, \mathbf{p}, t)/\partial t]_{\text{col}}$ is the collision operator for species σ . The evolution of \mathbf{E} and \mathbf{B} are given by the Maxwell equations [96]

$$\frac{\partial}{\partial \mathbf{r}} \times \mathbf{E}(\mathbf{r}, t) = -\frac{\partial \mathbf{B}(\mathbf{r}, t)}{\partial t}, \quad (2.2)$$

$$c^2 \frac{\partial}{\partial \mathbf{r}} \times \mathbf{B}(\mathbf{r}, t) = \frac{\mathbf{J}(\mathbf{r}, t)}{\epsilon_0} + \frac{\partial \mathbf{E}(\mathbf{r}, t)}{\partial t}, \quad (2.3)$$

$$\frac{\partial}{\partial \mathbf{r}} \cdot \mathbf{E}(\mathbf{r}, t) = \frac{\rho(\mathbf{r}, t)}{\epsilon_0}, \quad (2.4)$$

$$\frac{\partial}{\partial \mathbf{r}} \cdot \mathbf{B}(\mathbf{r}, t) = 0, \quad (2.5)$$

where ϵ_0 is the vacuum permittivity, and

$$\mathbf{J}(\mathbf{r}, t) = \sum_{\sigma} q_{\sigma} \int_{\text{all } \mathbf{p}} \mathbf{v} f_{\sigma}(\mathbf{r}, \mathbf{p}, t) d\mathbf{p}, \quad (2.6)$$

$$\rho(\mathbf{r}, t) = \sum_{\sigma} q_{\sigma} \int_{\text{all } \mathbf{p}} f_{\sigma}(\mathbf{r}, \mathbf{p}, t) d\mathbf{p} \quad (2.7)$$

are the current and charge densities, respectively. To obtain a wave equation, we differentiate Eq. (2.3) with respect to t and insert $\partial \mathbf{B} / \partial t$ from Eq. (2.2) to obtain

$$-c^2 \frac{\partial}{\partial \mathbf{r}} \times \left[\frac{\partial}{\partial \mathbf{r}} \times \mathbf{E}(\mathbf{r}, t) \right] - \frac{\partial^2 \mathbf{E}(\mathbf{r}, t)}{\partial t^2} = \frac{1}{\epsilon_0} \frac{\partial \mathbf{J}(\mathbf{r}, t)}{\partial t}. \quad (2.8)$$

Using a vector calculus identity [96], Eq. (2.8) may be recast as

$$\left[\left(c^2 \frac{\partial}{\partial \mathbf{r}} \cdot \frac{\partial}{\partial \mathbf{r}} - \frac{\partial^2}{\partial t^2} \right) \mathbf{1} - c^2 \frac{\partial}{\partial \mathbf{r}} \frac{\partial}{\partial \mathbf{r}} \right] \cdot \mathbf{E}(\mathbf{r}, t) = \frac{1}{\epsilon_0} \frac{\partial \mathbf{J}(\mathbf{r}, t)}{\partial t}, \quad (2.9)$$

where $\mathbf{1}$ is the 3-dimensional identity matrix. Since we are interested in weakly nonlinear phenomena, we write $\mathbf{J} = \mathbf{J}_1 + \mathbf{J}_{\text{nl}}$, with \mathbf{J}_1 being the linear current density and \mathbf{J}_{nl} being the nonlinear current density. \mathbf{J}_1 is the linear response of the plasma to \mathbf{E} and is hence given by [87]

$$\mathbf{J}_1(\mathbf{r}, t) = \int_{\text{all } (\mathbf{r}', t')} \boldsymbol{\sigma} \left(\mathbf{r} - \mathbf{r}', \frac{\mathbf{r} + \mathbf{r}'}{2}; t - t', \frac{t + t'}{2} \right) \cdot \mathbf{E}(\mathbf{r}', t') d\mathbf{r}' dt'; \quad (2.10)$$

$\boldsymbol{\sigma}$ is a conductivity tensor in physical space. Noting that $\mathbf{E}(\mathbf{r}, t) = \int_{\text{all } (\mathbf{r}', t')} \delta(\mathbf{r} - \mathbf{r}') \delta(t - t') \mathbf{E}(\mathbf{r}', t') d\mathbf{r}' dt'$, where δ is the Dirac delta distribution, Eq. (2.9) can be written in an integral form,

$$\int_{\text{all } (\mathbf{r}', t')} \left\{ \left[\left(c^2 \frac{\partial}{\partial \mathbf{r}} \cdot \frac{\partial}{\partial \mathbf{r}} - \frac{\partial^2}{\partial t^2} \right) \mathbf{1} - c^2 \frac{\partial}{\partial \mathbf{r}} \frac{\partial}{\partial \mathbf{r}} \right] \delta(\mathbf{r} - \mathbf{r}') \delta(t - t') - \frac{1}{\epsilon_0} \frac{\partial \boldsymbol{\sigma}}{\partial t} \left(\mathbf{r} - \mathbf{r}', \frac{\mathbf{r} + \mathbf{r}'}{2}; t - t', \frac{t + t'}{2} \right) \right\} \cdot \mathbf{E}(\mathbf{r}', t') d\mathbf{r}' dt' = \frac{1}{\epsilon_0} \frac{\partial \mathbf{J}_{\text{nl}}(\mathbf{r}, t)}{\partial t}, \quad (2.11)$$

which represents a general starting point for the discussion of plasma waves in this work. While the above equation is capable of describing essentially all macroscopic plasma wave phenomena, it is not feasible to calculate $\boldsymbol{\sigma}$ and \mathbf{J}_{nl} for an arbitrary inhomogeneous plasma; we shall therefore make approximations to study the phenomena of interest to us. In the present Chapter, we assume the plasma to be homogeneous (this constraint will be relaxed in Chapter 3), which means that $\boldsymbol{\sigma} = \boldsymbol{\sigma}(\mathbf{r} - \mathbf{r}', t - t')$. This turns the integral on the left hand side of Eq. (2.11) into a convolution integral, allowing the Fourier–Laplace transform of Eq. (2.11) to be evaluated using the convolution theorem [97]

$$\mathcal{D}(\mathbf{k}, \omega) \cdot \mathbf{E}(\mathbf{k}, \omega) = \left[(\omega^2 - c^2 k^2) \mathbf{1} + c^2 \mathbf{k} \mathbf{k} + \frac{i\omega \boldsymbol{\sigma}(\mathbf{k}, \omega)}{\epsilon_0} \right] \cdot \mathbf{E}(\mathbf{k}, \omega) = -\frac{i\omega \mathbf{J}_{\text{nl}}(\mathbf{k}, \omega)}{\epsilon_0}; \quad (2.12)$$

\mathcal{D} is the dispersion matrix, \mathbf{k} and ω are the wave vector and angular frequency of a given Fourier–Laplace mode, the Fourier–Laplace transform of a function $g(\mathbf{r}, t)$ is defined as

$$g(\mathbf{k}, \omega) = \int_{\text{all } \mathbf{r}} \left[\int_0^\infty g(\mathbf{r}, t) e^{i(\omega t - \mathbf{k} \cdot \mathbf{r})} dt \right] d\mathbf{r}, \quad (2.13)$$

and all quantities are taken to vanish at $t = 0$. To study linear waves, we set $\mathbf{J}_{\text{nl}} = \mathbf{0}$ which turns Eq. (2.12) into a homogeneous linear equation for \mathbf{E} . In order for such an equation to have a non-trivial solution ($\mathbf{E} \neq \mathbf{0}$), the determinant of \mathcal{D} must vanish [97], i.e.,

$$\det[\mathcal{D}(\mathbf{k}, \omega)] = \det \left[(\omega^2 - c^2 k^2) \mathbf{1} + c^2 \mathbf{k} \mathbf{k} + \frac{i\omega \boldsymbol{\sigma}(\mathbf{k}, \omega)}{\epsilon_0} \right] = 0. \quad (2.14)$$

Eq. (2.14) is the dispersion relation for linear waves in a homogeneous plasma, and solving it in different limits is the main objective of the remainder of this Chapter. Since the plasma response is contained in $\boldsymbol{\sigma}$, this essentially boils down to determining the conductivity of a plasma in Fourier–Laplace space.

2.1 Cold Electromagnetic Waves

As we are considering coupling of the electromagnetic waves used for ECRH to plasma waves, it is natural to start out with a description of electromagnetic waves. Although computation of absorption near the cyclotron harmonics requires a kinetic treatment [62, 63, 98], the basic propagation properties of electromagnetic plasma waves can be obtained from a cold fluid model, as the phase velocity of the waves is generally much larger than the thermal velocities of the plasma particles [99, 55]. This model, often referred to as the Altar–Appleton–Hartree model [55], is well-known and described in detail elsewhere [100, 99, 55]; therefore, we shall only provide a brief overview, focusing on the results which are incorporated later in this work. The fluid equations are obtained by taking moments of Eq. (2.1), i.e., multiplying by a power of \mathbf{v} and integrating over all \mathbf{p} . The zeroth moment yields the continuity equation,

$$\frac{\partial n_\sigma(\mathbf{r}, t)}{\partial t} + \frac{\partial}{\partial \mathbf{r}} \cdot [n_\sigma(\mathbf{r}, t) \mathbf{V}_\sigma(\mathbf{r}, t)] = 0, \quad (2.15)$$

where $n_\sigma = \int_{\text{all } \mathbf{p}} f_\sigma d\mathbf{p}$ is the (number) density of species σ and $\mathbf{V}_\sigma = \int_{\text{all } \mathbf{p}} \mathbf{v} f_\sigma d\mathbf{p} / n_\sigma$ is the fluid velocity of species σ . The cold fluid approximation is obtained by taking the first moment in the non-relativistic limit ($\mathbf{p} \approx m_\sigma \mathbf{v}$), ignoring the terms related to finite plasma pressure,

$$\begin{aligned} \frac{\partial \mathbf{V}_\sigma(\mathbf{r}, t)}{\partial t} + \mathbf{V}_\sigma(\mathbf{r}, t) \cdot \frac{\partial \mathbf{V}_\sigma(\mathbf{r}, t)}{\partial \mathbf{r}} &= \frac{q_\sigma}{m_\sigma} [\mathbf{E}(\mathbf{r}, t) + \mathbf{V}_\sigma(\mathbf{r}, t) \times \mathbf{B}(\mathbf{r}, t)] \\ &+ \sum_{\sigma'} \nu_{\sigma\sigma'}(\mathbf{r}, t) \cdot [\mathbf{V}_{\sigma'}(\mathbf{r}, t) - \mathbf{V}_\sigma(\mathbf{r}, t)]; \end{aligned} \quad (2.16)$$

Eq. (2.16) assumes the collisional drag of σ' on species σ to be proportional to the difference of their fluid velocities [101] and $\nu_{\sigma\sigma'}$ is a collision frequency matrix, obtained from the collision operator, determining the strength of the collisional drag of species σ' on species σ . Since we are concerned with waves used for ECRH that have $\omega \sim |\omega_{ce}| \gg \omega_{ci}$, we can generally ignore the response of the ions (and set $\mathbf{V}_i = \mathbf{0}$). This reduces the set of equations in Eqs. (2.15) and (2.16) to the equations for the electrons

$$\frac{\partial n_e(\mathbf{r}, t)}{\partial t} + \frac{\partial}{\partial \mathbf{r}} \cdot [n_e(\mathbf{r}, t) \mathbf{V}_e(\mathbf{r}, t)] = 0, \quad (2.17)$$

$$\frac{\partial \mathbf{V}_e(\mathbf{r}, t)}{\partial t} + \mathbf{V}_e(\mathbf{r}, t) \cdot \frac{\partial \mathbf{V}_e(\mathbf{r}, t)}{\partial \mathbf{r}} = -\frac{e}{m_e} [\mathbf{E}(\mathbf{r}, t) + \mathbf{V}_e(\mathbf{r}, t) \times \mathbf{B}(\mathbf{r}, t)] - \nu_{ei}(\mathbf{r}, t) \cdot \mathbf{V}_e(\mathbf{r}, t), \quad (2.18)$$

where ν_{ei} is the electron–ion collision frequency matrix, given by a Braginskii-style expression [55] (neutrals may also be included in it, but are not considered in this work). In order to calculate σ , which is required to obtain the dispersion relation, we linearize Eqs. (2.17) and (2.18) around a stationary, potentially inhomogeneous, equilibrium with $n_e = n_e^{(0)}(\mathbf{r})$, $\mathbf{B} = \mathbf{B}^{(0)}(\mathbf{r})$, $\nu_{ei} = \nu_{ei}^{(0)}(\mathbf{r})$, $\mathbf{V}_e = \mathbf{V}_e^{(0)} = \mathbf{0}$, and $\mathbf{E} = \mathbf{E}^{(0)} = \mathbf{0}$,

$$\frac{\partial n_{e,1}(\mathbf{r}, t)}{\partial t} + n_e^{(0)}(\mathbf{r}) \frac{\partial}{\partial \mathbf{r}} \cdot \mathbf{V}_{e,1}(\mathbf{r}, t) = 0, \quad (2.19)$$

$$\frac{\partial \mathbf{V}_{e,1}(\mathbf{r}, t)}{\partial t} = -\frac{e}{m_e} [\mathbf{E}(\mathbf{r}, t) + \mathbf{V}_{e,1}(\mathbf{r}, t) \times \mathbf{B}^{(0)}] - \nu_{ei}^{(0)}(\mathbf{r}) \cdot \mathbf{V}_{e,1}(\mathbf{r}, t); \quad (2.20)$$

$n_{e,1}$ and $\mathbf{V}_{e,1}$ represent the linearized response of the plasma to \mathbf{E} . According to Eq. (2.6), $\mathbf{J} = -en_e \mathbf{V}_e$, which has the linearized version $\mathbf{J}_1(\mathbf{r}, t) = -en_e^{(0)}(\mathbf{r}) \mathbf{V}_{e,1}(\mathbf{r}, t)$, so $n_{e,1}$ is unimportant for linearized, electromagnetic plasma waves; it does, however, enter in $\mathbf{V}_{e,1}$, as shown in Chapter 4. Plugging \mathbf{J}_1 into Eq. (2.20) yields

$$\frac{\partial \mathbf{J}_1(\mathbf{r}, t)}{\partial t} = \epsilon_0 \omega_{pe}^2(\mathbf{r}) \mathbf{E}(\mathbf{r}, t) + \mathbf{J}_1(\mathbf{r}, t) \times \boldsymbol{\omega}_{ce}(\mathbf{r}) - \nu_{ei}^{(0)}(\mathbf{r}) \cdot \mathbf{J}_1(\mathbf{r}, t), \quad (2.21)$$

where $\omega_{pe} = \sqrt{e^2 n_e^{(0)} / (\epsilon_0 m_e)}$ is the electron plasma frequency and $\boldsymbol{\omega}_{ce} = -e \mathbf{B}^{(0)} / m_e$ is the electron cyclotron frequency vector. Performing a Laplace transform in t on Eq. (2.21) and rearranging, we find

$$\mathbf{E}(\mathbf{r}, \omega) = -\frac{1}{\epsilon_0 \omega_{pe}^2(\mathbf{r})} (\mathbf{r}) [i\omega \mathbf{J}_1(\mathbf{r}, \omega) + \mathbf{J}_1(\mathbf{r}, \omega) \times \boldsymbol{\omega}_{ce}(\mathbf{r}) - \nu_{ei}^{(0)}(\mathbf{r}) \cdot \mathbf{J}_1(\mathbf{r}, \omega)]. \quad (2.22)$$

Taking $\mathbf{B}^{(0)}$ to point in a constant direction, which we define to be the z -direction, $\boldsymbol{\omega}_{ce} = \omega_{ce} \mathbf{e}_z$ and $\nu_{ei}^{(0)} = \nu_{ei}(\mathbf{e}_x \mathbf{e}_x + \mathbf{e}_y \mathbf{e}_y) + \nu_{ei\parallel} \mathbf{e}_z \mathbf{e}_z$ [55]. This allows Eq. (2.22) to be recast in the matrix–vector form,

$$\mathbf{E}(\mathbf{r}, \omega) = \frac{1}{\epsilon_0 \omega_{pe}^2(\mathbf{r})} \begin{bmatrix} -i\omega + \nu_{ei}(\mathbf{r}) & -\omega_{ce}(\mathbf{r}) & 0 \\ \omega_{ce}(\mathbf{r}) & -i\omega + \nu_{ei}(\mathbf{r}) & 0 \\ 0 & 0 & -i\omega + \nu_{ei\parallel}(\mathbf{r}) \end{bmatrix} \cdot \mathbf{J}_1(\mathbf{r}, \omega); \quad (2.23)$$

strictly speaking, a constant direction of $\mathbf{B}^{(0)}$ also requires $\mathbf{B}^{(0)}$ to be independent of \mathbf{r} , but as we are generally considering a mainly toroidal field, varying as $1/R$, for waves propagating mainly along the R -direction, we retain the \mathbf{r} -dependence. Eq. (2.23) can be inverted using standard linear algebra,

$$\mathbf{J}_1(\mathbf{r}, \omega) = \left\{ \begin{array}{ccc} \frac{\epsilon_0 \omega_{pe}^2(\mathbf{r})[-i\omega + \nu_{ei}(\mathbf{r})]}{[-i\omega + \nu_{ei}(\mathbf{r})]^2 + \omega_{ce}^2(\mathbf{r})} & \frac{\epsilon_0 \omega_{pe}^2(\mathbf{r})\omega_{ce}(\mathbf{r})}{[-i\omega + \nu_{ei}(\mathbf{r})]^2 + \omega_{ce}^2(\mathbf{r})} & 0 \\ \frac{-\epsilon_0 \omega_{pe}^2(\mathbf{r})\omega_{ce}(\mathbf{r})}{[-i\omega + \nu_{ei}(\mathbf{r})]^2 + \omega_{ce}^2(\mathbf{r})} & \frac{\epsilon_0 \omega_{pe}^2(\mathbf{r})[-i\omega + \nu_{ei}(\mathbf{r})]}{[-i\omega + \nu_{ei}(\mathbf{r})]^2 + \omega_{ce}^2(\mathbf{r})} & 0 \\ 0 & 0 & \frac{\epsilon_0 \omega_{pe}^2(\mathbf{r})}{-i\omega + \nu_{ei\parallel}(\mathbf{r})} \end{array} \right\} \cdot \mathbf{E}(\mathbf{r}, \omega). \quad (2.24)$$

We shall employ Eq. (2.24) when discussing field enhancement in inhomogeneous plasmas in Chapter 3; however, for the remainder of this Chapter we take the plasma to be homogeneous and additionally ignore collisions (set $\nu_{ei} = \nu_{ei\parallel} = 0$), as they are not essential when discussing the general characteristics of electromagnetic waves. With these assumptions, Eq. (2.24) may be Fourier transformed in \mathbf{r} , giving

$$\mathbf{J}_1(\mathbf{k}, \omega) = \boldsymbol{\sigma}(\mathbf{k}, \omega) \cdot \mathbf{E}(\mathbf{k}, \omega), \quad \boldsymbol{\sigma}(\mathbf{k}, \omega) = \begin{bmatrix} \frac{i\epsilon_0 \omega_{pe}^2 \omega}{\omega^2 - \omega_{ce}^2} & \frac{-\epsilon_0 \omega_{pe}^2 \omega_{ce}}{\omega^2 - \omega_{ce}^2} & 0 \\ \frac{\epsilon_0 \omega_{pe}^2 \omega_{ce}}{\omega^2 - \omega_{ce}^2} & \frac{i\epsilon_0 \omega_{pe}^2 \omega}{\omega^2 - \omega_{ce}^2} & 0 \\ 0 & 0 & \frac{i\epsilon_0 \omega_{pe}^2}{\omega} \end{bmatrix}. \quad (2.25)$$

Using $\boldsymbol{\sigma}$ from Eq. (2.25), $\mathcal{D}(\mathbf{k}, \omega) = [(\omega^2 - c^2 k^2)\mathbf{1} + c^2 \mathbf{k}\mathbf{k} + i\omega \boldsymbol{\sigma}(\mathbf{k}, \omega)/\epsilon_0]$ can be computed. Defining $\mathbf{k} = k \sin(\theta)\mathbf{e}_x + k \cos(\theta)\mathbf{e}_z$, where $\theta \in [0, \pi]$ is the angle between \mathbf{k} and $\mathbf{B}^{(0)}$, we find

$$\mathcal{D}(\mathbf{k}, \omega) = \begin{bmatrix} \omega^2 S - c^2 k^2 \cos^2(\theta) & -i\omega^2 D & c^2 k^2 \cos(\theta) \sin(\theta) \\ i\omega^2 D & \omega^2 S - c^2 k^2 & 0 \\ c^2 k^2 \cos(\theta) \sin(\theta) & 0 & \omega^2 \mathcal{P} - c^2 k^2 \sin^2(\theta) \end{bmatrix}, \quad (2.26)$$

where

$$S = 1 - \frac{\omega_{pe}^2}{\omega^2 - \omega_{ce}^2}, \quad D = \frac{\omega_{ce}}{\omega} \frac{\omega_{pe}^2}{\omega^2 - \omega_{ce}^2}, \quad \mathcal{P} = 1 - \frac{\omega_{pe}^2}{\omega^2} \quad (2.27)$$

are the Stix parameters [99]. The dispersion relation is found by requiring the determinant of \mathcal{D} to vanish,

$$\begin{aligned} \det[\mathcal{D}(\mathbf{k}, \omega)] &= [S \sin^2(\theta) + \mathcal{P} \cos^2(\theta)] \omega^2 c^4 k^4 \\ &\quad - \{\mathcal{P} S [1 + \cos^2(\theta)] + (S^2 - D^2) \sin^2(\theta)\} \omega^4 c^2 k^2 + \mathcal{P} (S^2 - D^2) \omega^6 = 0. \end{aligned} \quad (2.28)$$

Eq. (2.28) is a quadratic equation for k^2 which, when solved, yields

$$k^2 = \frac{\omega^2}{2c^2} \left\{ \frac{\mathcal{P}S[1 + \cos^2(\theta)] + (S^2 - D^2)\sin^2(\theta)}{S\sin^2(\theta) + \mathcal{P}\cos^2(\theta)} \pm \frac{\sqrt{(S^2 - D^2 - \mathcal{P}S)^2\sin^4(\theta) + 4\mathcal{P}^2D^2\cos^2(\theta)}}{S\sin^2(\theta) + \mathcal{P}\cos^2(\theta)} \right\}. \quad (2.29)$$

From Eq. (2.29) it is clear that a cold magnetized plasma supports two electromagnetic modes which can be either propagating ($k^2 > 0$) or evanescent ($k^2 < 0$) depending on the plasma parameters and the mode frequency. The points at which qualitative changes in the propagation characteristics of electromagnetic waves occur may be found by identifying the resonances ($|k| \rightarrow \infty$) and cutoffs ($k \rightarrow 0$) for propagation parallel to $\mathbf{B}^{(0)}$ ($\theta = 0$) and perpendicular to $\mathbf{B}^{(0)}$ ($\theta = \pi/2$), known as the principal resonances and cutoffs [99, 55]. For $\theta = 0$, the modes supported by Eq. (2.29) are referred to as the R- and L-modes,

$$\text{R-Mode: } k_{\text{R}}^2 = \frac{\omega^2}{c^2}(S + D) = \frac{\omega^2}{c^2} \frac{\omega(\omega + \omega_{ce}) - \omega_{pe}^2}{\omega(\omega + \omega_{ce})}, \quad (2.30)$$

$$\text{L-Mode: } k_{\text{L}}^2 = \frac{\omega^2}{c^2}(S - D) = \frac{\omega^2}{c^2} \frac{\omega(\omega - \omega_{ce}) - \omega_{pe}^2}{\omega(\omega - \omega_{ce})}. \quad (2.31)$$

Since $\omega_{ce} < 0$, the R-mode has a resonance at $\omega = |\omega_{ce}|$, while the L-mode has no resonance for $\omega > 0$. The resonance at $\omega = |\omega_{ce}|$ is the non-relativistic ECR. Cold plasma theory alone does not describe the behavior at the ECR, which requires the inclusion of kinetic and/or collisional effects, but as discussed in Chapter 1, the ECR is a point where electromagnetic waves are absorbed by the electrons. We also note that inserting Eqs. (2.30) and (2.31) in the dispersion equation $\mathcal{D}(\mathbf{k}, \omega) \cdot \mathbf{E}(\mathbf{k}, \omega) = \mathbf{0}$, with \mathcal{D} from Eq. (2.26) and $\theta = 0$, yields the polarization vectors $\mathbf{E}_{\text{R}} = [E_{x,\text{R}}, iE_{y,\text{R}}, 0]$ and $\mathbf{E}_{\text{L}} = [E_{x,\text{L}}, -iE_{y,\text{L}}, 0]$, such that the both modes are circularly polarized with the R-mode being right hand polarized and the L-mode being left hand polarized, which is the motivation for the R,L-nomenclature. The R-mode has a cutoff at $|\omega_{ce}|/\omega = 1 - \omega_{pe}^2/\omega^2$, while the L-mode has a cutoff at $|\omega_{ce}|/\omega = \omega_{pe}^2/\omega^2 - 1$; both cutoffs are given by the condition $\omega_{ce}^2/\omega^2 = (1 - \omega_{pe}^2/\omega^2)^2$. An R/L-mode encountering the R/L-cutoff will be reflected. Now, turning our attention to $\theta = \pi/2$, two different modes, referred to as the O- and X-modes, are supported by Eq. (2.29),

$$\text{O-Mode: } k_{\text{O}}^2 = \frac{\omega^2}{c^2}\mathcal{P} = \frac{\omega^2 - \omega_{pe}^2}{c^2}, \quad (2.32)$$

$$\text{X-Mode: } k_{\text{X}}^2 = \frac{\omega^2}{c^2} \frac{S^2 - D^2}{S} = \frac{\omega^2}{c^2} \frac{(S + D)(S - D)}{S} = \frac{\omega^2}{c^2} \left(1 - \frac{\omega_{pe}^2}{\omega^2} \frac{\omega^2 - \omega_{pe}^2}{\omega^2 - \omega_{UH}^2} \right), \quad (2.33)$$

where $\omega_{UH} = \sqrt{\omega_{pe}^2 + \omega_{ce}^2}$ is the upper hybrid (UH) frequency. The O-mode has a cutoff at $\omega = \omega_{pe}$ and no resonance; O-mode radiation is thus unaffected by $\mathbf{B}^{(0)}$ and reflected when its frequency is equal to the (electron) plasma frequency. We may find the O-mode polarization vector in a manner similar to the R- and L-mode polarization

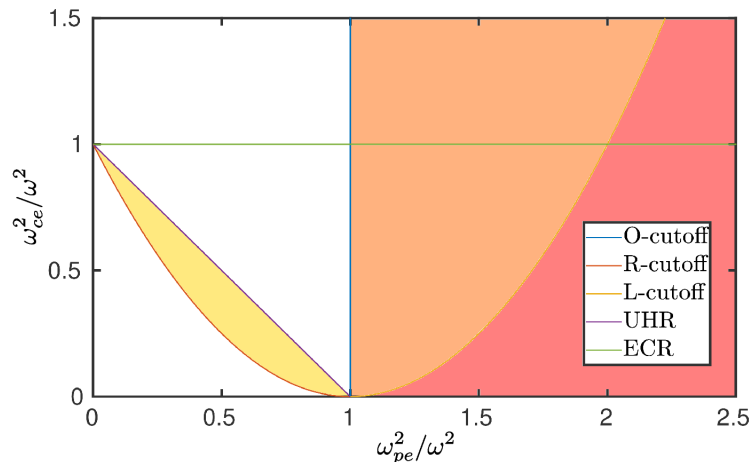


Figure 2.1 – CMA diagram. No propagating X-mode exists in the yellow shaded region, no propagating O-mode exists in the orange shaded region, and neither the O-mode nor the X-mode is propagating in the red shaded region.

vectors, $\mathbf{E}_O = [0, 0, E_{\parallel,O}]$, which shows that O-mode radiation is linearly polarized and only induces motion parallel to $\mathbf{B}^{(0)}$. The mode of interest for PDIs in this work is the X-mode, which is seen to have a resonance at $\omega = \omega_{UH}$, known as the upper hybrid resonance (UHR), and cutoffs at the R- and L-cutoffs ($S \pm D = 0$), characterized by the condition $\omega_{ce}^2/\omega^2 = (1 - \omega_{pe}^2/\omega^2)^2$. The X-mode polarization vector is found to be $\mathbf{E}_X = [(iD/S)E_{y,X}, E_{y,X}, 0]$. Since $E_{x,X} = i\{\omega_{ce}\omega_{pe}^2/[\omega(\omega^2 - \omega_{UH}^2)]\}E_{y,X}$, the x -component of \mathbf{E}_X attains a very large numerical value in the vicinity the UHR, making nonlinear effects, such as PDIs, important in this region. The behavior of X-mode radiation near the UHR requires the inclusion of kinetic and/or collisional effects, but generally involves linear conversion of the X-mode waves to electrostatic electron Bernstein waves (EBWs) at low collision frequencies and collisional absorption at high collision frequencies. Section 2.2 describes EBWs and the linear conversion process within an electrostatic, kinetic framework, while Section 3.3 describes X-mode amplification near the UHR in an inhomogeneous plasma, accounting for a finite collision frequency, but ignoring kinetic effects.

Evaluating the signs of Eqs. (2.32) and (2.33), we find that the O-mode is propagating for $\omega > \omega_{pe}$, while the X-mode is propagating for ω above the R-cutoff frequency, non-propagating for ω below the R-cutoff frequency and above ω_{UH} , propagating for ω below ω_{UH} and above the L-cutoff frequency, and non-propagating for ω below the L-cutoff frequency. These characteristics can be visualized using a Clemmow–Mullaly–Allis (CMA) diagram in which the O-cutoff, $\omega_{pe}^2/\omega^2 = 1$, R-cutoff, $|\omega_{ce}|/\omega = 1 - \omega_{pe}^2/\omega^2$, L-cutoff, $|\omega_{ce}|/\omega = \omega_{pe}^2/\omega^2 - 1$, UHR, $\omega_{UH}^2/\omega^2 = \omega_{pe}^2/\omega^2 + \omega_{ce}^2/\omega^2 = 1$, and ECR, $\omega_{ce}^2/\omega^2 = 1$, are plotted against ω_{pe}^2/ω^2 and ω_{ce}^2/ω^2 , since regions with distinct propagation characteristics are bounded by the above lines [99, 55]. Such a diagram with the regions of interest marked is seen in Fig. 2.1.

2.2 Electrostatic Waves and Electron Bernstein Waves

Having discussed cold electromagnetic waves, we now turn our attention to electrostatic plasma waves. Such waves only propagate in plasmas of finite density and have phase velocities much smaller than c . The latter fact allows the \mathbf{E} associated with the waves to be expressed as an electrostatic field, i.e., $\mathbf{E}(\mathbf{r}) = -\partial\phi(\mathbf{r}, t)/\partial\mathbf{r}$, where ϕ is the electrostatic potential. Rather than employing Eq. (2.11) to describe electrostatic waves, it is more efficient to insert the expression for \mathbf{E} in Eq. (2.4) to obtain the Poisson equation, which governs the evolution of ϕ ,

$$\frac{\partial}{\partial\mathbf{r}} \cdot \frac{\partial\phi(\mathbf{r}, t)}{\partial\mathbf{r}} = -\frac{\rho(\mathbf{r}, t)}{\epsilon_0}. \quad (2.34)$$

As was done with \mathbf{J} for the electromagnetic waves, we write $\rho = \rho_1 + \rho_{\text{nl}}$, where ρ_1 and ρ_{nl} are the linear and nonlinear response of ρ to ϕ , respectively (in this work, we take the equilibrium $\phi = \phi^{(0)} = 0$). ρ_1 may be expressed in a manner similar \mathbf{J}_1 ,

$$-\frac{\rho_1(\mathbf{r}, t)}{\epsilon_0} = \int_{\text{all}(\mathbf{r}', t')} X\left(\mathbf{r} - \mathbf{r}', \frac{\mathbf{r} + \mathbf{r}'}{2}; t - t', \frac{t + t'}{2}\right) \phi(\mathbf{r}', t') \, d\mathbf{r}' \, dt', \quad (2.35)$$

where X plays the role of a generalized susceptibility in physical space. X may be connected to $\boldsymbol{\sigma}$ through the charge continuity equation,

$$\frac{\partial\rho}{\partial t} + \frac{\partial}{\partial\mathbf{r}} \cdot \mathbf{J}(\mathbf{r}, t) = 0, \quad (2.36)$$

which is obtained by taking the divergence of Eq. (2.3) and inserting Eq. (2.4). Linearizing Eq. (2.36), $\partial\rho_1/\partial t = -(\partial/\partial\mathbf{r}) \cdot \mathbf{J}_1$, using Eqs. (2.10) and (2.35) with $\mathbf{E}(\mathbf{r}', t') = -\partial\phi(\mathbf{r}', t')/\partial\mathbf{r}'$, and integrating by parts, we find

$$\frac{\partial X}{\partial t}\left(\mathbf{r} - \mathbf{r}', \frac{\mathbf{r} + \mathbf{r}'}{2}; t - t', \frac{t + t'}{2}\right) = \frac{1}{\epsilon_0} \frac{\partial}{\partial\mathbf{r}'} \cdot \left[\frac{\partial}{\partial\mathbf{r}} \cdot \boldsymbol{\sigma}\left(\mathbf{r} - \mathbf{r}', \frac{\mathbf{r} + \mathbf{r}'}{2}; t - t', \frac{t + t'}{2}\right) \right]; \quad (2.37)$$

in a homogeneous plasma, where $X = X(\mathbf{r} - \mathbf{r}', t - t')$ and $\boldsymbol{\sigma} = \boldsymbol{\sigma}(\mathbf{r} - \mathbf{r}', t - t')$, Eq. (2.37) can further be Fourier–Laplace transformed to give $X(\mathbf{k}, \omega) = \mathbf{i}\mathbf{k} \cdot \boldsymbol{\sigma}(\mathbf{k}, \omega) \cdot \mathbf{k}/(\epsilon_0\omega)$. Now, returning to Eq. (2.34), plugging in Eq. (2.35), and using $\phi(\mathbf{r}, t) = \int_{\text{all}(\mathbf{r}', t')} \delta(\mathbf{r} - \mathbf{r}')\delta(t - t')\phi(\mathbf{r}', t') \, d\mathbf{r}' \, dt'$, we obtain an integral equation for electrostatic waves,

$$\int_{\text{all}(\mathbf{r}', t')} \left[X\left(\mathbf{r} - \mathbf{r}', \frac{\mathbf{r} + \mathbf{r}'}{2}; t - t', \frac{t + t'}{2}\right) - \frac{\partial}{\partial\mathbf{r}} \cdot \frac{\partial\delta(\mathbf{r} - \mathbf{r}')}{\partial\mathbf{r}} \delta(t - t') \right] \phi(\mathbf{r}', t') \, d\mathbf{r}' \, dt' = \frac{\rho_{\text{nl}}(\mathbf{r}, t)}{\epsilon_0}. \quad (2.38)$$

Eq. (2.38) is the main equation used for studying parametric decay instabilities in this work; in Chapter 3, we consider the left hand side in the semi-classical limit, while the right hand side is considered in Chapter 4. However, in the present Chapter, we assume the plasma to be homogeneous, i.e., $X = X(\mathbf{r} - \mathbf{r}', t - t')$, which turns the left hand side

of Eq. (2.38) into a convolution integral and allows the Fourier–Laplace transform of the equation to be evaluated using the convolution theorem [97],

$$\mathcal{D}(\mathbf{k}, \omega)\phi(\mathbf{k}, \omega) = [X(\mathbf{k}, \omega) + k^2]\phi(\mathbf{k}, \omega) = \frac{\rho_{\text{nl}}(\mathbf{k}, \omega)}{\epsilon_0}; \quad (2.39)$$

from Eqs. (2.37) and (2.12), the dispersion function $\mathcal{D}(\mathbf{k}, \omega) = k^2 + \mathbf{i}\mathbf{k} \cdot \boldsymbol{\sigma}(\mathbf{k}, \omega) \cdot \mathbf{k}/(\epsilon_0\omega) = \mathbf{k} \cdot \mathcal{D}(\mathbf{k}, \omega) \cdot \mathbf{k}/\omega^2$. To study linear waves, we set $\rho_{\text{nl}} = 0$. This turns Eq. (2.39) into a homogeneous equation which only has non-trivial solutions (with $\phi \neq 0$) if the dispersion relation

$$\mathcal{D}(\mathbf{k}, \omega) = X(\mathbf{k}, \omega) + k^2 = 0 \quad (2.40)$$

is satisfied. Eq. (2.40) plays the same role for electrostatic waves as Eq. (2.14) does for electromagnetic waves, and just as the plasma response was contained in $\boldsymbol{\sigma}$ for electromagnetic waves, it is contained in X for electrostatic waves.

Since electrostatic waves have phase velocities comparable with the thermal plasma particle velocities rather than c , their description generally requires a kinetic treatment of the plasma response. We thus return to Eq. (2.1), for now limiting our discussion to the electrons, as we are considering waves with $\omega \sim |\omega_{ce}| \gg \omega_{ci}$. In order to obtain X , Eq. (2.1) must be linearized around a background plasma which we take to be homogeneous and in thermal equilibrium. We further assume the plasma to be non-relativistic ($\mathbf{p} \approx m_e\mathbf{v}$) and the collision operator to be a particle conserving Krook operator [102, 103, 104], commonly used for studying PDIs [105, 106, 107, 13]. This gives

$$f_e^{(0)}(\mathbf{p}) = \frac{n_e^{(0)} e^{-p^2/(m_e v_{Te})^2}}{\pi^{3/2}(m_e v_{Te})^3}, \quad \left[\frac{\partial f_e(\mathbf{r}, \mathbf{p}, t)}{\partial t} \right]_{\text{col}} = \nu_e \left[\frac{n_e(\mathbf{r}, t)}{n_e^{(0)}} f_e^{(0)}(\mathbf{p}) - f_e(\mathbf{r}, \mathbf{p}, t) \right], \quad (2.41)$$

where $f_e^{(0)}(\mathbf{p})$ is the Maxwellian thermal equilibrium background distribution, $v_{Te} = \sqrt{2T_e/m_e}$ is the thermal electron speed (T_e is the electron temperature in energy units), and ν_e is a semi-empirical electron collision frequency which is usually set equal to ν_{ei} in a fully ionized plasma [104]. The above assumptions, along with the electrostatic approximations, $\mathbf{E} = -\partial\phi/\partial\mathbf{r}$ and $\mathbf{B} = \mathbf{B}^{(0)}$, allow Eq. (2.1) to be linearized and X to be found using the method of characteristics [105]. Since the details of the calculation are of little importance in what follows, we simply quote the result [105],

$$X(\mathbf{k}, \omega) = \frac{2\omega_{pe}^2}{v_{Te}^2} \frac{1 + \frac{\omega + i\nu_e}{k_{\parallel} v_{Te}} \sum_{n=-\infty}^{\infty} I_n(k_{\perp}^2 r_{Le}^2) e^{-k_{\perp}^2 r_{Le}^2} \mathcal{Z}\left(\frac{\omega + i\nu_e - n\omega_{ce}}{k_{\parallel} v_{Te}}\right)}{1 + \frac{i\nu_e}{k_{\parallel} v_{Te}} \sum_{n=-\infty}^{\infty} I_n(k_{\perp}^2 r_{Le}^2) e^{-k_{\perp}^2 r_{Le}^2} \mathcal{Z}\left(\frac{\omega + i\nu_e - n\omega_{ce}}{k_{\parallel} v_{Te}}\right)}, \quad (2.42)$$

where $r_{Le} = v_{Te}/(\sqrt{2}|\omega_{ce}|) = \sqrt{m_e T_e}/[eB^{(0)}]$ defines the thermal electron Larmor radius, k_{\parallel} and $k_{\perp} = \sqrt{k^2 - k_{\parallel}^2}$ are the components of \mathbf{k} parallel and perpendicular to $\mathbf{B}^{(0)}$, respectively, $\mathcal{Z}(\zeta) = (1/\sqrt{\pi}) \int_{-\infty}^{\infty} [e^{-\xi^2}/(\xi - \zeta)] d\xi$ is the Fried–Conte plasma dispersion function [99, 55], and I_n is a modified Bessel function of the first kind of order n [97].

Plugging Eq. (2.42) into Eq. (2.40) yields a dispersion relation with an infinite number of wave solutions; the waves with \mathbf{k} nearly perpendicular to $\mathbf{B}^{(0)}$ ($k_{\perp} \gg |k_{\parallel}|$) are collectively known as electron Bernstein waves (EBWs) [108] (except for the electrostatic approximation of the X-mode wave). In this regime, it generally holds that $|(\omega + i\nu_e - n\omega_{ce})/(k_{\parallel}v_{Te})| \gg 1$, permitting use of the large-argument asymptotic approximation of \mathcal{Z} , $\mathcal{Z}(\zeta) \approx -1/\zeta - 1/(2\zeta^3) + i e^{-\zeta^2}$ for $|\zeta| \gg 1$ (when the imaginary part of ζ is small) [55]. For $|\nu_e/\omega| \ll 1$, which is always the case in the present work, this causes the $-n$ th term to practically diverge near the n th EC harmonic, meaning that a solution with $\omega \approx n|\omega_{ce}|$ exists for all $n \in \mathbb{N}$; these solutions make up the bulk of the EBW modes. However, the EBWs of interest in this work belong to a special branch of the dispersion relation which merges with the slow X-mode at the UHR. This branch can be investigated by assuming $k_{\perp}^2 r_{Le}^2 \ll 1$ (in addition to $|(\omega + i\nu_e - n\omega_{ce})/(k_{\parallel}v_{Te})| \gg 1$ and $|\nu_e/\omega| \ll 1$) and carrying out an expansion of X to first order in all small quantities. The details of the calculation are given in [109]; here, we only quote the final result,

$$X(\mathbf{k}, \omega) \approx - \left[\frac{\omega_{pe}^2}{\omega^2 - \omega_{ce}^2} + \frac{3\omega_{pe}^2 \omega_{ce}^2 r_{Le}^2 k_{\perp}^2}{(\omega^2 - \omega_{ce}^2)(\omega^2 - 4\omega_{ce}^2)} - i \frac{\omega_{pe}^2 (\omega^2 + \omega_{ce}^2) \nu_e}{(\omega^2 - \omega_{ce}^2)^2 \omega} \right] k_{\perp}^2 - \left[\frac{\omega_{pe}^2}{\omega^2} - i \frac{\omega_{pe}^2 \omega}{|k_{\parallel}|^3 v_{Te}^3} e^{-\omega^2/(k_{\parallel}^2 v_{Te}^2)} \right] k_{\parallel}^2. \quad (2.43)$$

Inserting Eq. (2.43) in Eq. (2.40), remembering that $k^2 = k_{\perp}^2 + k_{\parallel}^2$, yields the dispersion relation

$$\mathcal{D}(\mathbf{k}, \omega) = \ell_{Te}^2 k_{\perp}^4 + S k_{\perp}^2 + \mathcal{P} k_{\parallel}^2 + iI = 0, \quad (2.44)$$

where S and \mathcal{P} are defined in Eq. (2.27), while

$$\ell_{Te}^2 = \frac{3\omega_{pe}^2 \omega_{ce}^2}{(4\omega_{ce}^2 - \omega^2)(\omega^2 - \omega_{ce}^2)} r_{Le}^2, \quad I = k_{\perp}^2 \frac{\omega_{pe}^2 (\omega^2 + \omega_{ce}^2) \nu_e}{(\omega^2 - \omega_{ce}^2)^2 \omega} + \frac{\omega_{pe}^2 \omega}{|k_{\parallel}| v_{Te}^3} e^{-\omega^2/(k_{\parallel}^2 v_{Te}^2)}. \quad (2.45)$$

We note that if we set $\nu_e = 0$ and use the cold plasma approximation, $\ell_{Te} = v_{Te} = 0$, the dispersion relation can be written as $\mathcal{D}(\mathbf{k}, \omega) = S k_{\perp}^2 + \mathcal{P} k_{\parallel}^2 = [S \sin^2(\theta) + \mathcal{P} \cos^2(\theta)] k^2 = 0$, which is equivalent to the electrostatic version of the cold plasma dispersion relation, as it should be.

As we are using a Laplace transform in t , ω is allowed to have an imaginary part which is important when discussing damping and instabilities. We write $\omega = \omega_j + i\gamma$, where $\omega_j \geq 0$ is the real frequency of the wave, with the subscript j characterizing a particular wave mode, and $\gamma \in \mathbb{C}$ includes the imaginary part of ω , with $\text{Re}(\gamma) < 0$ indicating damping and $\text{Re}(\gamma) > 0$ indicating instability; γ is allowed to have an imaginary part to account for frequency shifts due to wave–wave interactions. We generally assume that $\omega_j \gg |\gamma|$. Similarly writing $\mathcal{D} = \mathcal{D}' + i\mathcal{D}''$, with \mathcal{D}' being the part of \mathcal{D} not containing an explicit i and \mathcal{D}'' being the part containing an explicit i , e.g., $\mathcal{D}' = \ell_{Te}^2 k_{\perp}^4 + S k_{\perp}^2 + \mathcal{P} k_{\parallel}^2$ and $\mathcal{D}'' = I$ in Eq. (2.44), and assuming the ordering $|\mathcal{D}'| \gg |\mathcal{D}''|$ allows us to expand \mathcal{D} to first order

around (\mathbf{k}, ω_j) , yielding

$$\mathcal{D}(\mathbf{k}, \omega) \approx \mathcal{D}'(\mathbf{k}, \omega_j) + i \left[\mathcal{D}''(\mathbf{k}, \omega_j) + \gamma \frac{\partial \mathcal{D}'(\mathbf{k}, \omega)}{\partial \omega} \Big|_{\omega=\omega_j} \right]; \quad (2.46)$$

a similar expression holds for electromagnetic waves if we let $\mathcal{D} \rightarrow \det(\mathbf{D})$. $\mathcal{D}'(\mathbf{k}, \omega_j)$ and $\mathcal{D}''(\mathbf{k}, \omega_j)$ are both real, and for linear waves γ is also real, so within the approximation of Eq. (2.46), the real and imaginary parts of the dispersion relation $\mathcal{D}(\mathbf{k}, \omega) = 0$ become

$$\mathcal{D}'(\mathbf{k}, \omega_j) = 0, \quad (2.47)$$

$$\gamma = -\Gamma(\mathbf{k}, \omega_j) = -\frac{\mathcal{D}''(\mathbf{k}, \omega_j)}{\partial \mathcal{D}'(\mathbf{k}, \omega) / \partial \omega |_{\omega=\omega_j}}. \quad (2.48)$$

Eq. (2.47) determines the connection between ω_j and \mathbf{k} , while Eq. (2.48) determines the linear damping rate, Γ .

For the waves whose \mathcal{D} is given in Eq. (2.44), Eq. (2.47) gives

$$\mathcal{D}'(\mathbf{k}, \omega_j) = \ell_{Te,j}^2 k_{\perp}^4 + S_j k_{\perp}^2 + \mathcal{P}_j k_{\parallel}^2 = 0, \quad (2.49)$$

where $\ell_{Te,j}^2$, S_j , and \mathcal{P}_j are ℓ_{Te}^2 , S , and \mathcal{P} evaluated at $\omega = \omega_j$. Eq. (2.49) is a quadratic equation for k_{\perp}^2 which may be solved to give

$$(k_{\perp}^{\pm})^2 = -\frac{S_j}{2\ell_{Te,j}^2} \left(1 \pm \sqrt{1 - \frac{4\mathcal{P}_j k_{\parallel}^2 \ell_{Te,j}^2}{S_j^2}} \right). \quad (2.50)$$

Eq. (2.50) supports two modes that merge at $S_j^2 = 4\mathcal{P}_j k_{\parallel}^2 \ell_{Te,j}^2$, which reduces to $S_j = 0$, i.e., the UHR, in the cold plasma limit; it is thus capable of describing linear mode conversion at the UHR. We can gain insight into the modes supported by the dispersion relation by assuming $4\mathcal{P}_j k_{\parallel}^2 \ell_{Te,j}^2 / S_j^2 \ll 1$ and expanding the square root in Eq. (2.50) to first order in this parameter,

$$(k_{\perp}^{-})^2 \approx -\frac{\mathcal{P}_j}{S_j} k_{\parallel}^2, \quad (2.51)$$

$$(k_{\perp}^{+})^2 \approx -\frac{S_j}{\ell_{Te,j}^2} + \frac{\mathcal{P}_j}{S_j} k_{\parallel}^2. \quad (2.52)$$

Eq. (2.51) is the dispersion relation for electrostatic, cold plasma waves, e.g., the slow X-mode wave close to the UHR, while Eq. (2.52) describes an EBW which has a wave vector depending on $\ell_{Te,j}^2$. A useful approximation of Eq. (2.52) can be obtained if we consider \mathbf{k} to be almost perpendicular to $\mathbf{B}^{(0)}$, such that $k_{\parallel}^2 \ll |S_j (k_{\perp}^{+})^2 / \mathcal{P}_j|$. In this case, $S_j \approx -(k_{\perp}^{+})^2 \ell_{Te}^2$ can be inserted in the term proportional to k_{\parallel}^2 , giving

$$S_j \approx -(k_{\perp}^{+})^2 \ell_{Te,j}^2 - \mathcal{P}_j \frac{k_{\parallel}^2}{(k_{\perp}^{+})^2}. \quad (2.53)$$

Generally $|k_{\perp}^+ \ell_{Te,j}|^2 \sim |k_{\perp}^+ r_{Le}|^2 \ll 1$ and $|\mathcal{P}_j k_{\parallel}^2 / (k_{\perp}^+)^2| \ll 1$ in this case, so $|S_j| \ll 1$ and $\omega_j \approx \omega_{UH}$. This allows us to use the approximations $S_j \approx (\omega_j^2 - \omega_{UH}^2) / \omega_{pe}^2$, $\mathcal{P}_j \approx \omega_{ce}^2 / \omega_{UH}^2$, and $\ell_{Te,j}^2 \approx r_{Le}^2 / [1 - \omega_{pe}^2 / (3\omega_{ce}^2)]$ to find

$$\omega^2 \approx \omega_{UH}^2 - \omega_{pe}^2 \left[\frac{(k_{\perp}^+)^2 r_{Le}^2}{1 - \omega_{pe}^2 / (3\omega_{ce}^2)} + \frac{\omega_{ce}^2}{\omega_{UH}^2} \frac{k_{\parallel}^2}{(k_{\perp}^+)^2} \right], \quad (2.54)$$

which is used in [110, 111, 109, 13]. A further approximation can be obtained by writing $S_j \approx (\omega_j + \omega_{UH})(\omega_j - \omega_{UH}) / \omega_{pe}^2 \approx 2\omega_{UH}(\omega_j - \omega_{UH}) / \omega_{pe}^2$, with which

$$\omega \approx \omega_{UH} - \frac{\omega_{pe}^2}{2\omega_{UH}} \left[\frac{(k_{\perp}^+)^2 r_{Le}^2}{1 - \omega_{pe}^2 / (3\omega_{ce}^2)} + \frac{\omega_{ce}^2}{\omega_{UH}^2} \frac{k_{\parallel}^2}{(k_{\perp}^+)^2} \right]; \quad (2.55)$$

this approximation is used in [14].

While Eq. (2.50) may be used to study mode conversion at the UHR, its purely electrostatic nature makes it unsuitable in the case $k_{\parallel} = 0$, which is the one of most interest in this work. For $k_{\parallel} = 0$, $(k_{\perp}^-)^2 = 0$ and $(k_{\perp}^+)^2 = -S_j / \ell_{Te,j}^2$ is found, meaning that the cold branch of the dispersion relation is non-propagating. We can, however, obtain an *ad hoc* solution of this problem by requiring the cold branch to match the cold X-mode far from the UHR. To do this, we note that the cold electromagnetic dispersion relation in Eq. (2.28) may be multiplied by $\omega^2 / (c^2 k^2)$ to give

$$S k_{\perp}^2 + \mathcal{P} k_{\parallel}^2 - \frac{\omega^2}{c^2} \left[\mathcal{P} S \left(1 + \frac{k_{\parallel}^2}{k^2} \right) + (S^2 - D^2) \frac{k_{\perp}^2}{k^2} \right] + \frac{\omega^2}{c^2} \frac{\omega^2}{c^2 k^2} \mathcal{P} (S^2 - D^2) = 0, \quad (2.56)$$

where use has been made of $k_{\parallel} = k \cos(\theta)$ and $k_{\perp} = k \sin(\theta)$. Eq. (2.56) resembles the cold version of Eq. (2.49), but includes terms $\sim \omega^2 / c^2$ which are neglected in the electrostatic approximation. As the terms $\sim \omega^2 / c^2$ in Eq. (2.56) should lead to a dispersion relation matching that of the cold X-mode far from the UHR when $k_{\parallel} = 0$, we set $k_{\parallel} = 0$ and $k_{\perp}^2 \approx k_X^2 = (\omega^2 / c^2) (S^2 - D^2) / S$ in these to find

$$S k_{\perp}^2 + \mathcal{P} k_{\parallel}^2 - \frac{\omega^2}{c^2} (S^2 - D^2) \approx 0. \quad (2.57)$$

Based on Eq. (2.57), it seems that adding $-(\omega^2 / c^2) (S^2 - D^2)$ to \mathcal{D} in Eq. (2.44) should lead to a dispersion relation with the desired properties. Hence, we arrive at the corrected dispersion relation

$$\mathcal{D}(\mathbf{k}, \omega) = \ell_{Te}^2 k_{\perp}^4 + S k_{\perp}^2 + \mathcal{P} k_{\parallel}^2 - \frac{\omega^2}{c^2} (S^2 - D^2) + iI = 0, \quad (2.58)$$

which is similar to the ones used by [8, 9, 10, 11, 112, 12]. Approximating the solution of Eq. (2.58) by Eq. (2.47), we find

$$\mathcal{D}'(\mathbf{k}, \omega_j) = \ell_{Te,j}^2 k_{\perp}^4 + S_j k_{\perp}^2 + \mathcal{P}_j k_{\parallel}^2 - \frac{\omega_j^2}{c^2} (S_j^2 - D_j^2) = 0, \quad (2.59)$$

where D_j is D from Eq. (2.27) evaluated at $\omega = \omega_j$. Just as Eq. (2.49), Eq. (2.59) is a quadratic equation for k_{\perp}^2 , which can be solved to give

$$(k_{\perp}^{\pm})^2 = -\frac{S_j}{2\ell_{Te,j}^2} \left(1 \pm \sqrt{1 - \frac{4\mathcal{P}_j k_{\parallel}^2 \ell_{Te,j}^2}{S_j^2} + \frac{4\omega_j^2 \ell_{Te,j}^2}{c^2} \frac{S_j^2 - D_j^2}{S_j^2}} \right). \quad (2.60)$$

The two branches merge at $S_j^2 = 4\ell_{Te,j}^2[\mathcal{P}_j k_{\parallel}^2 - (\omega_j^2/c^2)(S_j^2 - D_j^2)]$, reducing to $S_j^2 = -4\ell_{Te,j}^2(\omega_j^2/c^2)(S_j^2 - D_j^2)$ at $k_{\parallel} = 0$, which we shall refer to as the warm UHR. By assuming $4|\ell_{Te,j}^2[\mathcal{P}_j k_{\parallel}^2 - (\omega_j^2/c^2)(S_j^2 - D_j^2)]| \ll 1$ and expanding the terms in the square root to first order in this parameter, we find

$$(k_{\perp}^{-})^2 \approx -\frac{\mathcal{P}_j}{S_j} k_{\parallel}^2 + \frac{\omega_j^2}{c^2} \frac{S_j^2 - D_j^2}{S_j}, \quad (2.61)$$

$$(k_{\perp}^{+})^2 \approx -\frac{S_j}{\ell_{Te,j}^2} + \frac{\mathcal{P}_j}{S_j} k_{\parallel}^2 - \frac{\omega_j^2}{c^2} \frac{S_j^2 - D_j^2}{S_j}. \quad (2.62)$$

Eq. (2.61) demonstrates that the cold branch of Eq. (2.59) approaches the cold X-mode far from the warm UHR, as wanted; Eq. (2.62) is a generalization of Eq. (2.52).

We finally consider the conditions for propagating EBWs when $k_{\parallel} = 0$ and $\ell_{Te,j}^2 > 0$; from Eq. (2.45), the latter condition is equivalent to $|\omega_{ce}| < \omega_j < 2|\omega_{ce}|$ and restricts the results to underdense and moderately overdense plasmas, similar to the ones found in conventional tokamaks. In this case, $(k_{\perp}^{+})^2 = -[S_j/(2\ell_{Te,j}^2)][1 + \sqrt{1 + 4\omega_j^2 \ell_{Te,j}^2 (S_j^2 - D_j^2)/(c^2 S_j^2)}]$, which can only be positive if

$$S_j = \frac{\omega_j^2 - \omega_{UH}^2}{\omega_j^2 - \omega_{ce}^2} < 0, \quad (2.63)$$

requiring

$$|\omega_{ce}| < \omega_j < \omega_{UH}, \quad (2.64)$$

which means that the EBWs exist on the same side of the UHR as the cold X-mode waves, as required for wave trapping. For the EBWs to be propagating, it is further necessary that the argument of the square root be positive. Remembering that $k_{X,j}^2 = (\omega^2/c^2)(S^2 - D^2)/S$, this may be written as

$$\ell_{Te,j}^2 < -\frac{S_j}{4k_{X,j}^2}, \quad (2.65)$$

where $k_{X,j}^2$ is k_X^2 evaluated at $\omega = \omega_j$. Plugging in the explicit expressions, Eq. (2.65) is recast in the form

$$T_e < T_e^c = \frac{(4\omega_{ce}^2/\omega_j^2 - 1)(1 - \omega_{pe}^2/\omega_j^2 - \omega_{ce}^2/\omega_j^2)^2}{12(\omega_{pe}^2/\omega_j^2)[\omega_{ce}^2/\omega_j^2 - (1 - \omega_{pe}^2/\omega_j^2)^2]} m_e c^2, \quad (2.66)$$

with T_e^c being a critical electron temperature above which the EBWs are no longer propagating. From Eq. (2.66), $T_e^c = 0$ for $\omega_j = 2|\omega_{ce}|$ and $\omega_j = \omega_{UH}$, which are the 2nd

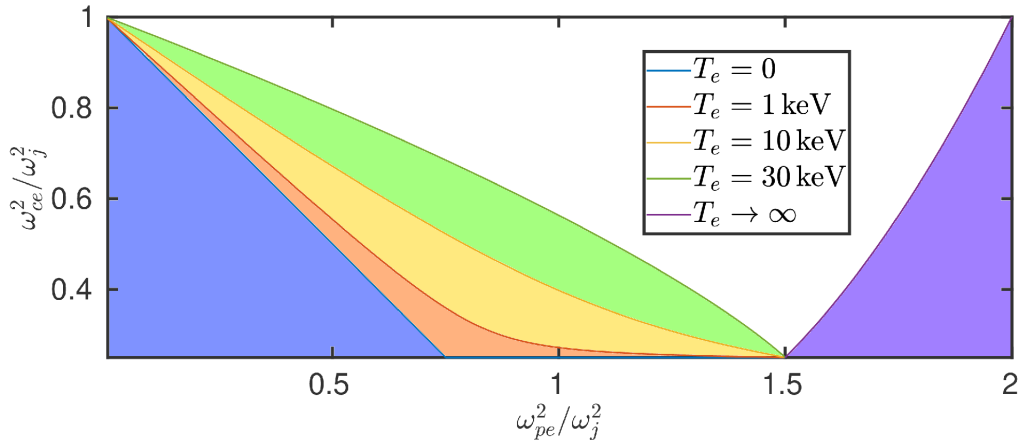


Figure 2.2 – Electron Bernstein wave CMA-like diagram where $\ell_{Te,j}^2 > 0$. No propagating EBWs exist in the blue or purple shaded regions at any T_e . For $T_e = 1$ keV, no propagating EBWs additionally exist in the orange shaded region, for $T_e = 10$ keV the yellow shaded region is added to the region with no propagation EBWs, and for $T_e = 30$ keV the green shaded region is finally added.

harmonic ECR and the cold UHR, respectively, while $T_e^c \rightarrow \infty$ for $\omega_{ce}^2/\omega_j^2 = (1 - \omega_{pe}^2/\omega_j^2)$, which is the cold X-mode cutoff condition, particularly the L-cutoff in this case; for ω_j below the L-cutoff frequency, $T_e^c < 0$ and no propagating EBWs exist. At $T_e = 0$ propagating EBWs will thus exist in the CMA region bounded by the ECR, $\omega_{ce}^2/\omega_j^2 = 1$, the cold UHR, $\omega_{UH}^2/\omega_j^2 = \omega_{pe}^2/\omega_j^2 + \omega_{ce}^2/\omega_j^2 = 1$, the 2nd harmonic ECR, $\omega_{ce}^2/\omega_j^2 = 1/4$, and the X-mode cutoff, $\omega_{ce}^2/\omega_j^2 = (1 - \omega_{pe}^2/\omega_j^2)^2$. At finite T_e , the 2nd harmonic ECR and the cold UHR are replaced by the line where $T_e = T_e^c$, with T_e^c defined in Eq. (2.66), which we refer to as the warm UHR. A CMA-like diagram showing the region with propagating EBWs at different T_e is found in Fig. 2.2.

2.3 Ion Bernstein and Warm Lower Hybrid Waves

So far, we have discussed waves in the EC frequency range for which the ion response could be neglected. However, PDIs often cause pump waves in the EC frequency range to decay to one daughter wave with a frequency close to that of the pump wave and one daughter wave with a frequency much lower than that of the pump wave, for which the ion response may be important. Confining our attention to electrostatic waves, we note that X may be written as a sum of electron and ion contributions,

$$X(\mathbf{k}, \omega) = X_e(\mathbf{k}, \omega) + \sum_i X_i(\mathbf{k}, \omega); \quad (2.67)$$

X_e is the electron susceptibility and X_i is the ion susceptibility, with the sum indicating the possibility of multiple ionic species. For a non-relativistic plasma with a Maxwellian background distribution and a particle conserving Krook collision operator, both of which

are seen in Eq. (2.41), X_e and X_i are given in the form of Eq. (2.42) (if the subscripts $e \rightarrow i$ for the ions). Confining our attention to \mathbf{k} almost perpendicular to $\mathbf{B}^{(0)}$, X_e may be approximated by Eq. (2.43), and since we are in the low-frequency regime, where $|\omega| \ll |\omega_{ce}|$, this can be further reduced to

$$X_e(\mathbf{k}, \omega) \approx \frac{\omega_{pe}^2}{\omega_{ce}^2} \left(1 - \frac{3}{4} r_{Le}^2 k_{\perp}^2 + i \frac{\nu_e}{\omega} \right) k_{\perp}^2 - \frac{\omega_{pe}^2}{\omega^2} \left[1 - i \frac{\omega^3}{|k_{\parallel}|^3 v_{Te}^3} e^{-\omega^2/(k_{\parallel}^2 v_{Te}^2)} \right] k_{\parallel}^2; \quad (2.68)$$

note that the requirement of $k_{\parallel}^2/k_{\perp}^2 \ll 1$ is much stricter in the low-frequency regime than in the high-frequency regime, as the coefficient of k_{\parallel}^2 , ω_{pe}^2/ω^2 , is numerically large in this case. X_i can be evaluated using different approximations. First, the ion collision frequency is generally small compared with that of the electrons, and we hence set $\nu_i \approx 0$ in X_i [109]. With this, we obtain

$$X_i(\mathbf{k}, \omega) = \frac{2\omega_{pi}^2}{v_{Ti}^2} \left[1 + \frac{\omega}{k_{\parallel} v_{Ti}} \sum_{n=-\infty}^{\infty} I_n(k_{\perp}^2 r_{Li}^2) e^{-k_{\perp}^2 r_{Li}^2} Z \left(\frac{\omega - n\omega_{ci}}{k_{\parallel} v_{Ti}} \right) \right]. \quad (2.69)$$

For propagation perpendicular to $\mathbf{B}^{(0)}$, we can use $Z[(\omega - n\omega_{ci})(k_{\parallel} v_{Ti})] \approx k_{\parallel} v_{Ti}/(n\omega_{ci} - \omega)$ and collect the $\pm n$ -terms, remembering that $I_n(k_{\perp}^2 r_{Li}^2) = I_{-n}(k_{\perp}^2 r_{Li}^2)$ for $n \in \mathbb{Z}$ and $1 = \sum_{n=-\infty}^{\infty} I_n(k_{\perp}^2 r_{Li}^2) e^{-k_{\perp}^2 r_{Li}^2}$ [113], to get

$$X_i(\mathbf{k}, \omega) \approx -\frac{2}{r_{Li}^2} \sum_{n=1}^{\infty} I_n(k_{\perp}^2 r_{Li}^2) e^{-k_{\perp}^2 r_{Li}^2} \frac{n^2 \omega_{pi}^2}{\omega^2 - n^2 \omega_{ci}^2}. \quad (2.70)$$

Just as for EBWs, the dispersion relation with X_i from Eq. (2.70) admits solutions with $\omega \approx n\omega_{ci}$, known as ion Bernstein waves (IBWs). If we take $k_{\perp}^2 r_{Li}^2 \ll 1$ and assume $\omega \approx m\omega_{ci}$ for $m \geq 2$, we can approximate Eq. (2.70) by keeping only the $n = 1$ and $n = m$ terms and using $I_n(k_{\perp}^2 r_{Li}^2) e^{-k_{\perp}^2 r_{Li}^2} \approx (k_{\perp}^2 r_{Li}^2)^n / (2^n n!)$ [113], giving

$$X_i(\mathbf{k}, \omega) \approx -k_{\perp}^2 \left[\frac{\omega_{pi}^2}{(m^2 - 1)\omega_{ci}^2} + \frac{(k_{\perp}^2 r_{Li}^2)^{m-1}}{2^m (m-1)!} \frac{\omega_{pi}^2}{\omega_{ci}(\omega - m\omega_{ci})} \right]. \quad (2.71)$$

For a simple, quasi-neutral plasma (with one ionic species), we can then insert X_i from Eq. (2.71) in the dispersion relation $\mathcal{D}(\mathbf{k}, \omega) = k^2 + X_e(\mathbf{k}, \omega) + X_i(\mathbf{k}, \omega) = 0$, along with $X_e(\mathbf{k}, \omega) \approx (\omega_{pe}^2/\omega_{ce}^2)k_{\perp}^2$ from Eq. (2.68) and $k^2 \approx k_{\perp}^2$, to find the dispersion relation for IBWs with $m \geq 2$,

$$\omega \approx m\omega_{ci} \left\{ 1 - \frac{(m^2 - 1)(k_{\perp}^2 r_{Li}^2)^{m-1}}{2^m (m-1)! [1 - (m^2 - 1)(\omega_{ci}^2/\omega_{pi}^2 + Z_i m_e/m_i)]} \right\}; \quad (2.72)$$

here, use has been made of the quasi-neutrality condition in a simple plasma, $n_e^{(0)} = Z_i n_i^{(0)}$, where $Z_i = q_i/e$ is the ion charge number. We note that Eq. (2.72) is equivalent to Eq. (4.277) of [55] if V_A is identified with the non-inductive Alfvén speed and m_e/m_i is neglected; the IBW dispersion relation with $m = 2$ from [55] was used in [14].

As was the case for EBWs, the IBW dispersion relation also has a special branch near a hybrid resonance. However, unlike the EBW-case, the special branch of the IBW dispersion relation generally occurs at large $k_{\perp}^2 r_{Li}^2$ and at high ion cyclotron harmonics, since $\omega_{pi}^2/\omega_{ci}^2 = [m_i/(Z_i m_e)]\omega_{pe}^2/\omega_{ce}^2 \gg \omega_{pe}^2/\omega_{ce}^2$. In this limit, the ion Larmor radius is large compared with the wavelength and the wave frequency is large compared with the ion cyclotron frequency. The ion response to the wave can thus, in some sense, be considered unmagnetized, which modifies X_i to [99, 55]

$$X_i(\mathbf{k}, \omega) = \frac{2\omega_{pi}^2}{v_{Ti}^2} \left[1 + \frac{\omega}{k v_{Ti}} \mathcal{Z} \left(\frac{\omega}{k v_{Ti}} \right) \right]. \quad (2.73)$$

While the approximation of unmagnetized ions may be shown to match the real part of the magnetized X_i from Eq. (2.69) for $k_{\perp}^2 r_{Li}^2 \gg 1$ and $|\omega| \gg \omega_{ci}$ [114, 55], the imaginary part related to Landau damping requires more careful discussion [61, 114, 60].

Returning to Eq. (2.73), the dispersion relation of the special branch is obtained by first using the asymptotic approximation of \mathcal{Z} [55],

$$\mathcal{Z} \left(\frac{\omega}{k v_{Ti}} \right) \approx -\frac{k v_{Ti}}{\omega} - \frac{1}{2} \frac{k^3 v_{Ti}^3}{\omega^3} - \frac{3}{4} \frac{k^5 v_{Ti}^5}{\omega^5} + i\sqrt{\pi} e^{-\omega^2/(k^2 v_{Ti}^2)}, \quad (2.74)$$

which recasts Eq. (2.73) as

$$X_i(\mathbf{k}, \omega) \approx -\frac{\omega_{pi}^2}{\omega^2} \left[1 + \frac{3}{2} \frac{k^2 v_{Ti}^2}{\omega^2} - i\sqrt{\pi} \frac{\omega^3}{k^3 v_{Ti}^3} e^{-\omega^2/(k^2 v_{Ti}^2)} \right] k^2. \quad (2.75)$$

Now, setting $k^2 \approx k_{\perp}^2$ and recalling that $v_{Ti}^2 = 2[T_i/(Z_i T_e)]\omega_{ci}|\omega_{ce}|r_{Le}^2$, the dispersion relation of the special branch in a simple, quasi-neutral plasma, $\mathcal{D}(\mathbf{k}, \omega) = k^2 + X_e(\mathbf{k}, \omega) + X_i(\mathbf{k}, \omega) = 0$ with X_e from Eq. (2.68) and X_i from Eq. (2.75), is found to be

$$\begin{aligned} \mathcal{D}(\mathbf{k}, \omega) = & \left[\frac{\omega_{UH}^2}{\omega_{ce}^2} - \frac{\omega_{pi}^2}{\omega^2} - 3 \left(\frac{\omega_{pe}^2}{4\omega_{ce}^2} + \frac{T_i}{Z_i T_e} \frac{\omega_{pi}^2 \omega_{ci} |\omega_{ce}|}{\omega^4} \right) r_{Le}^2 k_{\perp}^2 \right] k_{\perp}^2 - \frac{\omega_{pe}^2}{\omega^2} k_{\parallel}^2 \\ & + i \left[\frac{\omega_{pe}^2}{\omega_{ce}^2} \frac{\nu_e}{\omega} k_{\perp}^2 + \frac{\omega_{pi}^2 \omega}{k_{\perp} v_{Ti}^3} e^{-\omega^2/(k_{\perp}^2 v_{Ti}^2)} + \frac{\omega_{pe}^2 \omega}{|k_{\parallel}| v_{Te}^3} e^{-\omega^2/(k_{\parallel}^2 v_{Te}^2)} \right] = 0, \end{aligned} \quad (2.76)$$

where use has been made of the fact that $1 + \omega_{pe}^2/\omega_{ce}^2 = \omega_{UH}^2/\omega_{ce}^2$. We approximate the solution of Eq. (2.76) by Eq. (2.47), $\mathcal{D}'(\mathbf{k}, \omega_j) = 0$, and multiply the resulting expression by ω_j^2 to obtain

$$\frac{\omega_{UH}^2}{\omega_{ce}^2} \omega_j^2 - \omega_{pi}^2 - 3 \left(\frac{\omega_{pe}^2}{4\omega_{ce}^2} \omega_j^2 + \frac{T_i}{Z_i T_e} \frac{\omega_{pi}^2 \omega_{ci} |\omega_{ce}|}{\omega_j^2} \right) r_{Le}^2 k_{\perp}^2 - \omega_{pe}^2 \frac{k_{\parallel}^2}{k_{\perp}^2} = 0. \quad (2.77)$$

Eq. (2.77) may be rewritten as a quadratic equation for ω_j^2 , which can be solved with the usual method, but here we consider the limit of $r_{Le}^2 k_{\perp}^2 \ll 1$ (since $r_{Li} \gg r_{Le}$, this is still possible for large $r_{Li}^2 k_{\perp}^2$) and $k_{\parallel}^2/k_{\perp}^2 \ll 1$, where an approximate solution, $\omega_j \approx$

$|\omega_{ce}| \omega_{pi} / \omega_{UH} = \omega_{LH}$, may be obtained by neglecting the terms proportional to $r_{Le}^2 k_{\perp}^2$ and $k_{\parallel}^2 / k_{\perp}^2$. ω_{LH} is the so-called lower hybrid (LH) frequency at which a resonance for cold plasma waves, similar to the UHR, exists if the ion response is included in the cold plasma model [99, 55]. Substituting $\omega_j \approx \omega_{LH}$ into the terms proportional to $r_{Le}^2 k_{\perp}^2$ and $k_{\parallel}^2 / k_{\perp}^2$ in Eq. (2.77), we obtain the dispersion relation for the special branch of the IBW dispersion relation, which we refer to as the dispersion relation for warm LH waves,

$$\omega^2 \approx \omega_{LH}^2 \left[1 + 3 \left(\frac{\omega_{pe}^2}{4\omega_{UH}^2} + \frac{T_i}{Z_i T_e} \frac{\omega_{UH}^2}{\omega_{pe}^2} \right) r_{Le}^2 k_{\perp}^2 + \frac{m_i}{Z_i m_e} \frac{k_{\parallel}^2}{k_{\perp}^2} \right]; \quad (2.78)$$

the warm LH wave dispersion relation in Eq. (2.78) was also utilized in [109, 13].

Chapter 3

Semi-Classical Wave Theory

The waves of interest in the present work have been introduced with the assumption of completely homogeneous media. Realistic media, and fusion plasmas in particular, do, however, always possess some level of inhomogeneity. In the cases of interest to us, the length and time scales (\mathcal{L} and \mathcal{T} , respectively) over which the properties of the medium vary significantly are large compared with the wavelength and period of the wave phenomenon. This places us in the semi-classical region where the full inhomogeneous wave propagation problem may be significantly simplified by use of the geometrical optics approximation and generalized WKBJ (Wentzel–Kramers–Brillouin–Jeffreys) methods. Even in the semi-classical region, the inhomogeneity turns out to be extremely important for determining the threshold of PDIs, and we hence devote this Chapter to describing the theory of semi-classical waves.

In Section 3.1, we introduce the geometrical optics approximation as a generalization of classical mechanics to the quanta associated with wave phenomena. This allows us to derive the geometrical optics ray equations, determining the propagation of waves (and particles) in the semi-classical region, as well as to discuss the damping and electric field of ECRH beams in ASDEX Upgrade specifically. In Section 3.2, we generalize the WKBJ approximations, known from quantum mechanics, to obtain equations of motion for waves with arbitrary dispersion relations within the semi-classical region. These equations form the basis of the theory of parametric decay instabilities in Chapter 4. Finally, in Section 3.3, we turn to a specific example of interest in this work, namely amplification of X-mode waves near the UHR. While this cannot be determined within the usual semi-classical approximations, it can be handled by means of a different generalization of the WKBJ approximations, known as the uniform approximation, which is presented and applied.

3.1 Geometrical Optics as a Generalization of Classical Mechanics

It is well-known that the ray equations of geometrical optics are equivalent to the Hamiltonian equations describing motion of particles in classical mechanics [115, 116]. We can thus scarcely avoid the inference that geometrical optics represents an extension of classical mechanics to the motion of quanta associated with wave phenomena, be it photons, phonons, plasmons, polaritons, etc. This interpretation is confirmed by noting that the Hamiltonian, H , and canonical momentum, \mathbf{p} , associated with a wave quantum of real frequency ω_j and wave vector \mathbf{k} yield the geometrical optics ray equations as their canonical equations of motion by use of the Einstein [117] ($H = \hbar\omega_j$) and de Broglie [31] ($\mathbf{p} = \hbar\mathbf{k}$) relations, i.e.,

$$\omega_j(t) = \omega(\mathbf{r}(t), \mathbf{k}(t), t), \quad \left. \frac{d\mathbf{r}(t)}{dt} = \frac{\partial\omega_j(\mathbf{r}, \mathbf{k}, t)}{\partial\mathbf{k}} \right|_{\substack{\mathbf{r} = \mathbf{r}(t), \\ \mathbf{k} = \mathbf{k}(t)}}, \quad \left. \frac{d\mathbf{k}(t)}{dt} = -\frac{\partial\omega_j(\mathbf{r}, \mathbf{k}, t)}{\partial\mathbf{r}} \right|_{\substack{\mathbf{r} = \mathbf{r}(t), \\ \mathbf{k} = \mathbf{k}(t)}}, \quad (3.1)$$

where \mathbf{r} is the generalized coordinate vector and t is time. The first part of Eq. (3.1) expresses that ω_j is given by the dispersion relation $\omega_j(\mathbf{r}, \mathbf{k}, t)$ of the wave phenomenon in question; the second part of Eq. (3.1) expresses that the wave quanta move at the local group velocity (note how naturally this obtained compared with conventional treatments); the third part of Eq. (3.1) describes the rate of change of \mathbf{k} , showing that \mathbf{k} is conserved along invariant directions, as expected from its proportionality to \mathbf{p} . From Eq. (3.1), the development of ω_j along a ray may also be calculated,

$$\left. \frac{d\omega_j(t)}{dt} = \frac{\partial\omega_j(\mathbf{r}, \mathbf{k}, t)}{\partial t} \right|_{\mathbf{r}=\mathbf{r}(t), \mathbf{k}=\mathbf{k}(t)}. \quad (3.2)$$

Eq. (3.2) shows that ω_j is a constant of motion for stationary media, confirming its role as the Hamiltonian of the wave quanta. The conservation of ω_j and H , as well as \mathbf{k} and \mathbf{p} , demonstrated above is the basis of the selection rules derived in Chapter 1. We emphasize that $\omega_j(\mathbf{r}, \mathbf{k}, t)$ may refer to any wave (or particle) phenomenon and allows the study of wave (and particle) propagation in non-stationary, inhomogeneous, anisotropic media within the geometrical optics approximations. It is, however, not even necessary to have an explicit expression for ω_j from the dispersion relation; we can simply consider a dispersion relation of the type $\mathcal{D}'(\mathbf{r}, \mathbf{k}, \omega_j(\mathbf{r}, \mathbf{k}, t), t) = 0$, from which the geometrical optics ray equations may be written as

$$\begin{aligned} \mathcal{D}'(\mathbf{r}(t), \mathbf{k}(t), \omega_j(t), t) = 0, \quad \left. \frac{d\mathbf{r}(t)}{dt} = -\frac{\partial\mathcal{D}'(\mathbf{r}, \mathbf{k}, \omega_j, t)/\partial\mathbf{k}}{\partial\mathcal{D}'(\mathbf{r}, \mathbf{k}, \omega_j, t)/\partial\omega_j} \right|_{\substack{\mathbf{r} = \mathbf{r}(t), \\ \mathbf{k} = \mathbf{k}(t), \\ \omega_j = \omega_j(t)}}, \\ \left. \frac{d\mathbf{k}(t)}{dt} = \frac{\partial\mathcal{D}'(\mathbf{r}, \mathbf{k}, \omega_j, t)/\partial\mathbf{r}}{\partial\mathcal{D}'(\mathbf{r}, \mathbf{k}, \omega_j, t)/\partial\omega_j} \right|_{\substack{\mathbf{r} = \mathbf{r}(t), \\ \mathbf{k} = \mathbf{k}(t), \\ \omega_j = \omega_j(t)}}, \quad \left. \frac{d\omega(t)}{dt} = -\frac{\partial\mathcal{D}'(\mathbf{r}, \mathbf{k}, \omega_j, t)/\partial t}{\partial\mathcal{D}'(\mathbf{r}, \mathbf{k}, \omega_j, t)/\partial\omega_j} \right|_{\substack{\mathbf{r} = \mathbf{r}(t), \\ \mathbf{k} = \mathbf{k}(t), \\ \omega_j = \omega_j(t)}}, \end{aligned} \quad (3.3)$$

which was noted by [118, 119, 120]. Eq. (3.3) can particularly be applied to the electrostatic waves from Chapter 2, as well as to the electromagnetic waves if $\mathcal{D} \rightarrow \det(\mathcal{D})$. The ray tracing equations are slightly simplified by assuming a stationary medium, leading to constant ω_j , and parametrizing the equations of motion in terms of the arc length of the trajectories, s , where $ds = |\partial\omega_j(\mathbf{r}, \mathbf{k})/\partial\mathbf{k}|_{\mathbf{r}=\mathbf{r}(t), \mathbf{k}=\mathbf{k}(t)} dt$ [116, 109],

$$\begin{aligned} \mathcal{D}'(\mathbf{r}(s), \mathbf{k}(s), \omega_j) = 0, \quad \frac{d\mathbf{r}(s)}{ds} &= -\text{sign} \left[\frac{\partial\mathcal{D}'(\mathbf{r}, \mathbf{k}, \omega_j)}{\partial\omega_j} \right] \frac{\partial\mathcal{D}'(\mathbf{r}, \mathbf{k}, \omega_j)/\partial\mathbf{k}}{|\partial\mathcal{D}'(\mathbf{r}, \mathbf{k}, \omega_j)/\partial\mathbf{k}|} \bigg|_{\substack{\mathbf{r}=\mathbf{r}(s), \\ \mathbf{k}=\mathbf{k}(s)}}, \\ \frac{d\mathbf{k}(s)}{ds} &= \text{sign} \left[\frac{\partial\mathcal{D}'(\mathbf{r}, \mathbf{k}, \omega_j)}{\partial\omega_j} \right] \frac{\partial\mathcal{D}'(\mathbf{r}, \mathbf{k}, \omega_j)/\partial\mathbf{r}}{|\partial\mathcal{D}'(\mathbf{r}, \mathbf{k}, \omega_j)/\partial\mathbf{k}|} \bigg|_{\substack{\mathbf{r}=\mathbf{r}(s), \\ \mathbf{k}=\mathbf{k}(s)}}, \end{aligned} \quad (3.4)$$

sign is the signum function. In this work, the propagation of X-mode and O-mode radiation from gyrotrons and wall reflections is modeled using Eq. (3.4) for a dispersion relation based on the analytical approximations of [121, 122], which is essentially the dispersion relation of Eq. (2.28) with corrections due to finite T_e and relativistic electrons. Eqs. (3.3) and (3.4) consider wave (and particle) propagation in the absence of damping. Weak damping can be included by using the linear damping rate from Eq. (2.48) and integrating over the trajectories given by Eq. (3.3). Doing this, the ratio of the power propagating along the ray at $t = t_{\text{end}}$, P_{end} , to the power which was originally injected at $t = t_0$, P_0 , may be written as $P_{\text{end}}/P_0 = e^{-\tau}$, where

$$\tau = 2 \int_{t_0}^{t_{\text{end}}} \Gamma(\mathbf{r}(t), \mathbf{k}(t), \omega_j(t), t) dt = 2 \int_{t_0}^{t_{\text{end}}} \frac{\mathcal{D}''(\mathbf{r}, \mathbf{k}, \omega_j, t)}{\partial\mathcal{D}'(\mathbf{r}, \mathbf{k}, \omega_j, t)/\partial\omega_j} \bigg|_{\substack{\mathbf{r}=\mathbf{r}(t), \\ \mathbf{k}=\mathbf{k}(t), \\ \omega_j=\omega_j(t)}} dt \quad (3.5)$$

is the optical thickness, and the factor of 2 comes from the fact that P is proportional to the square of the wave amplitude [55]. For a stationary medium, we can further express τ in terms of s ,

$$\begin{aligned} \tau &= 2 \int_{s_0}^{s_{\text{end}}} \frac{\Gamma(\mathbf{r}, \mathbf{k}, \omega_j)}{|\partial\omega_j(\mathbf{r}, \mathbf{k})/\partial\mathbf{k}|} \bigg|_{\substack{\mathbf{r}=\mathbf{r}(s), \\ \mathbf{k}=\mathbf{k}(s)}} ds \\ &= 2 \int_{s_0}^{s_{\text{end}}} \text{sign} \left[\frac{\partial\mathcal{D}'(\mathbf{r}, \mathbf{k}, \omega_j)}{\partial\omega_j} \right] \frac{\mathcal{D}''(\mathbf{r}, \mathbf{k}, \omega_j)}{|\partial\mathcal{D}'(\mathbf{r}, \mathbf{k}, \omega_j)/\partial\mathbf{k}|} \bigg|_{\substack{\mathbf{r}=\mathbf{r}(s), \\ \mathbf{k}=\mathbf{k}(s)}} ds; \end{aligned} \quad (3.6)$$

s_0 and s_{end} are the s -values corresponding to t_0 and t_{end} in Eq. (3.5), and the integrand in Eq. (3.6) is the spatial damping rate of the waves. In this work, τ from the launching position of O-mode and X-mode waves is evaluated using Eq. (3.6) and a relativistic model of EC absorption based on the analytical approximations in [121, 122].

When discussing the PDI threshold, it is very useful to connect the electric field amplitude of a quasi-monochromatic pump wave, $|\mathbf{E}|$, to the injected beam power, P_0 , as this is the quantity which is known experimentally; in this work, the physical electric field is always defined as the real part of the electric field amplitude vector multiplied by a (complex) phase factor of unit amplitude. This may be done using the relation between $|\mathbf{E}|$ and the

local wave energy density from [55], along with the fact that energy propagates along a geometrical optics ray with speed $|\partial\omega_j(\mathbf{k}, \mathbf{r})/\partial\mathbf{k}|$, to find the local intensity of the beam. Then assuming a Gaussian profile of $|\mathbf{E}|$ around the beam center, $|\mathbf{E}(s, \rho)| = |\mathbf{E}(s, 0)| e^{-\rho^2/W^2(s)}$, where ρ is the distance from the central geometrical optics ray of the beam and $W(s)$ is the beam width, and integrating over the coordinates perpendicular to s yields [109, 13],

$$|\mathbf{E}(s, 0)| = \sqrt{\frac{8P(s)}{\pi\epsilon_0 W^2(s) |\partial\omega_j(\mathbf{k}, s)/\partial\mathbf{k}|_{\mathbf{k}=\mathbf{k}(s)} \mathbf{e}^*(s) \cdot \partial\{\mathcal{H}[\mathcal{D}(\mathbf{k}(s), \omega)]/\omega\}/\partial\omega|_{\omega=\omega_j} \cdot \mathbf{e}(s)}}, \quad (3.7)$$

with $\mathbf{e}(s)$ being a unit polarization vector of the wave at position s along the central beam ray and $\mathcal{H}[\mathcal{D}]$ being the Hermitian part of \mathcal{D} ; for the cold electromagnetic pump waves in this work, $\mathcal{H}[\mathcal{D}]$ is simply \mathcal{D} from Eq. (2.26). When looking at the directly injected beam, $P(s) = P_0 e^{-\tau}$, while a for beam which has undergone reflection/mode conversion, $P(s) = \mathcal{F}P_0 e^{-\tau}$, where \mathcal{F} is a factor describing the efficiency of the reflection/mode conversion process. W can in general be determined from beam tracing codes such as TORBEAM [123] and WKBeam [124], but here we assume it to be equal to that of a Gaussian beam propagating in vacuo [125]

$$W(s) = W_0 \sqrt{1 + \frac{4c^2(s - s_0)^2}{\omega_j^2 W_0^4}}. \quad (3.8)$$

In Eq. (3.8), W_0 is the beam width at the focus of the beam, which is taken to be 2.29 cm for the ECRH beams at ASDEX Upgrade, s_0 is the location of the beam focus with respect to the zero of s ; setting $s = 0$ at the ECRH launchers, gives $s_0 = 85.4$ cm for the ECRH beams at ASDEX Upgrade.

3.2 Generalized WKBJ Methods

The geometrical optics methods discussed in Section 3.1 are of great use when discussing linear wave propagation in plasmas. However, they treat ω_j and \mathbf{k} as the Hamiltonian and canonical momentum of a classical particle and thus fail to take the phase variation, which is crucial for nonlinear wave phenomena, properly into account. Fortunately, methods capable of handling the wave phenomena more directly in the semi-classical limit, known as generalized WKBJ methods, have been developed [126, 127]. These methods start out with an integral form of the wave equation, e.g., Eq. (2.11) or Eq. (2.38), and approximate the linear response using semi-classical arguments. While the methods are applicable to matrix–vector wave equations such as Eq. (2.11) [127], we shall only apply them to electrostatic waves and hence use the simpler scalar dispersion relation from Eq. (2.38),

$$\frac{\rho_{\text{nl}}(\mathbf{r}, t)}{\epsilon_0} = \int_{\text{all}(\mathbf{r}', t')} \mathcal{D} \left(\mathbf{r} - \mathbf{r}', \frac{\mathbf{r} + \mathbf{r}'}{2}; t - t', \frac{t + t'}{2} \right) \phi(\mathbf{r}', t') \, d\mathbf{r}' \, dt', \quad (3.9)$$

where

$$\mathcal{D}\left(\mathbf{r}-\mathbf{r}', \frac{\mathbf{r}+\mathbf{r}'}{2}; t-t', \frac{t+t'}{2}\right) = X\left(\mathbf{r}-\mathbf{r}', \frac{\mathbf{r}+\mathbf{r}'}{2}; t-t', \frac{t+t'}{2}\right) - \frac{\partial}{\partial \mathbf{r}} \cdot \frac{\partial \delta(\mathbf{r}-\mathbf{r}')}{\partial \mathbf{r}}. \quad (3.10)$$

We further simplify Eq. (3.9) by considering a stationary medium which is only inhomogeneous along the x -direction, i.e., a plasma slab, and taking ϕ to have the form of a single WKB-mode,

$$\phi(\mathbf{r}', t') = \text{Re}[A(\mathbf{r}', t') e^{i\theta(\mathbf{r}', t')}], \quad (3.11)$$

where A is a slowly varying amplitude (or envelope) function and the phase function (or eikonal) $\theta(\mathbf{r}', t') = \int_0^{x'} k_x(x'') dx'' + k_y y' + k_z z' - \omega t'$ gives a fast plane wave-like variation; more general solutions can be constructed by superposition of WKB-modes. With these assumptions, Eq. (3.9) becomes

$$\frac{\rho_{\text{nl}}(\mathbf{r}, t)}{\epsilon_0} = \text{Re} \left[\int_{\text{all}(\mathbf{r}', t')} \mathcal{D}\left(\mathbf{r}-\mathbf{r}', \frac{x+x'}{2}; t-t'\right) A(\mathbf{r}', t') e^{i\theta(\mathbf{r}', t')} d\mathbf{r}' dt' \right]. \quad (3.12)$$

We now invoke the WKB approximations in which \mathcal{D} is a sharply peaked function of $\mathbf{r}-\mathbf{r}'$ and $t-t'$, only carrying a weak dependence on $(x+x')/2$ due to the weak inhomogeneity. The first assumption allows us to Taylor expand $A(\mathbf{r}', t')$ around the point (\mathbf{r}, t) to obtain

$$A(\mathbf{r}', t') = \sum_{j=0}^{\infty} \sum_{l=0}^{\infty} \sum_{m=0}^{\infty} \sum_{n=0}^{\infty} \frac{(x'-x)^j (y'-y)^l (z'-z)^m (t'-t)^n}{j! l! m! n!} \frac{\partial^{j+l+m+n} A(x, y, z, t)}{\partial x^j \partial y^l \partial z^m \partial t^n}. \quad (3.13)$$

The second assumption allows us to Taylor expand \mathcal{D} around x in the second argument,

$$\mathcal{D}\left(\mathbf{r}-\mathbf{r}', \frac{x+x'}{2}; t-t'\right) = \sum_{p=0}^{\infty} \frac{(x'-x)^p}{2^p p!} \frac{\partial^p \mathcal{D}(\mathbf{r}-\mathbf{r}', x; t-t')}{\partial x^p}. \quad (3.14)$$

Inserting Eqs. (3.13) and (3.14) in Eq. (3.12), also using that $\theta(\mathbf{r}', t') = \theta(\mathbf{r}'-\mathbf{r}, t'-t) + \theta(\mathbf{r}, t)$, we find

$$\begin{aligned} \frac{\rho_{\text{nl}}(\mathbf{r}, t)}{\epsilon_0} = \text{Re} & \left[e^{i\theta(\mathbf{r}, t)} \sum_{j=0}^{\infty} \sum_{l=0}^{\infty} \sum_{m=0}^{\infty} \sum_{n=0}^{\infty} \sum_{p=0}^{\infty} \frac{1}{2^p j! l! m! n! p!} \frac{\partial^{j+l+m+n} A(\mathbf{r}, t)}{\partial x^j \partial y^l \partial z^m \partial t^n} \right. \\ & \times \left. \int_{\text{all}(\mathbf{r}', t')} (x'-x)^{j+p} (y'-y)^l (z'-z)^m (t'-t)^n \frac{\partial^p \mathcal{D}(\mathbf{r}-\mathbf{r}', x; t-t')}{\partial x^p} e^{i\theta(\mathbf{r}'-\mathbf{r}, t'-t)} d\mathbf{r}' dt' \right]. \end{aligned} \quad (3.15)$$

With the assumption of a localized \mathcal{D} with respect to $x-x'$, we can expand $\int_x^{x'} k_x(x'') dx'' = \sum_{n=0}^{\infty} [(x'-x)^{n+1}/(n+1)!] \partial^n k_x(x)/\partial x^n$ and obtain a good approximation by keeping only the leading term, $\int_x^{x'} k_x(x'') dx'' \approx k_x(x)(x'-x)$. Plugging this in, $\theta(\mathbf{r}'-\mathbf{r}, t'-t) \approx$

$k_x(x)(x' - x) + k_y(y' - y) + k_z(z' - z) - \omega(t' - t)$, and the integrands of Eq. (3.15) may be simplified by noting that

$$(x' - x)^{j+p}(y' - y)^l(z' - z)^m(t' - t)^n e^{i\theta(r'-r, t'-t)} \approx (-i)^{j+p+l+m-n} \times \frac{\partial^{j+p+l+m+n} [e^{i\theta(r'-r, t'-t)}]}{\partial k_x^{j+p} \partial k_y^l \partial k_z^m \partial \omega^n} \Big|_{k_x=k_x(x)}, \quad (3.16)$$

which shows that the integrals are derivatives of the Fourier–Laplace transform of \mathcal{D} , i.e., the well-known dispersion relation in a homogeneous medium extended to hold locally at each point in space. Substituting these results back into Eq. (3.15) yields

$$\frac{\rho_{\text{nl}}(\mathbf{r}, t)}{\epsilon_0} \approx \text{Re} \left[e^{i\theta(\mathbf{r}, t)} \sum_{j=0}^{\infty} \sum_{l=0}^{\infty} \sum_{m=0}^{\infty} \sum_{n=0}^{\infty} \sum_{p=0}^{\infty} \frac{(-i)^{j+p+l+m-n}}{2^p j! l! m! n! p!} \frac{\partial^{j+l+m+n} A(\mathbf{r}, t)}{\partial x^j \partial y^l \partial z^m \partial t^n} \times \frac{\partial^{j+2p+l+m+n} \mathcal{D}(\mathbf{k}, x, \omega)}{\partial k_x^{j+p} \partial k_y^l \partial k_z^m \partial \omega^n \partial x^p} \Big|_{k_x=k_x(x)} \right]. \quad (3.17)$$

In the semi-classical region the x -, y -, and z -derivatives of A and \mathcal{D} can be taken as order $1/\mathcal{L} \ll k$ and the t -derivatives can be taken as order $1/\mathcal{T} \ll |\omega|$, while the k_x -, k_y -, and k_z -derivatives of \mathcal{D} can be taken as order $1/k$ and the ω derivative can be taken as order $1/|\omega|$. This causes the sums in Eq. (3.17) to converge rapidly. In the extreme case, it is permissible to keep only the term where $j = l = m = n = p = 0$ and the terms where one of the indices is 1 while the rest are 0, with which

$$\frac{\rho_{\text{nl}}(\mathbf{r}, t)}{\epsilon_0} \approx \text{Re} \left\{ e^{i\theta(\mathbf{r}, t)} \left[A(\mathbf{r}, t) \mathcal{D}(\mathbf{k}, x, \omega) + i \frac{\partial A(\mathbf{r}, t)}{\partial t} \frac{\partial \mathcal{D}(\mathbf{k}, x, \omega)}{\partial \omega} - i \frac{\partial A(\mathbf{r}, t)}{\partial \mathbf{r}} \cdot \frac{\partial \mathcal{D}(\mathbf{k}, x, \omega)}{\partial \mathbf{k}} - \frac{i}{2} A(\mathbf{r}, t) \frac{\partial^2 \mathcal{D}(\mathbf{k}, x, \omega)}{\partial k_x \partial x} \right] \Big|_{k_x=k_x(x)} \right\}. \quad (3.18)$$

Introducing $a(\mathbf{r}, t)$, where $A(\mathbf{r}, t) = a(\mathbf{r}, t) / \sqrt{\partial \mathcal{D}(\mathbf{k}, x, \omega) / \partial k_x |_{k_x=k_x(x)}}$, allows us to eliminate the term proportional to $\partial^2 \mathcal{D}(\mathbf{k}, x, \omega) / (\partial k_x \partial x) |_{k_x=k_x(x)}$,

$$\frac{\rho_{\text{nl}}(\mathbf{r}, t)}{\epsilon_0} \approx \text{Re} \left\{ \frac{e^{i\theta(\mathbf{r}, t)}}{\sqrt{\partial \mathcal{D}(\mathbf{k}, x, \omega) / \partial k_x}} \left[\mathcal{D}(\mathbf{k}, x, \omega) a(\mathbf{r}, t) + i \frac{\partial \mathcal{D}(\mathbf{k}, x, \omega)}{\partial \omega} \frac{\partial a(\mathbf{r}, t)}{\partial t} - i \frac{\partial \mathcal{D}(\mathbf{k}, x, \omega)}{\partial \mathbf{k}} \cdot \frac{\partial a(\mathbf{r}, t)}{\partial \mathbf{r}} \right] \Big|_{k_x=k_x(x)} \right\}, \quad (3.19)$$

and further utilizing the weak damping approximation of Eq. (2.46) along with the WKB ansatz ($\mathcal{D}'(\mathbf{k}(x), x, \omega_j) = 0$) yields $\mathcal{D}(\mathbf{k}, x, \omega) \approx i \mathcal{D}''(\mathbf{k}, x, \omega_j)$, $\partial \mathcal{D}(\mathbf{k}, x, \omega) / \partial \mathbf{k} \approx$

$\partial\mathcal{D}'(\mathbf{k}, x, \omega_j)/\partial\mathbf{k}$, and $\partial\mathcal{D}(\mathbf{k}, x, \omega)/\partial\omega \approx \partial\mathcal{D}'(\mathbf{k}, x, \omega)/\partial\omega|_{\omega=\omega_j}$, from which we obtain

$$\frac{\rho_{\text{nl}}(\mathbf{r}, t)}{\epsilon_0} \approx \text{Re} \left\{ \frac{i e^{i\theta(\mathbf{r}, t)}}{\sqrt{\partial\mathcal{D}'(\mathbf{k}, x, \omega)/\partial k_x}} \left[\mathcal{D}''(\mathbf{k}, x, \omega) a(\mathbf{r}, t) + \frac{\partial\mathcal{D}'(\mathbf{k}, x, \omega)}{\partial\omega} \frac{\partial a(\mathbf{r}, t)}{\partial t} - \frac{\partial\mathcal{D}'(\mathbf{k}, x, \omega)}{\partial\mathbf{k}} \cdot \frac{\partial a(\mathbf{r}, t)}{\partial\mathbf{r}} \right] \Big|_{k_x=k_x(x), \omega=\omega_j} \right\}. \quad (3.20)$$

Factoring out $\partial\mathcal{D}'/\partial\omega$, while recalling that $\Gamma = \mathcal{D}''/(\partial\mathcal{D}'/\partial\omega)$ is the linear damping rate and $\mathbf{v} = -(\partial\mathcal{D}/\partial\mathbf{k})/(\partial\mathcal{D}'/\partial\omega)$ is the group velocity of the wave, finally yields

$$\frac{\rho_{\text{nl}}(\mathbf{r}, t)}{\epsilon_0} \approx \text{Re} \left\{ \frac{i[\partial\mathcal{D}(\mathbf{k}, x, \omega)/\partial\omega] e^{i\theta(\mathbf{r}, t)}}{\sqrt{\partial\mathcal{D}'(\mathbf{k}, x, \omega)/\partial k_x}} \left[\Gamma(\mathbf{k}, x, \omega) a(\mathbf{r}, t) + \frac{\partial a(\mathbf{r}, t)}{\partial t} + \mathbf{v}(\mathbf{k}, x, \omega) \cdot \frac{\partial a(\mathbf{r}, t)}{\partial\mathbf{r}} \right] \Big|_{k_x=k_x(x), \omega=\omega_j} \right\}. \quad (3.21)$$

Eq. (3.21) demonstrates the characteristics of linear waves deduced within the geometrical optics approximation in Section 3.1. To see this, we note that for linear waves, $\rho_{\text{nl}} = 0$, Eq. (3.21) is equivalent to

$$\frac{\partial a(\mathbf{r}, t)}{\partial t} + \mathbf{v}(\mathbf{k}(x), x, \omega_j) \cdot \frac{\partial a(\mathbf{r}, t)}{\partial\mathbf{r}} = -\Gamma(\mathbf{k}(x), x, \omega_j) a(\mathbf{r}, t). \quad (3.22)$$

The left hand side of Eq. (3.22) is the convective time derivative of a along trajectories moving with velocity \mathbf{v} , i.e., the geometrical optics ray trajectories from Section 3.1. We thus find

$$\frac{da(t)}{dt} = -\Gamma(\mathbf{k}(t), x(t), \omega_j) a(t), \quad (3.23)$$

where $a(t) = a(\mathbf{r}(t), t)$, and $\mathbf{r}(t)$, $\mathbf{k}(t)$ are given by Eq. (3.3). Integrating Eq. (3.23) with respect to t yields an optical thickness similar to that given by Eqs. (3.5) and (3.6). Eq. (3.23) further shows that, in the absence of damping, a is conserved along the geometrical optics trajectories, meaning that the wave amplitude A varies as $1/\sqrt{\partial\mathcal{D}'/\partial k_x}$. This is a generalization of the well-known WKBJ amplitude variation for the time-independent Schrödinger equation, which has $\mathcal{D}'(\mathbf{k}, x, \omega_j) = \hbar^2 k^2/(2m_\sigma) - \hbar\omega_j + V(x)$ and hence $A \propto 1/\sqrt{k_x}$ [128]; it expresses the conservation of wave energy along the geometrical optics rays in the absence of damping.

We finally note that the treatment of wave trapping and losses from the regions where trapped waves exist, which are crucial for evaluating the threshold of the PDIs in Chapter 5, requires the inclusion 2nd order terms from the expansion in Eq. (3.17) [126]. The Bohr–Sommerfeld conditions resulting from the trapping conditions along the x -direction [126, 8, 9] may be derived from geometrical optics arguments to be introduced in Chapter 4. Here, we simply observe that expanding a dispersion relation like Eq. (2.59), for which

$\partial^2 \mathcal{D}/(\partial k_y \partial k_{\parallel}) = 0$, to 2nd order along the y - and z -directions yields

$$\frac{\rho_{nl}(\mathbf{r}, t)}{\epsilon_0} \approx \text{Re} \left\{ \frac{e^{i\theta(r,t)}}{\sqrt{\partial \mathcal{D}'(\mathbf{k}, x, \omega)/\partial k_x}} \left[i \mathcal{D}''(\mathbf{k}, x, \omega) a(\mathbf{r}, t) + i \frac{\partial \mathcal{D}'(\mathbf{k}, x, \omega)}{\partial \omega} \frac{\partial a(\mathbf{r}, t)}{\partial t} \right. \right. \\ \left. \left. - i \frac{\partial \mathcal{D}'(\mathbf{k}, x, \omega)}{\partial \mathbf{k}} \cdot \frac{\partial a(\mathbf{r}, t)}{\partial \mathbf{r}} - \frac{1}{2} \frac{\partial^2 \mathcal{D}'(\mathbf{k}, x, \omega)}{\partial k_y^2} \frac{\partial^2 a(\mathbf{r}, t)}{\partial y^2} \right. \right. \\ \left. \left. - \frac{1}{2} \frac{\partial^2 \mathcal{D}'(\mathbf{k}, x, \omega)}{\partial k_{\parallel}^2} \frac{\partial^2 a(\mathbf{r}, t)}{\partial z^2} \right] \Big|_{k_x=k_x(x), \omega=\omega_j} \right\}. \quad (3.24)$$

3.3 X-Mode Amplification from the Uniform Approximation

To discuss the amplification of X-mode waves, we insert \mathbf{J}_1 from Eq. (2.24) as \mathbf{J} in Eq. (2.8), remembering that the wave is assumed to have a harmonic time variation of angular frequency ω_0 , assume the wave and plasma parameters to only depend on the x -coordinate, which is perpendicular to $\mathbf{B}^{(0)} = B^{(0)} \mathbf{e}_z$, and consider only the x - and y -components of \mathbf{E} (referred to as E_{0x} and E_{0y} ; the physical electric field is obtained by taking the real part of the complex values including the harmonic time dependence), as these are the components related to X-mode propagation perpendicular to $\mathbf{B}^{(0)}$. With these assumptions, we arrive at two equations also found in [129],

$$\frac{d^2 E_{0y}(x)}{dx^2} + k_0^2(x) E_{0y}(x) = 0, \quad k_0^2(x) = \frac{\omega_0^2}{c^2} \left[1 - \frac{\omega_{pe}^2(x)}{\omega_0^2} \frac{\omega_0^2 - \omega_{pe}^2(x)}{\omega_0^2 - \omega_{UH}^2(x)} \right], \quad (3.25)$$

$$E_{0x}(x) = i \frac{\omega_{ce}(x)}{\omega_0} \frac{\omega_{pe}^2(x)}{\omega_0^2 - \omega_{UH}^2(x) + i[2\omega_0^2 - \omega_{pe}^2(x)]\nu_{ei}(x)/\omega_0} E_{0y}(x); \quad (3.26)$$

collisions have been neglected in Eq. (3.25), while they have been retained in Eq. (3.26), assuming $\nu_{ei}/\omega_0 \ll 1$.

3.3.1 The Uniform Approximation

Now that we have stated the problem, all that remains is for us to solve Eq. (3.25) near the UHR with appropriate boundary conditions. Because we are interested in general profiles of $k_0^2(x)$, it is not feasible to solve Eq. (3.25) exactly, so we shall instead seek an approximate solution using the so-called uniform approximation, described in [130, 131, 132]. The uniform approximation is based on mapping an expression like Eq. (3.25) onto another differential equation possessing an exactly known solution, which then allows an approximate solution of Eq. (3.25). Suppose that $\varphi(\sigma)$ is a known function satisfying the differential equation,

$$\frac{d^2 \varphi(\sigma)}{d\sigma^2} + Q(\sigma) \varphi(\sigma) = 0, \quad (3.27)$$

where $Q(\sigma)$ is also a known function resembling $k_0^2(x)$ in some way. It is generally possible to write $E_{0y}(x) = f(x)\phi(\sigma(x))$, which may be plugged into Eq. (3.25). Doing this, while using Eq. (3.27) to eliminate $d^2\varphi/d\sigma^2|_{\sigma=\sigma(x)}$, we obtain

$$\begin{aligned} & \left[2 \frac{df(x)}{dx} \frac{d\sigma(x)}{dx} + f(x) \frac{d^2\sigma(x)}{dx^2} \right] \frac{d\varphi(\sigma)}{d\sigma} \Big|_{\sigma=\sigma(x)} \\ & + \left\{ k_0^2(x)f(x) - Q(\sigma(x))f(x) \left[\frac{d\sigma(x)}{dx} \right]^2 + \frac{d^2f(x)}{dx^2} \right\} \varphi(\sigma(x)) = 0. \end{aligned} \quad (3.28)$$

The term proportional to $d\varphi/d\sigma|_{\sigma=\sigma(x)}$ may be eliminated by taking $f(x) = 1/\sqrt{d\sigma(x)/dx}$, giving an amplitude variation similar to that from the generalized WKB method. With this, Eq. (3.28) is satisfied for $\varphi(\sigma(x)) \neq 0$ if

$$k_0^2(x) = Q(\sigma(x)) \left[\frac{d\sigma(x)}{dx} \right]^2 - \frac{1}{\sqrt{d\sigma(x)/dx}} \frac{d^2}{dx^2} \left[\frac{1}{\sqrt{d\sigma(x)/dx}} \right]. \quad (3.29)$$

So far the calculation is exact. The uniform approximation consists in neglecting the second term of Eq. (3.29) and setting $k_0^2(x) = Q(\sigma(x))[d\sigma(x)/dx]^2$; this is permitted if $k_0^2(x)$ and $Q(\sigma)$ are sufficiently similar, as the second term will vanish if $\sigma(x)$ is a linear function of x . With the uniform approximation, Eq. (3.29) may be rearranged to give the following implicit definition of $\sigma(x)$,

$$\int_{\sigma(x_0)}^{\sigma(x)} \sqrt{Q(\sigma')} d\sigma' = \int_{x_0}^x k_0(x') dx'; \quad (3.30)$$

x_0 and $\sigma(x_0)$ represent a known pair of equivalent points for $k_0^2(x)$ and $Q(\sigma)$. We conclude this Subsection with a small note on the sense in which $Q(\sigma)$ should resemble $k_0^2(x)$ if accurate results are to be obtained from the uniform approximation. As waves are propagating for $k_0^2(x) > 0$ and evanescent for $k_0^2(x) < 0$, the points at which $k_0^2(x)$ changes sign represent points at which the solution changes character, from propagating to evanescent or vice versa, and they are hence known as transition points. The sign of $k_0^2(x)$ may change either at points where $k_0^2(x) \rightarrow 0$ (cutoffs) or at points where $|k_0^2(x)| \rightarrow \infty$ (resonances). If $k_0^2(x)$ possesses a particular number and structure of transition points, the uniform approximation will only yield accurate results if $Q(\sigma)$ possesses a similar number and structure of transition points, as Eq. (3.25) can only be mapped to Eq. (3.27) in a smooth fashion at the transition points if they occur at equivalent points of $k_0^2(x)$ and $Q(\sigma)$. The requirement that the transition points occur at equivalent points of $k_0^2(x)$ and $Q(\sigma)$ additionally imposes the condition

$$\int_{\sigma(x_i)}^{\sigma(x_j)} \sqrt{Q(\sigma')} d\sigma' = \int_{x_i}^{x_j} k_0(x') dx', \quad (3.31)$$

where x_i, x_j are the i th, j th transition points of $k_0^2(x)$ and $\sigma(x_i), \sigma(x_j)$ are the i th, j th transition points of $Q(\sigma)$, for all i, j .

3.3.2 Field Enhancement near the Upper Hybrid Resonance

Having reviewed the uniform approximation within a general setting, we now turn our attention to the specific case of field enhancement of an X-mode wave near the UHR. The X-mode $k_0^2(x)$ given by Eq. (3.25) possesses transition points at locations where one of the following conditions is satisfied, $\omega_{UH}(x_0) = \omega_0$ (the UHR), $[\omega_{ce}^2(x_1)/4 + \omega_{pe}^2(x_1)]^{1/2} + |\omega_{ce}(x_1)|/2 = \omega_0$ (the R-cutoff), or $[\omega_{ce}^2(x_2)/4 + \omega_{pe}^2(x_2)]^{1/2} - |\omega_{ce}(x_2)|/2 = \omega_0$ (the L-cutoff). Here, we shall only be concerned with the case of $k_0^2(x)$ possessing a single resonance at x_0 , where $\omega_{UH}(x_0) = \omega_0$, and no cut-offs; we note that cases containing a single resonance between the two cut-offs, as is appropriate in ionospheric studies, have been treated by [133]. We assume the pole of $k_0^2(x)$ at x_0 to be simple, $k_0^2(x \rightarrow x_0) \propto 1/(x - x_0)$, which requires $d\omega_{UH}(x)/dx|_{x=x_0} \neq 0$, as is seen by a Taylor expansion of $\omega_{UH}(x)$ around x_0 in Eq. (3.25). In this case, the simplest choice of $Q(\sigma)$ mimicking $k_0^2(x)$ for $|x| < \infty$ is $Q(\sigma) = 1/\sigma$, which has a simple pole at $\sigma = 0$, meaning that x_0 and $\sigma(x_0) = 0$ are equivalent points of $k_0^2(x)$ and $Q(\sigma)$. Plugging the above results into Eq. (3.30), we obtain

$$\sqrt{\sigma}(x) = \frac{1}{2} \int_{x_0}^x k_0(x') dx', \quad \frac{d\sigma(x)}{dx} = \frac{k_0(x)}{2} \int_{x_0}^x k_0(x') dx', \quad (3.32)$$

from which

$$E_{0y}(x) = \frac{\varphi(\sigma(x))}{\sqrt{d\sigma(x)/dx}} = \sqrt{\frac{2}{k_0(x) \int_{x_0}^x k_0(x') dx'}} \varphi\left(\frac{1}{4} \left[\int_{x_0}^x k_0(x') dx'\right]^2\right). \quad (3.33)$$

The general solution of Eq. (3.27) with $Q(\sigma) = 1/\sigma$ is [133]

$$\varphi(\sigma) = \sqrt{\sigma} [\mathcal{K}_1 H_1^{(1)}(2\sqrt{\sigma}) + \mathcal{K}_2 H_1^{(2)}(2\sqrt{\sigma})], \quad (3.34)$$

where $H_1^{(1)}$ is a Hankel function of the 1st kind of order 1, $H_1^{(2)}$ is a Hankel function of the 2nd kind of order 1, and $\mathcal{K}_1, \mathcal{K}_2$ are constants. We are interested in solutions which are decaying on the evanescent side of the UHR. Such solutions will generally involve only one kind of Hankel function, as seen from the asymptotic forms of these functions [113]. With $\sqrt{\sigma}(x)$ given by Eq. (3.32), $H_1^{(1)}$ is the appropriate Hankel function if the waves are propagating for $x < x_0$ (equivalent to $k_0^2(x > x_0) < 0$), while $H_1^{(2)}$ is the appropriate Hankel function if the waves are propagating for $x > x_0$ (equivalent to $k_0^2(x > x_0) > 0$). The above results may be written as

$$\varphi(\sigma) = \mathcal{K} \sqrt{\sigma} H_1(2\sqrt{\sigma}), \quad (3.35)$$

where

$$H_1 = \begin{cases} H_1^{(1)} & \text{for } k_0^2(x > x_0) < 0 \\ H_1^{(2)} & \text{for } k_0^2(x > x_0) > 0 \end{cases} \quad (3.36)$$

and \mathcal{K} is a constant. When Eq. (3.35) is plugged into Eq. (3.33) with $\sqrt{\sigma}(x)$ from Eq. (3.32), we finally obtain $E_{0y}(x)$ within the uniform approximation,

$$E_{0y}(x) = \frac{\mathcal{K}}{\sqrt{2k_0(x)}} \sqrt{\int_{x_0}^x k_0(x') dx'} H_1 \left[\int_{x_0}^x k_0(x') dx' \right]. \quad (3.37)$$

\mathcal{K} is proportional to the electric field amplitude and may be related to the beam power, P , if we interpret $E_{0y}(x)$ as the y -component of the electric field at the centre of a Gaussian beam of width W propagating along the x -direction. To do this, we note that, far from the UHR, the asymptotic form of H_1 [113] may be used to write

$$E_{0y}(x) \approx \frac{\mathcal{K}}{\sqrt{\pi k_0(x)}} e^{-i \operatorname{sign}[k_0^2(x > x_0)] [\int_{x_0}^x k_0(x') dx' - 3\pi/4]} \quad \text{for} \quad \left| \int_{x_0}^x k_0(x') dx' \right| \gg 1, \quad (3.38)$$

which is similar to the WKBJ solution of [9] if

$$|\mathcal{K}| = \sqrt{\frac{4P\omega_0}{\epsilon_0 c^2 W^2}}; \quad (3.39)$$

note that our definition of W agrees with that of [125] rather than that of [9]. Setting the phase angle of \mathcal{K} to zero and allowing P and W to be slowly varying functions of x determined from beam or ray tracing, we thus obtain

$$E_{0y}(x) = \sqrt{\frac{2P(x)}{\epsilon_0 c W^2(x)} \frac{\omega_0}{c k_0(x)} \int_{x_0}^x k_0(x') dx'} H_1 \left[\int_{x_0}^x k_0(x') dx' \right]. \quad (3.40)$$

Far away from the UHR, the approximate version of $E_{0y}(x)$ then becomes

$$E_{0y}(x) \approx \sqrt{\frac{4P(x)}{\pi \epsilon_0 c W^2(x)} \frac{\omega_0}{c k_0(x)}} e^{-i \operatorname{sign}[k_0^2(x > x_0)] [\int_{x_0}^x k_0(x') dx' - 3\pi/4]} \quad \text{for} \quad \left| \int_{x_0}^x k_0(x') dx' \right| \gg 1, \quad (3.41)$$

and if the point is further located in vacuo, where $k_0(x_v) = \omega_0/c$, this may be reduced to

$$E_{0y}(x_v) \approx \sqrt{\frac{4P(x_v)}{\pi \epsilon_0 c W^2(x_v)}} e^{-i \operatorname{sign}[k_0^2(x > x_0)] [\int_{x_0}^{x_v} k_0(x') dx' - 3\pi/4]} \quad \text{for} \quad \left| \int_{x_0}^{x_v} k_0(x') dx' \right| \gg 1. \quad (3.42)$$

In vacuo it also holds that $E_{0x}(x_v) = 0$, and taking the vacuum region to be located on the side of x_0 where a propagating wave exists, such that $\int_{x_0}^{x_v} k_0(x') dx' \in \mathbb{R}$, the electric field amplitude becomes

$$|\mathbf{E}(x_v)|^2 = |E_{0y}(x_v)|^2 = \frac{4P(x_v)}{\pi \epsilon_0 c W^2(x_v)}, \quad (3.43)$$

which is just the standard result at the centre of a Gaussian beam in vacuo [125]. To estimate the field enhancement near the UHR, we use the small argument approximation of H_1 [113] to write Eq. (3.40) as

$$E_{0y}(x) \approx i \operatorname{sign}[k_0^2(x > x_0)] \sqrt{\frac{8P(x)}{\pi^2 \epsilon_0 c W^2(x)} \frac{\omega_0}{c k_0(x) \int_{x_0}^x k_0(x') dx'}} \quad \text{for} \quad \left| \int_{x_0}^x k_0(x') dx' \right| \ll 1. \quad (3.44)$$

We also note that, by Taylor expanding $\omega_{UH}(x)$ around x_0 , the lowest order approximation of $k_0(x)$ near x_0 is found to be

$$k_0(x) \approx \frac{K}{\sqrt{x-x_0}}, \quad K = \frac{|\omega_{ce}(x_0)|\omega_{pe}(x_0)}{c[2\omega_0 d\omega_{UH}(x)/dx|_{x=x_0}]^{1/2}}, \quad (3.45)$$

and using this form of $k_0(x)$, we further have $\int_{x_0}^x k_0(x') dx' \approx 2K\sqrt{x-x_0}$, with which

$$E_{0y}(x) \approx i \operatorname{sign}[k_0^2(x > x_0)] \sqrt{\frac{8P(x)}{\pi^2 \epsilon_0 c W^2(x)} \frac{c\omega_0^2 d\omega_{UH}(x)/dx|_{x=x_0}}{\omega_{ce}^2(x_0)\omega_{pe}^2(x_0)}} \quad \text{for} \quad \left| \int_{x_0}^x k_0(x') dx' \right| \ll 1. \quad (3.46)$$

Eq. (3.46) becomes exact at $x = x_0$, and we may thus evaluate the electric field amplitude at x_0 , using Eqs. (3.26) and (3.46) together,

$$\begin{aligned} |\mathbf{E}(x_0)|^2 &= |E_{0x}(x_0)|^2 + |E_{0y}(x_0)|^2 \\ &= \frac{8P(x_0)}{\pi^2 \epsilon_0 c W^2(x_0)} \frac{c\omega_0^2 |d\omega_{UH}(x)/dx|_{x=x_0}}{\omega_{ce}^2(x_0)\omega_{pe}^2(x_0)} \left\{ \frac{\omega_{ce}^2(x_0)}{\nu^2(x_0)} \frac{\omega_{pe}^4(x_0)}{[2\omega_0^2 - \omega_{pe}^2(x_0)]^2} + 1 \right\}. \end{aligned} \quad (3.47)$$

The square field enhancement, F , is simply obtained as the ratio between Eqs. (3.47) and (3.43),

$$F = \frac{|\mathbf{E}(x_0)|^2}{|\mathbf{E}(x_v)|^2} = \frac{2}{\pi} \frac{P(x_0)}{P(x_v)} \frac{W^2(x_v)}{W^2(x_0)} \frac{c\omega_0^2 |d\omega_{UH}(x)/dx|_{x=x_0}}{\omega_{ce}^2(x_0)\omega_{pe}^2(x_0)} \left\{ \frac{\omega_{ce}^2(x_0)}{\nu_{ei}^2(x_0)} \frac{\omega_{pe}^4(x_0)}{[2\omega_0^2 - \omega_{pe}^2(x_0)]^2} + 1 \right\}. \quad (3.48)$$

In order to cast F in a more illuminating form, we evaluate $d\omega_{UH}(x)/dx$ in terms of the density gradient scale length, $L_n(x) = n_e(x)/[dn_e(x)/dx]$, and the magnetic field strength gradient scale length, $L_B(x) = B(x)/[dB(x)/dx]$,

$$\frac{d\omega_{UH}(x)}{dx} = \frac{1}{2\omega_{UH}(x)} \left[\frac{d\omega_{pe}^2(x)}{dx} + \frac{d\omega_{ce}^2(x)}{dx} \right] = \frac{1}{2\omega_{UH}(x)} \left[\frac{\omega_{pe}^2(x)}{L_n(x)} + \frac{2\omega_{ce}^2(x)}{L_B(x)} \right], \quad (3.49)$$

and plug the above expression into Eq. (3.48), remembering that $\omega_{UH}(x_0) = \omega_0$,

$$F = \frac{1}{\pi} \frac{P(x_0)}{P(x_v)} \frac{W^2(x_v)}{W^2(x_0)} \left| \frac{c\omega_0}{\omega_{ce}^2(x_0)L_n(x_0)} + \frac{2c\omega_0}{\omega_{pe}^2(x_0)L_B(x_0)} \right| \left\{ \frac{\omega_{ce}^2(x_0)}{\nu_{ei}^2(x_0)} \frac{\omega_{pe}^4(x_0)}{[2\omega_0^2 - \omega_{pe}^2(x_0)]^2} + 1 \right\}. \quad (3.50)$$

This form of F clearly illustrates the dependence on P , W , ν_{ei} , and the gradient length scales of the basic plasma parameters: F scales with $P(x_0)/W^2(x_0)$, i.e., F is proportional to the central beam intensity at x_0 . Significant field amplification may arise from the factor $\omega_{ce}^2(x_0)/\nu_{ei}^2(x_0) \gg 1$, which also shows the approximate proportionality of F to $1/\nu_{ei}^2(x_0)$. F is moderated by the fact that the fact that $|c\omega_0/[\omega_{ce}^2(x_0)L_n(x_0)] + 2c\omega_0/[\omega_{pe}^2(x_0)L_B(x_0)]| \ll 1$ in cases where semi-classical methods, such as the uniform approximation, are appropriate, and the proportionality to this factor additionally shows that F will generally increase for larger gradients of $n_e(x)$ and $B(x)$ at x_0 . Eq. (3.50) is

also valid if the vacuum wave is in O-mode, as the X-mode and O-mode dispersion relations are identical in vacuo. This fact allows us to express F for the case considered in Chapter 6, as well as [13, 14], with x_v being located at the gyrotron launcher,

$$F \approx \frac{\mathcal{F} e^{-\tau} W^2(x_v)}{\pi W^2(x_0)} \left| \frac{c\omega_0}{\omega_{ce}^2(x_0)L_n(x_0)} + \frac{2c\omega_0}{\omega_{pe}^2(x_0)L_B(x_0)} \right| \frac{\omega_{ce}^2(x_0)}{\nu^2(x_0)} \frac{\omega_{pe}^4(x_0)}{[2\omega_0^2 - \omega_{pe}^2(x_0)]^2}; \quad (3.51)$$

\mathcal{F} is the fraction of power coupled to the plasma in X-mode upon the high-field side wall reflection, τ is the total optical thickness from the gyrotron launcher to the UHR, and we have neglected 1 in comparison with $[\omega_{ce}^2(x_0)/\nu^2(x_0)]\{\omega_{pe}^4(x_0)/[2\omega_0^2 - \omega_{pe}^2(x_0)]^2\} \gg 1$. For typical parameters of 105 GHz CTS at ASDEX Upgrade, $F \sim 10^6$ when $\mathcal{F} e^{-\tau} \sim 1$, which is in agreement with maximum field enhancement found numerically in [13]. While the above expression gives a well-defined answer to the question of field enhancement right at the UHR, we note that the variation of $|\mathbf{E}(x)|^2$ is very rapid in this region, meaning that questions related to PDIs are best addressed by considering the full electric field given by the uniform approximation, or obtained from a numerical solution of the field enhancement differential equations, as done in [13, 14], over the relevant PDI length scale.

Chapter 4

Parametric Decay Theory

Having introduced the necessary basic concepts, we are now in a position to discuss PDIs. A number of different, not always consistent, approaches to treating PDIs exist, e.g. [134, 135, 106, 136, 137, 55, 8, 13, 138], so a few remarks on the framework presented here are in order. Our goal is to investigate PDIs near the UHR and the second-harmonic UHR in ASDEX Upgrade. The PDIs near the UHR are treated within the dipole approximation using the kinetic framework presented in [109, 13]. This framework has the advantage of delivering the growth rate of PDIs directly from kinetic theory, and is thus capable of handling Landau damping and other hot plasma effects which are important near the UHR. However, in its basic form, it only considers electrostatic daughter waves, treats the pump wave within the dipole approximation ($k_0 \approx 0$), and has no direct way of handling inhomogeneities. The last point in particular makes it unsuitable for treating the PDIs near the second-harmonic UHR which rely on trapping of the (approximately) half-frequency waves they excite near a maximum of the UH frequency to reduce their threshold to a level accessible for gyrotron radiation. For the PDIs near the second-harmonic UHR we therefore utilize the framework of [8, 9, 12] where the nonlinear current or charge densities are calculated based on fluid models and inserted on the right hand side of the generalized WKB equations from Chapter 2. This framework has the advantage of allowing inhomogeneities to be treated within a semi-classical setting, makes no dipole approximation when treating the pump wave, and may easily be extended to electromagnetic daughter waves. However, the calculation of the nonlinear current and charge densities relies on fluid models which are only valid for cold plasmas, so no hot plasma effects are taken into account when computing the coupling coefficients, and the cold plasma models used may not even reproduce the results of kinetic theory in the low-temperature limit unless great care is taken [139, 140, 141]. There are thus advantages and drawbacks to both frameworks, with either one treating cases which are not easily accessible to the other.

As the Author has already presented the kinetic framework in detail in [109, 13], the latter of which is included in this work, we shall simply apply it in Chapter 6 and refer to the aforementioned sources for the details. This Chapter is instead devoted to the framework of [8, 9, 12], which could benefit from a more unified treatment than what is

available in typical journal articles. In Section 4.1, we discuss the calculation of nonlinear charge densities, which constitutes the basic component of this framework. In Section 4.2, we demonstrate the occurrence of PDIs from the basic equations, covering homogeneous media, where we derive the basic growth rate of PDIs, and inhomogeneous, monotonic media, where we rederive the Piliya–Rosenbluth criterion with less reliance on complex analysis than the original sources. In Section 4.3, we cover the more complicated case of PDIs involving trapped daughter waves, which is of importance in Chapter 5. Finally, Section 4.4 briefly discusses saturation of PDIs.

4.1 Calculation of Nonlinear Charge Densities

The fundamental process responsible for PDIs is nonlinear interaction between linear wave modes induced by a large-amplitude pump wave. In this Section we hence compute the nonlinear charge densities, which represent this coupling for electrostatic waves; for electromagnetic waves one can similarly compute nonlinear current densities [139, 140, 141, 9, 12]. To keep matters relatively simple, our calculations are carried out within cold plasma theory. We note that accurate results may require the use of kinetic theory even in the low-temperature limit [139, 140, 141], but as our treatment of the plasma is in any case highly idealized, the cold plasma model is considered sufficient for the subsequent estimates. The equations of motion of species σ in a cold plasma are Eqs. (2.15) and (2.16), which are repeated below, ignoring collisions,

$$\frac{\partial n_\sigma(\mathbf{r}, t)}{\partial t} + \frac{\partial}{\partial \mathbf{r}} \cdot [n_\sigma(\mathbf{r}, t) \mathbf{V}_\sigma(\mathbf{r}, t)] = 0, \quad (4.1)$$

$$\frac{\partial \mathbf{V}_\sigma(\mathbf{r}, t)}{\partial t} + \mathbf{V}_\sigma(\mathbf{r}, t) \cdot \frac{\partial \mathbf{V}_\sigma(\mathbf{r}, t)}{\partial \mathbf{r}} = \frac{q_\sigma}{m_\sigma} [\mathbf{E}(\mathbf{r}, t) + \mathbf{V}_\sigma(\mathbf{r}, t) \times \mathbf{B}(\mathbf{r}, t)]. \quad (4.2)$$

PDIs originate from the quadratic terms, $(\partial/\partial \mathbf{r}) \cdot (n_\sigma \mathbf{V}_\sigma)$ and $\mathbf{V}_\sigma \cdot (\partial \mathbf{V}_\sigma / \partial \mathbf{r})$, in Eqs. (4.1) and (4.2). We now consider three-wave interactions in a homogeneous plasma (effects of inhomogeneities are included in Section 4.2) by superposing three plane waves on top of a plasma equilibrium with $n_\sigma(\mathbf{r}, t) = n_\sigma^{(0)}$, $\mathbf{E}(\mathbf{r}, t) = \mathbf{V}_\sigma(\mathbf{r}, t) = \mathbf{0}$, $\mathbf{B}(\mathbf{r}, t) = \mathbf{B}^{(0)}$, which gives

$$n_\sigma(\mathbf{r}, t) = n_\sigma^{(0)} + \text{Re} \left[n_{\sigma 0} e^{i(\mathbf{k}_0 \cdot \mathbf{r} - \omega_0 t)} + n_{\sigma 1} e^{i(\mathbf{k}_1 \cdot \mathbf{r} - \omega_1 t)} + n_{\sigma 2} e^{i(\mathbf{k}_2 \cdot \mathbf{r} - \omega_2 t)} \right], \quad (4.3)$$

$$\mathbf{V}_\sigma(\mathbf{r}, t) = \text{Re} \left[\mathbf{V}_{\sigma 0} e^{i(\mathbf{k}_0 \cdot \mathbf{r} - \omega_0 t)} + \mathbf{V}_{\sigma 1} e^{i(\mathbf{k}_1 \cdot \mathbf{r} - \omega_1 t)} + \mathbf{V}_{\sigma 2} e^{i(\mathbf{k}_2 \cdot \mathbf{r} - \omega_2 t)} \right], \quad (4.4)$$

$$\mathbf{E}(\mathbf{r}, t) = \text{Re} \left[\mathbf{E}_0 e^{i(\mathbf{k}_0 \cdot \mathbf{r} - \omega_0 t)} - i\mathbf{k}_1 A_1 e^{i(\mathbf{k}_1 \cdot \mathbf{r} - \omega_1 t)} - i\mathbf{k}_2 A_2 e^{i(\mathbf{k}_2 \cdot \mathbf{r} - \omega_2 t)} \right]; \quad (4.5)$$

$n_{\sigma j}$ and $\mathbf{V}_{\sigma j}$ for $j = 0, 1, 2$ are the density perturbation and fluid velocity amplitudes associated with the pump (subscript 0) and daughter waves (subscripts 1 and 2), \mathbf{E}_0 is the electric field amplitude associated with the pump wave, which can be electromagnetic, A_j for $j = 1, 2$ is the potential amplitude associated with the (electrostatic) daughter waves,

and $\mathbf{B}(\mathbf{r}, t) \approx \mathbf{B}^{(0)}$ since we are dealing with a non-relativistic plasma. We further take the plane waves to satisfy the selection rules $\omega_0 = \omega_1 + \omega_2$ and $\mathbf{k}_0 = \mathbf{k}_1 + \mathbf{k}_2$, allowing the quadratic terms in Eqs. (4.1) and (4.2) to produce one of the waves from the two other waves. To proceed we write $n_{\sigma j} = n_{\sigma j,1} + n_{\sigma j,\text{nl}}$ and $\mathbf{V}_{\sigma j} = \mathbf{V}_{\sigma j,1} + \mathbf{V}_{\sigma j,\text{nl}}$, where $n_{\sigma j,1}$, $\mathbf{V}_{\sigma j,1}$ are the linear response of $n_{\sigma j}$, $\mathbf{V}_{\sigma j}$ to \mathbf{E}_j and $n_{\sigma j,\text{nl}}$, $\mathbf{V}_{\sigma j,\text{nl}}$ are the nonlinear response of $n_{\sigma j}$, $\mathbf{V}_{\sigma j}$; as the waves are considered weakly nonlinear, we assume $|n_{\sigma j,1}| \gg |n_{\sigma j,\text{nl}}|$ and $|\mathbf{V}_{\sigma j,1}| \gg |\mathbf{V}_{\sigma j,\text{nl}}|$. The linear response within cold plasma theory was treated in Section 2.1, and repeating the same calculation here, noting that $n_{\sigma j}$ and $\mathbf{V}_{\sigma j}$ are essentially Fourier–Laplace amplitudes, we find

$$n_{\sigma j,1} = \frac{\mathbf{k}_j \cdot \mathbf{V}_{\sigma j,1}}{\omega_j} n_{\sigma}^{(0)}, \quad (4.6)$$

$$\mathbf{V}_{\sigma j,1} = \frac{q_{\sigma}}{m_{\sigma}} \mathbf{M}_{\sigma j} \cdot \mathbf{E}_j, \quad \mathbf{M}_{\sigma j} = \begin{bmatrix} \frac{i\omega_j}{\omega_j^2 - \omega_{c\sigma}^2} & -\frac{\omega_{c\sigma}}{\omega_j^2 - \omega_{c\sigma}^2} & 0 \\ \frac{\omega_{c\sigma}}{\omega_j^2 - \omega_{c\sigma}^2} & \frac{i\omega_j}{\omega_j^2 - \omega_{c\sigma}^2} & 0 \\ 0 & 0 & \frac{i}{\omega_j} \end{bmatrix}. \quad (4.7)$$

The nonlinear response is obtained by inserting Eqs. (4.3), (4.4), (4.5), and $\mathbf{B}(\mathbf{r}, t) \approx \mathbf{B}^{(0)}$ in Eqs. (4.1) and (4.2), remembering the selection rules $\omega_0 = \omega_1 + \omega_2$ and $\mathbf{k}_0 = \mathbf{k}_1 + \mathbf{k}_2$. For instance, collecting the terms varying as $e^{i\mathbf{k}_1 \cdot \mathbf{r} - i\omega_1 t}$ in Eq. (4.1) yields

$$n_{\sigma 1,\text{nl}} \approx \frac{\mathbf{k}_1}{\omega_1} \cdot \left[n_{\sigma}^{(0)} \mathbf{V}_{\sigma 1,\text{nl}} + \frac{n_{\sigma 0,1} \mathbf{V}_{\sigma 2,1}^*}{2} + \frac{n_{\sigma 2,1}^* \mathbf{V}_{\sigma 0,1}}{2} \right], \quad (4.8)$$

where we have only included the nonlinear terms to 1st order, since $|n_{\sigma j,1}| \gg |n_{\sigma j,\text{nl}}|$ and $|\mathbf{V}_{\sigma j,1}| \gg |\mathbf{V}_{\sigma j,\text{nl}}|$. From Eqs. (4.6) and (4.7), $\mathbf{V}_{\sigma 0,1} = q_{\sigma} \mathbf{M}_{\sigma 0} \cdot \mathbf{E}_0 / m_{\sigma}$, $\mathbf{V}_{\sigma 2,1}^* = iq_{\sigma} \mathbf{M}_{\sigma 2}^* \cdot \mathbf{k}_2 A_2^* / m_{\sigma}$, $n_{\sigma 0,1} = n_{\sigma}^{(0)} \mathbf{k}_0 \cdot \mathbf{V}_{\sigma 0,1} / \omega_0$, and $n_{\sigma 2,1}^* = n_{\sigma}^{(0)} \mathbf{k}_2 \cdot \mathbf{V}_{\sigma 2,1}^* / \omega_2$. To find $\mathbf{V}_{\sigma 1,\text{nl}}$, we collect the terms varying as $e^{i\mathbf{k}_1 \cdot \mathbf{r} - i\omega_1 t}$ in Eq. (4.2), again keeping only the 1st order nonlinear terms,

$$-i\omega_1 \mathbf{V}_{\sigma 1,\text{nl}} - \mathbf{V}_{\sigma 1,\text{nl}} \times \boldsymbol{\omega}_{c\sigma} = \frac{i(\mathbf{V}_{\sigma 0,1} \cdot \mathbf{k}_2) \mathbf{V}_{\sigma 2,1}^*}{2} - \frac{i(\mathbf{V}_{\sigma 2,1}^* \cdot \mathbf{k}_0) \mathbf{V}_{\sigma 0,1}}{2}. \quad (4.9)$$

Eq. (4.9) is equivalent to the equation governing $\mathbf{V}_{\sigma 1,1}$ if we let $\mathbf{E}_1 \rightarrow im_{\sigma} [(\mathbf{V}_{\sigma 0,1} \cdot \mathbf{k}_2) \mathbf{V}_{\sigma 2,1}^* - (\mathbf{V}_{\sigma 2,1}^* \cdot \mathbf{k}_0) \mathbf{V}_{\sigma 0,1}] / (2q_{\sigma})$, and its solution is hence given by Eq. (4.7) as

$$\mathbf{V}_{\sigma 1,\text{nl}} = \frac{i}{2} \mathbf{M}_{\sigma 1} \cdot [(\mathbf{V}_{\sigma 0,1} \cdot \mathbf{k}_2) \mathbf{V}_{\sigma 2,1}^* - (\mathbf{V}_{\sigma 2,1}^* \cdot \mathbf{k}_0) \mathbf{V}_{\sigma 0,1}]. \quad (4.10)$$

Plugging the above results into Eq. (4.8) finally gives

$$n_{\sigma 1,\text{nl}} \approx \frac{\mathbf{k}_1}{2\omega_1} \cdot \left\{ i\mathbf{M}_{\sigma 1} \cdot [(\mathbf{V}_{\sigma 0,1} \cdot \mathbf{k}_2) \mathbf{V}_{\sigma 2,1}^* - (\mathbf{V}_{\sigma 2,1}^* \cdot \mathbf{k}_0) \mathbf{V}_{\sigma 0,1}] + \frac{(\mathbf{k}_0 \cdot \mathbf{V}_{\sigma 0,1}) \mathbf{V}_{\sigma 2,1}^*}{\omega_0} + \frac{(\mathbf{k}_2 \cdot \mathbf{V}_{\sigma 2,1}^*) \mathbf{V}_{\sigma 0,1}}{\omega_2} \right\} n_{\sigma}^{(0)}, \quad (4.11)$$

which is an explicit expression for the nonlinear density amplitude of species σ for the mode characterized by (\mathbf{k}_1, ω_1) when $\mathbf{V}_{\sigma j,1}$ from Eq. (4.7) is inserted. Further, using the fact that the daughter wave indices may be interchanged ($1 \leftrightarrow 2$) and taking the complex conjugate, we find

$$n_{\sigma 2, \text{nl}}^* \approx \frac{\mathbf{k}_2}{2\omega_2} \cdot \left\{ -i\mathbf{M}_{\sigma 2}^* \cdot [(\mathbf{V}_{\sigma 0,1}^* \cdot \mathbf{k}_1)\mathbf{V}_{\sigma 1,1} - (\mathbf{V}_{\sigma 1,1} \cdot \mathbf{k}_0)\mathbf{V}_{\sigma 0,1}^*] + \frac{(\mathbf{k}_0 \cdot \mathbf{V}_{\sigma 0,1}^*)\mathbf{V}_{\sigma 1,1}}{\omega_0} + \frac{(\mathbf{k}_1 \cdot \mathbf{V}_{\sigma 1,1})\mathbf{V}_{\sigma 0,1}^*}{\omega_1} \right\} n_{\sigma}^{(0)}, \quad (4.12)$$

providing us with the nonlinear density amplitudes for both daughter waves. Eqs. (4.11) and (4.12), along with Eq. (4.7), show that $n_{\sigma 1, \text{nl}} \propto |\mathbf{E}_0|A_2^*$ and $n_{\sigma 2, \text{nl}}^* \propto |\mathbf{E}_0^*|A_1$, meaning that the nonlinear current densities for (\mathbf{k}_1, ω_1) and (\mathbf{k}_2, ω_2) may be written as

$$\rho_{1, \text{nl}} = \sum_{\sigma} q_{\sigma} n_{\sigma 1, \text{nl}} = \alpha_{12} |\mathbf{E}_0| A_2^*, \quad \rho_{2, \text{nl}}^* = \sum_{\sigma} q_{\sigma} n_{\sigma 2, \text{nl}}^* = \alpha_{21}^* |\mathbf{E}_0^*| A_1, \quad (4.13)$$

where α_{12} and α_{21}^* are nonlinear coupling coefficients independent of the wave amplitudes. The effect of the nonlinear charge density is thus to couple the two daughter wave amplitudes to each other with a coupling strength proportional to the pump wave amplitude. In the cases of interest in this work, we always have $\omega_0 \gtrsim |\omega_{ce}|$, making the ion response to the pump wave negligible. We can thus approximate $\rho_{\text{nl}} \approx -en_{e, \text{nl}}$, from which

$$\alpha_{12} \approx \frac{\epsilon_0}{2} \frac{\omega_{ce}}{B^{(0)}} \omega_{pe}^2 \frac{\mathbf{k}_1}{\omega_1} \cdot \left\{ \mathbf{M}_{e1} \cdot [(\mathbf{k}_0 \cdot \mathbf{M}_{e2}^* \cdot \mathbf{k}_2)\mathbf{M}_{e0} \cdot \mathbf{e}_0 - (\mathbf{k}_2 \cdot \mathbf{M}_{e0} \cdot \mathbf{e}_0)\mathbf{M}_{e2}^* \cdot \mathbf{k}_2] + \frac{i(\mathbf{k}_0 \cdot \mathbf{M}_{e0} \cdot \mathbf{e}_0)\mathbf{M}_{e2}^* \cdot \mathbf{k}_2}{\omega_0} + \frac{i(\mathbf{k}_2 \cdot \mathbf{M}_{e2}^* \cdot \mathbf{k}_2)\mathbf{M}_{e0} \cdot \mathbf{e}_0}{\omega_2} \right\}, \quad (4.14)$$

$$\alpha_{21}^* \approx \frac{\epsilon_0}{2} \frac{\omega_{ce}}{B^{(0)}} \omega_{pe}^2 \frac{\mathbf{k}_2}{\omega_2} \cdot \left\{ \mathbf{M}_{e2}^* \cdot [(\mathbf{k}_0 \cdot \mathbf{M}_{e1} \cdot \mathbf{k}_1)\mathbf{M}_{e0}^* \cdot \mathbf{e}_0^* - (\mathbf{k}_1 \cdot \mathbf{M}_{e0}^* \cdot \mathbf{e}_0^*)\mathbf{M}_{e1} \cdot \mathbf{k}_1] - \frac{i(\mathbf{k}_0 \cdot \mathbf{M}_{e0}^* \cdot \mathbf{e}_0^*)\mathbf{M}_{e1} \cdot \mathbf{k}_1}{\omega_0} - \frac{i(\mathbf{k}_1 \cdot \mathbf{M}_{e1} \cdot \mathbf{k}_1)\mathbf{M}_{e0}^* \cdot \mathbf{e}_0^*}{\omega_1} \right\}, \quad (4.15)$$

with $\mathbf{e}_0 = \mathbf{E}_0/|\mathbf{E}_0|$ being the pump wave polarization unit vector.

While Eqs. (4.7), (4.13), (4.14), and (4.15) provide a full description of the nonlinear charge density for the onset of PDIs, it is instructive to evaluate $\rho_{1, \text{nl}}$ and $\rho_{2, \text{nl}}^*$ explicitly in some simple cases. To this end, we consider an X-mode pump wave propagating along the x -direction ($\mathbf{k}_0 = k_0 \mathbf{e}_x$) decaying to two electrostatic waves, also propagating primarily along the x -direction ($\mathbf{k}_1 \approx k_{1x} \mathbf{e}_x$ and $\mathbf{k}_2 \approx k_{2x} \mathbf{e}_x$). If we further assume that $\omega_1 \approx \omega_2 \approx \omega_{UH}$, which is the case of interest in Chapter 5, it holds that $\omega_0 \approx 2\omega_{UH}$, leading to $|E_{0x}| = |\{i\omega_{ce}\omega_{pe}^2/[\omega_0(\omega_0^2 - \omega_{UH}^2)]\}E_{0y}| \approx [|\omega_{ce}|\omega_{pe}^2/(6\omega_{UH}^3)]|E_{0y}| \leq |E_{0y}|/3^{5/2} \approx 0.06415|E_{0y}|$; it is thus permissible neglect E_{0x} relative to E_{0y} . With these simplifications and using the selection rules, $\rho_{1, \text{nl}}$ and $\rho_{2, \text{nl}}^*$ may be evaluated, following some tedious but straightforward

algebra,

$$\rho_{1, \text{nl}} \approx -\frac{\epsilon_0}{2} \frac{\omega_{pe}^2 \omega_{ce}^2 \omega_1 k_{1x}^2 k_{2x}}{(\omega_0^2 - \omega_{ce}^2)(\omega_1^2 - \omega_{ce}^2)(\omega_2^2 - \omega_{ce}^2)} \left\{ \frac{\omega_2 - \omega_1}{\omega_1} + \frac{k_0}{k_{1x}} \left[1 + \frac{\omega_0 \omega_2}{\omega_1^2} + \frac{\omega_2}{\omega_0} \left(1 - \frac{\omega_{ce}^2}{\omega_1^2} \right) \right] \right\} \frac{E_{0y}}{B^{(0)}} A_2^*, \quad (4.16)$$

$$\rho_{2, \text{nl}}^* \approx \frac{\epsilon_0}{2} \frac{\omega_{pe}^2 \omega_{ce}^2 \omega_2 k_{2x}^2 k_{1x}}{(\omega_0^2 - \omega_{ce}^2)(\omega_1^2 - \omega_{ce}^2)(\omega_2^2 - \omega_{ce}^2)} \left\{ \frac{\omega_2 - \omega_1}{\omega_2} - \frac{k_0}{k_{2x}} \left[1 + \frac{\omega_0 \omega_1}{\omega_2^2} + \frac{\omega_1}{\omega_0} \left(1 - \frac{\omega_{ce}^2}{\omega_2^2} \right) \right] \right\} \frac{E_{0y}^*}{B^{(0)}} A_1. \quad (4.17)$$

Eqs. (4.16) and (4.17) are equivalent to Eq. (A.7) from [8], except for the terms $(\omega_2/\omega_0)(1 - \omega_{ce}^2/\omega_1^2)$ and $(\omega_1/\omega_0)(1 - \omega_{ce}^2/\omega_2^2)$. This may be seen by converting Eqs. (4.16) and (4.17) to Gaussian units [96], noting that $k_{1x} = q_1$ and $k_{2x} = -q_2$ in [8], and remembering that we have defined \mathbf{E} and ρ in physical space in terms of the real part of the amplitudes, while [8] uses complex conjugates without the factor 1/2 included when taking the real part. The extra terms in Eqs. (4.16) and (4.17) relative to Eq. (A.7) from [8] originate from the fact that we retain the electron density perturbation at (\mathbf{k}_0, ω_0) , $n_{e0,1}$, which is neglected in [8]. When $\omega_1 \approx \omega_2 \approx \omega_0/2$, Eqs. (4.16) and (4.17) reduce to

$$\rho_{1, \text{nl}} \approx -\frac{\epsilon_0}{2} \frac{\omega_{pe}^2 \omega_{ce}^2 \omega_1 k_0 k_{1x} k_{2x}}{(\omega_0^2 - \omega_{ce}^2)(\omega_1^2 - \omega_{ce}^2)(\omega_2^2 - \omega_{ce}^2)} \left[3 + \frac{1}{2} \left(1 - \frac{\omega_{ce}^2}{\omega_1^2} \right) \right] \frac{E_{0y}}{B^{(0)}} A_2^*, \quad (4.18)$$

$$\rho_{2, \text{nl}}^* \approx -\frac{\epsilon_0}{2} \frac{\omega_{pe}^2 \omega_{ce}^2 \omega_2 k_0 k_{1x} k_{2x}}{(\omega_0^2 - \omega_{ce}^2)(\omega_1^2 - \omega_{ce}^2)(\omega_2^2 - \omega_{ce}^2)} \left[3 + \frac{1}{2} \left(1 - \frac{\omega_{ce}^2}{\omega_2^2} \right) \right] \frac{E_{0y}^*}{B^{(0)}} A_1. \quad (4.19)$$

For $\omega_1 \approx \omega_{UH}$, the extra terms in Eqs. (4.18) and (4.19), $(1/2)(1 - \omega_{ce}^2/\omega_1^2) \approx \omega_{pe}^2/(2\omega_{UH}^2) < 1/2$, are small compared with the dominant terms of value 3, which justifies neglecting them in [8].

We also consider the case in which the pump wave is electrostatic and mainly propagates along the x -direction; the daughter waves are assumed to propagate mainly along the x -direction as well. As this case is relevant for the secondary PDI near the second-harmonic UHR [9, 10, 11, 12], we refer to the pump wave as $(\mathbf{k}_2 \approx k_{2x} \mathbf{e}_x, \omega_2)$, the high-frequency daughter wave as $(\mathbf{k}'_2 \approx k'_{2x} \mathbf{e}_x, \omega'_2)$, and the low-frequency daughter wave as $(\mathbf{k}_{\text{LF}} \approx k_{\text{LF}x} \mathbf{e}_x, \omega_{\text{LF}})$; the waves are assumed to satisfy the selection rules $\mathbf{k}_2 = \mathbf{k}'_2 + \mathbf{k}_{\text{LF}}$ and $\omega_2 = \omega'_2 + \omega_{\text{LF}}$. Inserting $\mathbf{E}_2 \approx -ik_{2x} A_2 \mathbf{e}_x$ for the pump electric field and using the k_x selection rule yields

$$\rho'_{2, \text{nl}} \approx -\frac{\epsilon_0}{2} \frac{\omega_{pe}^2 |\omega_{ce}|}{B^{(0)}} \frac{k_{2x} k'_{2x} k_{\text{LF}x} \omega_2 \omega'_2 \omega_{\text{LF}}}{(\omega_2^2 - \omega_{ce}^2)(\omega_2'^2 - \omega_{ce}^2)(\omega_{\text{LF}}^2 - \omega_{ce}^2)} \left(\frac{k_{2x}}{\omega_2} + \frac{k'_{2x}}{\omega_2'} + \frac{k_{\text{LF}x}}{\omega_{\text{LF}}} \right) A_2 A_{\text{LF}}^*, \quad (4.20)$$

$$\rho_{\text{LF}, \text{nl}}^* \approx -\frac{\epsilon_0 \omega_{pe}^2 |\omega_{ce}|}{2 B^{(0)}} \frac{k_{2x} k'_{2x} k_{\text{LF}x} \omega_2 \omega'_2 \omega_{\text{LF}}}{(\omega_2^2 - \omega_{ce}^2)(\omega_2'^2 - \omega_{ce}^2)(\omega_{\text{LF}}^2 - \omega_{ce}^2)} \left(\frac{k_{2x}}{\omega_2} + \frac{k'_{2x}}{\omega_2'} + \frac{k_{\text{LF}x}}{\omega_{\text{LF}}} \right) A_2^* A_2'. \quad (4.21)$$

Eq. (4.20) is equivalent to an expression from [9], when account is taken for the differences in units and definitions between this work and [9]. As indicated by the nomenclature, we take the daughter wave characterized by $(\mathbf{k}_{\text{LF}}, \omega_{\text{LF}})$ to be a low-frequency daughter wave (in the LH frequency range), while (\mathbf{k}_2, ω_2) and $(\mathbf{k}'_2, \omega'_2)$ are both assumed to be EBWs with frequencies near the UH frequency, i.e., we assume that $\omega_{\text{LF}} \ll \omega_2 \approx \omega_2' \approx \omega_{UH} \sim |\omega_{ce}|$ and further set $k_{\text{LF}x} \sim k_{2x} \sim k'_{2x}$. With these assumptions, Eqs. (4.20) and (4.21) may be approximated as

$$\rho'_{2, \text{nl}} \approx \frac{\epsilon_0 k_{2x} k'_{2x} k_{\text{LF}x}^2 \omega_2 \omega_2'}{2 B^{(0)} \omega_{pe}^2 |\omega_{ce}|} A_2 A_{\text{LF}}^*, \quad \rho_{\text{LF}, \text{nl}}^* \approx \frac{\epsilon_0 k_{2x} k'_{2x} k_{\text{LF}x}^2 \omega_2 \omega_2'}{2 B^{(0)} \omega_{pe}^2 |\omega_{ce}|} A_2^* A_2'; \quad (4.22)$$

just as Eq. (4.20), Eq. (4.22) is similar to expressions found in [9]. We finally note that the nonlinear current at (\mathbf{k}_2, ω_2) may be calculated by repeating the calculations in this Section with the terms having the appropriate WKB phase variation and is found to be

$$\begin{aligned} \rho_{2, \text{nl}}^* &= -\frac{\epsilon_0 \omega_{pe}^2 |\omega_{ce}|}{2 B^{(0)}} \frac{k_{2x} k'_{2x} k_{\text{LF}x} \omega_2 \omega_2' \omega_{\text{LF}}}{(\omega_2^2 - \omega_{ce}^2)(\omega_2'^2 - \omega_{ce}^2)(\omega_{\text{LF}}^2 - \omega_{ce}^2)} \left(\frac{k_{2x}}{\omega_2} + \frac{k'_{2x}}{\omega_2'} + \frac{k_{\text{LF}x}}{\omega_{\text{LF}}} \right) A_2^* A_{\text{LF}}^* \\ &\approx \frac{\epsilon_0 k_{2x} k'_{2x} k_{\text{LF}x}^2 \omega_2 \omega_2'}{2 B^{(0)} \omega_{pe}^2 |\omega_{ce}|} A_2^* A_{\text{LF}}^*. \end{aligned} \quad (4.23)$$

Eq. (4.23) is of use when discussing saturation of PDIs in Section 4.4.

4.2 Onset of Parametric Decay Instabilities with Free Daughter Waves

Having accounted for both the linear and the nonlinear responses, we are now in a position to discuss PDIs. To do this we insert $\rho_{\text{nl}}(\mathbf{r}, t) = \text{Re}\{\rho_{1, \text{nl}} e^{i[\theta_0(\mathbf{r}, t) - \theta_2(\mathbf{r}, t)]}\}$ in Eq. (3.21); note that the WKB phase of $\rho_{1, \text{nl}}$ is not $\theta_1(\mathbf{r}, t) = \int^x k_{1x}(x') dx' + k_{1y}y + k_{1\parallel}z - \omega_1 t$ exactly, but rather $\theta_0(\mathbf{r}, t) - \theta_2(\mathbf{r}, t) = \int^x [k_{0x}(x') - k_{2x}(x')] dx' + k_{1y}y + k_{1\parallel}z - \omega_1 t$. Introducing the wave vector mismatch along the x -direction, $\Delta = k_{0x} - k_{1x} - k_{2x}$, and considering waves propagating along the x -direction, Eq. (3.21) may be recast as

$$i\Gamma_1 a_1 + i\frac{\partial a_1}{\partial t} + iv_{1x} \frac{\partial a_1}{\partial x} = \nu_{12} e^{i \int^x \Delta dx'} |\mathbf{E}_0| a_2^*, \quad (4.24)$$

where Γ_1 and v_{1x} are Γ and v_x evaluated at $(\mathbf{k}_1, x, \omega_1)$, and

$$\nu_{12} = \frac{\alpha_{12}}{\epsilon_0 (\partial \mathcal{D}'_1 / \partial \omega)} \frac{\sqrt{\partial \mathcal{D}'_1 / \partial k_x}}{(\sqrt{\partial \mathcal{D}'_2 / \partial k_x})^*} \quad (4.25)$$

is the nonlinear coupling factor, modified to account for the use of the conserved amplitude $a = A\sqrt{\partial\mathcal{D}'/\partial k_x}$ and divided by $\partial\mathcal{D}'/\partial\omega$. A similar calculation for $\rho_{\text{nl}}(\mathbf{r}, t) = \text{Re}\{\rho_{2, \text{nl}} e^{i[\theta_0(\mathbf{r}, t) - \theta_1(\mathbf{r}, t)]}\}$ yields

$$-i\Gamma_2 a_2 - i\frac{\partial a_2^*}{\partial t} - iv_{2x} \frac{\partial a_2^*}{\partial x} = \nu_{21}^* e^{-i\int^x \Delta dx'} |\mathbf{E}_0^*| a_1; \quad (4.26)$$

Γ_2 and v_{2x} are Γ and v_x evaluated at $(\mathbf{k}_2, x, \omega_2)$, and

$$\nu_{21}^* = \frac{\alpha_{21}^*}{\epsilon_0(\partial\mathcal{D}'_2/\partial\omega)} \frac{(\sqrt{\partial\mathcal{D}'_2/\partial k_x})^*}{\sqrt{\partial\mathcal{D}'_1/\partial k_x}}, \quad (4.27)$$

just as for the other daughter waves. While Eqs. (4.24) and (4.26) are inadequate for describing PDIs involving trapped daughter waves, they provide an adequate description of PDIs with free daughter waves which serve as a natural starting point. We particularly consider such PDIs in homogeneous media and in monotonic, inhomogeneous media.

4.2.1 Onset of Parametric Decay Instabilities in Homogeneous Media

In a homogeneous medium, the selection rules may be satisfied everywhere, such that $\Delta = 0$. We further assume the daughter wave amplitudes to be homogeneous, i.e., $\partial a_1/\partial x = \partial a_2^*/\partial x = 0$, which reduces Eqs. (4.24) and (4.26) to

$$i\Gamma_1 a_1 + i\frac{\partial a_1}{\partial t} = \nu_{12} |\mathbf{E}_0| a_2^*, \quad -i\Gamma_2 a_2^* - i\frac{\partial a_2^*}{\partial t} = \nu_{21}^* |\mathbf{E}_0^*| a_1. \quad (4.28)$$

Isolating a_2^* in the first part of Eq. (4.28), $a_2^* = i[(\partial a_1/\partial t) + \Gamma_1 a_1]/(\nu_{12} |\mathbf{E}_0|)$, and substituting it into the second part, ignoring the the variation of \mathbf{E}_0 with t , yields

$$\frac{\partial^2 a_1}{\partial t^2} + (\Gamma_1 + \Gamma_2) \frac{\partial a_1}{\partial t} + (\Gamma_1 \Gamma_2 - \nu_{12} \nu_{21}^* |\mathbf{E}_0|^2) a_1 = 0. \quad (4.29)$$

Eq. (4.29) is a second-order, ordinary differential equation with constant coefficients. It can be solved by assuming $a_1 \propto e^{\gamma t}$, which results in a quadratic equation for γ ,

$$\gamma^2 + (\Gamma_1 + \Gamma_2)\gamma + (\Gamma_1 \Gamma_2 - \nu_{12} \nu_{21}^* |\mathbf{E}_0|^2) = 0. \quad (4.30)$$

This quadratic equation is solved using the usual method

$$\gamma = \pm \sqrt{\nu_{12} \nu_{21}^* |\mathbf{E}_0|^2 + \left(\frac{\Gamma_1 - \Gamma_2}{2}\right)^2} - \frac{\Gamma_1 + \Gamma_2}{2}. \quad (4.31)$$

We note that this γ is similar in form to the ones from [106, 109, 13]. The solution of Eq. (4.29) will grow exponentially if one of the roots has $\text{Re}(\gamma) > 0$. This initial behavior is characteristic of absolute instabilities [95], and the occurrence of such instabilities will inevitably couple pump wave power into the daughter waves until they reach a saturated amplitude, to be discussed in Section 4.4. Assuming $\nu_{12} \nu_{21}^* > 0$, which is at least true for

EBW/X-mode wave daughters with the same frequency, leads to real γ in Eq. (4.31) and further means that only the root with + in front of the square root has the possibility of $\gamma > 0$ for linearly stable waves ($\Gamma_1, \Gamma_2 > 0$). A PDI ($\gamma > 0$) will occur once $|\mathbf{E}_0|$ exceeds a threshold, $|\mathbf{E}_0^{\text{th}}|$; the instability condition can be written as

$$|\mathbf{E}_0| > |\mathbf{E}_0^{\text{th}}| = \sqrt{\frac{\Gamma_1 \Gamma_2}{\nu_{12} \nu_{21}^*}}. \quad (4.32)$$

Eq. (4.32) finally gives an explicit expression for the pump wave amplitude threshold which must be exceeded to excite PDIs in a homogeneous medium. The threshold is seen to increase with increasing daughter wave damping ($\Gamma_1 \Gamma_2$) and decrease with increasing nonlinear coupling strength ($\nu_{12} \nu_{21}^*$), in agreement with what is intuitively expected for nonlinear excitation of weakly damped waves.

4.2.2 Onset of Parametric Decay Instabilities in Monotonic, Inhomogeneous Media

The PDI threshold given by Eq. (4.32) is mainly determined by collisional damping which tends to be very weak in fusion plasmas. Naïvely applying Eq. (4.32) would thus imply the occurrence of PDIs at very small pump wave amplitudes, at odds with the general success of linear theories in describing high-power wave heating and current drive in fusion plasmas. In order to obtain a realistic estimate of the impact of PDIs, it is thus necessary to take inhomogeneities into account, as first noted by [89, 90, 91, 142]. To do this, we return to Eqs. (4.24) and (4.26), ignoring the damping terms and considering only steady state solutions with $\partial a_1 / \partial t = \partial a_2^* / \partial t = 0$ (when considering saturation of PDIs for free waves, non-stationary solutions have to be considered, as done in [91, 142]),

$$i v_{1x} \frac{\partial a_1}{\partial x} = \nu_{12} e^{i \int^x \Delta dx'} |\mathbf{E}_0| a_2^*, \quad -i v_{2x} \frac{\partial a_2^*}{\partial x} = \nu_{12}^* e^{-i \int^x \Delta dx'} |\mathbf{E}_0^*| a_1. \quad (4.33)$$

Just as in the homogeneous case, we isolate a_2^* in the first part of Eq. (4.33), $a_2^* = i v_{1x} (\partial a_1 / \partial x) e^{-i \int^x \Delta dx'} / (\nu_{12} |\mathbf{E}_0|)$, and insert this in the second part of Eq. (4.33), neglecting the variation of v_{1x} , ν_{12} , and $|\mathbf{E}_0|$ with x , since they are only assumed to vary significantly on the geometrical optics length scale \mathcal{L} . Additionally canceling out the exponential terms and rearranging, this yields

$$\frac{\partial^2 a_1}{\partial x^2} - i \Delta \frac{\partial a_1}{\partial x} - \frac{\nu_{12} \nu_{21}^* |\mathbf{E}_0|^2}{v_{1x} v_{2x}} a_1 = 0. \quad (4.34)$$

We now assume $v_{1x} v_{2x} > 0$ (as well as $\nu_{12} \nu_{21}^* > 0$), which is the case for EBW/X-mode wave daughters in underdense and moderately overdense plasmas, and approximately solve Eq. (4.34) using the method applied find to convective instabilities of trapped waves in [8]; note that the final result regarding wave amplification also holds for $v_{1x} v_{2x} < 0$ [90]. The method from [8] assumes a_1 to have a WKBJ-like form, $a_1 = \alpha_1 e^{\int^x \kappa dx'}$, where α_1 can be considered constant and κ is a slowly varying spatial growth rate. Inserting this ansatz

in Eq. (4.34) results in a quadratic equation for κ , $\kappa^2 - i\Delta\kappa - \nu_{12}\nu_{21}^*|\mathbf{E}_0|^2/(v_{1x}v_{2x}) = 0$, which may be solved to give

$$\kappa = \frac{i\Delta}{2} \pm \sqrt{\frac{\nu_{12}\nu_{21}^*|\mathbf{E}_0|^2}{v_{1x}v_{2x}} - \frac{\Delta^2}{4}}. \quad (4.35)$$

We consider waves moving in the positive x -direction ($v_{1x}, v_{2x} > 0$); the argument is similar for waves moving in the negative x -direction. As the waves move from $x = -\infty$ to $x = \infty$, they should experience amplification due to the PDI, meaning that we should choose the root of κ containing a potentially positive real part, i.e., the one with $+$ in front of the square root in Eq. (4.35). Based on this, the logarithm of the wave power (proportional to $|a_1|^2$) at an arbitrary value of x relative to that at $x = -\infty$ is

$$\ln \left[\frac{|a_1(x)|^2}{|a_1(-\infty)|^2} \right] = 2 \int_{-\infty}^x \text{Re}(\kappa) dx' = 2 \int_{-\infty}^x \text{Re} \left[\sqrt{\frac{\nu_{12}\nu_{21}^*|\mathbf{E}_0|^2}{v_{1x}v_{2x}} - \frac{\Delta^2}{4}} \right] dx'. \quad (4.36)$$

We note that $\text{Re}(\kappa) \neq 0$ requires $|\Delta| < 2\sqrt{\nu_{12}\nu_{21}^*|\mathbf{E}_0|^2/v_{1x}v_{2x}}$, meaning that the integral in Eq. (4.36) only has contributions from points where $|\Delta|$ is small. Assuming the variation of the plasma parameters to be monotonic, such that $\Delta = 0$ is only satisfied at one point ($x = x_r$), it is then acceptable to replace Δ by its first-order Taylor expansion around $x = x_r$, $\Delta \approx d\Delta/dx|_{x=x_r}(x - x_r)$, in the integrand of Eq. (4.36). After this, Eq. (4.36) can be evaluated by substituting the integration variable (x') with $\xi = |d\Delta/dx|_{x=x_r}|\sqrt{v_{1x}v_{2x}}(x - x_r)/(2\sqrt{\nu_{12}\nu_{21}^*|\mathbf{E}_0|^2})|$, noting that $\text{Re}(\kappa) \neq 0$ for $|\xi| < 1$, and using the indefinite integral $\int \sqrt{1 - \xi^2} d\xi = [\xi\sqrt{1 - \xi^2} + \arcsin(\xi)]/2$ [113],

$$\ln \left[\frac{|a_1(x)|^2}{|a_1(-\infty)|^2} \right] = \begin{cases} 0 & \text{for } \xi < -1, \\ \frac{2\nu_{12}\nu_{21}^*|\mathbf{E}_0|^2}{|d\Delta/dx|_{x=x_r}v_{1x}v_{2x}} \left[\xi\sqrt{1 - \xi^2} + \arcsin(\xi) + \frac{\pi}{2} \right] & \text{for } \xi \in [-1, 1], \\ \frac{2\pi\nu_{12}\nu_{21}^*|\mathbf{E}_0|^2}{|d\Delta/dx|_{x=x_r}v_{1x}v_{2x}} & \text{for } \xi > 1; \end{cases} \quad (4.37)$$

an expression equivalent to Eq. (4.37) is found in [91]. Unlike the homogeneous case, PDIs in inhomogeneous media do not possess an absolute threshold above which the daughter amplitude grows exponentially in time. The instability is instead convective and characterized by a finite spatial power gain G [95], which may be determined from Eq. (4.37),

$$G = \ln \left[\frac{|a_1(\infty)|^2}{|a_1(-\infty)|^2} \right] = \frac{2\pi\nu_{12}\nu_{21}^*|\mathbf{E}_0|^2}{|d\Delta/dx|_{x=x_r}v_{1x}v_{2x}}. \quad (4.38)$$

Noting that $\nu_{12}\nu_{21}^*|\mathbf{E}_0|^2 = \gamma^2$ for an equivalent homogeneous medium (since we are ignoring damping), defining $l_r = 1/\sqrt{|d\Delta/dx|} \sim \sqrt{\mathcal{L}/k}$ as a length scale over which the k_x selection rule is approximately satisfied, and remembering that the same G is found for $v_{1x}v_{2x} < 0$ if we let $v_{1x}v_{2x} \rightarrow |v_{1x}v_{2x}|$ [90], Eq. (4.38) may be written in the more familiar form [89, 90, 91, 106],

$$G = \frac{2\pi\gamma^2 l_r^2}{|v_{1x}v_{2x}|}. \quad (4.39)$$

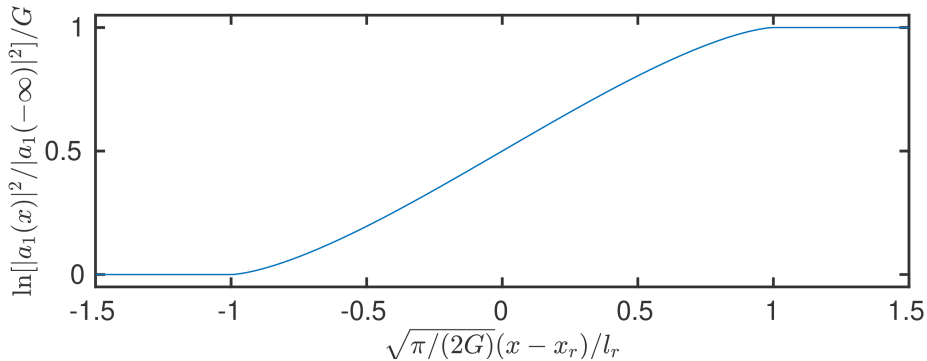


Figure 4.1 – Amplification in a monotonic, inhomogeneous medium when $v_{1x}, v_{2x} > 0$.

Eq. (4.39) shows higher gains for larger PDI growth rates, longer distances with approximate satisfaction of the k_x selection rule, and slower daughter waves, all which is in agreement with what is intuitively expected for PDIs involving weakly damped daughter waves. Returning to Eqs. (4.37) and (4.38), noting that $\xi = \sqrt{\pi/(2G)}(x - x_r)/l_r$, allows us to draw the spatial daughter wave amplification profile seen in Fig. 4.1. From Fig. 4.1, it is clear that amplification occurs for a small range of x -values, $x \in [x_r - l_r\sqrt{2G/\pi}, x_r + l_r\sqrt{2G/\pi}]$, around x_r . Inhomogeneities thus convert exponential growth everywhere in space into growth around the point where the k_x selection rule is satisfied; the growth rate is the same as in the homogeneous case at $x = x_r$, but decreases as Δ increases, and vanishes when $|x - x_r| > l_r\sqrt{2G/\pi}$.

As a final point of this Section, we discuss the problem of defining a PDI threshold in an inhomogeneous medium. The above discussion indicates that $G > 0$ whenever $\gamma > 0$ in an equivalent homogeneous medium, and the PDI threshold in an inhomogeneous medium is thus, in a strict sense, the same as that in a homogeneous medium. However, the daughter waves entering the amplification region are essentially the ones excited by thermal fluctuations, so the initial power which gets amplified is very small, meaning that a significant positive G is required in order for the PDI to have observable consequences. A simple way of capturing this is to define a threshold, G^{th} , and consider the PDI to occur in an inhomogeneous medium when $G > G^{\text{th}}$. The standard choice, which we shall also employ, is $G^{\text{th}} = 2\pi$ [106], corresponding to $|a_1(\infty)|^2/|a_1(-\infty)|^2 = e^{G^{\text{th}}} = e^{2\pi} \approx 535.5$; in Chapter 6, this choice is shown provide a good description of the PDI threshold near the UHR. With the choice $G^{\text{th}} = 2\pi$, we can also define a pump wave amplitude condition for PDIs in inhomogeneous media similar to Eq. (4.32), using $G > G^{\text{th}}$, Eq. (4.39), and $\gamma^2 = \nu_{12}\nu_{21}^*|\mathbf{E}_0|^2$,

$$|\mathbf{E}_0| > |\mathbf{E}_0^{\text{th}}| = \sqrt{\frac{|v_{1x}/l_r| |v_{2x}/l_r|}{\nu_{12}\nu_{21}^*}}. \quad (4.40)$$

Eq. (4.40) has exactly the same form as Eq. (4.32) if the daughter wave damping rate, Γ , is replaced by the convective loss rate from the region where the k_x selection rule is approximately satisfied, $|v_x/l_r|$, i.e., the inverse time it takes a daughter wave to pass through this region. Lower thresholds are obtained for daughter waves spending more

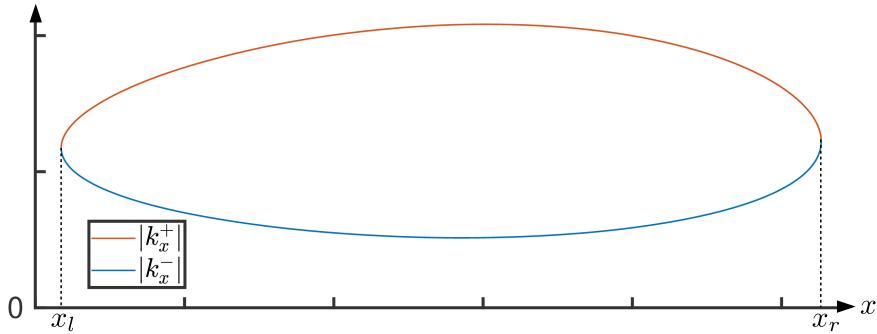


Figure 4.2 – Dispersion curves of a trapped wave.

time in the amplification region and for larger nonlinear coupling factors, as expected.

4.3 Onset of Parametric Decay Instabilities with Trapped Daughter Waves

Our discussion of PDIs up to this point has assumed that the daughter waves are propagating freely through the plasma, allowing them to be described by a single WKB mode and limiting them to passing through an amplification region in an inhomogeneous medium a single time. It is simple enough to describe a wave passing through a finite number of amplification regions though, one simply adds up the gains from each region to obtain the overall gain. However, a new situation occurs when daughter waves, or a fraction of the daughter wave power, are trapped around one or more amplification regions, since their power can now be amplified an infinite number of times. In these cases, PDIs become absolute if the daughter wave power experiences a net gain over one cycle through the trapping region [88]. The case of most interest to us is that in which both daughter waves are trapped around a maximum of the UH frequency, but we note that having fully trapped daughter waves is a sufficient, rather than a necessary, condition for absolute PDIs of this type. A scenario with absolute PDIs without fully trapped daughter waves is, for instance, given in [143].

In the semi-classical region, trapped waves may be described as a superposition of two of the WKB modes discussed in Section 3.2. The modes coalesce at the turning points of the trapping region (x_l and x_r , where $v_x = 0$), as seen in Fig. 4.2, indicating linear conversion of one wave into the other at these locations. We consider the case in which the sign of the wave vector component along the trapping direction, taken to be the x -direction, does not change, i.e., a resonance of the cold waves. In this case, the two modes, characterized by wave vector x -components k_x^+ and k_x^- , satisfy $|k_x^+| \geq |k_x^-|$ everywhere in the trapping region, with the equality being fulfilled at the turning points; the nomenclature is chosen to be directly applicable to the EBWs and X-mode waves discussed in Section 2.2. In order for a trapped wave to be a stationary state of the system, the $+$ and $-$ waves should carry the same power and therefore have $|a^+| = |a^-|$. We shall assume such a stationary state,

but allow the overall amplitude, C , to depend on y , z , and t , which is acceptable if the variation with respect to these variables is slow (adiabatic) compared with $1/k_x$ and $1/\omega_j$. Thus, we write

$$\phi(\mathbf{r}, t) = \text{Re} \left\{ C(y, z, t) \left[\frac{e^{i\theta^+(x)}}{\sqrt{\partial\mathcal{D}^+/\partial k_x}} + \frac{e^{i\theta^-(x)}}{\sqrt{\partial\mathcal{D}^-/\partial k_x}} \right] \right\} \quad \text{for } x \in [x_l, x_r], \quad (4.41)$$

where $\theta^\pm = \int^x k_x^\pm dx' + k_y y + k_\parallel z - \omega_j t$ are WKB phases of the \pm waves, which may have a constant shift relative to each other due to mode conversion at the turning points, and $\partial\mathcal{D}'^\pm/\partial k_x = \partial\mathcal{D}'(\mathbf{k}, x, \omega)/\partial k_x|_{k_x=k_x^\pm(x), \omega=\omega_j}$. In order to have a stationary state, we must further require the phase acquired by the wave when going around the trapping region once to be a multiple of 2π , as ϕ would be multi-valued otherwise. The phase shift associated with wave propagation is $\oint \mathbf{k} \cdot d\mathbf{r} = \int_{x_l}^{x_r} k_x^+ dx + \int_{x_r}^{x_l} k_x^- dx$, while each mode conversion is associated with a phase shift of $\pm\pi/2$ and add up to $\pm\pi$ over a full cycle [126]. This gives rise to the Bohr–Sommerfeld quantization rule, which may also be derived from more formal WKB arguments [126, 130],

$$\oint \mathbf{k} \cdot d\mathbf{r} = (2l + 1)\pi, \quad (4.42)$$

with $l \in \mathbb{Z}$. Inserting $\oint \mathbf{k} \cdot d\mathbf{r} = \int_{x_l}^{x_r} k_x^+ dx + \int_{x_r}^{x_l} k_x^- dx = \int_{x_l}^{x_r} (k_x^+ - k_x^-) dx$, noting that k_x^+ and k_x^- have the same sign in the cases of interest to us (also remembering that $|k_x^+| \geq |k_x^-|$), and realizing that the solutions with $l = m \geq 0$ and $l = -m - 1$ are equivalent, simply corresponding to an inversion of the x -axis ($k_x \rightarrow -k_x$), we obtain a simplified version of Eq. (4.42), also found in [126],

$$\int_{x_l}^{x_r} (|k_x^+| - |k_x^-|) dx = (2m + 1)\pi, \quad (4.43)$$

where $n \in \mathbb{N}_0$. When discussing PDIs involving trapped daughter waves, two distinct pairs of trapped waves, each satisfying Eq. (4.43), must be considered,

$$\int_{x_{1l}}^{x_{1r}} (|k_{1x}^+| - |k_{1x}^-|) dx = (2m + 1)\pi, \quad \int_{x_{2l}}^{x_{2r}} (|k_{2x}^+| - |k_{2x}^-|) dx = (2n + 1)\pi. \quad (4.44)$$

In addition to Eq. (4.44), \mathbf{k}_1, ω_1 and \mathbf{k}_2, ω_2 should also satisfy the PDI selection rules, $k_{1y} = k_{0y} - k_{2y}$, $k_{1\parallel} = k_{0\parallel} - k_{2\parallel}$, and $\omega_1 = \omega_0 - \omega_2$, as well as the selection rule $k_{1x}^\pm(x) = k_{0x}(x) - k_{2x}^\pm(x)$ for at least one combination of \pm at some x ; if the daughter waves belong to the same dispersion relation and have $\omega_1 = \omega_2 = \omega_0/2$, which is the case of most interest in this work, it will hold that $|k_{1x}^+(x)| = |k_{0x}(x)| + |k_{2x}^-(x)|$ for (at least) two x -values, so long as $|k_{0x}| < \max(|k_{1x}^+|) - \min(|k_{1x}^-|)$, as we shall generally assume. We particularly analyze the case of trapped EBW and X-mode daughters with an X-mode pump wave propagating along the x -direction and additionally take $k_\parallel = 0$ for the daughters to minimize convective losses along $\mathbf{B}^{(0)}$. In this case, we can evaluate Eq. (4.44) using Eq. (2.60),

$$|k_{jx}^\pm| = \sqrt{-\frac{S_j}{2\ell_{Te,j}^2} \left(1 \pm \sqrt{1 + \frac{4\omega_j^2 \ell_{Te,j}^2}{c^2} \frac{S_j^2 - D_j^2}{S_j^2}} \right) - k_{jy}^2}, \quad (4.45)$$

where $j = 1, 2$, and we note that $k_{1y} = -k_{2y}$, $\omega_1 = \omega_0 - \omega_2$.

To derive the threshold of PDIs with trapped daughter waves, we apply Eq. (3.24) to each of the WKB modes in Eq. (4.41), yielding

$$\begin{aligned}
& i \left[\frac{\mathcal{D}_j''^+ e^{i\theta_j^+}}{\sqrt{\partial \mathcal{D}_j^+ / \partial k_x}} + \frac{\mathcal{D}_j''^- e^{i\theta_j^-}}{\sqrt{\partial \mathcal{D}_j^- / \partial k_x}} \right] C_j + i \left[\frac{(\partial \mathcal{D}_j^+ / \partial \omega) e^{i\theta_j^+}}{\sqrt{\partial \mathcal{D}_j^+ / \partial k_x}} + \frac{(\partial \mathcal{D}_j^- / \partial \omega) e^{i\theta_j^-}}{\sqrt{\partial \mathcal{D}_j^- / \partial k_x}} \right] \frac{\partial C_j}{\partial t} \\
& - \sum_{i=y,z} \left\{ i \left[\frac{(\partial \mathcal{D}_j^+ / \partial k_i) e^{i\theta_j^+}}{\sqrt{\partial \mathcal{D}_j^+ / \partial k_x}} + \frac{(\partial \mathcal{D}_j^- / \partial k_i) e^{i\theta_j^-}}{\sqrt{\partial \mathcal{D}_j^- / \partial k_x}} \right] \frac{\partial C_j}{\partial i} \right. \\
& \quad \left. + \left[\frac{(\partial^2 \mathcal{D}_j^+ / \partial k_i^2) e^{i\theta_j^+}}{2\sqrt{\partial \mathcal{D}_j^+ / \partial k_x}} + \frac{(\partial^2 \mathcal{D}_j^- / \partial k_i^2) e^{i\theta_j^-}}{2\sqrt{\partial \mathcal{D}_j^- / \partial k_x}} \right] \frac{\partial^2 C_j}{\partial i^2} \right\} = \frac{\rho_{j,\text{nl}}^+ + \rho_{j,\text{nl}}^-}{\epsilon_0};
\end{aligned} \tag{4.46}$$

the subscript $j = 1, 2$ again signifies that the quantities are related to one of the trapped daughter waves, and $\rho_{j,\text{nl}}^+$, $\rho_{j,\text{nl}}^-$ are the components of the nonlinear charge density which may satisfy the k_x selection for the $+$, $-$ branches of the dispersion relation, respectively. Eq. (4.46) is now multiplied by $e^{-\theta_j^+} / (\sqrt{\partial \mathcal{D}_j^+ / \partial k_x})^* + e^{-\theta_j^-} / (\sqrt{\partial \mathcal{D}_j^- / \partial k_x})^*$ and integrated over the trapping region. Neglecting the terms with a fast WKB phase variation, as these are assumed to mix to zero when integrated over the trapping region, Eq. (4.46) may be written as

$$\begin{aligned}
& i \langle \mathcal{D}_j'' \rangle C_j + i \left\langle \frac{\partial \mathcal{D}_j'}{\partial \omega} \right\rangle \frac{\partial C_j}{\partial t} - i \left\langle \frac{\partial \mathcal{D}_j'}{\partial k_y} \right\rangle \frac{\partial C_j}{\partial y} - i \left\langle \frac{\partial \mathcal{D}_j'}{\partial k_{\parallel}} \right\rangle \frac{\partial C_j}{\partial z} \\
& - \frac{1}{2} \left\langle \frac{\partial^2 \mathcal{D}_j'}{\partial k_y^2} \right\rangle \frac{\partial^2 C_j}{\partial y^2} - \frac{1}{2} \left\langle \frac{\partial^2 \mathcal{D}_j'}{\partial k_{\parallel}^2} \right\rangle \frac{\partial^2 C_j}{\partial z^2} = \mathcal{P}_{j,\text{nl}},
\end{aligned} \tag{4.47}$$

where

$$\langle g_j \rangle = \frac{1}{\mathcal{N}_j} \int_{x_{jl}}^{x_{jr}} \left[\frac{g_j^+(x)}{|\partial \mathcal{D}_j^+ / \partial k_x|} + \frac{g_j^-(x)}{|\partial \mathcal{D}_j^- / \partial k_x|} \right] dx \tag{4.48}$$

is the average of a function g over the trapping region weighted by the (norm squared) daughter wave amplitude,

$$\mathcal{P}_{j,\text{nl}} = \frac{1}{\epsilon_0 \mathcal{N}_j} \int_{x_{jl}}^{x_{jr}} \left[\frac{\rho_{j,\text{nl}}^+(x) e^{-i\theta_j^+(x)}}{(\sqrt{\partial \mathcal{D}_j^+ / \partial k_x})^*} + \frac{\rho_{j,\text{nl}}^-(x) e^{-i\theta_j^-(x)}}{(\sqrt{\partial \mathcal{D}_j^- / \partial k_x})^*} \right] dx \tag{4.49}$$

is a nonlinear coupling factor, and

$$\mathcal{N}_j = \int_{x_{jl}}^{x_{jr}} \left(\frac{1}{|\partial \mathcal{D}_j^+ / \partial k_x|} + \frac{1}{|\partial \mathcal{D}_j^- / \partial k_x|} \right) dx \tag{4.50}$$

is a normalization constant. Dividing Eq. (4.47) by $\langle \partial \mathcal{D}'_j / \partial \omega \rangle$, we obtain an equation which is very similar to those governing PDIs involving free daughter waves,

$$i\Gamma_j C_j + i \frac{\partial C_j}{\partial t} + i v_{jy} \frac{\partial C_j}{\partial y} + i v_{jz} \frac{\partial C_j}{\partial z} - \Lambda_{jy} \frac{\partial^2 C_j}{\partial y^2} - \Lambda_{jz} \frac{\partial^2 C_j}{\partial z^2} = \frac{\mathcal{P}_{j,\text{nl}}}{\langle \partial \mathcal{D}'_j / \partial \omega \rangle}, \quad (4.51)$$

with $\Gamma_j = \langle \mathcal{D}''_j \rangle / \langle \partial \mathcal{D}'_j / \partial \omega \rangle$ being a damping rate, $v_{jy,z} = -\langle \partial \mathcal{D}'_j / \partial k_{y,\parallel} \rangle / \langle \partial \mathcal{D}'_j / \partial \omega \rangle$ being group velocities along the y - and z -directions, and $\Lambda_{jy,z} = (1/2) \langle \partial^2 \mathcal{D}'_j / \partial k_{y,\parallel}^2 \rangle / \langle \partial \mathcal{D}'_j / \partial \omega \rangle$ being diffraction coefficients along the y - and z -directions. As in the case with free daughter waves, $\mathcal{P}_{j,\text{nl}}$ can generally be written as a product of the complex conjugate amplitude of the other daughter wave, the pump wave amplitude, and an amplitude-independent factor determining the nonlinear coupling strength. The general case is rather complicated, so we focus on the particular case of interest in this work, where $\omega_1 \approx \omega_2 \approx \omega_0/2 \approx \omega_{UH}$. We take the X-mode pump wave to propagate along the x -direction with $k_0 > 0$, and further assume that $k_{1x} > 0$ and $k_{2x} < 0$. In this case, the k_x selection rule can be satisfied for k_{1x}^+ and k_{2x}^- ($k_0 = k_{1x}^+ + k_{2x}^-$ at some x), and further utilizing the approximate nonlinear charge densities from Eqs. (4.18) and (4.19), we find

$$\begin{aligned} \mathcal{P}_{1,\text{nl}} &\approx \frac{1}{\epsilon_0 \mathcal{N}_1} \int_{x_{1l}}^{x_{1r}} \frac{\rho_{1,\text{nl}} e^{i \int^x (k_0 - k_{1x}^+ - k_{2x}^-) dx'}}{\left(\sqrt{\partial \mathcal{D}'_1 / \partial k_x} \right)^*} dx \\ &\approx -\frac{\omega_1 C_2^*}{2 \mathcal{N}_1} \left[\int_{x_l}^{x_r} \frac{E_{0y}}{B^{(0)}} \frac{\omega_{pe}^2 \omega_{ce}^2 k_0 k_{1x}^+ k_{2x}^-}{(\omega_0^2 - \omega_{ce}^2)(\omega_1^2 - \omega_{ce}^2)(\omega_2^2 - \omega_{ce}^2)} \right. \end{aligned} \quad (4.52)$$

$$\left. \times \frac{3 + (1 - \omega_{ce}^2 / \omega_1^2) / 2}{\left(\sqrt{\partial \mathcal{D}'_1 / \partial k_x} \right)^* \left(\sqrt{\partial \mathcal{D}'_2 / \partial k_x} \right)^*} e^{i \int^x (k_0 - k_{1x}^+ - k_{2x}^-) dx'} dx \right],$$

$$\begin{aligned} \mathcal{P}_{2,\text{nl}}^* &\approx \frac{1}{\epsilon_0 \mathcal{N}_2} \int_{x_{2l}}^{x_{2r}} \frac{\rho_{2,\text{nl}}^* e^{-i \int^x (k_0 - k_{1x}^+ - k_{2x}^-) dx'}}{\sqrt{\partial \mathcal{D}'_2 / \partial k_x}} dx \\ &\approx -\frac{\omega_2 C_1}{2 \mathcal{N}_2} \left[\int_{x_l}^{x_r} \frac{E_{0y}^*}{B^{(0)}} \frac{\omega_{pe}^2 \omega_{ce}^2 k_0 k_{1x}^+ k_{2x}^-}{(\omega_0^2 - \omega_{ce}^2)(\omega_1^2 - \omega_{ce}^2)(\omega_2^2 - \omega_{ce}^2)} \right. \end{aligned} \quad (4.53)$$

$$\left. \times \frac{3 + (1 - \omega_{ce}^2 / \omega_2^2) / 2}{\sqrt{\partial \mathcal{D}'_1 / \partial k_x} \sqrt{\partial \mathcal{D}'_2 / \partial k_x}} e^{-i \int^x (k_0 - k_{1x}^+ - k_{2x}^-) dx'} dx \right],$$

where $x_l = \max(x_{1l}, x_{2l})$ and $x_r = \min(x_{1r}, x_{2r})$ mark the limits of the region in which both trapped daughter waves are propagating. If the integrals in Eqs. (4.52) and (4.53) are evaluated using the stationary phase approximation [97], only the regions around the points where the k_x selection rule ($k_0 = k_{1x}^+ + k_{2x}^-$) is satisfied are found to contribute, and expressions for the nonlinear coupling factors similar to the ones from [8, 9] are found. However, even with the stationary phase approximation, the nonlinear coupling factors

can only be evaluated numerically for realistic plasma profiles, so we shall simply keep the integral forms from Eqs. (4.52) and (4.53) and evaluate the integrals numerically. Plugging Eqs. (4.52) and (4.53) into Eq. (4.51) and its complex conjugate, also factoring out C_2^* and C_1 from Eqs. (4.52) and (4.53), yields the equations describing the onset of PDIs with trapped daughter waves for $\omega_1 \approx \omega_2 \approx \omega_0/2 \approx \omega_{UH}$,

$$i\Gamma_1 C_1 + i\frac{\partial C_1}{\partial t} + iv_{1y}\frac{\partial C_1}{\partial y} + iv_{1z}\frac{\partial C_1}{\partial z} - \Lambda_{1y}\frac{\partial^2 C_1}{\partial y^2} - \Lambda_{1z}\frac{\partial^2 C_1}{\partial z^2} = \gamma_{12}(y, z)C_2^*, \quad (4.54)$$

$$-i\Gamma_2 C_2^* - i\frac{\partial C_2^*}{\partial t} - iv_{2y}\frac{\partial C_2^*}{\partial y} - iv_{2z}\frac{\partial C_2^*}{\partial z} - \Lambda_{2y}\frac{\partial^2 C_2^*}{\partial y^2} - \Lambda_{2z}\frac{\partial^2 C_2^*}{\partial z^2} = \gamma_{21}^*(y, z)C_1; \quad (4.55)$$

here,

$$\gamma_{12}(y, z) \approx -\frac{\omega_1}{2\mathcal{N}_1\langle\partial\mathcal{D}'_1/\partial\omega\rangle} \left[\int_{x_l}^{x_r} \frac{E_{0y}(x, y, z)}{B^{(0)}} \frac{\omega_{pe}^2 \omega_{ce}^2 k_0 k_{1x}^+ k_{2x}^-}{(\omega_0^2 - \omega_{ce}^2)(\omega_1^2 - \omega_{ce}^2)(\omega_2^2 - \omega_{ce}^2)} \right. \\ \left. \times \frac{3 + (1 - \omega_{ce}^2/\omega_1^2)/2}{\left(\sqrt{\partial\mathcal{D}'_1^+/\partial k_x}\right)^* \left(\sqrt{\partial\mathcal{D}'_2^-/\partial k_x}\right)^*} e^{i\int^x (k_0 - k_{1x}^+ - k_{2x}^-) dx'} dx \right], \quad (4.56)$$

$$\gamma_{21}^*(y, z) \approx -\frac{\omega_2}{2\mathcal{N}_2\langle\partial\mathcal{D}'_2/\partial\omega\rangle} \left[\int_{x_l}^{x_r} \frac{E_{0y}^*(x, y, z)}{B^{(0)}} \frac{\omega_{pe}^2 \omega_{ce}^2 k_0 k_{1x}^+ k_{2x}^-}{(\omega_0^2 - \omega_{ce}^2)(\omega_1^2 - \omega_{ce}^2)(\omega_2^2 - \omega_{ce}^2)} \right. \\ \left. \times \frac{3 + (1 - \omega_{ce}^2/\omega_2^2)/2}{\sqrt{\partial\mathcal{D}'_1^+/\partial k_x} \sqrt{\partial\mathcal{D}'_2^-/\partial k_x}} e^{-i\int^x (k_0 - k_{1x}^+ - k_{2x}^-) dx'} dx \right] \quad (4.57)$$

are nonlinear coupling coefficients proportional to the pump wave amplitude. Apart from some differences in the sign conventions, which are ultimately unimportant when discussing PDIs, and the inclusion $v_{1,2z}$, Eqs. (4.54) and (4.55) are equivalent to Eq. (20) from [8]. When discussing PDIs of the ECRH beams in ASDEX Upgrades, it can generally be assumed that the ECRH beams have a Gaussian field distribution [123] with a width, W , that is essentially constant in the trapping region, allowing us to write $\gamma_{12}(y, z) = \gamma_{12}(0, 0)e^{-(y^2+z^2)/W^2}$ and $\gamma_{21}^*(y, z) = \gamma_{21}^*(0, 0)e^{-(y^2+z^2)/W^2}$. W can be obtained by assuming free space-like beam propagation [125], or by using a beam tracing code such as TORBEAM [123] or WKBeam [124]; since our results are in any case highly simplified, we generally employ the former. We further set $v_{1z} = v_{2z} = 0$ in order to minimize convective losses along the z -direction, with which Eqs. (4.54) and (4.55) become

$$i\Gamma_1 C_1 + i\frac{\partial C_1}{\partial t} + iv_{1y}\frac{\partial C_1}{\partial y} - \Lambda_{1y}\frac{\partial^2 C_1}{\partial y^2} - \Lambda_{1z}\frac{\partial^2 C_1}{\partial z^2} = \gamma_{12}(0, 0)e^{-(y^2+z^2)/W^2} C_2^*, \quad (4.58)$$

$$-i\Gamma_2 C_2^* - i\frac{\partial C_2^*}{\partial t} - iv_{2y}\frac{\partial C_2^*}{\partial y} - \Lambda_{2y}\frac{\partial^2 C_2^*}{\partial y^2} - \Lambda_{2z}\frac{\partial^2 C_2^*}{\partial z^2} = \gamma_{21}^*(0, 0)e^{-(y^2+z^2)/W^2} C_1. \quad (4.59)$$

If $|\mathbf{E}_0|$ is assumed to be unaffected by the PDI, which is reasonable during the onset of the instability, Eqs. (4.58) and (4.59) are a pair of coupled, linear, partial differential equations.

These can be solved numerically, subject to the boundary conditions discussed in [8, 9], in order to obtain the threshold of the trapped wave PDI. In principle, Eqs. (4.58) and (4.59) should be solved for all the permissible combinations of modes given by Eq. (4.44), with $|k_{jx}^\pm|$ from Eq. (4.45), and the PDI threshold given as the threshold for the mode combination with the lowest threshold; note that γ_{12} and γ_{21}^* may take different forms than those in Eqs. (4.56) and (4.57), depending on the directions of k_{1x} and k_{2x} for the daughter wave modes capable of satisfying the k_x selection rule. As previously mentioned, we shall mainly consider the case of $\omega_1 = \omega_2 = \omega_0/2$, where Eqs. (4.56) and (4.57) provide the correct γ_{12} and γ_{21}^* , and since this will already reduce the accuracy of our threshold to a rough estimate, we shall also be content with using approximate analytical solutions of Eqs. (4.58) and (4.59); these solutions also provide additional insight into the physics.

We are interested in absolute instabilities and therefore investigate solutions of Eqs. (4.58) and (4.59) varying as $C_1, C_2^* \propto e^{\gamma t}$. If we additionally ignore diffraction losses along the y -direction (set $\Lambda_{1,2y} = 0$), since these are generally small compared with the convection losses, we obtain

$$i(\Gamma_1 + \gamma)C_1 + iv_{1y} \frac{\partial C_1}{\partial y} - \Lambda_{1z} \frac{\partial^2 C_1}{\partial z^2} = \gamma_{12}(0, 0) e^{-(y^2+z^2)/W^2} C_2^*, \quad (4.60)$$

$$-i(\Gamma_2 + \gamma)C_2^* - iv_{2y} \frac{\partial C_2^*}{\partial y} - \Lambda_{2z} \frac{\partial^2 C_2^*}{\partial z^2} = \gamma_{21}^*(0, 0) e^{-(y^2+z^2)/W^2} C_1. \quad (4.61)$$

While simpler than Eqs. (4.58) and (4.59), Eqs. (4.60) and (4.61) are still non-separable partial differential equations without a simple analytical solution. To simplify the problem, we follow [8] and replace the Gaussian $|\mathbf{E}_0|$ -distribution by a rectangular uniform one, $e^{-(y^2+z^2)/W^2} \rightarrow \Theta(y)\Theta(2L_y - y)\Theta(z + L_z)\Theta(L_z - z)$, where Θ is the Heaviside step function and L_y, L_z are the (half) beam widths in the y -, z -directions (the beam is translated in the y -direction to simplify the subsequent calculations). The choice $L_y = L_z = \sqrt{\pi/8}W$ will cause the beam to carry the same power as the Gaussian one, but in order to allow a non-slab geometry to be taken at least approximately into account, we shall keep them arbitrary for now. Unfortunately, even the above simplification does not lead to a tractable solution, so we shall additionally assume that either diffraction losses along the z -direction or convection losses along the y -direction dominate, i.e., that the ratio $|v_y \partial C / \partial y| / |\Lambda_z \partial^2 C / \partial z^2| \sim (L_z / L_y) (|v_y| L_z / |\Lambda_z|)$ is either very small (diffraction losses along z dominate) or very large (convection losses along y dominate).

In the case where $|v_y \partial C / \partial y| / |\Lambda_z \partial^2 C / \partial z^2| \ll 1$, we can neglect the terms proportional to $v_{1,2y}$ and arrive at a set of equations which only depends on z ,

$$i(\Gamma_1 + \gamma)C_1 - \Lambda_{1z} \frac{\partial^2 C_1}{\partial z^2} = \gamma_{12}(0, 0) \Theta(z + L_z) \Theta(L_z - z) C_2^* \quad (4.62)$$

$$-i(\Gamma_2 + \gamma)C_2^* - \Lambda_{2z} \frac{\partial^2 C_2^*}{\partial z^2} = \gamma_{21}^*(0, 0) \Theta(z + L_z) \Theta(L_z - z) C_1. \quad (4.63)$$

For $|z| > L_z$, Eqs. (4.62) and (4.63) are just independent, homogeneous, ordinary differential equations with constant coefficients for C_1 and C_2^* . Their solutions are found by the

usual method, $C_1 = \mathcal{A}_1 e^{z\sqrt{i(\gamma+\Gamma_1)/\Lambda_{1z}}} + \mathcal{B}_1 e^{-z\sqrt{i(\gamma+\Gamma_1)/\Lambda_{1z}}}$ and $C_2^* = \mathcal{A}_2^* e^{z\sqrt{-i(\gamma+\Gamma_2)/\Lambda_{2z}}} + \mathcal{B}_2^* e^{z\sqrt{-i(\gamma+\Gamma_2)/\Lambda_{2z}}}$, where $\mathcal{A}_{1,2}$ and $\mathcal{B}_{1,2}$ are constants determined by the boundary conditions. For $|z| < L_z$ the right hand sides of Eqs. (4.62) and (4.63) are non-zero due to the coupling induced by the nonlinear current density. Isolating C_2^* in Eq. (4.62) and plugging the result into Eq. (4.63) in this region yields

$$\frac{\partial^4 C_1}{\partial z^4} + i \left(\frac{\gamma + \Gamma_2}{\Lambda_{2z}} - \frac{\gamma + \Gamma_1}{\Lambda_{1z}} \right) \frac{\partial^2 C_1}{\partial z^2} + \frac{\gamma_{12}(0,0)\gamma_{21}(0,0) - (\gamma + \Gamma_1)(\gamma + \Gamma_2)}{\Lambda_{1z}\Lambda_{2z}} C_1 = 0. \quad (4.64)$$

Eq. (4.62) may be solved by the standard method, i.e., by assuming $C_1 \propto e^{Q_z z}$ and solving for Q_z^2 ,

$$Q_z^2 = i \left(\frac{\gamma + \Gamma_1}{2\Lambda_{1z}} - \frac{\gamma + \Gamma_2}{2\Lambda_{2z}} \right) \pm \sqrt{\frac{\gamma_{12}(0,0)\gamma_{21}^*(0,0)}{\Lambda_{1z}\Lambda_{2z}} - \left(\frac{\gamma + \Gamma_1}{2\Lambda_{1z}} + \frac{\gamma + \Gamma_2}{2\Lambda_{2z}} \right)^2}. \quad (4.65)$$

The generally complex Q_z -values obtained from Eq. (4.65) are somewhat difficult to interpret, but in the special case where $\omega_1 = \omega_2 = \omega_0/2$, it holds that $\Lambda_{1z} = \Lambda_{2z} = \Lambda_z$ and $\Gamma_1 = \Gamma_2 = \Gamma$, reducing Eq. (4.65) to

$$Q_z^2 = \pm \frac{\sqrt{\gamma_{12}(0,0)\gamma_{21}^*(0,0) - (\gamma + \Gamma)^2}}{|\Lambda_z|}. \quad (4.66)$$

Defining $Q_z = [\gamma_{12}(0,0)\gamma_{21}^*(0,0) - (\gamma + \Gamma)^2]^{1/4}/\sqrt{|\Lambda_z|}$, we then have $Q_z = \pm Q_z$ and $Q_z = \pm i Q_z$, meaning that the solution of Eq. (4.64) can be written as linear combination of the regular and hyperbolic cosine and sine functions, i.e., $C_1 = \mathcal{C}_1 \cos(Q_z z) + \mathcal{E}_1 \sin(Q_z z) + \mathcal{G}_1 \cosh(Q_z z) + \mathcal{H}_1 \sinh(Q_z z)$, where \mathcal{C}_1 , \mathcal{E}_1 , \mathcal{G}_1 , and \mathcal{H}_1 are constants determined by the boundary conditions (C_2^* may be expressed in a similar way). In order to determine the appropriate boundary conditions, we write Eq. (4.64) with $\Gamma_1 = \Gamma_2 = \Gamma$ and $\Lambda_{1z} = \Lambda_{2z} = \Lambda_z$,

$$\frac{\partial^4 C_1}{\partial z^4} + \frac{\gamma_{12}(0,0)\gamma_{21}^*(0,0) - (\gamma + \Gamma)^2}{\Lambda_z^2} C_1 = 0 \quad \text{for } |z| < L_z, \quad (4.67)$$

while also noting that Eq. (4.62) yields

$$\frac{\partial^4 C_1}{\partial z^4} + \frac{(\gamma + \Gamma)^2}{\Lambda_z^2} C_1 = 0 \quad \text{for } |z| > L_z, \quad (4.68)$$

when differentiated twice. Eqs. (4.67) and (4.68) may be combined to read

$$\frac{\partial^4 C_1}{\partial z^4} + \frac{[\gamma_{12}(0,0)\gamma_{21}^*(0,0) - 2(\gamma + \Gamma)^2]\Theta(z + L_z)\Theta(L_z - z) + (\gamma + \Gamma)^2}{\Lambda_z^2} C_1 = 0, \quad (4.69)$$

showing that the problem is effectively equivalent to a finite potential well. Integrating Eq. (4.69) from $z = L_z^-$ to $z = L_z^+$ and from $z = -L_z^-$ to $z = -L_z^+$, yields the boundary conditions that C_1 , $\partial C_1/\partial z$, $\partial^2 C_1/\partial z^2$, and $\partial^3 C_1/\partial z^3$ be continuous at $z = \pm L_z$. We additionally require that $C_1 \rightarrow 0$ as $|z| \rightarrow \infty$ in order for the daughter wave energy to be

finite. Taking $\text{Re}[\sqrt{i(\gamma + \Gamma)/\Lambda_z}] > 0$, $C_1 \rightarrow 0$ for $|z| \rightarrow \infty$ requires $\mathcal{A}_1 = 0$ for $z > L_z$ and $\mathcal{B}_1 = 0$ for $z < -L_z$. Due to the symmetry of the problem, we further know that C_1 will be either an even or an odd function of z , i.e., we can write $C_1 = \mathcal{C}_1 \cos(\mathcal{Q}_z z) + \mathcal{G}_1 \cosh(\mathcal{Q}_z z)$ for $|z| < L_z$ with $\mathcal{A}_1(z < -L_z) = \mathcal{B}_1(z > L_z)$, or $C_1 = \mathcal{E}_1 \sin(\mathcal{Q}_z z) + \mathcal{H}_1 \sinh(\mathcal{Q}_z z)$ for $|z| < L_z$ with $\mathcal{A}_1(z < -L_z) = -\mathcal{B}_1(z > L_z)$. The even solutions have the lowest PDI threshold, since they can have a maximum of $|C_1|$ at the beam center, and are therefore the ones considered in detail. The requirements of continuity at $z = \pm L_z$ will be fulfilled if continuity is satisfied at $z = L_z$ for an even (and odd) solution. The requirement of continuity of C_1 , $\partial C_1/\partial z$, $\partial^2 C_1/\partial z^2$, and $\partial^3 C_1/\partial z^3$ at $z = L_z$ for an even solution may be expressed as

$$C_1 \cos(\mathcal{Q}_z L_z) + \mathcal{G}_1 \cosh(\mathcal{Q}_z L_z) = \mathcal{B}_1 e^{-L_z \sqrt{i(\gamma + \Gamma)/\Lambda_z}}, \quad (4.70)$$

$$- \mathcal{Q}_z C_1 \sin(\mathcal{Q}_z L_z) + \mathcal{Q}_z \mathcal{G}_1 \sinh(\mathcal{Q}_z L_z) = -\sqrt{\frac{i(\gamma + \Gamma)}{\Lambda_z}} \mathcal{B}_1 e^{-L_z \sqrt{i(\gamma + \Gamma)/\Lambda_z}}, \quad (4.71)$$

$$- \mathcal{Q}_z^2 C_1 \cos(\mathcal{Q}_z L_z) + \mathcal{Q}_z^2 \mathcal{G}_1 \cosh(\mathcal{Q}_z L_z) = i \frac{\gamma + \Gamma}{\Lambda_z} \mathcal{B}_1 e^{-L_z \sqrt{i(\gamma + \Gamma)/\Lambda_z}}, \quad (4.72)$$

$$\mathcal{Q}_z^3 C_1 \sin(\mathcal{Q}_z L_z) + \mathcal{Q}_z^3 \mathcal{G}_1 \sinh(\mathcal{Q}_z L_z) = -\left[\frac{i(\gamma + \Gamma)}{\Lambda_z}\right]^{3/2} \mathcal{B}_1 e^{-L_z \sqrt{i(\gamma + \Gamma)/\Lambda_z}}. \quad (4.73)$$

With $\mathcal{C}_1 \neq 0$, which is necessary to have a maximum of $|C_1|$ at the beam center, Eqs. (4.70), (4.71), (4.72), and (4.73) will have a solution when

$$\mathcal{Q}_z L_z \tan(\mathcal{Q}_z L_z) = \sqrt{\frac{i(\gamma + \Gamma)}{\Lambda_z}} L_z. \quad (4.74)$$

Eq. (4.74) is a transcendental equation determining the bound states of the finite potential well, just as in the well-known quantum mechanical problem [128]. We are interested in the solution with the lowest threshold, for which we can assume $|\mathcal{Q}_z L_z| \ll 1$ and use the approximation $\tan(\mathcal{Q}_z L_z) \approx \mathcal{Q}_z L_z$. Inserting this in Eq. (4.74) yields a quadratic equation for $\gamma + \Gamma$, which can be solved using the standard method,

$$\gamma = -i \frac{\Lambda_z}{2L_z^2} \pm \sqrt{\gamma_{12}(0,0)\gamma_{21}^*(0,0) - \left(\frac{\Lambda_z}{2L_z^2}\right)^2} - \Gamma. \quad (4.75)$$

Apart from the sign of the leading imaginary term, which is unimportant for the PDI threshold, Eq. (4.75) is equivalent to an expression from [8]. From Eqs. (4.56) and (4.57), we note that

$$\begin{aligned} \gamma_{12}(0,0)\gamma_{21}^*(0,0) &= \frac{\omega_1^2}{4\mathcal{N}_1^2 \langle \partial \mathcal{D}'_1 / \partial \omega \rangle^2} \left| \int_{x_l}^{x_r} \frac{E_{0y}(x,0,0)}{B^{(0)}} \frac{\omega_{pe}^2 \omega_{ce}^2 k_0 |k_{1x}^+| |k_{1x}^-|}{(4\omega_1^2 - \omega_{ce}^2)(\omega_1^2 - \omega_{ce}^2)^2} \right. \\ &\quad \left. \times \frac{3 + (1 - \omega_{ce}^2/\omega_1^2)/2}{\sqrt{\partial \mathcal{D}'_1^+ / \partial k_x} \sqrt{\partial \mathcal{D}'_1^- / \partial k_x}} e^{i \int_{x_l}^x (k_0 + |k_{1x}^-| - |k_{1x}^+|) dx'} dx \right|^2 > 0 \end{aligned} \quad (4.76)$$

for $\omega_1 = \omega_2 = \omega_0/2$, meaning that the argument of the square root in Eq. (4.75) will be positive when the + root has $\text{Re}(\gamma) > 0$, which is the condition for an absolute PDI to occur. The PDI condition can thus be expressed as

$$\gamma_{12}(0,0)\gamma_{21}^*(0,0) > \Gamma^2 + \left(\frac{\Lambda_z}{2L_z^2}\right)^2. \quad (4.77)$$

Remembering that $\gamma_{12}(0,0)\gamma_{21}^*(0,0)$ is proportional to the injected beam power, P_0 (since it is proportional to the squared pump wave amplitude), we can rewrite Eq. (4.77) as a condition for P_0 ,

$$P_0 > P_0^{\text{th}} = \frac{\Gamma^2 + [\Lambda_z/(2L_z^2)]^2}{\gamma_{12}^{\text{ref}}(0,0)\gamma_{21}^{\text{ref}*}(0,0)} P_0^{\text{ref}}, \quad (4.78)$$

where P_0^{th} is the PDI threshold in terms of the injected beam power and P_0^{ref} is a reference injected beam power used when calculating $\gamma_{12}^{\text{ref}}(0,0)\gamma_{21}^{\text{ref}*}(0,0)$. As expected, the threshold decreases with decreasing damping, Γ , decreasing diffraction losses along the z -direction, $\Lambda_z/(2L_z^2)$, and increasing nonlinear coupling, $\gamma_{12}^{\text{ref}}(0,0)\gamma_{21}^{\text{ref}*}(0,0)/P_0^{\text{ref}}$.

We now turn our attention to the case of $|v_y \partial C / \partial y| / |\Lambda_z \partial^2 C / \partial z^2| \gg 1$ where we can neglect the terms proportional to $\Lambda_{1,2z}$ and arrive at a set of equations which only depends on y ,

$$i(\Gamma_1 + \gamma)C_1 + iv_{1y} \frac{\partial C_1}{\partial y} = \gamma_{12}(0,0)\Theta(y)\Theta(2L_y - y)C_2^*, \quad (4.79)$$

$$-i(\Gamma_2 + \gamma)C_2^* - iv_{2y} \frac{\partial C_2^*}{\partial y} = \gamma_{21}^*(0,0)\Theta(y)\Theta(2L_y - y)C_1. \quad (4.80)$$

For $y < 0$ and $y > 2L_y$, Eqs. (4.79) and (4.80) are independent, first-order ordinary differential equations with the solutions $C_1 = \mathcal{A}_1 e^{-(\Gamma_1 + \gamma)y/v_{1y}}$ and $C_2^* = \mathcal{A}_2^* e^{-(\Gamma_2 + \gamma)y/v_{2y}}$, where $\mathcal{A}_{1,2}$ are again constant coefficients determined by the boundary conditions. Just as in the case where diffraction losses along z dominated, we find the solution for $y \in]0, 2L_y[$ by isolating C_2^* in Eq. (4.79) and inserting the resulting expression in Eq. (4.80), from which

$$\frac{\partial^2 C_1}{\partial y^2} + \left(\frac{\gamma + \Gamma_1}{v_{1y}} + \frac{\gamma + \Gamma_2}{v_{2y}}\right) \frac{\partial C_1}{\partial y} - \frac{\gamma_{12}(0,0)\gamma_{21}^*(0,0) - (\Gamma_1 + \gamma)(\Gamma_2 + \gamma)}{v_{1y}v_{2y}} C_1 = 0. \quad (4.81)$$

Seeking a solution $C_1 \propto e^{Q_y y}$ of Eq. (4.81) yields

$$Q_y = -\frac{\gamma + \Gamma_1}{2v_{1y}} - \frac{\gamma + \Gamma_2}{2v_{2y}} \pm \sqrt{\frac{\gamma_{12}(0,0)\gamma_{21}^*(0,0)}{v_{1y}v_{2y}} + \left(\frac{\gamma + \Gamma_1}{2v_{1y}} - \frac{\gamma + \Gamma_2}{2v_{2y}}\right)^2}. \quad (4.82)$$

As earlier, we shall simplify Eq. (4.82) by assuming $\omega_1 = \omega_2 = \omega_0/2$. This again leads to $\Gamma_1 = \Gamma_2 = \Gamma$, but since \mathcal{D}' is an even function of k_y , its derivative $\partial \mathcal{D}' / \partial k_y$ is an odd function of k_y , and remembering that $k_{1y} = -k_{2y}$, along with $v_{jy} = \langle \partial \mathcal{D}'_j / \partial k_y \rangle / \langle \partial \mathcal{D}'_j / \partial \omega \rangle$, thus gives $v_{1y} = -v_{2y}$. We take $v_{1y} = v_y > 0$, which recasts Eq. (4.82) as

$$Q_y = \pm i \frac{\sqrt{\gamma_{12}(0,0)\gamma_{21}^*(0,0) - (\gamma + \Gamma)^2}}{v_y}. \quad (4.83)$$

Just as before, we define $\mathcal{Q}_y = \sqrt{\gamma_{12}(0,0)\gamma_{21}^*(0,0) - (\gamma + \Gamma)^2}/v_y$, allowing us to write $C_1 = \mathcal{B}_1 \cos(\mathcal{Q}_y y) + \mathcal{C}_1 \sin(\mathcal{Q}_y y)$, where \mathcal{B}_1 and \mathcal{C}_1 are constants determined by the boundary conditions (C_2^* can be expressed in a similar manner). Again, we require $C_1, C_2^* \rightarrow 0$ for $|y| \rightarrow \infty$ to have finite daughter wave energy, and integrating Eqs. (4.79) and (4.80) from $y = 0^-$ to $y = 0^+$ and from $y = 2L_y^-$ to $y = 2L_y^+$ further requires C_1 and C_2^* to be continuous across these points. Taking $\text{Re}(\gamma + \Gamma) > 0$, $C_1 \rightarrow 0$ for $y \rightarrow -\infty$ means that $\mathcal{A}_1 = 0$ for $y < 0$, and continuity of C_1 at $y = 0$ thus implies that $C_1 = \mathcal{B}_1 \sin(\mathcal{Q}_y y)$. For $y \in]0, 2L_y[$, Eq. (4.79) therefore gives

$$C_2^* = \frac{i\mathcal{B}_1}{\gamma_{12}(0,0)} [(\gamma + \Gamma) \sin(\mathcal{Q}_y y) + v_y \mathcal{Q}_y \cos(\mathcal{Q}_y y)], \quad (4.84)$$

and $C_2^* \rightarrow 0$ for $y \rightarrow \infty$ requires that $\mathcal{A}_2^* = 0$ for $y > 2L_y$, so continuity of C_2^* at $y = 2L_y$ for $\mathcal{B}_1 \neq 0$ implies that

$$2\mathcal{Q}_y L_y \cot(2\mathcal{Q}_y L_y) = -\frac{2(\gamma + \Gamma)L_y}{v_y}. \quad (4.85)$$

Eq. (4.85) is a transcendental equation determining the allowed forms of C_1 and C_2^* . It is somewhat similar to Eq. (4.74), but we note that due to the presence of a cotangent on the left hand side, Eq. (4.85) does not allow an approximate solution for $|\mathcal{Q}_y L_y| \ll 1$ by means of Taylor expansion. Instead, we may assume that $2|\gamma + \Gamma|L_y/v_y \ll 1$, such that the zeros of the cotangent, $2\mathcal{Q}_y L_y \approx \pi(s + 1/2)$ with $s \in \mathbb{N}_0$, can be taken as approximate solutions. Doing this yields

$$\gamma \approx \sqrt{\gamma_{12}(0,0)\gamma_{21}^*(0,0) - \frac{\pi^2 v_y^2}{4L_y^2} \left(s + \frac{1}{2}\right)^2} - \Gamma. \quad (4.86)$$

The lowest threshold is evidently obtained for $s = 0$, and the PDI condition may thus be expressed as

$$\gamma_{12}(0,0)\gamma_{21}^*(0,0) > \Gamma^2 + \left(\frac{\pi v_y}{4L_y}\right)^2. \quad (4.87)$$

This PDI condition gives a different threshold than the analytical estimate in Eq. (34) of [8]. We note that a threshold similar to the one in [8] can be obtained if v_y is allowed to switch sign at the beam center; this does, however, seem inconsistent with the assumption that the WKB modes are quasi-independent of one another. Further, the ratio between the analytical thresholds given by convection losses along y and diffraction losses along z in [8] is of a different order than the ratio between the associated terms in Eqs. (4.60) and (4.61), i.e., one can find a higher threshold due to diffraction losses along z than convection losses along y even though $|v_y \partial C_1 / \partial y| / |\Lambda_z \partial^2 C_1 / \partial z^2| \gg 1$, particularly at low Γ . The threshold implied by Eq. (4.87) does not have this shortcoming and is additionally shown to approximately match the PDI threshold during ELMs at ASDEX Upgrade in Chapter 5. We now convert Eq. (4.87) to a condition on P_0 , again using that $\gamma_{12}(0,0)\gamma_{21}^*(0,0) \propto P_0$,

$$P_0 > P_0^{\text{th}} \approx \frac{\Gamma^2 + [\pi v_y / (4L_y)]^2}{\gamma_{12}^{\text{ref}}(0,0)\gamma_{21}^{\text{ref}*}(0,0)} P_0^{\text{ref}}; \quad (4.88)$$

P_0^{th} is seen to decrease with decreasing damping, Γ , decreasing convective losses along the y -direction, $\pi v_y/(4L_y)$, and increasing nonlinear coupling, $\gamma_{12}^{\text{ref}}(0,0)\gamma_{21}^{\text{ref}*}(0,0)/P_0^{\text{ref}}$, as expected.

4.3.1 Algorithm for Computing the Power Threshold of Parametric Decay Instabilities Involving Trapped Waves

As the pieces needed for calculating P_0^{th} are somewhat scattered throughout this Thesis, we add this Subsection to allow for more easy reference. First of all, we assume that $\omega_1 = \omega_2 = \omega_0/2$, which reduces the initial problem to finding the parameters of a single trapped mode. Given that a profile allowing trapping of the $\omega_0/2$ -waves has been identified, this may be done using Eqs. (4.44) and (4.45),

$$\int_{x_{1l}}^{x_{1r}} (|k_{1x}^+| - |k_{1x}^-|) dx = (2m + 1)\pi, \quad (4.89)$$

$$|k_{1x}^\pm| = \sqrt{-\frac{S_1}{2\ell_{Te,1}^2} \left(1 \pm \sqrt{1 + \frac{4\omega_1^2 \ell_{Te,1}^2}{c^2} \frac{S_1^2 - D_1^2}{S_1^2}} \right)} - k_{1y}^2. \quad (4.90)$$

m is found by computing the integral in Eq. (4.89) for $k_{1y} = 0$ and picking the largest integer leading to a right hand side of Eq. (4.89) below this value. Minimizing the difference between the right and left hand sides numerically yields k_{1y} of the trapped mode, and the above choice of m should result in the smallest possible $|k_{1y}|$, leading to the lowest convection losses along the y -direction. Once the mode is identified, the necessary averaged parameters in the trapping region should be calculated using Eqs. (2.44) and (4.48). In order to find $\gamma_{12}(0,0)\gamma_{21}^*(0,0)$, it is necessary to obtain E_{0y} of the pump wave from Eq. (3.7), the unit polarization vector from Chapter 2, and $P(s) = P_0^{\text{ref}} e^{-\tau(s)}$, after which the integral in Eq. (4.76) is performed. Once the above steps have been completed, P_0^{th} is obtained from the maximum of the values in Eqs. (4.78) and (4.88), using appropriate values of L_y and L_z . If there are no special conditions, we set $L_y = L_z = \sqrt{\pi/8}W$, with W being the pump beam width in the trapping region.

4.4 Saturation of Parametric Decay Instabilities

So far, we have presented the theory of the onset of PDIs, determining the pump amplitude/power threshold above which PDIs occur. When PDIs are observed, they will, however, usually have reached a nonlinearly saturated state. We therefore briefly discuss the properties of such saturated states and the processes which may lead to saturation in this Section.

If we confine ourselves to the WKBJ PDI equations valid during of the onset in an inhomogeneous medium with free daughter waves, the saturated regime is described by [91, 142].

However, ordinarily, additional nonlinear processes will become important during the saturation phase. These include secondary PDIs of the excited daughter waves [9, 10] and depletion of the pump wave [11, 12]. Both of the aforementioned processes reduce the growth rate of the primary instability and may lead to a saturated state, in which the nonlinear wave generation is balanced by the losses [9, 10, 11, 12]. To keep the discussion relevant for the trapped daughter wave PDIs considered in this work, we consider a specific example in which a primary EBW daughter, characterized by (\mathbf{k}_2, ω_2) , decays to a secondary EBW daughter, characterized by $(\mathbf{k}'_2, \omega'_2)$, and a low-frequency daughter wave, characterized by $(\mathbf{k}_{\text{LF}}, \omega_{\text{LF}})$. It is assumed that a further decay involving a low-frequency daughter wave would cause the (tertiary) EBW to be free and thus increase the threshold of the instability to a level above what is accessible with ECRH, allowing us to focus on a single secondary PDI. The low-frequency daughter wave is taken as free and propagating mainly along the x -direction, so it can be described by Eq. (3.24) where only the convective term along the x -direction is retained,

$$\frac{\partial a_{\text{LF}}^*}{\partial x} = -\frac{i\rho_{\text{LF}, \text{nl}}^* e^{i\theta_{\text{LF}}}}{\epsilon_0 (\sqrt{\partial \mathcal{D}'_{\text{LF}} / \partial k_x})^*}. \quad (4.91)$$

Inserting $\rho_{\text{LF}, \text{nl}}$ from Eq. (4.22), accounting for the fact that (\mathbf{k}_2, ω_2) and $(\mathbf{k}'_2, \omega'_2)$ are trapped, Eq. (4.91) can be integrated to yield

$$a_{\text{LF}}^* = -iC_2^* C'_2 \int_{x_{2l}}^x \nu_{\text{LF}2'}^*(x') dx', \quad (4.92)$$

where

$$\begin{aligned} \nu_{\text{LF}2'}^*(x') = & \frac{k_{2x} k'_{2x} k_{\text{LF}x}^2 \omega_2 \omega'_2}{2B^{(0)} |\omega_{ce} \omega_{pe}^2|} \frac{e^{i \int^{x'} k_{\text{LF}x} dx''}}{(\sqrt{\partial \mathcal{D}'_{\text{LF}} / \partial k_x})^*} \left[\frac{e^{-i \int^{x'} k_{2x}^+ dx''}}{(\sqrt{\partial \mathcal{D}'_2 / \partial k_x})^*} + \frac{e^{-i \int^{x'} k_{2x}^- dx''}}{(\sqrt{\partial \mathcal{D}'_2 / \partial k_x})^*} \right] \\ & \times \left(\frac{e^{i \int^{x'} k_{2x}^+ dx''}}{\sqrt{\partial \mathcal{D}'_2 / \partial k_x}} + \frac{e^{i \int^{x'} k_{2x}^- dx''}}{\sqrt{\partial \mathcal{D}'_2 / \partial k_x}} \right) \end{aligned} \quad (4.93)$$

is a nonlinear coupling factor. Inserting Eq. (4.92) in $\rho'_{2, \text{nl}}$ from Eq. (4.22) and repeating the calculations from Section 4.3 then yields

$$i\Gamma'_2 C'_2 + i \frac{\partial C'_2}{\partial t} + i v'_{2y} \frac{\partial C'_2}{\partial y} - \Lambda'_{2y} \frac{\partial^2 C'_2}{\partial y^2} - \Lambda'_{2z} \frac{\partial^2 C'_2}{\partial z^2} = -i\nu_{2'2} |C_2|^2 C'_2, \quad (4.94)$$

with

$$\nu_{2'2} = \frac{1}{\mathcal{N}'_2 \langle \partial \mathcal{D}'_2 / \partial \omega \rangle} \int_{x_{2l}}^{x_{2r}} \nu_{\text{LF}2'}(x) \left[\int_{x_{2l}}^x \nu_{\text{LF}2'}^*(x') dx' \right] dx \quad (4.95)$$

being the nonlinear coupling factor describing the full effect of the secondary PDI on the EBW. In order to obtain an approximate saturation value of $|C_2|$, we ignore the time derivative, damping, and y diffraction losses on the left hand side of Eq. (4.94). Then the magnitude of the left hand side can be estimated as $|C'_2|/\tau'$, where $\tau' = \min(L_y/|v'_{2y}|, L_z^2/|\Lambda'_{2z}|)$,

which should balance the right hand side, giving [10]

$$|C_2|^2 \approx \frac{1}{|\nu_{2'2}|\tau'}. \quad (4.96)$$

The saturation amplitudes of the other daughter wave amplitudes can also be found. This is done by using Eq. (4.54),

$$i\Gamma C_1 + i\frac{\partial C_1}{\partial t} + iv_{1y}\frac{\partial C_1}{\partial y} - \Lambda_{1y}\frac{\partial^2 C_1}{\partial y^2} - \Lambda_{1z}\frac{\partial^2 C_1}{\partial z^2} = \gamma_{12}C_2^*, \quad (4.97)$$

and Eq. (4.55), where we also include the nonlinear charge density from Eq. (4.23) with a_{LF}^* from Eq. (4.92),

$$-i\Gamma_2 C_2^* - i\frac{\partial C_2^*}{\partial t} - iv_{2y}\frac{\partial C_2^*}{\partial y} - \Lambda_{2y}\frac{\partial^2 C_2^*}{\partial y^2} - \Lambda_{2z}\frac{\partial^2 C_2^*}{\partial z^2} = \gamma_{21}^* C_1 - i\nu_{22'}^* |C_2'|^2 C_2^*; \quad (4.98)$$

here,

$$\nu_{22'}^* = \frac{1}{\mathcal{N}_2 \langle \partial \mathcal{D}'_2 / \partial \omega \rangle} \int_{x_{2l}}^{x_{2r}} \nu_{\text{LF}2'}(x) \left[\int_{x_{2l}}^x \nu_{\text{LF}2'}^*(x') dx' \right] dx. \quad (4.99)$$

Setting $\omega_1 = \omega_2 = \omega_0/2$ ($|\gamma_{12}| = |\gamma_{21}^*| = \sqrt{\gamma_{12}\gamma_{21}^*}$) and introducing $c_1 = |\sqrt{\mathcal{N}_1 \langle \partial \mathcal{D}'_1 / \partial \omega \rangle} C_1|$, $c_2 = |(\sqrt{\mathcal{N}_2 \langle \partial \mathcal{D}'_2 / \partial \omega \rangle})^* C_2^*|$, $c'_2 = |\sqrt{\mathcal{N}'_2 \langle \partial \mathcal{D}'_{2'} / \partial \omega \rangle} C'_2|$, allows Eqs. (4.94), (4.97), and (4.98) to be written in a symmetric form where $\sqrt{\gamma_{12}\gamma_{21}^*}$ characterizes the strength of the primary PDI and

$$\nu'_2 = \frac{1}{\mathcal{N}_2 \mathcal{N}'_2 |\langle \partial \mathcal{D}'_2 / \partial \omega \rangle \langle \partial \mathcal{D}'_{2'} / \partial \omega \rangle|} \left| \int_{x_{2l}}^{x_{2r}} \nu_{\text{LF}2'}(x) \left[\int_{x_{2l}}^x \nu_{\text{LF}2'}^*(x') dx' \right] dx \right| \quad (4.100)$$

characterizes the strength of the secondary PDI. In this form, c_1 , c_2 , and c'_2 are further proxies for the square root of the daughter plasmon numbers of each wave [9, 10], and assuming that the secondary PDI has consumed the majority of the (\mathbf{k}_2, ω_2) -plasmons, we may set $c_1 \approx c'_2$. Requiring the absolute values of the terms on the right hand side of Eq. (4.98) to balance each other then yields the saturation amplitudes,

$$c_1 \approx c'_2 \approx \sqrt{\frac{\gamma_{12}\gamma_{21}^*\tau'}{\nu'_2}}. \quad (4.101)$$

A model similar to the one presented here is found in [10], which shows good agreement between the estimated saturation amplitudes and numerical modeling. [10] finds that up to 6 % of the injected ECRH power can be coupled into the daughter waves by the above mechanism for the investigated TEXTOR-like parameters; taking pump depletion into account changes this fraction to 10 % [12]. We note that the fraction of pump power coupled to the daughter waves depends strongly on the number of secondary PDIs allowed by the plasma profile. In [9], for instance, three secondary PDIs are possible, leading to up to 24 % of the pump power being transferred to the daughter waves. When an even number of secondary decays occur, pump depletion must be taken into account for saturation to

occur [93] and very high fractions of the pump power, up to 60 %, may be coupled to the daughter waves. While PDI-mediated absorption of 45 % of the power of an injected X-mode beam has recently been reported in a low-temperature plasma filament [94], the fraction of ECRH power that can be coupled to electrostatic daughter waves through PDIs in a tokamak remains uncertain, as the wave trapping is usually a highly intermittent phenomenon; this is, however, an obvious point of interest for future investigations.

As a final point of this Section, we note that the primary and secondary daughter waves, (\mathbf{k}_2, ω_2) and $(\mathbf{k}'_2, \omega'_2)$, may combine to produce electromagnetic waves with a frequency $\omega'_0 = \omega_2 + \omega'_2 = 2\omega_2 - \omega_{\text{LF}} \approx \omega_0 - \omega_{\text{LF}}$ [9]. These waves can escape the plasma and be observed by the CTS diagnostic; this is the mechanism through which the trapped wave PDI was originally detected [144]. The spectral power of the electromagnetic waves from combination was found to agree with the observed spectral power during PDI experiments at TEXTOR [9]. The CTS system at ASDEX Upgrade is now additionally equipped with a channel detecting electromagnetic waves near $\omega_0/2$, for which the spectral power can also be compared with theoretical predictions [92].

Chapter 5

Parametric Decay Instabilities near the Second-Harmonic Upper Hybrid Resonance

Now that the theoretical background for parametric decay of an X-mode pump wave into EBWs and X-mode waves with $\omega_1 \approx \omega_2 \approx \omega_0/2$ has been established, the time has come to investigate scenarios in which such PDIs come into play at ASDEX Upgrade. We remind the reader that these PDIs require wave trapping in order to reduce their power threshold to a level attainable with the gyrotron sources installed at ASDEX Upgrade ($\lesssim 1$ MW) [64, 65]. In underdense and moderately overdense plasmas (where $\ell_{Te1,2}^2 > 0$), e.g., found in ASDEX Upgrade and other conventional tokamaks, the daughter waves (both EBWs and X-mode waves) propagate for $\omega_{1,2} < \omega_{UH}$ in the cold limit; at finite T_e the propagation criterion is given by Eq. (2.66). The daughter waves can thus be trapped around a maximum of the UH frequency, where they will have $\omega_1 \approx \omega_2 \approx \omega_{UH}$. The decay condition for the pump wave is hence $\omega_0 \approx 2\omega_{UH}$, so the PDI may occur when ω_{UH} has maximum near the second-harmonic UH frequency of the pump wave. Since $\omega_{UH}^2 = \omega_{pe}^2 + \omega_{ce}^2$, such a maximum can occur due to a maximum of n_e , B , or both. In conventional tokamaks, the magnetic pressure, $\epsilon_0 c^2 B^2/2$, is generally much larger than the kinetic (electron) pressure, $n_e T_e$, meaning that B is mainly determined by the externally generated toroidal magnetic field, which is proportional to $1/R$ [42]. Any maximum of ω_{UH} can therefore be taken to be due to a maximum of n_e along the propagation direction of an ECRH beam, and we are hence led to investigate situations in which non-monotonic n_e -profiles occur in tokamaks, with the additional restriction that $\omega_0 \approx 2\omega_{UH}$ should be true near a local maximum.

As mentioned in Chapter 1, non-monotonic n_e -profiles occur in connection with MHD activity, such as ELMs and magnetic islands; PDIs during ELMs are investigated in Section 5.1 and PDIs during rotating magnetic islands are investigated in Section 5.2. Another case where non-monotonic n_e -profiles may lead to PDIs occurs during pellet fueling of the plasma, which is considered in Section 5.3. Finally, a non-monotonic n_e -profile is always present around the plasma center, and PDIs in this region are treated in Section 5.4; such

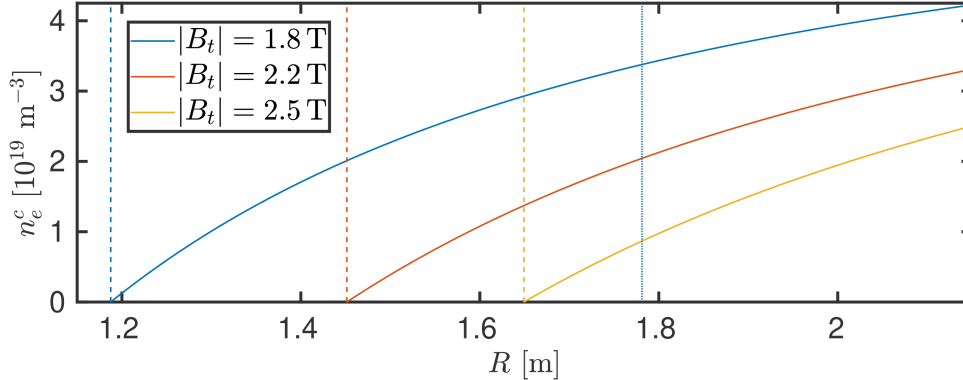


Figure 5.1 – n_e^c at different B_t for a 140 GHz pump wave in ASDEX Upgrade ($R_0 = 1.65$ m and $a = 0.5$ m). The solid lines mark n_e^c , the dashed vertical lines mark the second-harmonic ECR, and the dotted vertical line marks the third-harmonic ECR for $|B_t| = 1.8$ T.

PDIs may also be relevant for other configurations with fixed non-monotonic n_e -profiles, e.g., the island divertors in Wendelstein 7-X [145].

In this Chapter, all gyrotrons are operated in X-mode at the standard heating frequency, $\omega_0 \approx 2\pi \times 140$ GHz, used in ASDEX Upgrade. Investigating the condition $\omega_0 = 2\omega_{UH}$, which gives the minimum value of n_e at a local maximum allowing trapping of daughter waves with $\omega_1 = \omega_2 = \omega_0/2$ for a given B and $T_e = 0$, n_e^c , permits us to draw some rough conclusions about the plasma scenarios where PDIs can be expected in connection with different phenomena leading to non-monotonic n_e -profiles. Taking B to be determined by the externally generated toroidal field, $B \approx |B_t|R_0/R$, with B_t being the toroidal magnetic field at the plasma center ($R = R_0$), allows us to write

$$n_e^c = \frac{\epsilon_0 m_e}{e^2} \left(\frac{\omega_0^2}{4} - \omega_{ce}^2 \right) \approx \frac{\epsilon_0 m_e}{e^2} \left(\frac{\omega_0^2}{4} - \frac{e^2 B_t^2 R_0^2}{m_e^2 R^2} \right). \quad (5.1)$$

Plots of n_e^c for a 140 GHz pump wave in ASDEX Upgrade ($R_0 = 1.65$ m and $a = 0.5$ m) at the $|B_t|$ -values of relevance in this work (1.8 T, 2.2 T, and 2.5 T), along with the second- and third-harmonic ECRs, are seen in Fig. 5.1. As is clear from Eq. (5.1), a higher $|B_t|$ leads to a lower n_e^c , and for $B \approx B_t R_0/R$ above that of the second-harmonic ECR, $\omega_0 = 2|\omega_{ce}|$, n_e^c becomes negative, making it impossible to trap the daughter waves. At the standard magnetic field of ASDEX Upgrade, $|B_t| = 2.5$ T, which leads to a central second-harmonic ECR, the PDI can thus only be excited on the low-field side of the torus and additionally requires $n_e < 2.5 \times 10^{19} \text{ m}^{-3}$. While $n_e < 2.5 \times 10^{19} \text{ m}^{-3}$ may be achieved in the bulk of an L-mode plasma, the usual H-mode scenarios at ASDEX Upgrade will exceed this value in the density pedestal, meaning that PDIs may occur in connection with ELMs, but generally not during magnetic islands, at the standard $|B_t|$. When $|B_t|$ is reduced to 2.2 T, the situation is qualitatively similar to that at 2.5 T; the second-harmonic ECR is moved somewhat to the high-field side and n_e^c is slightly larger, making it more feasible to observe PDIs in connection with magnetic islands, particularly in L-mode plasmas. The greatest possibility of PDIs occurring in the bulk plasma, e.g., during magnetic islands,

during pellet injection, and near the plasma center, is, however, achieved at $|B_t| = 1.8$ T, which is the lowest $|B_t|$ permitting reliable 140 GHz X-mode ECRH at ASDEX Upgrade. At this field, ECRH power is first absorbed at the third-harmonic ECR close to the plasma center, while the second-harmonic ECR is located far on the high-field side and acts as a beam dump for the power not absorbed at the third-harmonic ECR. If the third harmonic ECR is optically thick, PDIs can only occur on the low-field side of the torus, but since $\tau \propto [T_e/(m_e c^2)]^2$ for the third-harmonic X-mode ECR [62, 63], its absorption depends strongly on T_e and must be checked by ray/beam tracing (a rule of thumb is that the third-harmonic ECR will be optically thick when $T_e > 2$ keV at its location in ASDEX Upgrade). Even at $|B_t| = 1.8$ T, daughter wave trapping requires $n_e < 4.25 \times 10^{19} \text{ m}^{-3}$, which usually requires H-mode discharges to be performed close to a boronization [47] or a boron drop [48] with density pump out due to resonant magnetic perturbations [49] in order to have wave trapping in the bulk plasma; such discharges are, for instance, performed to study ELM suppression and the ITER baseline scenario at ASDEX Upgrade.

5.1 Parametric Decay Instabilities in Connection with Edge Localized Modes

We now turn our attention to PDIs during ELMs, which, following the reasoning presented above, are investigated in discharges with $|B_t| = 2.5$ T. As seen in Fig. 5.2 and expected from Fig. 5.1, all discharges considered in this Section have central second-harmonic ECRs and warm second-harmonic UHRs, obtained from Eq. (2.66) for 70 GHz waves, near the plasma edge; in the discharges, \mathbf{B} is determined using the CLISTE code [82], while n_e and T_e are determined using IDA [76].

It is noted that PDIs during ELMs have already been observed through the occurrence of side bands of the gyrotron lines at ASDEX Upgrade [21, 20] (some of the material presented here is based on [20]), and that somewhat similar PDIs were investigated theoretically in [112]. Additionally, there are several other mechanisms than PDIs that allow the generation of strong microwave signals during ELMs. These include ECE from fast electrons in the core due to reduction of the optical thickness of the plasma edge during ELMs [146, 147, 148, 149, 150] and ECE from fast electrons generated during the ELM crashes themselves [147, 150, 151, 152, 153]. Such mechanisms can, however, not explain signals near the gyrotron frequency when $|B_t| = 2.5$ T, as these frequencies correspond to cyclotron emission from electrons near the plasma center which are virtually unaffected by ELMs. Strong signals related to scattering of the ECRH beam by waves in the ICRH or LH frequency range generated by fast ions might explain the strong signals near the ECRH frequency by regular three-wave mixing, but can be excluded by the fact that the observed signal depends nonlinearly on the ECRH power, as will be shown. We finally note that the fact that the signals below the ECRH frequency are consistently seen to be stronger than those above the ECRH frequency is a general indication that the signals shown in this, and subsequent, Sections may be attributed to PDIs. Apart from the evidence for the PDI-origin of the signals near the ECRH frequency provided below, we also show that the

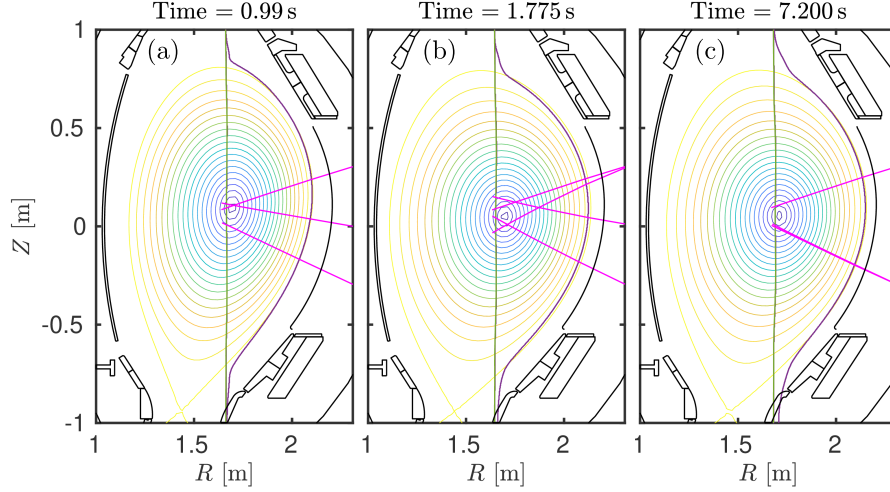


Figure 5.2 – Plasma scenarios with spikes during ELMs in ASDEX Upgrade: #35676 (a), #36583 (b), and #33616 (c). Green lines are the 140 GHz second-harmonic ECR, magenta lines are gyrotron beams, and purple lines are the 70 GHz warm UHR. Pane (a) and (c) appeared in [20].

PDIs generate microwave emissions near half the gyrotron frequency (70 GHz), as expected theoretically [92].

Fig. 5.3 shows the slow (filter bank) CTS signal from a channel just below the ECRH frequency along with the divertor current, where the spikes indicate the occurrence of ELMs, in ASDEX Upgrade #35676 and #36583. The correlation of the microwave bursts with the ELMs during the ELMy phase is very clear, but it is also evident that quasi-continuous strong microwave signals occur before the start of the ELMy phase in both #35676 and #36583. The fact that the strong signals are followed by a quiescent phase before the start of the ELMy phase suggests that they are related to PDIs in the turbulent structures present at the edge of L-mode discharges [16]. In #35676, the signal is seen to develop in a continuous fashion, while the signal in #36583 is inherently bursty, even before the start of the ELMs. This is due to the probe gyrotron being operated in a pulsed mode, visible in pane (a) of Fig. 5.4, from 1.59 – 1.8 s in #36583, unlike the continuous wave ECRH beam which is used as a probe in #35676 and later in #36583. The differences in background (ECE) levels in Fig. 5.3 are due to a more central CTS view in #35676 compared with #36583, and the background level in #36583 is essentially the intrinsic noise of the CTS channel. Pane (a) of Fig. 5.4 also shows that the signal in #36583 originates from the probe gyrotron beam near the plasma edge, which is viewed by the CTS radiometer, as expected for PDI-generated signals. Strong microwave signals only occur when the probe gyrotron is turned on, and the ECRH power is kept constant by pulses from another gyrotron, which has no overlap with the CTS view, when the probe gyrotron is off, eliminating the possibility of the different microwave signals being due to differences in electron heating. The probe gyrotron pulses in #36583 additionally include analog modulation, seen in the zoom in on pulse #1 in pane (b) of Fig. 5.4, allowing

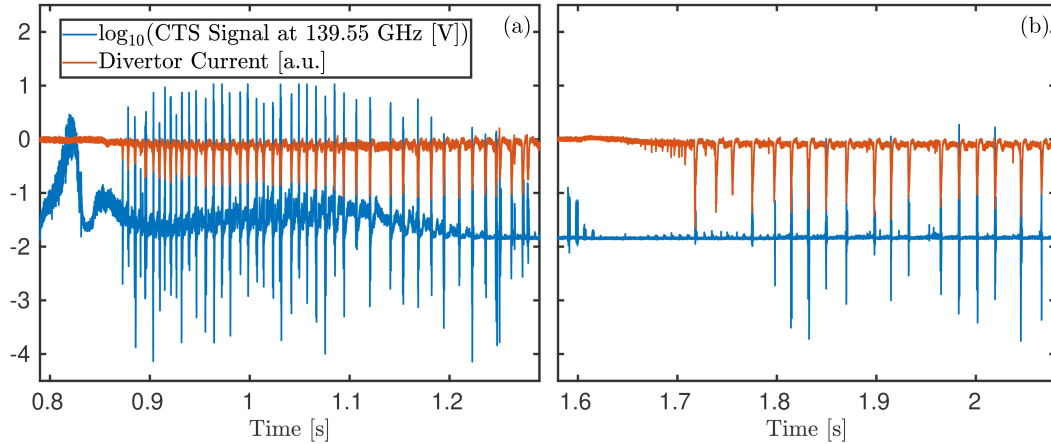


Figure 5.3 – Slow CTS signal at 139.55 GHz and divertor current versus time in ASDEX Upgrade #35676 (a) and #36583 (b). A strong correlation is visible.

the dependence of the CTS signal on the probe gyrotron power, P_0 , to be investigated; this is done in Fig. 5.5. The microwave signal depends nonlinearly on P_0 , both in the pulses before the ELMy phase and during the ELMs themselves, as expected for PDIs. For the pulses before the ELMy phase, the PDI gyrotron power threshold, inferred from the P_0 -value where the CTS signal starts deviating from the background level, is seen to increase from 200 – 250 kW in pulse #1 to 350 – 400 kW in pulse #4. This indicates a strong dependence of the threshold on n_e at the edge, which is increasing rapidly during this phase. During the pulses where ELMs occur, a PDI gyrotron power threshold of 220 – 225 kW is observed in both cases, though the bursty nature of the signal in these pulses makes it unclear if the actual threshold is lower.

As in the pre-ELM phase, the maximum CTS signal during ELMs, recorded in the periods with constant P_0 in #35676 (0.8 – 4.0 s) and #36583 (1.8 – 7.5 s), has a strong dependence on n_e at the pedestal top. This is shown in Fig. 5.6 by plotting the maximum CTS signal during the ELMs versus n_e at $\rho_{\text{pol}} = 0.92$, which is close to the pedestal top in all cases; the unclear dependence in #36583 is due to the variation of n_e being within the uncertainty of the IDA profiles. Evidently, the strongest signals occur at low n_e . In order to investigate nature of the difference, we select two ELMs in #35676, one with low n_e at 0.99 s and one with high n_e at 3.129 s; the n_e and T_e profiles at these time points are seen in panes (a) and (b) of Fig. 5.7. Fig. 5.8 shows signals from the fast CTS system during the selected ELMs, both the ones near 140 GHz, in panes (1a) and (1b), and the ones near 70 GHz, in panes (2a) and (2b), along with the divertor current in panes (3a) and (3b); the signals in #36583 are similar to those at low n_e . In both panes (1a) and (1b) of Fig. 5.8, the ELM crash is associated with the spikes extending from the low-frequency edge of the notch filter to the lowest frequency covered by the radiometer. The quasi-continuous lines from 138.5 – 139 GHz before and after the ELM crash in pane (1a) of Fig. 5.8 are likely related to PDIs in the n_e -structures set up by inter-ELM modes, which is consistent with their character changing as a result of the ELM crash. At the higher n_e in pane (1b) of Fig.

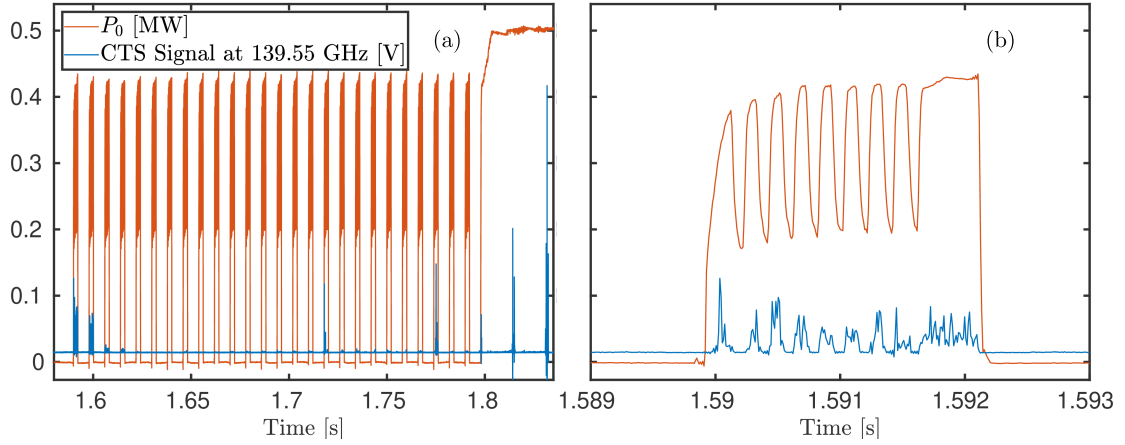


Figure 5.4 – P_0 pulses with analog modulations and CTS signal in ASDEX Upgrade #36583. Pane (a) shows an overview of the pulses and the beginning of the continuous wave phase after the pulses; pane (b) shows the signals during pulse #1.

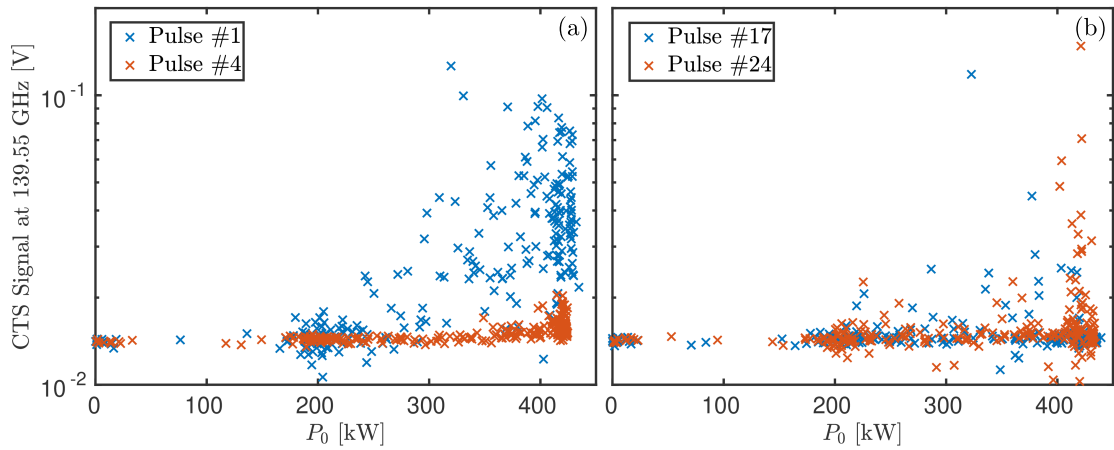


Figure 5.5 – Plot of P_0 versus the CTS signal at 139.55 GHz to determine P_0^{th} in ASDEX Upgrade #36583. Pane (a) shows pulses before the start of the ELM phase, while pane (b) shows pulses in which ELM crashes occur.

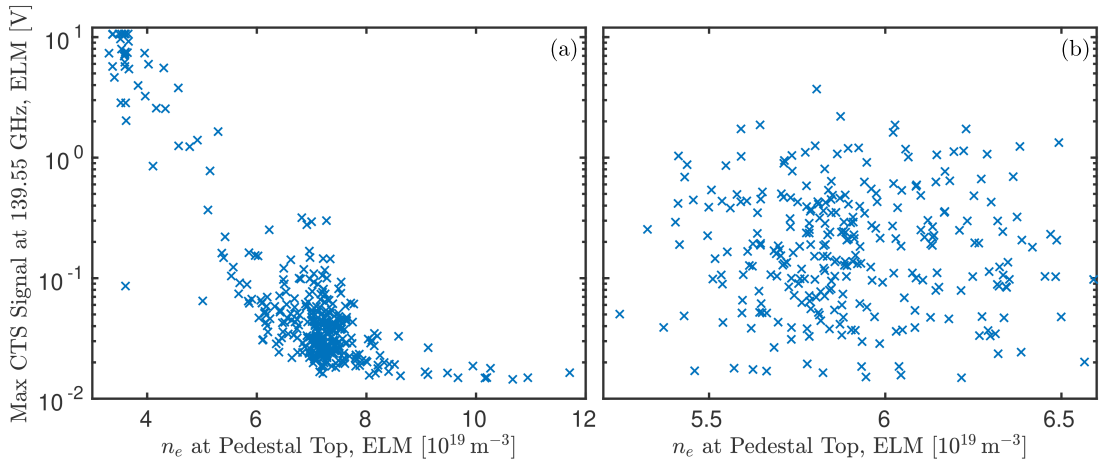


Figure 5.6 – Maximum CTS signal at 139.55 GHz during ELMs versus n_e at the pedestal top ($\rho_{\text{pol}} = 0.92$) in ASDEX Upgrade #35676 (a) and #36583 (b).

5.8, the quasi-continuous lines disappear, except for a small amount of activity just before the ELM crash. The fast signals near 70 GHz are seen in panes (2a) and (2b) of Fig. 5.8. Since the LO frequency is 70.5 GHz, it is clear that strong microwave signals occur in both cases around the time of the ELMs, as expected for PDIs near the second-harmonic UHR [92], but we also note significant bursts just before the ELM crashes are observed in the divertor currents; whether these are related to the ELM or its precursor is unclear as of yet. Further, the setup used for detection of 70 GHz waves is still in a preliminary state, since it does not permit signals up- and down-shifted with respect to the LO to be distinguished and may also show interference with signals near 140 GHz, so the 70 GHz signals have not been analyzed in detail.

In order to characterize the spikes near the ECRH frequency during ELMs, histograms of their duration based on the observations from the fast CTS system throughout #35676 and #36583 are shown in Fig. 5.9. The histograms are constructed by integrating the fast CTS data in the frequency range 139.25 – 139.65 GHz, where the strong signals occur during ELMs, smoothing the data, and extracting the duration of spikes with prominences exceeding a set level to exclude non-PDI-related signals. The majority of the spikes last 2 – 5 μs and no spike lasts more than 12 μs ; the mean duration in #36583 is somewhat larger than in #35676 (4.6 μs versus 3.1 μs), but the distributions are similar overall. The spike duration distributions found in Fig. 5.9 is consistent with the passage time of the n_e -structures allowing trapping during an ELM crash through an ECRH beam. This is demonstrated in Fig. 5.10, which shows the evolution of n_e and the warm 70 GHz UHR according to a JOREK simulation [154] of an ELM in ASDEX Upgrade [155]. The simulated discharge is ASDEX Upgrade #33616 at 7.200 s, for which the plasma scenario is seen in Fig. 5.2; #33616 is very similar to #36583 and also reasonably similar to the early phase of #35676. In the snapshots shown in Fig. 5.10, the simulation time, t , runs from 52.1 – 60.5 μs and during this time interval (8.4 μs), a region allowing trapping of two 70 GHz UH plasmons, which is necessary for PDIs to generate microwave bursts,

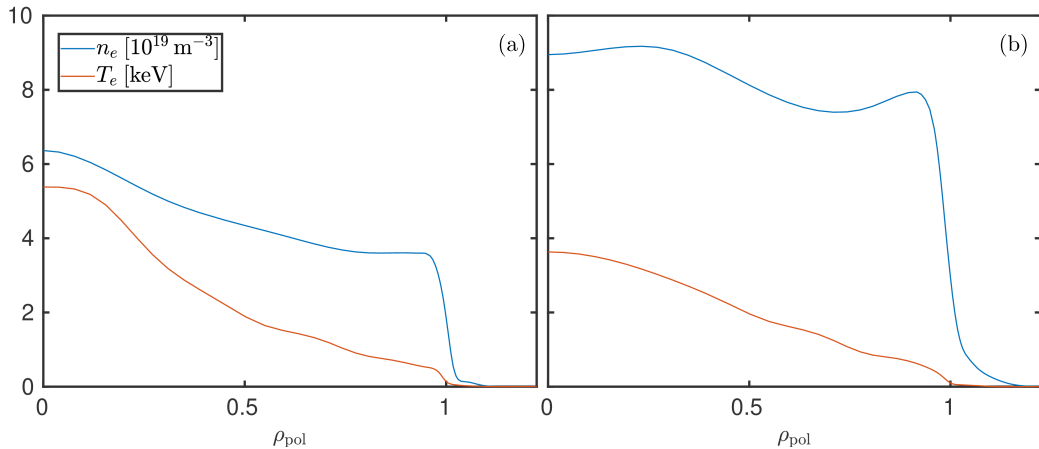


Figure 5.7 – IDA n_e - and T_e -profiles during ELMs in ASDEX Upgrade #35676. Pane (a) is associated with the ELM at 0.990s and has a low $n_e = 3.6 \times 10^{19} \text{ m}^{-3}$ at the pedestal top ($\rho_{\text{pol}} = 0.92$); pane (b) is associated with the ELM at 3.129s and has a high $n_e = 7.9 \times 10^{19} \text{ m}^{-3}$ at the pedestal top.

passes through the lower set of beams. $8.4 \mu\text{s}$ thus represents an upper bound of the burst duration which is similar to the experimental value of $12 \mu\text{s}$. We can further use the theory developed in Chapter 4 to estimate the ECRH power threshold which must be exceeded to excite PDIs when the trapping region crosses the central rays of the beams; the plasma and beam parameters used for these calculations are extracted along the lower beams in Fig. 5.10 at $t = 55.4 \mu\text{s}$ and shown in Fig. 5.11. Fig. 5.11 shows $k_{1x}^{\pm} = |k_{1x}^{\pm}|$ and $k_0 - k_{2x}^{\pm} = k_0 + |k_{1x}^{\pm}|$; the points at which these curves overlap satisfy the k_x -selection rule of the PDI. Convective losses along y dominate, and threshold values of 133 kW and 136 kW are found for the two beams following the steps in Subsection 4.3.1, if we set $L_y = 1 \text{ cm}$ based on the size of the trapping region in the simulation ($L_z = \sqrt{\pi/8W}$ and $W = 2.873 \text{ cm}$ are also used here). Use of the estimates from [8] give significantly lower thresholds, 891 W and 938 W, respectively [20], with the threshold due to diffraction losses along z being higher than that due to convection losses along y , despite the domination of the y -loss terms. The threshold values of 133–136 kW are similar to the experimentally estimated threshold in #36583 (220–225 kW based on Fig. 5.5), providing further evidence in favor of the second-harmonic UHR PDI theory of the microwave bursts. The lack of a perfect agreement between theory and experiment is expected due to the highly simplified theoretical model, the MHD nature of the ELM simulation, and the fact that the simulation is of a different, albeit very similar, discharge.

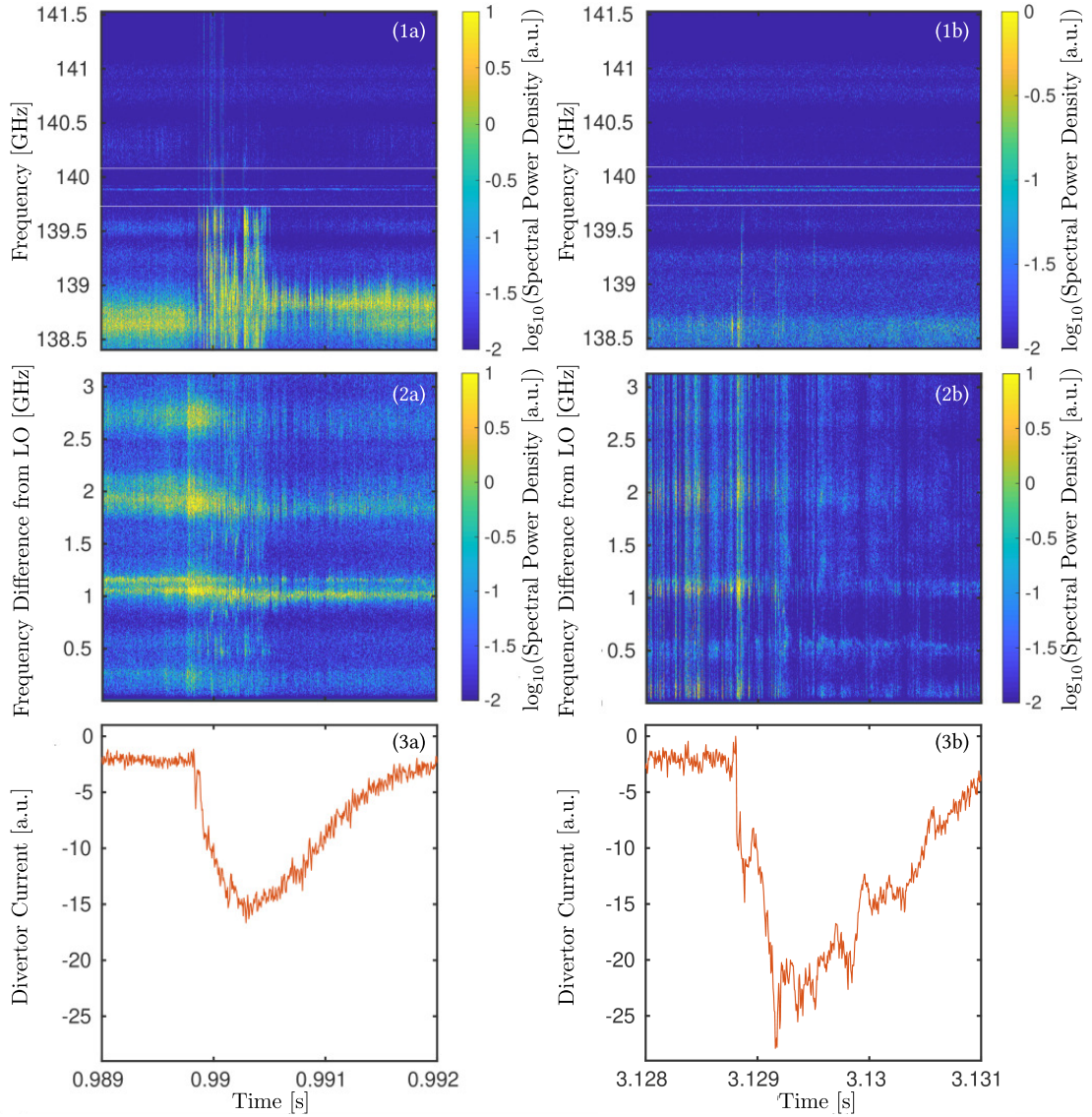


Figure 5.8 – ELM signals during an ELM at low n_e and one at high n_e in ASDEX Upgrade #35676. Panes (a) are related to the ELM at low n_e , while panes (b) are related to the ELM at high n_e . Panes (1a) and (1b) show the fast CTS signal near 140 GHz (the white lines mark the edges of the notch filter around the ECRH frequencies); panes (2a) and (2b) show the fast signals near 70 GHz; panes (3a) and (3b) show the divertor current. Pane (1a) appeared in [20].

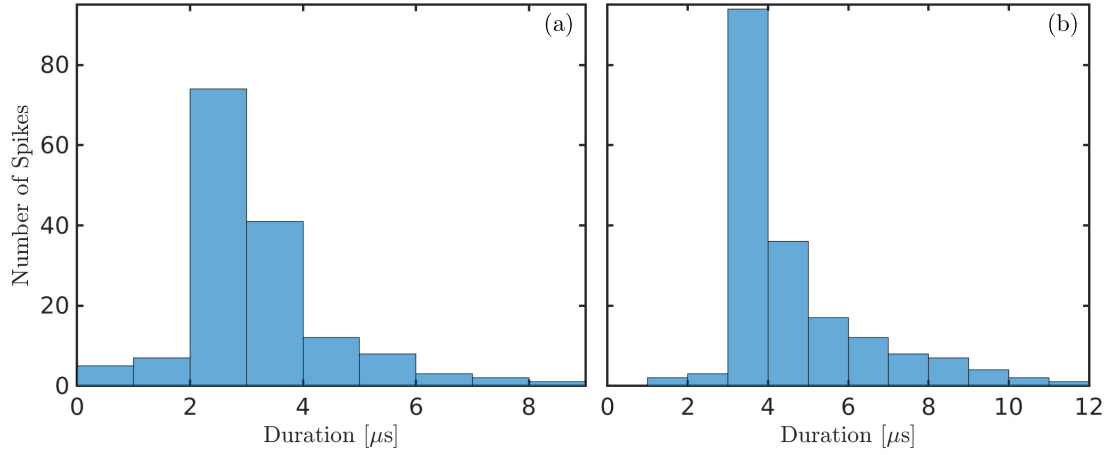


Figure 5.9 – Histogram of the duration of the spikes from 139.25–139.65 GHz during ELMs in ASDEX Upgrade #35676 (a) and #36583. In #35676, the mean duration is $3.1 \mu\text{s}$ and the standard deviation of the duration is $1.3 \mu\text{s}$; in #36583, the mean duration is $4.6 \mu\text{s}$ and the standard deviation of the duration is $1.8 \mu\text{s}$. A figure similar to pane (a) appeared in [20].

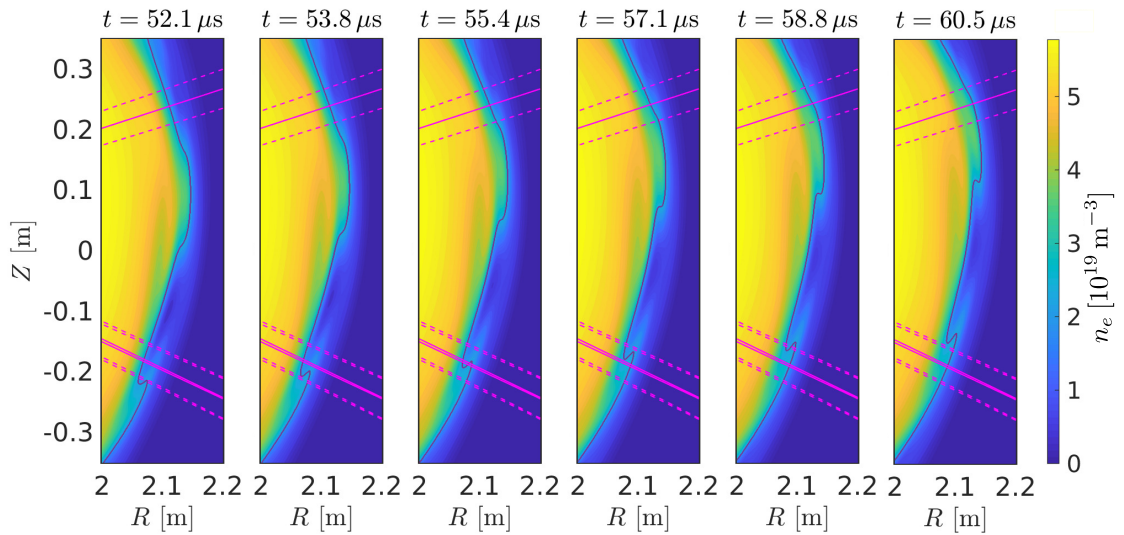


Figure 5.10 – Evolution of n_e and the warm 70 GHz UHR (purple line) in the JOREK simulation of ASDEX Upgrade #33616. The solid magenta lines mark the gyrotron central beam rays; the dashed lines mark the beam widths. This figure appeared with some minor modifications in [20].

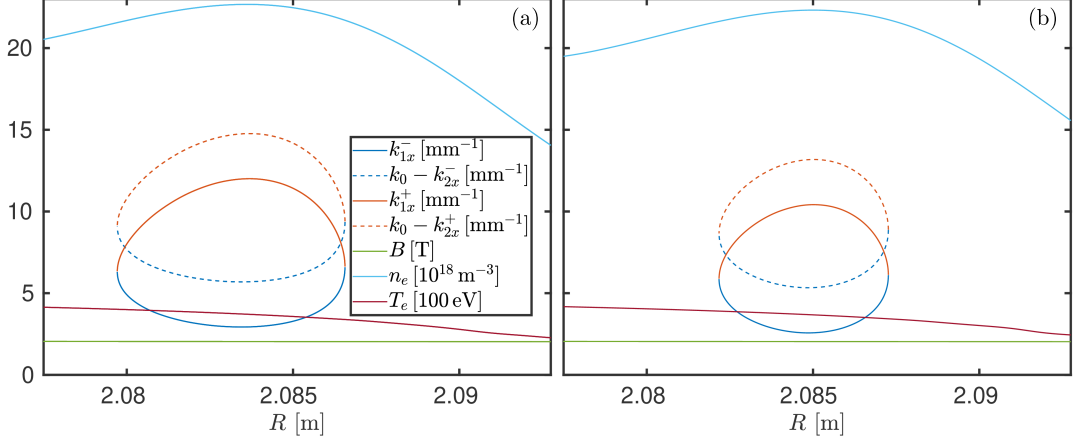


Figure 5.11 – Plasma and wave parameters in the trapping regions of the lower beams at $t = 55.4 \mu\text{s}$ in the JOREK simulation of ASDEX Upgrade #33616 (see Fig. 5.10). Pane (a) shows the situation for the beam with a PDI threshold of 133 kW; pane (b) shows the situation for the beam with a PDI threshold of 136 kW.

5.2 Parametric Decay Instabilities in Connection with Rotating Magnetic Islands

We now consider PDIs during rotating magnetic islands. A magnetic island may possess a local maximum of n_e near its O-point, allowing trapping of the EBWs/X-mode waves when $\omega_0 \approx 2\omega_{UH}$ is additionally satisfied at the island position. Rotating magnetic islands with $\omega_0 \approx 2\omega_{UH}$ at the O-point are thus expected to give rise to PDI-generated microwave bursts when the O-point crosses an ECRH beam, i.e., the bursts occur quasi-periodically at rate determined by the island rotation frequency. Microwave bursts near ω_0 with the above phenomenology were first observed by the CTS system during second-harmonic X-mode ECRH at TEXTOR [144, 156]. The explanation of these microwave bursts was what originally prompted the development of the trapped-wave PDI theory described in Section 4.4 [8, 9, 10, 11, 12]. We note that PDIs during rotating magnetic islands with $\omega_0 \approx \omega_{UH}$ may also occur for O-mode ECRH [157], although the experimental evidence related to tokamaks is still inconclusive [158].

At TEXTOR, magnetic islands rotating with a frequency of 974 Hz could be triggered through magnetic perturbations generated by the dynamic ergodic divertor [144, 156]. The magnetic perturbation coils at ASDEX Upgrade are capable of generating slowly rotating (0.5 Hz) magnetic islands in low-density L-mode discharges, but rather than pursuing this route, our focus was on natural magnetic islands, e.g., occurring during neoclassical tearing modes (NTMs), as these are the islands of potential concern in future devices such as ITER. Despite several attempts, no reliable setup for generating such islands with strong PDI signals was found, likely due to the several criteria, relying on quasi-random factors such as NTM-generation, which needed to be satisfied simultaneously. Nevertheless, strong PDI-like signals related to rotating magnetic islands were observed in several discharges,

the plasma scenarios of which are seen in the top row of Fig. 5.12; we additionally show plasma scenarios from two discharges for which no strong signals related to the islands were observed, despite the island intersecting the second-harmonic UHR very close to the ECRH beams, in the lower row of Fig. 5.12. Four of the discharges in Fig. 5.12 (#35939, #35527, #35185, and #35355) were H-mode ELM suppression discharges with $|B_t| = 1.8$ T (third-harmonic X-mode ECRH) and resonant magnetic perturbations, which brings n_e to a range where the 140 GHz second-harmonic UHR occurs in the bulk plasma, as expected from Fig. 5.1. We note that the strong signals in #35939 and #35527 both occurred at times with limited power absorption at the third-harmonic ECR (52 % and 12 %, respectively) due to low T_e , which left sufficient power in ECRH beams to drive PDIs at the island locations on the high-field side. The remaining discharge in Fig. 5.12 (#35186) was a limiter L-mode discharge with $|B_t| = 2.2$ T heated by a single gyrotron (second-harmonic X-mode ECRH on the high-field side), designed to allow comparison between turbulence measurements and simulations, but fortunately for us also very close to the scenarios in which PDI-generated microwave bursts were observed at TEXTOR [144, 156]. In all cases, the occurrence of a rotating magnetic island has been identified by quasi-periodic signals in the soft X-ray, magnetic diagnostic, and ECE systems; the ρ_{pol} -locations of the islands are determined using the ECE system [75]. As seen in Fig. 5.12, the warm 70 GHz UHR is located close to the islands at the shown time points in all the discharges, and as we shall see, strong microwave bursts with a PDI-origin occur at all the time points shown in the top row of Fig. 5.12. In #35527, it appears that wave trapping may also occur near the plasma center. However, the diagnostics used in the IDA reconstruction of n_e have essentially no coverage at the plasma center, so this should not be attributed too much significance; in spite of this, PDIs near the plasma center may account for strong microwave signals at another point in #35527, as discussed in Section 5.4.

The strong microwave signals in #35939 were observed by the ECE system and are of particular interest, as they lead to a permanent degradation of one of the ECE mixers. Both the strong microwave signals and the mixer degradation are shown in Fig. 5.13. The strong microwave signals occur near half the gyrotron frequency, as expected theoretically [92], and have a repetition rate matching that of the rotating island (around 2 kHz), as identified by the soft X-ray and magnetic diagnostics. ECE mixer degradation occurs after the second microwave spike and leads to a permanent reduction of the radiation temperature measured by the channels using the low-frequency ECE mixer by approximately 25 %, necessitating a recalibration.

In #35186 and #35527, strong microwave signals near the gyrotron frequencies were observed using the CTS system and their consequences were less dire. The fast CTS system allowed the detailed behavior of the microwave signals near the gyrotron frequency during island rotation to be identified, as seen in Figs. 5.14 and 5.15 (the fast 70 GHz system was not operational at the time #35186 and #35527 were performed). In #35186 (Fig. 5.14), the island rotates with a frequency around 1 kHz and during each rotation, lines chirping down (and up) from the gyrotron frequency occur, followed by lines chirping back to the gyrotron frequency; these signals resemble the ones observed at TEXTOR [144, 156]. In #35527 (Fig. 5.15), the island rotation is faster, approximately 5 kHz, but the qualitative

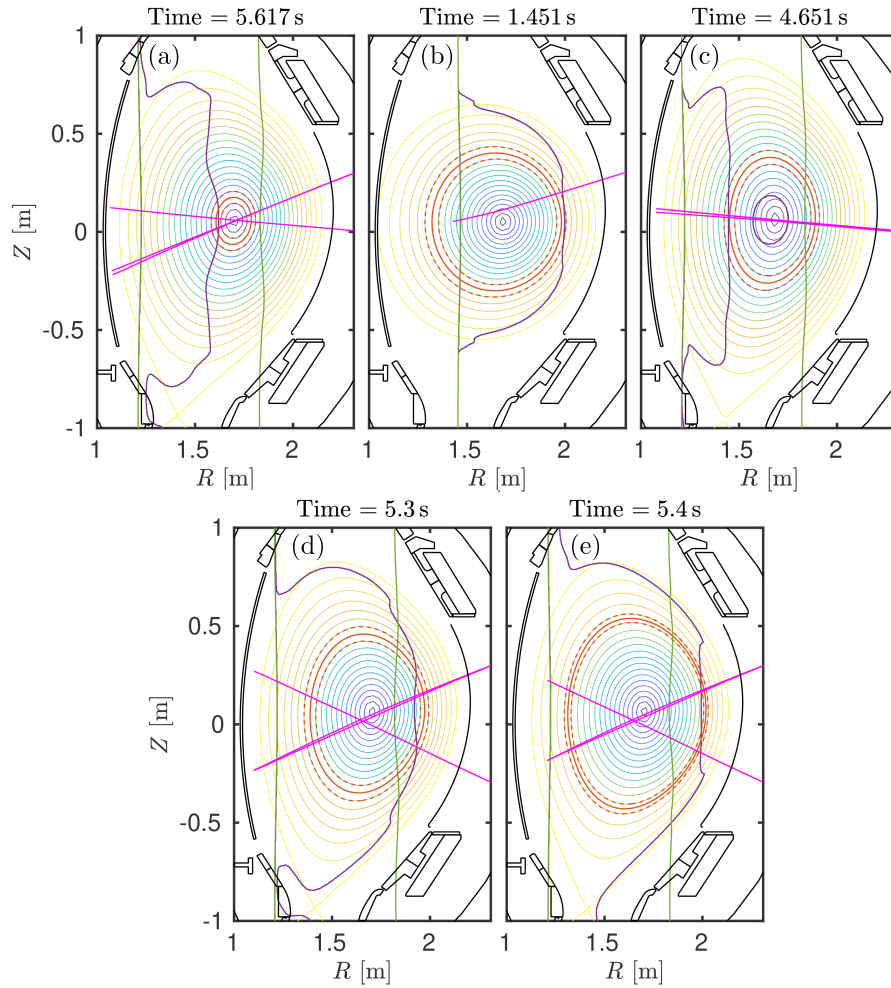


Figure 5.12 – Plasma scenarios with rotating magnetic islands near the warm 70 GHz UHR in ASDEX Upgrade: (a) #35939, (b) #35186, (c) #35527, (d) #35185, (e) #35355. In scenarios (a), (b), and (c), strong microwave bursts occur at a rate determined by the island rotation frequency, while no such signals are observed in scenarios (d) and (e). Green lines are ECR harmonics, orange lines indicate the ρ_{pol} -position of the island, magenta lines are gyrotron beams, and purple lines are the 70 GHz warm UHR.

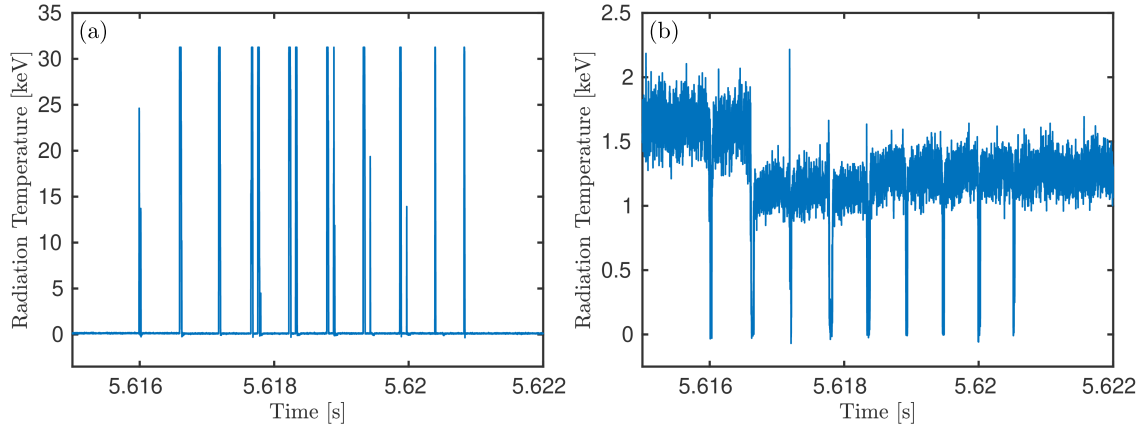


Figure 5.13 – Degradation of ECE mixer during a rotating magnetic island in ASDEX Upgrade #35939. Pane (a) shows the signal from a channel around 75.5 GHz; pane (b) shows the signal from a channel around 87.9 GHz.

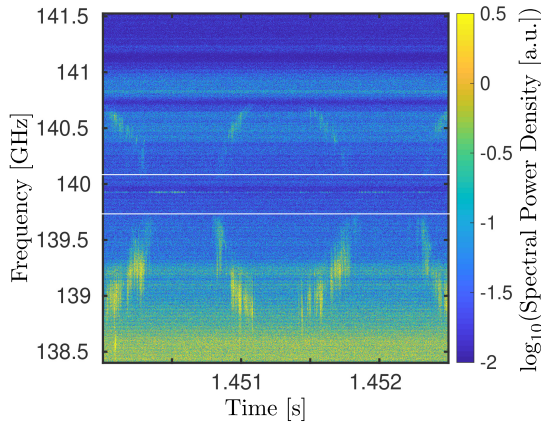


Figure 5.14 – Fast CTS signal near 140 GHz during a rotating magnetic island in ASDEX Upgrade #35186. The white lines mark the edges of the notch filter around the gyrotron line. Spikes occur with a repetition rate determined by the mode frequency.

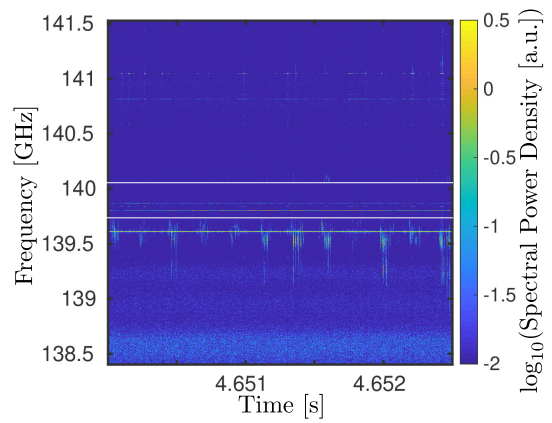


Figure 5.15 – Fast CTS signal near 140 GHz during a rotating magnetic island in ASDEX Upgrade #35527. The white lines mark the edges of the notch filter around the gyrotron lines. Spikes occur with a repetition rate determined by the mode frequency.

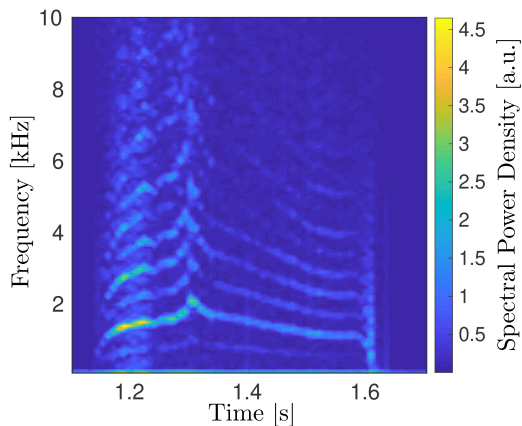


Figure 5.16 – Spectrogram of the CTS channel from 139.0–139.1 GHz during the rotating island in ASDEX Upgrade #35186.

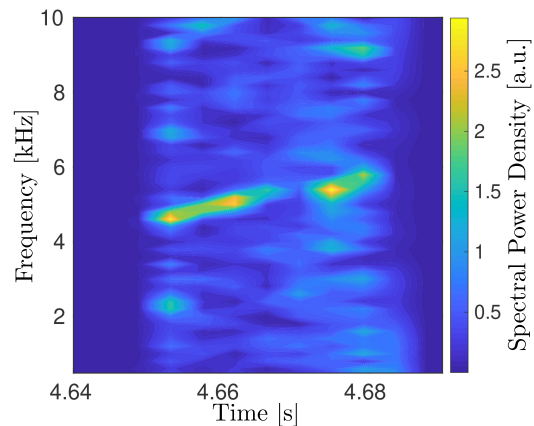


Figure 5.17 – Spectrogram of the CTS channel from 139.4–139.5 GHz during the rotating island in ASDEX Upgrade #35527.

development of the gyrotron side bands during island rotation appears similar to #35186. Using the slow CTS system, it is possible to track the development of the island rotation frequency over a longer period of time. This may be done by creating spectrograms of the signal from a channel affected by the periodic bursts associated with the rotation of the island; for #35186 and #35527, such spectrograms are seen in Figs. 5.16 and 5.17, respectively. Particularly, in #35186 it is possible to follow the island rotation and eventual locking through the spikes in the slow CTS system, and the resulting spectrograms appear very similar to the ones obtained from the soft X-ray and magnetic diagnostics (though with different strength of the various harmonics), supporting that the signal is related to the island rotation. The spectrogram for #35527 also matches up with soft X-ray and magnetic diagnostics, but the much shorter duration of the island-related signals in this discharge does not allow a thorough comparison.

While no detailed n_e -profiles in the islands at ASDEX Upgrade during the microwave bursts could be obtained due to the lack of a reliable setup, B , n_e , and T_e at the overlap between the island and the ECRH beams from CLISTE and IDA could still be compared with proximity to the 70 GHz warm UHR given by Eq. (2.66), which is necessary to allow trapping with a relatively small n_e -bump. As seen in Fig. 5.18, and also indicated in Fig. 5.12, all points at which the strong microwave signals are observed occur close to the warm 70 GHz UHR, as expected for PDI-generated bursts. It is, however, noted that islands with parameters close to the warm 70 GHz UHR without strong microwave signals also occur, as indicated by the purple dots from #35185 and #35355 in Fig. 5.18. We note that the islands in #35185 and #35355 are present during a period of increasing n_e , displacing the second-harmonic UHR from inside to outside mode location at the intersection with the ECRH beam, which is evident from the existence of purple dots on both sides of the T_e^c -surface in Fig. 5.18. This means that a PDI signal related to these islands should have occurred at some point if the n_e -bump around the island O-points were sufficiently large to

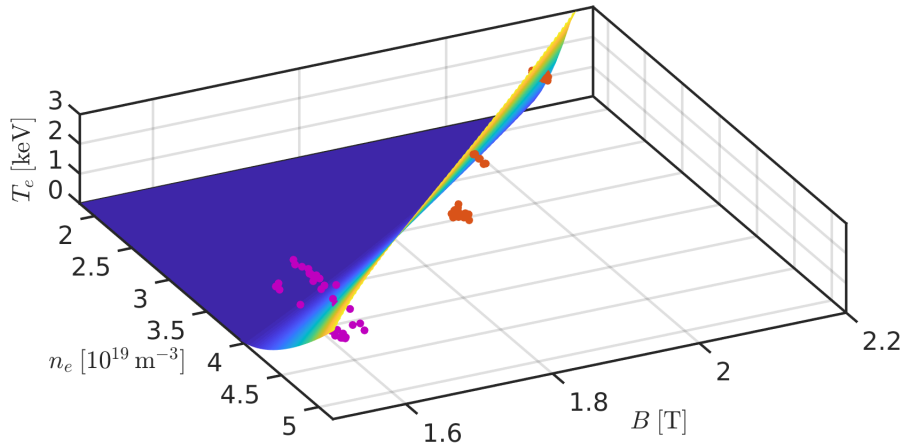


Figure 5.18 – Observations of PDIs during rotating magnetic islands in ASDEX Upgrade. The orange dots indicate plasma parameters at the intersection of the island center and a central ECRH beam ray when island-related PDIs have been observed, purple dots indicate the same parameters where no island-related PDIs were observed, and the surface marks T_e^c for 70 GHz UH waves (propagating 70 GHz UH waves exist below the surface).

allow trapping of 70 GHz daughter waves. Thus, the simple condition of having a rotating island near the warm second-harmonic UHR appears to be necessary, but insufficient, for the generation of strong PDI-related microwave bursts. In order to obtain a more solid criterion, more detailed knowledge of the island n_e -profiles, which can, for instance, be obtained by properly timed Thomson scattering measurements [159], is required.

5.3 Parametric Decay Instabilities in Connection with Pellet Injection

Another situation in which the non-monotonic n_e -profiles required for trapped-wave PDIs near the second-harmonic UHR may occur is when the plasma is fueled by pellet injection. The pellets consist of frozen hydrogen isotopes, deuterium in the ASDEX Upgrade discharges discussed here, injected into and ablated by the plasma; pellet fueling is an alternative to more conventional gas fueling. In future devices, such as ITER, gas fueling is predicted to provide poor penetration of the hydrogen isotopes to the plasma core which is not an issue for pellet fueling [53]. Additionally, pellet fueling allows core plasma densities well above the Greenwald limit to be obtained [52]. Both these factors make pellet fueling the expected main fueling scheme of a magnetic confinement fusion reactor. Ordinarily, pellet fueled discharges at ASDEX Upgrade have high densities, placing them outside the region where PDIs near the second-harmonic UHR of the gyrotron radiation are expected. However, by combining pellet fueling, magnetic perturbations, and a low magnetic field ($|B_t| = 1.8$ T), it is possible to obtain profiles allowing such PDIs [54].

An example of the microwave signal recorded by the slow CTS system just below the

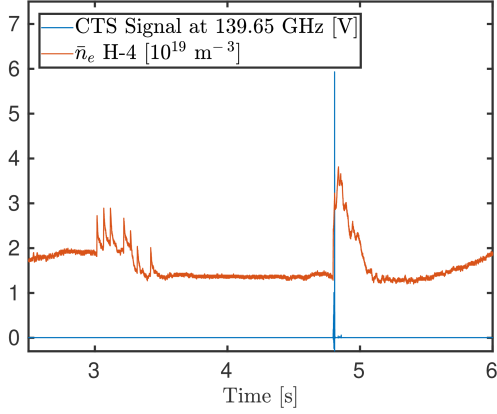


Figure 5.19 – Slow CTS signal from 139.6–139.7 GHz and line-averaged edge density versus time in ASDEX Upgrade #35554. Pellets are injected from 3.0–3.5 s. A strong CTS signal is observed during the edge density spike at 4.8 s.

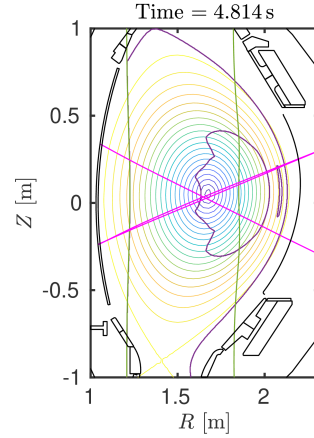


Figure 5.20 – Thomson scattering plasma scenario with PDIs during edge density spike in ASDEX Upgrade #35554. Green lines are ECR harmonics, magenta lines are gyrotron beams, and purple lines are the 70 GHz warm UHR.

gyrotron frequency in such a discharge, along with the line-averaged edge density from an interferometer channel near the plasma edge, \bar{n}_e H-4, in an ASDEX Upgrade discharge of this type (#35554) is seen in Fig. 5.19. In #35554, pellets are injected from 3.0–3.5 s, where they are observed as spikes in \bar{n}_e H-4. The injection of the pellets is not associated with any strong microwave signal, and while this may be attributed to the edge density being too low in #35554, a similar discharge with an edge density scan by pellet injection passing $4.25 \times 10^{19} \text{ m}^{-3}$ (#35866), where trapped-wave PDIs are expected according to Fig. 5.1, also showed a lack of strong microwave signals in connection with pellet injection. However, another \bar{n}_e H-4 spike, which is associated with a strong microwave signal, occurs in #35554 around 4.8 s due to a locked mode.

The n_e -profiles associated with this edge density spike do allow trapping of 70 GHz EBWs/X-mode waves if only Thomson scattering is taken into account (the full IDA-profiles are flatter and do not allow trapping), as seen in Figs. 5.20 and 5.21. The PDI threshold, P_0^{th} , determined by the theory of Section 4.3, is again dominated by losses along the y -direction. With $L_y = L_z = \sqrt{\pi/8}W$ and $W = 2.64 \text{ cm}$, it becomes 250 kW for the plasma and wave parameters shown in Fig. 5.21. It is possible to determine P_0^{th} for the Thomson scattering equilibria allowing trapping around 4.8 s in #35554; the resulting time trace is shown in Fig. 5.22. Clearly, P_0^{th} has a large spread, with the main determining factor being the size of the amplification regions compared with the trapping region; the threshold is, however, consistently below P_0 from 4.813–4.817 s, indicating that PDIs may occur at some time points. The accuracy of P_0^{th} is clearly limited by the spatial resolution of the Thomson scattering data, as is evident from the almost piece-wise linear behavior of the wave numbers in Fig. 5.21. There is also the issue of interpolation in time between the actual Thomson scattering measurements in Fig. 5.22, which is further corroborated

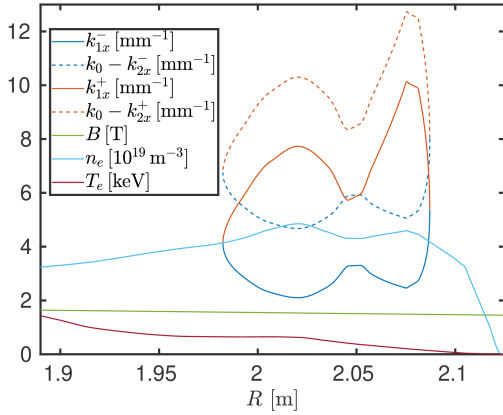


Figure 5.21 – Plasma and wave parameters in the trapping region of the lower beam at 4.814 s for the Thomson scattering equilibrium in ASDEX Upgrade #35554. A power threshold of 250 kW is obtained for the shown parameters.

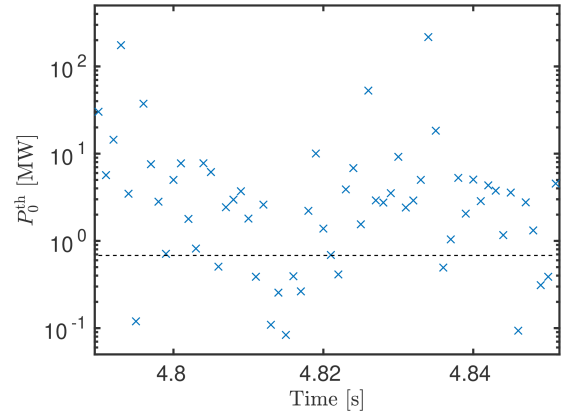


Figure 5.22 – P_0^{th} during the edge density spike in ASDEX Upgrade #35554. Large fluctuations are observed, but from 4.813 – 4.817 s, thresholds below P_0 , marked by the dashed black line, are found consistently.

by the fact that the predicted times with low thresholds do not line up with the microwave bursts in the CTS system. Fig. 5.22 is, nevertheless, qualitatively correct, and the above analysis illustrates the possible applications of the theory from Section 4.3.

Overall, it thus seems that PDIs can occur in the ECRH beams during edge density spikes, but that they do not occur during pellet injection at ASDEX Upgrade. The most likely explanation for this is that the ECRH system is switched off for a short period (~ 1 ms) around the injection of a pellet in order to avoid the possibility of encountering a cutoff during the initial density spike. While wave trapping requires a far smaller density spike than what is necessary to reach the X-mode cutoff, it appears that the safety precautions implemented to avoid the cutoff are also sufficient to avoid PDIs during pellet injection at ASDEX Upgrade.

5.4 Parametric Decay Instabilities near the Plasma Center

The final case of PDIs near the second-harmonic UHR considered in this work involves daughter waves trapped in the non-monotonic n_e -profile near the plasma center. Such PDIs were used to provide an explanation of strong microwave signals near the gyrotron frequency observed using CTS at low n_e in TEXTOR [156]. They have additionally been observed in low-temperature plasma filaments [160, 94], and recent studies of such systems further indicate that they occur for O-mode radiation with $\omega_0 \approx \omega_{UH}$ at the plasma center [161], making them potentially relevant for ITER.

As seen in pane (c) of Fig. 5.12, the n_e -profile in #35527 may allow trapping of 70 GHz EBWs/X-mode waves near the plasma center. While this does not appear to be the case at

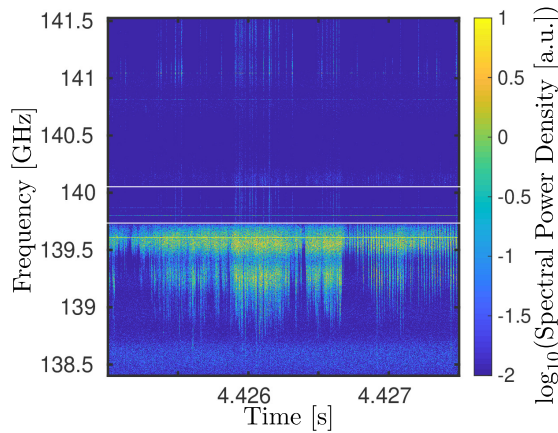


Figure 5.23 – Fast CTS signal near 140 GHz during central PDI in ASDEX Upgrade #35527. The white lines mark the edges of the notch filter around the gyrotron lines.

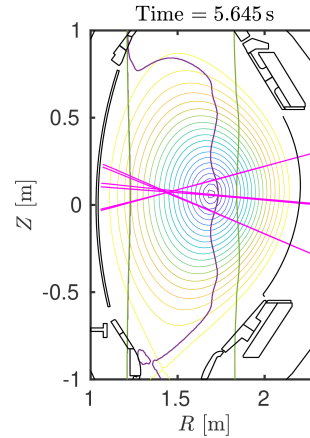


Figure 5.24 – Plasma scenario with central PDIs in ASDEX Upgrade #36149. Green lines are ECR harmonics, magenta lines are gyrotron beams, and purple lines are the 70 GHz warm UHR.

the time point shown in Section 5.2, it is consistent with the spectrum observed near the gyrotron frequencies by the fast CTS system at an earlier time point, shown in Fig. 5.23. As for the point with island-related PDIs in #35527, the plasma has degraded confinement at the time points shown in Fig. 5.23, meaning that only around 14 % of the ECRH power is absorbed at the third-harmonic ECR for each of the beams, leaving sufficient power to drive PDIs near the plasma center. Unlike the case with island-related PDIs, the signal in Fig. 5.23 is quasi-continuous, as expected for a signal generated by PDIs in the quasi-permanent cavity around the plasma center.

Another discharge with PDIs near the plasma center is identified by ECE mixer degradation in ASDEX Upgrade #36149. This ITER-baseline plasma scenario is seen in Fig. 5.24, from which it is clear that the second-harmonic UHR is located very close to the plasma center. The plasma confinement is not significantly degraded at the time of the strong microwave signals near half the gyrotron frequency, seen in pane (a) of Fig. 5.25, meaning that approximately 73 % of the ECRH power is absorbed before reaching the plasma center. However, since the gyrotrons are operated at high power in the discharges, this still leaves around 200 kW from each of the beams to drive PDIs. The strong microwave signals in Fig. 5.25 have a quasi-continuous structure with intermittent quiescent phases, matching what is expected if the second-harmonic UHR fluctuates around the plasma center. The strong microwave signals lead to a permanent ECE radiation temperature reduction of approximately 45 % for the channels covered by the low-frequency mixer, necessitating a recalibration.

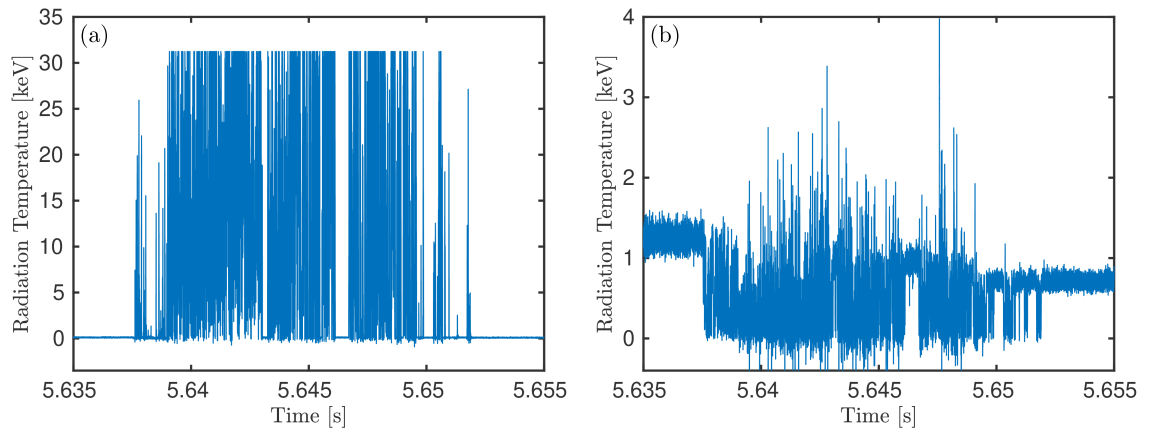


Figure 5.25 – Degradation of ECE mixer during central PDI in ASDEX Upgrade #36149. Pane (a) shows the signal from a channel around 75.5 GHz; pane (b) shows the signal from a channel around 87.9 GHz.

Chapter 6

Parametric Decay Instabilities near the Upper Hybrid Resonance

With the PDI of trapped waves for a pump wave near the second-harmonic UHR considered, we now return to the more classical case of PDIs in which the pump wave is itself close to the UHR. As was noted in Chapter 2, the UHR is a resonance for cold X-mode waves, and such waves therefore undergo strong field enhancement near the UHR. A relatively simple model of this field enhancement, based on the uniform approximation, was presented in Section 3.3 and found to be in qualitative agreement with a numerical 1D model of the enhancement of cold X-mode waves near the UHR, which is utilized in the present Chapter. While the field enhancement of X-mode waves near the UHR means that the PDI threshold can be exceeded for relatively low beam powers (~ 10 kW in ASDEX Upgrade), the UHR is not directly accessible to X-mode radiation launched from the low-field side of the torus, since such radiation will encounter the R-cutoff before reaching the UHR (see Fig. 2.1). If the evanescence region between the R-cutoff and the UHR is small, it is possible for the X-mode radiation to tunnel through it and reach the UHR [129]. However, in medium-sized and large tokamaks, the evanescence region is too broad for tunneling to be effective. In order for X-mode radiation to reach the UHR and drive PDIs, it is thus necessary to either launch X-mode radiation from the high-field side [162, 163, 164] or inject O-mode radiation from the low-field side which is subsequently converted to X-mode radiation [165, 164, 166, 167, 168, 169, 170, 109, 15, 13, 19, 14]. When X-mode radiation is launched from the high-field side, it must pass through the ECR before reaching the UHR (see Fig. 2.1), imposing the additional constraint that the ECR should not be optically thick for the X-mode radiation if PDIs are to occur, which was the case in the relatively small tokamaks where such experiments have been performed [162, 163, 164]. Two main schemes for converting O-mode radiation to X-mode radiation capable of reaching the UHR exist: reflection from the high-field side vessel wall (or a polarizing mirror on the high-field side vessel wall) and O-X-B heating.

O-X-B heating is a scheme for heating overdense plasmas ($\omega_{pe} > |\omega_{ce}|$ at the plasma center), which are particularly prevalent in stellarators and spherical tokamaks. It involves injecting

O-mode radiation at a particular angle, such that the maximal fraction of the injected radiation is converted to X-mode upon reflection from the O-mode cutoff ($\omega_0 = \omega_{pe}$). The reflected X-mode radiation then reaches the UHR without passing the ECR, resulting in PDIs [166, 167, 168], although the bulk of the X-mode power is converted linearly to EBWs, which are not limited by the electromagnetic cutoffs, allowing them to be absorbed at the ECR or one of its harmonics.

The ASDEX Upgrade plasmas considered in this work are underdense, so no O-X-B heating has been performed to study PDIs at the UHR. The standard 105 GHz O-mode CTS scenario does, however, operate with the ECR far on the high-field side (and none of its harmonics in the plasma) to minimize the ECE background. This allows a significant fraction of the injected O-mode radiation to reach the high-field side wall, where it is reflected and partially converted to X-mode. If a significant fraction of the reflected X-mode radiation is transmitted by the ECR, the X-mode power reaching the UHR can be sufficient to drive PDIs [15, 18, 13, 19, 14]. The above mechanism is responsible for the generation of strong signals hampering CTS at ASDEX Upgrade and is hence studied in detail in the present Chapter. We note that a similar mechanism may be responsible for hampering CTS at the LHD stellarator [170], and that PDIs at the UHR for reflected ECRH radiation were observed at the Wendelstein VII-A stellarator [165] and the TCA tokamak [164]. Before discussing the specific PDIs of interest in this Chapter, we also note that (oblique) O-mode radiation may itself drive PDIs at the UHR in the presence of a non-monotonic density profile allowing trapping of an EBW/X-mode wave pair [157]. Such PDIs have recently been observed to cause anomalous absorption of 20 % of the injected O-mode ECRH power in a low-temperature plasma filament [161]. Since such PDIs occur during O-mode ECRH at the fundamental ECR, they could potentially have a significant impact on the ECRH performance during NTMs at ITER; present experiments at the FTU tokamak have, however, yielded few conclusive results regarding this concern [158].

The primary PDI at the UHR is expected to be decay of the X-mode pump wave to an EBW and a (low-frequency) LH wave based on theoretical considerations [137, 171, 143, 138, 18, 13]. This is in agreement with the experimental evidence [162, 165, 163, 164, 166, 167, 168, 170, 15, 18, 13, 14] and numerical simulations [172, 173, 174, 17]. The threshold of the primary PDI expected theoretically [13] is further found to be in agreement with the experimental threshold obtained by analog modulation of the gyrotron power at ASDEX Upgrade [14], and recent particle-in-cell simulations of a plasma with parameters similar to those of an ASDEX Upgrade plasma [17] are also found to yield a primary PDI threshold in agreement with [13]. Secondary PDIs occurring near the UHR at ASDEX Upgrade are indicated to be decay of the primary daughter EBWs to secondary daughter EBWs and second-order IBWs based on the gyrotron modulation experiments [14], which further indicate a tertiary PDI in the form of decay of the X-mode pump wave to EBWs and arbitrary-order IBWs.

Since the results described above have been presented in detail in [13, 14] as a part of the present PhD project and are based on a somewhat different PDI framework than the one presented in this work, we include [13, 14] in their entirety below. As indicated by the above discussion, [13] mainly deals with the theoretical background and a preliminary experiment

(#28286) at ASDEX Upgrade, while [14] demonstrates the experimental validity of the theoretical thresholds and the occurrence of secondary and tertiary PDIs in an ASDEX Upgrade discharge (#34575) with a sweep of B_t and analog modulation of the gyrotron power.

Parametric decay instability near the upper hybrid resonance in magnetically confined fusion plasmas

S K Hansen^{1,2}, S K Nielsen², M Salewski² , M Stejner², J Stober¹ and the ASDEX Upgrade team¹

¹Max-Planck-Institut für Plasmaphysik, Boltzmannstraße, D-85748 Garching bei München, Germany

²Department of Physics, Technical University of Denmark, Fysikvej, DK-2800 Kgs. Lyngby, Denmark

E-mail: Soeren.Kjer.Hansen@ipp.mpg.de

Received 3 April 2017, revised 22 May 2017

Accepted for publication 14 June 2017

Published 11 August 2017



CrossMark

Abstract

In this paper we investigate parametric decay of an electromagnetic pump wave into two electrostatic daughter waves, particularly an X-mode pump wave decaying into a warm upper hybrid wave (a limit of an electron Bernstein wave) and a warm lower hybrid wave. We describe the general theory of the above parametric decay instability (PDI), unifying earlier treatments, and show that it may occur in underdense and weakly overdense plasmas. The PDI theory is used to explain anomalous sidebands observed in collective Thomson scattering (CTS) spectra at the ASDEX Upgrade tokamak. The theory may also account for similar observations during CTS experiments in stellarators, as well as in some 1st harmonic electron cyclotron resonance and O-X-B heating experiments.

Keywords: PDI, UHR, UH, LH, CTS, ECRH, electron Bernstein wave

(Some figures may appear in colour only in the online journal)

1. Introduction

A parametric decay instability (PDI) is the result of three-wave interactions by which an incident (pump) wave decays to two daughter waves. PDIs may occur in some media under the influence of pump radiation with sufficiently high energy density, e.g. in plasmas heated/diagnosed by gyrotron radiation. Energy and momentum conservation in the three-wave processes impose the selection rules that the sum of the daughter wave frequencies and wave vectors should be that of the pump wave, resulting in frequency-shifted radiation which interferes with millimetre-wave diagnostics such as electron cyclotron (EC) emission and collective Thomson scattering (CTS). This is of particular concern in future fusion reactors which cannot be easily diagnosed by other means. In this work we focus on parametric decay of an electromagnetic pump wave into two electrostatic daughter waves, specifically the case of an X-mode pump wave decaying into a warm upper hybrid (UH) wave (a limiting form of an electron Bernstein wave) and a warm lower hybrid (LH) wave near the

upper hybrid resonance (UHR) of the pump wave. We generalise the results of [1–3] and discuss their relation to other treatments [4, 5]. The main motivation is observations of strong PDI-like sidebands during CTS experiments at the ASDEX Upgrade tokamak [6] and the LHD stellarator [7, 8].

Early PDI theory for unmagnetised and magnetised plasmas was pioneered by [9, 10] and extended to include collisional effects, which usually determine the PDI threshold in homogeneous plasmas, by [11]. Piliya and Rosenbluth separately showed that the PDI threshold could be significantly higher for an inhomogeneous plasma due to convective losses of the daughter waves from the region where the PDI selection rules are satisfied [12–14]. The above results indicate that PDIs are only likely to occur near resonances, e.g. the UHR, and cut-offs of the pump radiation at the gyrotron powers available in typical experiments, due to field enhancement effects in these regions [15]. An important exception to this rule, which has received some attention recently, occurs in regions of non-monotonic plasma profiles where the daughter waves may become trapped, reducing the

PDI threshold to a level closer to that of a homogeneous plasma [16]; the backscattering instability is another example of this type [17].

PDI near the UHR have been studied theoretically by a number of authors. The first work on direct parametric decay of an electromagnetic pump wave into warm UH waves and LH waves was [4], which found the growth rate of this PDI in the limit of long daughter wave wavelengths relative to the ion Larmor radius, a condition rarely satisfied in magnetically confined fusion plasmas. Direct parametric decay of an electromagnetic pump wave into a warm UH wave and a strongly damped low-frequency electrostatic quasi-mode, which is particularly relevant in tokamaks, was first considered by Ott, Hui and Chu [18] who concluded that it would be unlikely to occur for gyrotron radiation. However, their treatment neglected field enhancement effects and used a non-standard parametric dispersion relation. Using the standard parametric dispersion relation, and accounting roughly for field enhancement near the UHR, Porkolab [2] showed that the PDI in which an X-mode pump wave decays into a warm UH wave in which an X-mode pump wave decays into a warm UH wave and an LH quasi-mode could occur during 1st harmonic X-mode EC resonance heating (ECRH) on the Versator II tokamak, as later confirmed experimentally [3]. The theoretical part of the present paper mainly deals with generalising the results from [1–3]. Further theoretical work on direct parametric decay of electromagnetic pump waves to electrostatic daughter waves near the UHR is presented in [5, 19, 20]. Other theoretical papers focus on parametric decay of warm UH waves, generated by linear mode conversion, into other warm UH waves and electrostatic low-frequency waves [17, 21] or into electromagnetic high-frequency waves and electrostatic low-frequency (LH) waves [22, 23]. Many of the theoretical results have been reproduced in numerical simulations [24–27].

A PDI at the UHR was first observed in mercury vapour tube discharges through the excitation of LH oscillations by sufficiently strong microwave radiation [28]. Similar observations were reported for linear hot-cathode helium discharges [29] and the FM-I spherator [30]. This type of PDI was also observed in connection with 1st harmonic ECRH of optically thin plasmas in the Versator II, FT-1 and TCA tokamaks [3, 31, 32], as well as in the Wendelstein 7-A stellarator [33, 34]. These results were reviewed by [35, 36]. In ionospheric modification experiments, the presence of a so-called down-shifted maximum feature in the stimulated electromagnetic emission spectra has been attributed to a related PDI [23]. PDIs near the UHR involving LH daughter waves have additionally been used to confirm the occurrence of O-X-B heating in overdense plasmas of the Wendelstein 7-AS stellarator [37, 38] and the MAST spherical tokamak [39].

This paper is arranged as follows. In section 2, we review the general theory of PDIs for electromagnetic pump waves decaying into electrostatic daughter waves in a homogeneous plasma and its generalisation to weakly inhomogeneous plasmas, providing a unified treatment and re-examining the existing literature. In section 3, we specialise to PDIs near the UHR, investigating the conditions under which these may occur and generalising the theories of parametric decay into

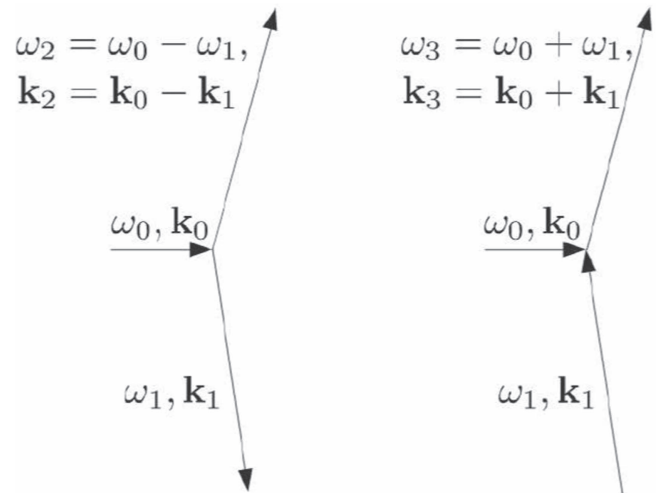


Figure 1. Diagrams showing the most important parametric three-wave processes; to the left, decay of the pump wave (ω_0, \mathbf{k}_0) into a low-frequency wave (ω_1, \mathbf{k}_1) and a down-shifted high-frequency wave ($\omega_2 = \omega_0 - \omega_1, \mathbf{k}_2 = \mathbf{k}_0 - \mathbf{k}_1$); to the right, scattering of the pump wave by a low-frequency wave exciting an up-shifted high-frequency wave ($\omega_3 = \omega_0 + \omega_1, \mathbf{k}_3 = \mathbf{k}_0 + \mathbf{k}_1$).

warm UH and warm LH waves of [1–3]. Finally, we investigate the above PDI in ASDEX Upgrade and compare the theoretical predictions with experimentally observed CTS spectra in section 4.

2. PDI theory

In this section we present the basic theory of parametric decay of an electromagnetic pump wave to electrostatic daughter waves in a magnetised plasma. Apart from allowing us to introduce the concepts needed when discussing PDIs near the UHR, this is motivated by the existence of large number of different, not always consistent, treatments in the literature, e.g. [4, 5, 10, 11, 18–20, 35, 40], which seem to warrant some discussion and clarification. Our treatment follows that of [1] quite closely.

The main parametric three-wave processes are decay of the pump wave into two daughter waves and scattering of the pump wave by one of the daughter waves, as illustrated in figure 1; PDIs are associated with the decay process, but in order to interpret PDI spectra, and to have a complete theory, it is necessary to consider the scattering process as well. Processes involving more than three waves may also occur, but these represent higher-order effects. Energy and momentum conservation in the three-wave processes impose selection rules for the frequencies, ω , and wave vectors, \mathbf{k} , of the involved waves,

$$\begin{aligned} \omega_2 &= \omega_0 - \omega_1, & \mathbf{k}_2 &= \mathbf{k}_0 - \mathbf{k}_1, \\ \omega_3 &= \omega_0 + \omega_1, & \mathbf{k}_3 &= \mathbf{k}_0 + \mathbf{k}_1, \end{aligned} \quad (1)$$

where subscript 0 refers to the pump wave, subscript 1 refers to the low-frequency daughter wave, and subscripts 2 and 3 refer to the down- and up-shifted high-frequency daughter

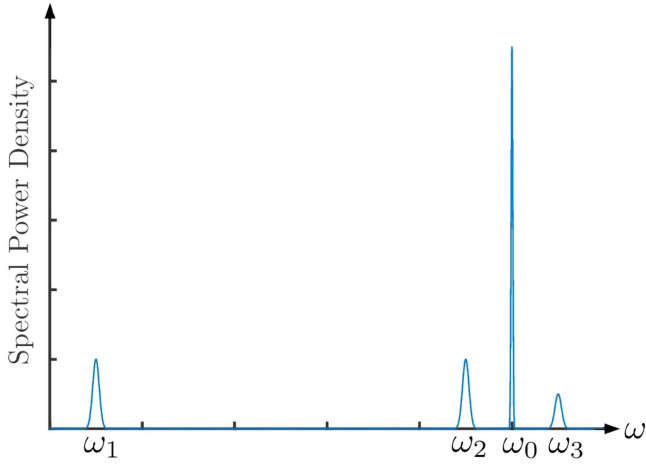


Figure 2. Idealised frequency power spectrum excited by a PDI. Apart from the pump peak (ω_0), a low-frequency daughter peak (ω_1) and high-frequency daughter peaks, one down-shifted (ω_2) and one up-shifted (ω_3), occur. Peaks are generally observed when ω_1 , ω_2 and ω_3 coincide with linear modes.

waves, respectively. A PDI will generally only occur if the selection rules can be satisfied by linear modes of the plasma, as the pump power necessary for a PDI to occur under normal circumstances increases with the damping rate of the daughter waves; however, in some cases the low-frequency daughter wave may be a heavily damped quasi-mode. The above considerations lead to an idealised PDI frequency spectrum, seen in figure 2, which is a hallmark of PDIs.

2.1. Motion of an electromagnetically driven plasma particle

To describe the PDI of interest we first consider the motion of a single plasma particle with mass m_σ and charge q_σ , located at position $\mathbf{r}(t)$ and moving with a velocity $\mathbf{v}(t) = d\mathbf{r}(t)/dt$ at time t . The particle is acted on by a steady homogeneous magnetic field \mathbf{B} and a plane electromagnetic pump wave with an electric field $\text{Re}[\mathbf{E}_0 e^{i\mathbf{k}_0 \cdot \mathbf{r}(t) - \omega_0 t}]$ and a magnetic field $\text{Re}[\mathbf{B}_0 e^{i\mathbf{k}_0 \cdot \mathbf{r}(t) - \omega_0 t}]$. We assume the particle to be non-relativistic and invoke the dipole approximation for the electromagnetic pump wave, $\mathbf{k}_0 \approx \mathbf{0}$, which allows us to neglect the effect of the wave magnetic field and to write the wave electric field as $\text{Re}(\mathbf{E}_0 e^{-i\omega_0 t})$; the dipole approximation is generally permissible due to the high phase velocity (long wavelength) of the electromagnetic pump wave compared with the electrostatic daughter waves, but may be relaxed if necessary [19]. Taking the background magnetic field along the z -axis, $\mathbf{B} = B\mathbf{e}_z$, the equation of motion becomes

$$\frac{d\mathbf{v}(t)}{dt} = \omega_{c\sigma} \mathbf{v}(t) \times \mathbf{e}_z + \text{Re} \left(\frac{q_\sigma \mathbf{E}_0}{m_\sigma} e^{-i\omega_0 t} \right), \quad (2)$$

where $\omega_{c\sigma} = q_\sigma B/m_\sigma$ is the cyclotron frequency (with sign) of species σ . (2) is a set of inhomogeneous, linear, ordinary differential equations, the general solution of which is a given by a particular solution of the inhomogeneous problem and a general solution of the homogeneous problem. The general homogeneous solution is cyclotron motion of the particle in

a constant magnetic field, i.e. the characteristics used for determining the linear response of a collisionless plasma. PDIs originate from the particular inhomogeneous solution which can be found by substituting the ansatz $\mathbf{v}_{p\sigma}(t) = \text{Re}(\mathbf{v}_{p0\sigma} e^{-i\omega_0 t})$ into (2), solving for $\mathbf{v}_{p0\sigma}$, and integrating once more with respect to t , looking for a solution of the form $\mathbf{r}_{p\sigma}(t) = \text{Re}(\mathbf{r}_{p0\sigma} e^{-i\omega_0 t})$,

$$\mathbf{r}_{p\sigma}(t) = \text{Re} \left(\frac{i\mathbf{v}_{p0\sigma}}{\omega_0} e^{-i\omega_0 t} \right),$$

$$\mathbf{v}_{p0\sigma} = \frac{q_\sigma}{m_\sigma} \begin{bmatrix} (i\omega_0 E_{0x} - \omega_{c\sigma} E_{0y}) / (\omega_0^2 - \omega_{c\sigma}^2) \\ (\omega_{c\sigma} E_{0x} + i\omega_0 E_{0y}) / (\omega_0^2 - \omega_{c\sigma}^2) \\ E_{0z} / \omega_0 \end{bmatrix}. \quad (3)$$

The free energy responsible for driving PDIs is the kinetic energy associated with this motion. The complex displacement vector, $\mathbf{r}_{p0\sigma} = i\mathbf{v}_{p0\sigma}/\omega_0$, agrees with the one given in (3) of [19] for electrons.

2.2. Kinetic theory of PDIs in homogeneous plasmas

The goal of this section is to derive the temporal PDI growth rate, γ , for the case of small amplitude electrostatic daughter waves in a homogeneous, charge neutral plasma. This problem has previously been considered by a number of authors, e.g. in [4, 5, 10, 11, 18, 35, 40], and we shall point out when our results agree/disagree with some of this earlier work. PDIs with electrostatic daughter waves are governed by the Boltzmann–Poisson system with external fields $\mathbf{B} = B\mathbf{e}_z$ and $\text{Re}(\mathbf{E}_0 e^{-i\omega_0 t})$,

$$\frac{\partial f_\sigma(\mathbf{r}, \mathbf{v}, t)}{\partial t} + \mathbf{v} \cdot \frac{\partial f_\sigma(\mathbf{r}, \mathbf{v}, t)}{\partial \mathbf{r}} + \left[-\frac{q_\sigma}{m_\sigma} \frac{\partial \phi(\mathbf{r}, t)}{\partial \mathbf{r}} + \omega_{c\sigma} \mathbf{v} \times \mathbf{e}_z + \text{Re} \left(\frac{q_\sigma \mathbf{E}_0}{m_\sigma} e^{-i\omega_0 t} \right) \right] \cdot \frac{\partial f_\sigma(\mathbf{r}, \mathbf{v}, t)}{\partial \mathbf{v}} = \left[\frac{\partial f_\sigma(\mathbf{r}, \mathbf{v}, t)}{\partial t} \right]_{\text{col}}, \quad (4)$$

$$\frac{\partial}{\partial \mathbf{r}} \cdot \frac{\partial \phi(\mathbf{r}, t)}{\partial \mathbf{r}} = -\frac{1}{\epsilon_0} \sum_\sigma q_\sigma n_\sigma(\mathbf{r}, t), \quad (5)$$

where $f_\sigma(\mathbf{r}, \mathbf{v}, t)$ is the distribution function of species σ , $n_\sigma(\mathbf{r}, t) = \int_{\text{all } \mathbf{v}} f_\sigma(\mathbf{r}, \mathbf{v}, t) d\mathbf{v}$ is the number density of species σ , $\phi(\mathbf{r}, t)$ is the electrostatic potential associated with the daughter waves, $[\partial f_\sigma(\mathbf{r}, \mathbf{v}, t)/\partial t]_{\text{col}}$ is the collision operator of species σ , and ϵ_0 is the vacuum permittivity. Evidently, the pump wave introduces an explicit dependence on t which makes the above equations more complicated than the usual Boltzmann–Poisson system in a magnetised plasma. However, by going into frames oscillating with the velocity induced by the pump wave for each species σ , $\mathbf{v}_{p\sigma}(t)$, inertial forces will cancel the explicitly t -dependent pump term, $\text{Re}[(q_\sigma \mathbf{E}_0/m_\sigma) e^{-i\omega_0 t}]$. In these frames the position is defined as $\mathbf{x} = \mathbf{r} - \mathbf{r}_{p\sigma}(t)$, the velocity is defined as $\mathbf{u} = \mathbf{v} - \mathbf{v}_{p\sigma}(t)$, and the Boltzmann equation becomes

$$\begin{aligned} & \frac{\partial F_\sigma(\mathbf{x}, \mathbf{u}, t)}{\partial t} + \mathbf{u} \cdot \frac{\partial F_\sigma(\mathbf{x}, \mathbf{u}, t)}{\partial \mathbf{x}} \\ & + \left[-\frac{q_\sigma}{m_\sigma} \frac{\partial \Phi_\sigma(\mathbf{x}, t)}{\partial \mathbf{x}} + \omega_{c\sigma} \mathbf{u} \times \mathbf{e}_z \right] \\ & \cdot \frac{\partial F_\sigma(\mathbf{x}, \mathbf{u}, t)}{\partial \mathbf{u}} = \left[\frac{\partial F_\sigma(\mathbf{x}, \mathbf{u}, t)}{\partial t} \right]_{\text{col}}, \end{aligned} \quad (6)$$

where $F_\sigma(\mathbf{x}, \mathbf{u}, t) = f_\sigma(\mathbf{r}, \mathbf{v}, t)$ is the distribution function, $\Phi_\sigma(\mathbf{x}, t) = \phi(\mathbf{r}, t)$ is the electrostatic potential associated with the daughter waves, and $[\partial F_\sigma(\mathbf{x}, \mathbf{u}, t)/\partial t]_{\text{col}} = [\partial f_\sigma(\mathbf{r}, \mathbf{v}, t)/\partial t]_{\text{col}}$ is the collision operator, all in the frame of species σ . This is a standard form of the Boltzmann equation used in the kinetic description of electrostatic waves. Since we are assuming the amplitude of the daughter waves to be small and the unperturbed plasma to be homogeneous and charge neutral, we can carry through an order 1 perturbation analysis for electrostatic waves in which we take $F_\sigma(\mathbf{x}, \mathbf{u}, t) = F_\sigma^{(0)}(\mathbf{u}) + F_\sigma^{(1)}(\mathbf{x}, \mathbf{u}, t)$, $\Phi_\sigma(\mathbf{x}, t) = \Phi_\sigma^{(1)}(\mathbf{x}, t)$, and neglect products of the perturbation terms with superscript (1). The general result of this procedure is a local, linear relation between the Fourier–Laplace transforms of the perturbed number density $N_\sigma^{(1)}(\mathbf{x}, t) = \int_{\text{all } \mathbf{u}} F_\sigma^{(1)}(\mathbf{x}, \mathbf{u}, t) d\mathbf{u}$ and $\Phi_\sigma(\mathbf{x}, t)$. Defining the Fourier–Laplace transform as $\tilde{g}(\mathbf{k}, \omega) = \int_{\text{all } \mathbf{x}} \int_0^\infty g(\mathbf{x}, t) e^{i\omega t - i\mathbf{k} \cdot \mathbf{x}} dt d\mathbf{x}$, with \mathbf{k} being a real wave vector and ω being a complex frequency related to a particular daughter wave mode, we may thus write

$$q_\sigma \tilde{N}_\sigma^{(1)}(\mathbf{k}, \omega) = -\epsilon_0 k^2 \chi_\sigma(\mathbf{k}, \omega) \tilde{\Phi}_\sigma(\mathbf{k}, \omega), \quad (7)$$

where $\chi_\sigma(\mathbf{k}, \omega)$ is the linear susceptibility of species σ for the mode characterised by (\mathbf{k}, ω) ; in writing this, we have set the perturbations to zero at $t = 0$. The temporal growth rate of the PDI in a homogeneous plasma is given by the imaginary part of ω , $\gamma = \text{Im}(\omega)$, and is the quantity in which we are ultimately interested. $\chi_\sigma(\mathbf{k}, \omega)$ is determined by $F_\sigma^{(0)}(\mathbf{u})$ and $[\partial F_\sigma(\mathbf{x}, \mathbf{u}, t)/\partial t]_{\text{col}}$, which are considered to be a Maxwellian distribution and a particle conserving Krook collision operator in this paper:

$$\begin{aligned} F_\sigma^{(0)}(\mathbf{u}) &= \frac{N_\sigma^{(0)}}{\pi^{3/2} v_{T\sigma}^3} e^{-u^2/v_{T\sigma}^2}, \quad \left[\frac{\partial F_\sigma(\mathbf{x}, \mathbf{u}, t)}{\partial t} \right]_{\text{col}} \\ &= \nu_\sigma \left[\frac{N_\sigma^{(1)}(\mathbf{x}, t)}{N_\sigma^{(0)}} F_\sigma^{(0)}(\mathbf{u}) - F_\sigma^{(1)}(\mathbf{x}, \mathbf{u}, t) \right], \end{aligned} \quad (8)$$

where $N_\sigma^{(0)}$ is the unperturbed number density of species σ , $v_{T\sigma} = \sqrt{2T_\sigma/m_\sigma}$ is the thermal velocity of species σ , with temperature T_σ , and ν_σ is a phenomenological collision frequency of species σ , which we shall equate with the Coulomb collision frequency of species σ , as is customary [41]. For the above $F_\sigma^{(0)}(\mathbf{u})$ and $[\partial F_\sigma(\mathbf{x}, \mathbf{u}, t)/\partial t]_{\text{col}}$, $\chi_\sigma(\mathbf{k}, \omega)$ becomes [11],

$$\begin{aligned} \chi_\sigma(\mathbf{k}, \omega) &= \frac{2\omega_{p\sigma}^2}{k^2 v_{T\sigma}^2} \\ &\times \frac{1 + \frac{\omega + i\nu_\sigma}{k_z v_{T\sigma}} \sum_{n=-\infty}^{\infty} I_n(k_\perp^2 r_{L\sigma}^2) e^{-k_\perp^2 r_{L\sigma}^2} Z\left(\frac{\omega + i\nu_\sigma - n\omega_{c\sigma}}{k_z v_{T\sigma}}\right)}{1 + \frac{i\nu_\sigma}{k_z v_{T\sigma}} \sum_{n=-\infty}^{\infty} I_n(k_\perp^2 r_{L\sigma}^2) e^{-k_\perp^2 r_{L\sigma}^2} Z\left(\frac{\omega + i\nu_\sigma - n\omega_{c\sigma}}{k_z v_{T\sigma}}\right)}, \end{aligned} \quad (9)$$

with $k_\perp^2 = k_x^2 + k_y^2$ being the wave number perpendicular to \mathbf{B} , $\omega_{p\sigma}^2 = q_\sigma^2 N_\sigma^{(0)}/(\epsilon_0 m_\sigma)$ being the plasma frequency of species σ , $r_{L\sigma} = v_{T\sigma}/(\sqrt{2}|\omega_{c\sigma}|)$ defining the Larmor radius of species σ , I_n being the order n modified Bessel function of the 1st kind, and Z being the Fried–Conte plasma dispersion function. In case of the ions we shall also employ $\chi_\sigma(\mathbf{k}, \omega)$ for an unmagnetised plasma with the same $F_\sigma^{(0)}(\mathbf{u})$ and $[\partial F_\sigma(\mathbf{x}, \mathbf{u}, t)/\partial t]_{\text{col}}$ [41],

$$\chi_\sigma(\mathbf{k}, \omega) = \frac{2\omega_{p\sigma}^2}{k^2 v_{T\sigma}^2} \frac{1 + \frac{\omega + i\nu_\sigma}{k v_{T\sigma}} Z\left(\frac{\omega + i\nu_\sigma}{k v_{T\sigma}}\right)}{1 + \frac{i\nu_\sigma}{k v_{T\sigma}} Z\left(\frac{\omega + i\nu_\sigma}{k v_{T\sigma}}\right)}; \quad (10)$$

the justification for this is discussed in section 3.2.

The problem now is to express $\tilde{\Phi}_\sigma(\mathbf{k}, \omega)$, which is evaluated in a different frame for each species, in terms of the potential in the lab frame. This may be done by using the definition of the Fourier–Laplace transform to write,

$$\begin{aligned} \tilde{\Phi}_\sigma(\mathbf{k}, \omega) &= \int_{\text{all } \mathbf{x}} \left[\int_0^\infty \Phi_\sigma(\mathbf{x}, t) e^{i\omega t - i\mathbf{k} \cdot \mathbf{x}} dt \right] d\mathbf{x} \\ &= \int_{\text{all } \mathbf{r}} \left[\int_0^\infty \phi(\mathbf{r}, t) e^{i\omega t + i\mathbf{k} \cdot \mathbf{r}_{p\sigma}(t)} dt \right] e^{-i\mathbf{k} \cdot \mathbf{r}} d\mathbf{r}, \end{aligned} \quad (11)$$

which reduces the problem to evaluating $e^{i\mathbf{k} \cdot \mathbf{r}_{p\sigma}(t)}$ and the Fourier–Laplace integrals. Evaluation of $e^{i\mathbf{k} \cdot \mathbf{r}_{p\sigma}(t)}$ is facilitated by noting that, from (3) and the fact that \mathbf{k} is real, $\mathbf{k} \cdot \mathbf{r}_{p\sigma}(t) = \text{Re}[i(\mathbf{k} \cdot \mathbf{v}_{p0\sigma}/\omega_0) e^{-i\omega_0 t}] = \mu_\sigma \sin(\omega_0 t - \beta_\sigma)$, where μ_σ and β_σ are the amplitude and phase angle of $\mathbf{k} \cdot \mathbf{v}_{p0\sigma}/\omega_0$, respectively. Using a Fourier series identity, we then find $e^{i\mathbf{k} \cdot \mathbf{r}_{p\sigma}(t)} = e^{i\mu_\sigma \sin(\omega_0 t - \beta_\sigma)} = \sum_{n=-\infty}^{\infty} J_n(\mu_\sigma) e^{in(\omega_0 t - \beta_\sigma)}$, where J_n is the order n Bessel function of the 1st kind. With this, the Fourier–Laplace integrals of (11) may be evaluated, and (7) written as

$$\begin{aligned} q_\sigma \tilde{N}_\sigma^{(1)}(\mathbf{k}, \omega) &= -\epsilon_0 k^2 \chi_\sigma(\mathbf{k}, \omega) \\ &\times \sum_{n=-\infty}^{\infty} J_n(\mu_\sigma) e^{-in\beta_\sigma} \tilde{\phi}(\mathbf{k}, \omega + n\omega_0). \end{aligned} \quad (12)$$

By Fourier–Laplace transforming the Poisson equation with a charge neutral unperturbed plasma, $(\partial/\partial \mathbf{r}) \cdot \partial \phi(\mathbf{r}, t)/\partial \mathbf{r} = -(1/\epsilon_0) \sum_\sigma q_\sigma N_\sigma^{(1)}(\mathbf{r} - \mathbf{r}_{p\sigma}(t), t)$, we similarly find

$$\tilde{\phi}(\mathbf{k}, \omega) = \frac{1}{\epsilon_0 k^2} \sum_\sigma \sum_{n=-\infty}^{\infty} J_n(-\mu_\sigma) e^{-in\beta_\sigma} q_\sigma \tilde{N}_\sigma^{(1)}(\mathbf{k}, \omega + n\omega_0). \quad (13)$$

(12) and (13) constitute a set of linear equations describing the coupling between various electrostatic Fourier–Laplace modes due to the pump wave. These equations form a general basis for the theory of PDIs with small amplitude electrostatic daughter waves in a homogeneous plasma within the dipole approximation. They were also derived or used as a starting point by [11, 35, 40]; [11] generalised the result to inhomogeneous plasmas. $\mu_\sigma = |\mathbf{k} \cdot \mathbf{v}_{p0\sigma}|/\omega_0$ describes the coupling strength between different Fourier–Laplace modes and is a central quantity in PDI theory; inserting $\mathbf{v}_{p0\sigma}$ from (3),

$$\mu_\sigma = \frac{|q_\sigma|}{m_\sigma \omega_0^2} \sqrt{\left[\frac{\text{Im}(k_x E_{0x} + k_y E_{0y}) + (\omega_{c\sigma}/\omega_0) \text{Re}(k_x E_{0y} - k_y E_{0x})}{1 - (\omega_{c\sigma}/\omega_0)^2} + k_z \text{Im}(E_{0z}) \right]^2 + \left[\frac{\text{Re}(k_x E_{0x} + k_y E_{0y}) - (\omega_{c\sigma}/\omega_0) \text{Im}(k_x E_{0y} - k_y E_{0x})}{1 - (\omega_{c\sigma}/\omega_0)^2} + k_z \text{Re}(E_{0z}) \right]^2}, \quad (14)$$

which shows the general proportionality to $|q_\sigma E_0|k/(m_\sigma \omega_0^2)$, as well as the dependence on polarisation of the pump wave, the direction of \mathbf{k} and $\omega_{c\sigma}/\omega_0$, for the coupling between electrostatic Fourier–Laplace modes at different frequencies in the presence of the pump wave. β_σ in (12) and (13) does not have any particular physical significance and may be changed by shifting point at which $t = 0$. It is clear from (12) and (13) that only modes differing by integer multiples of ω_0 interact. This is a manifestation of the frequency selection rule for parametric processes; in particular, the three-wave interactions are related to the $n = \pm 1$ terms. No coupling between modes with different \mathbf{k} exists due to the dipole approximation, $\mathbf{k}_0 \approx \mathbf{0}$. To recover the selection rules of (1) from the above equations, we use the fact that the requirement of real $\phi(\mathbf{r}, t)$ and $N_\sigma^{(1)}(\mathbf{x}, t)$ results in $\tilde{\phi}(\mathbf{k}, \omega) = \tilde{\phi}^*(-\mathbf{k}, -\omega^*)$, $\tilde{N}_\sigma^{(1)}(\mathbf{k}, \omega) = \tilde{N}_\sigma^{(1)*}(-\mathbf{k}, -\omega^*)$ and $\chi_\sigma(\mathbf{k}, \omega) = \chi_\sigma^*(-\mathbf{k}, -\omega^*)$, allowing the signs of \mathbf{k} and $\text{Re}(\omega)$ to be changed for any given mode.

Specialising (12) and (13) to the case of an electron ($\sigma = e$) and ion ($\sigma = i$) plasma, when $\omega_{ci}/\omega_0 \approx 1$ for any ionic species, we find $\mu_i/\mu_e \leq O(m_e/m_i) \ll 1$ which allows us assume a linear ion response, $\mu_i \approx 0$, for moderate values of μ_e . With this, $J_n(\pm\mu_i) = \delta_{n0}$, and (12) and (13) become

$$\sum_i Z_i \tilde{N}_i^{(1)}(\mathbf{k}, \omega) = -\frac{\epsilon_0 k^2}{e} \sum_i \chi_i(\mathbf{k}, \omega) \tilde{\phi}(\mathbf{k}, \omega), \quad (15)$$

$$\tilde{N}_e^{(1)}(\mathbf{k}, \omega) = \frac{\epsilon_0 k^2}{e} \chi_e(\mathbf{k}, \omega) \sum_{n=-\infty}^{\infty} J_n(\mu_e) e^{-in\beta_e} \tilde{\phi}(\mathbf{k}, \omega + n\omega_0) \quad (16)$$

$$\tilde{\phi}(\mathbf{k}, \omega) = \frac{e}{\epsilon_0 k^2} \left[\sum_i Z_i \tilde{N}_i^{(1)}(\mathbf{k}, \omega) - \sum_{m=-\infty}^{\infty} J_m(-\mu_e) \times e^{-im\beta_e} \tilde{N}_e^{(1)}(\mathbf{k}, \omega + m\omega_0) \right], \quad (17)$$

where e is the elementary charge, $Z_i = q_i/e$ is the charge number of the ionic species i , and all ionic terms of (12) have been summed. As the unknown quantities in the above equations are $\sum_i Z_i \tilde{N}_i^{(1)}(\mathbf{k}, \omega + n\omega_0)$, $\tilde{N}_e^{(1)}(\mathbf{k}, \omega + n\omega_0)$ and $\tilde{\phi}(\mathbf{k}, \omega + n\omega_0)$, the addition of multiple ionic species does not complicate the problem with a linear ion response, provided that $\chi_{i,e}(\mathbf{k}, \omega)$ may still be determined. Substituting (17) into (15) and (16), and using Neumann's addition theorem to simplify the double sum in (16), $\sum_{n=-\infty}^{\infty} \sum_{m=-\infty}^{\infty} J_n(\mu_e) J_m(-\mu_e) e^{-i(n+m)\beta_e} \tilde{N}_e^{(1)}(\mathbf{k}, \omega + (n+m)\omega_0) = \tilde{N}_e^{(1)}(\mathbf{k}, \omega)$, we find

$$\left[1 + \sum_i \chi_i(\mathbf{k}, \omega) \right] \sum_i Z_i \tilde{N}_i^{(1)}(\mathbf{k}, \omega) = \sum_i \chi_i(\mathbf{k}, \omega) \times \sum_{n=-\infty}^{\infty} J_n(-\mu_e) e^{-in\beta_e} \tilde{N}_e^{(1)}(\mathbf{k}, \omega + n\omega_0), \quad (18)$$

$$[1 + \chi_e(\mathbf{k}, \omega)] \tilde{N}_e^{(1)}(\mathbf{k}, \omega) = \chi_e(\mathbf{k}, \omega) \times \sum_{n=-\infty}^{\infty} J_n(\mu_e) e^{-in\beta_e} \sum_i Z_i \tilde{N}_i^{(1)}(\mathbf{k}, \omega + n\omega_0). \quad (19)$$

These equations constitute the general basis for describing PDIs with electrostatic daughter waves in electron–ion plasmas within the dipole approximation when $\omega_{ci} \neq \omega_0$. Similar equations were derived by [4, 11, 40]; the expressions in [11] additionally contain terms related to plasma inhomogeneities, and the double sum in (11) of [40] vanishes by Neumann's addition theorem.

In the limit of weak coupling, $\mu_e \ll 1$, (18) and (19) may be solved by considering only the ($n = 0, \pm 1$)-terms, giving a general parametric dispersion relation found in [4, 35, 40]; [4] only considers the ($n = 0, -1$)-terms. However, since we are interested in a gyrotron pump wave, which satisfies $\omega_0 \sim |\omega_{ce}| \gg \omega_{pi}, \omega_{ci}$, we can ignore the ion response at frequencies comparable to ω_0 , as was done by [10, 11]. Associating ω with the low-frequency daughter wave, we can thus write $\sum_i Z_i \tilde{N}_i^{(1)}(\mathbf{k}, \omega + n\omega_0) \approx \sum_i Z_i \tilde{N}_i^{(1)}(\mathbf{k}, \omega) \delta_{n0}$, with which (19) becomes

$$\tilde{N}_e^{(1)}(\mathbf{k}, \omega + n\omega_0) = \frac{\chi_e(\mathbf{k}, \omega + n\omega_0)}{1 + \chi_e(\mathbf{k}, \omega + n\omega_0)} J_{-n}(\mu_e) \times e^{in\beta_e} \sum_i Z_i \tilde{N}_i^{(1)}(\mathbf{k}, \omega). \quad (20)$$

Plugging this into (18), remembering that $J_n(-\mu_e)J_{-n}(\mu_e) = J_n^2(\mu_e)$, we arrive at a dispersion relation describing PDIs for pump waves of arbitrary amplitude in the EC frequency range,

$$1 + \sum_i \chi_i(\mathbf{k}, \omega) = \sum_i \chi_i(\mathbf{k}, \omega) \times \sum_{n=-\infty}^{\infty} J_n^2(\mu_e) \frac{\chi_e(\mathbf{k}, \omega + n\omega_0)}{1 + \chi_e(\mathbf{k}, \omega + n\omega_0)}, \quad (21)$$

also found in [10]. In the weak coupling limit, generally relevant to gyrotron radiation (which has power levels $\lesssim 1$ MW) [42], the Bessel functions may be Taylor expanded to order μ_e^2 ($J_0^2(\mu_e) \approx 1 - \mu_e^2/2$, $J_{\pm 1}^2(\mu_e) \approx \mu_e^2/4$, the

remaining terms are negligible), yielding

$$1 + \sum_i \chi_i(\mathbf{k}, \omega) + \chi_e(\mathbf{k}, \omega) = \frac{\mu_e^2}{4} \sum_i \chi_i(\mathbf{k}, \omega) \times \left[2 - \frac{1 + \chi_e(\mathbf{k}, \omega)}{1 + \chi_e(\mathbf{k}, \omega - \omega_0)} - \frac{1 + \chi_e(\mathbf{k}, \omega)}{1 + \chi_e(\mathbf{k}, \omega + \omega_0)} \right]; \quad (22)$$

the identity $-\chi_e(\mathbf{k}, \omega)/[1 + \chi_e(\mathbf{k}, \omega)] + \chi_e(\mathbf{k}, \omega \pm \omega_0)/[1 + \chi_e(\mathbf{k}, \omega \pm \omega_0)] = 1/[1 + \chi_e(\mathbf{k}, \omega)] - 1/[1 + \chi_e(\mathbf{k}, \omega \pm \omega_0)]$ has been used to rewrite the terms in the bracket on the right hand side. Introducing the dielectric function $\epsilon(\mathbf{k}, \omega) = 1 + \sum_i \chi_i(\mathbf{k}, \omega) + \chi_e(\mathbf{k}, \omega)$, noting that $\epsilon(\mathbf{k}, \omega \pm \omega_0) \approx 1 + \chi_e(\mathbf{k}, \omega \pm \omega_0)$, and neglecting the first term in the bracket on the right hand side of (22), we arrive at the weak coupling parametric dispersion relation,

$$\epsilon(\mathbf{k}, \omega) = -\frac{\mu_e^2}{4} \sum_i \chi_i(\mathbf{k}, \omega) [1 + \chi_e(\mathbf{k}, \omega)] \times \left[\frac{1}{\epsilon(\mathbf{k}, \omega - \omega_0)} + \frac{1}{\epsilon(\mathbf{k}, \omega + \omega_0)} \right]. \quad (23)$$

This form illustrates the coupling between the low-frequency daughter wave, characterised by $(\mathbf{k}, \omega = \omega_1 + i\gamma)$, the down-shifted high-frequency daughter wave, characterised by $(\mathbf{k}, \omega - \omega_0 = -\omega_2 + i\gamma)$, and the up-shifted high-frequency daughter wave, characterised by $(\mathbf{k}, \omega + \omega_0 = \omega_3 + i\gamma)$, due to the finite amplitude of the pump wave (through μ_e^2). The coupling will be extremely small, and the low-frequency daughter wave response almost linear ($\epsilon(\mathbf{k}, \omega) \approx 0$), for the usual case of $\mu_e \ll 1$, unless $\epsilon(\mathbf{k}, \omega \pm \omega_0) \approx 0$. Thus, the high-frequency modes should correspond (almost) to linear plasma modes, which also justifies neglecting the first term in the bracket on the right hand side of (22). If $\epsilon(\mathbf{k}, \omega) \approx 0$ remains valid, a PDI ($\gamma > 0$ in a homogeneous plasma) may occur for $\mu_e \ll 1$, confirming the correctness of the simplified picture in figure 2.

Parametric dispersion relations equivalent to (23) are found in [20, 40]; note that the one given by [40] is derived

its version of (23), generally reducing the validity of the subsequent formulae to PDIs with low-frequency daughter waves satisfying the quasi-neutrality condition $|\chi_e(\mathbf{k}, \omega)| \gg 1$; this is particularly not satisfied by warm LH wave propagating nearly perpendicularly to \mathbf{B} , which is the case of interest in the present paper. The parametric dispersion relation from [4] also agrees with (23) for $\chi_i(\mathbf{k}, \omega \pm \omega_0) \approx 0$ and $\chi_e(\mathbf{k}, \omega \pm \omega_0) \approx -1$ if only the down-shifted high-frequency daughter wave is considered. Ott, Hui and Chu [18] derive their parametric dispersion relation from rather different arguments about the ponderomotive force acting on the electrons and the related density perturbations experienced by the ions. The final result does, however, resemble (23) if the substitutions $1 + \chi_e(\mathbf{k}, \omega) \rightarrow \chi_e(\mathbf{k}, \omega)$ and $\sum_i \chi_i(\mathbf{k}, \omega) \rightarrow 1 + \sum_i \chi_i(\mathbf{k}, \omega)$ are made; the variational approach of [5] appears to produce the same result in the weak coupling and dipole limit, as shown in section 3.2. The results of [5, 18] do not agree with the previous ones, and thus a re-examination of these and related expressions, e.g. the one in [43], may be of interest. We note that all expressions agree for low-frequency daughter waves satisfying the quasi-neutrality conditions $|\chi_{i,e}(\mathbf{k}, \omega)| \gg 1$, but that (23) is preferable for pump waves in the EC frequency range where this condition may not be satisfied.

(23) does still not give γ explicitly and must in general be solved numerically. However, by using the earlier results we can obtain relatively simple expressions for the limiting cases of most interest. We consider the down-shifted high-frequency mode to be on resonance, $\epsilon(\mathbf{k}, -\omega_2 + i\gamma) \approx 0$, and neglect the contribution of the up-shifted high-frequency mode, which is permissible if the damping rates of the high-frequency modes are small compared to ω_1 . In this case we can take $\text{Re}[\epsilon(\mathbf{k}, -\omega_2)] = 0$ and expand $\epsilon(\mathbf{k}, -\omega_2 + i\gamma)$ around $(\mathbf{k}, -\omega_2)$, using $\epsilon(\mathbf{k}, -\omega_2) = \epsilon^*(-\mathbf{k}, \omega_2)$, to find $\epsilon(\mathbf{k}, \omega - \omega_0) \approx -i\{\partial \text{Re}[\epsilon(-\mathbf{k}, \omega)]/\partial \omega\}|_{\omega=\omega_2} [\gamma + \Gamma(-\mathbf{k}, \omega_2)]$, where the linear damping rate of the down-shifted high-frequency mode is $\Gamma(-\mathbf{k}, \omega_2) = \text{Im}[\epsilon(-\mathbf{k}, \omega_2)]/\{\partial \text{Re}[\epsilon(-\mathbf{k}, \omega)]/\partial \omega\}|_{\omega=\omega_2}$. Plugging the above results into (23), and isolating $\gamma + \Gamma(-\mathbf{k}, \omega_2)$, gives

$$\begin{aligned} \gamma + \Gamma(-\mathbf{k}, \omega_2) &= -\frac{\mu_e^2}{4} \text{Re} \left\{ \frac{i \sum_i \chi_i(\mathbf{k}, \omega) [1 + \chi_e(\mathbf{k}, \omega)]}{\epsilon(\mathbf{k}, \omega) \{\partial \text{Re}[\epsilon(-\mathbf{k}, \omega)]/\partial \omega\}|_{\omega=\omega_2}} \right\} \\ &= \frac{\mu_e^2}{4} \frac{|\sum_i \chi_i(\mathbf{k}, \omega)|^2 \text{Im}[\chi_e(\mathbf{k}, \omega)] + |1 + \chi_e(\mathbf{k}, \omega)|^2 \sum_i \text{Im}[\chi_i(\mathbf{k}, \omega)]}{|\epsilon(\mathbf{k}, \omega)|^2 \{\partial \text{Re}[\epsilon(-\mathbf{k}, \omega)]/\partial \omega\}|_{\omega=\omega_2}}. \end{aligned} \quad (24)$$

assuming an LH pump wave, and thus based on some rather different assumptions. The parametric dispersion relation from [19] agrees with (23) within the dipole approximation. The general weak coupling parametric dispersion relation in (28a) of [35] agrees with our (23) for $\chi_i(\mathbf{k}, \omega \pm \omega_0) \approx 0$ and $\chi_e(\mathbf{k}, \omega \pm \omega_0) \approx -1$, as we have assumed. However, in going from (28a) to (28b), [35] assumes $|\chi_{e,i}(\mathbf{k}, \omega)| \gg |\chi_{e,i}(\mathbf{k}, \omega \pm \omega_0)|$, which causes $1 + \chi_e(\mathbf{k}, \omega) \rightarrow \chi_e(\mathbf{k}, \omega)$ in

The above equations lead to two different expressions for γ depending on the conditions satisfied by the low-frequency mode. The two cases are known as resonant and non-resonant PDIs, respectively. For resonant PDIs, the low-frequency mode is also weakly damped, $\omega_1 \gg \Gamma(\mathbf{k}, \omega_1)$, and we can take $\text{Re}[\epsilon(\mathbf{k}, \omega_1)] = 0$ and expand $\epsilon(\mathbf{k}, \omega_1 + i\gamma)$ around (\mathbf{k}, ω_1) to find $\epsilon(\mathbf{k}, \omega) \approx i\{\partial \text{Re}[\epsilon(\mathbf{k}, \omega)]/\partial \omega\}|_{\omega=\omega_1} [\gamma + \Gamma(\mathbf{k}, \omega_1)]$, with which (24) may be rewritten as

$$[\gamma + \Gamma(\mathbf{k}, \omega_1)][\gamma + \Gamma(-\mathbf{k}, \omega_2)] = -\frac{\mu_e^2}{4} \frac{\sum_i \text{Re}[\chi_i(\mathbf{k}, \omega_1)] \{1 + \text{Re}[\chi_e(\mathbf{k}, \omega_1)]\}}{\{\partial \text{Re}[\epsilon(\mathbf{k}, \omega)]/\partial \omega\}|_{\omega=\omega_1} \{\partial \text{Re}[\epsilon(-\mathbf{k}, \omega)]/\partial \omega\}|_{\omega=\omega_2}}, \quad (25)$$

where the order 0 expressions, $\chi_e(\mathbf{k}, \omega) \approx \text{Re}[\chi_e(\mathbf{k}, \omega_1)]$ and $\chi_i(\mathbf{k}, \omega) \approx \text{Re}[\chi_i(\mathbf{k}, \omega_1)]$, have been used in the numerator; (25) is similar to (A2) from [4] for $\chi_i(-\mathbf{k}, \omega_2) \approx 0$ and $\chi_e(-\mathbf{k}, \omega_2) \approx -1$. This quadratic equation for γ is easily solved (showing only the possibly positive root),

$$\gamma = \frac{1}{2} \left[\sqrt{[\Gamma(\mathbf{k}, \omega_1) - \Gamma(-\mathbf{k}, \omega_2)]^2 - \frac{\mu_e^2 \sum_i \text{Re}[\chi_i(\mathbf{k}, \omega_1)] \{1 + \text{Re}[\chi_e(\mathbf{k}, \omega_1)]\}}{\{\partial \text{Re}[\epsilon(\mathbf{k}, \omega)]/\partial \omega\}|_{\omega=\omega_1} \{\partial \text{Re}[\epsilon(-\mathbf{k}, \omega)]/\partial \omega\}|_{\omega=\omega_2}}} - \Gamma(\mathbf{k}, \omega_1) - \Gamma(-\mathbf{k}, \omega_2) \right], \quad (26)$$

and the PDI threshold ($\gamma > 0$) in a homogeneous plasma may be expressed as the condition

$$\mu_e^2 > -\frac{4 \text{Im}[\epsilon(\mathbf{k}, \omega_1)] \text{Im}[\epsilon(-\mathbf{k}, \omega_2)]}{\sum_i \text{Re}[\chi_i(\mathbf{k}, \omega_1)] \{1 + \text{Re}[\chi_e(\mathbf{k}, \omega_1)]\}}. \quad (27)$$

For non-resonant PDIs, the low-frequency mode is not weakly damped ($\epsilon(\mathbf{k}, \omega_1) \not\approx 0$), and the right hand side of (24) may be approximated by its value at $\omega = \omega_1$ without the assumption of small $\text{Im}[\chi_e(\mathbf{k}, \omega)]$ and $\text{Im}[\chi_i(\mathbf{k}, \omega)]$,

$$\gamma = \frac{\mu_e^2}{4} \frac{\left[\sum_i \chi_i(\mathbf{k}, \omega_1)^2 \text{Im}[\chi_e(\mathbf{k}, \omega_1)] + |1 + \chi_e(\mathbf{k}, \omega_1)|^2 \sum_i \text{Im}[\chi_i(\mathbf{k}, \omega_1)] \right]}{|\epsilon(\mathbf{k}, \omega_1)|^2 \{\partial \text{Re}[\epsilon(-\mathbf{k}, \omega)]/\partial \omega\}|_{\omega=\omega_2}} - \Gamma(-\mathbf{k}, \omega_2); \quad (28)$$

an equation similar to (28) is used as a starting point by [2]. (28) yields the homogeneous plasma PDI threshold,

$$\mu_e^2 > \frac{4 \text{Im}[\epsilon(-\mathbf{k}, \omega_2)] |\epsilon(\mathbf{k}, \omega_1)|^2}{\left[\sum_i \chi_i(\mathbf{k}, \omega_1)^2 \text{Im}[\chi_e(\mathbf{k}, \omega_1)] + |1 + \chi_e(\mathbf{k}, \omega_1)|^2 \sum_i \text{Im}[\chi_i(\mathbf{k}, \omega_1)] \right]}. \quad (29)$$

It is seen that both the resonant and the non-resonant PDIs in a homogeneous plasma need the pump wave amplitude ($|E_0| \propto \mu_e$) to exceed a certain threshold, principally determined by the daughter wave damping, in order to occur. However, while the resonant PDI threshold increases with both the low- and high-frequency daughter wave damping, through $\text{Im}[\epsilon(\mathbf{k}, \omega_1)]$ and $\text{Im}[\epsilon(-\mathbf{k}, \omega_2)]$, the non-resonant PDI threshold increases with damping of the high-frequency daughter wave, but does not occur without damping of the low-frequency daughter wave. The above observations point to an important difference between the resonant and

non-resonant PDIs. The resonant PDI can be seen as a pure wave-wave interaction, in which the beating of one daughter wave with the pump wave amplifies the other daughter wave and vice versa [44]. This results in a fairly symmetric treatment of the two daughter waves, which is generally

adequately described by fluid models. The non-resonant PDI can rather be seen as a wave-particle interaction, in which energy is transferred from the pump wave to the high-frequency daughter wave through nonlinear Landau damping of the low-frequency daughter wave [45]. This results in a treatment of the high-frequency daughter wave which is virtually independent of the low-frequency daughter wave and generally requires a kinetic description.

2.3. PDIs in inhomogeneous plasmas

Although we have now derived thresholds for PDIs in homogeneous plasmas, these are generally far below the thresholds observed in real inhomogeneous plasmas. The main reason for this is that the \mathbf{k} selection rule for the waves involved in a PDI is only approximately satisfied in a small region through which a significant amplification of the thermal background daughter waves has to occur in order for the PDI to have measurable consequences. Within the geometric optics approximation, we may convert the temporal growth rate in a homogeneous medium

into a local spatial growth rate $\gamma/v_g(\mathbf{k}, \omega)$ along the ray, where $v_g(\mathbf{k}, \omega) = |\{\partial \text{Re}[\epsilon(\mathbf{k}, \omega)]/\partial \mathbf{k}\}/\{\partial \text{Re}[\epsilon(\mathbf{k}, \omega)]/\partial \omega\}|$ is the magnitude of the group velocity (the speed of energy transport along the ray). From this, the power gain of the high-frequency daughter waves in the case of non-resonant PDIs, $G = \ln(P_{\text{out}}/P_{\text{in}})$, may be calculated as [18, 46],

$$G = \int_{\text{ray}} \frac{2\gamma(\mathbf{r}(s), \mathbf{k}(s), \omega_1, \omega_2)}{v_g(\mathbf{r}(s), -\mathbf{k}(s), \omega_2)} ds, \quad (30)$$

where the integral is over a segment of the ray of the high-frequency daughter wave for given initial conditions and s is a parameter characterising length along the ray. Assuming that γ is only significant in a small region around the point $s = s_r$, at which the selection rule is exactly satisfied for a particular low-frequency quasi-mode, and that the ray only traverses this region once, we can write

$$G \approx \frac{2\gamma(\mathbf{r}(s_r), \mathbf{k}(s_r), \omega_1, \omega_2)\ell(s_r)}{v_g(\mathbf{r}(s_r), -\mathbf{k}(s_r), \omega_2)}, \quad (31)$$

with $\ell(s_r)$ being the length along the ray around s_r with significant γ . A threshold is obtained by requiring G to be sufficiently large. For instance, [13] defines the threshold to be $G > 2\pi$, corresponding to $P_{\text{out}}/P_{\text{in}} > 535$, which we shall also use, keeping in mind that PDIs may be observable for slightly lower values of G . Note that the threshold may be significantly reduced if the amplification region is traversed several times by the ray of the high-frequency daughter wave without significant damping between the individual passes. This may happen if the high-frequency daughter wave is trapped due to a non-monotonic plasma profile around the amplification region [16] or in the case of a backscattering instability [17]. However, $\gamma > 0$ represents the lowest possible threshold in all cases.

For the case of a resonant PDI in a plasma slab with monotonically varying parameters along the x -direction and daughter waves propagating along the x -direction, [12–14] showed that, within the WKB approximation,

$$G = \frac{2\pi\gamma^2(x_r, k_x(x_r), \omega_1, \omega_2)l^2(x_r, \omega_1, \omega_2)}{v_g(x_r, k_x(x_r), \omega_1)v_g(x_r, -k_x(x_r), \omega_2)}. \quad (32)$$

Here, $x = x_r$ is the x -value at which the selection rules are exactly satisfied, $l^2(x_r, \omega_1, \omega_2) = 1/|\{[\partial k_x(x, \omega_1)/\partial x]_{x=x_r} - [\partial k_x(x, \omega_2)/\partial x]_{x=x_r}\}|$ is the length scale over which the $k_x(x)$ -selection rule is well satisfied, and we have retained the dipole approximation, $k_0(x) \approx 0$. This G is seen to be quite similar to the one for non-resonant decay from (31); the main difference is that the high-frequency and low-frequency daughter waves enter G in a symmetric fashion, as expected for the resonant PDI, and that $l(x_r)$, unlike $\ell(s_r)$, is not arbitrary. While the application of (32) to a realistic 3D plasma may not provide the actual threshold, since it only addresses wave propagation along a gradient with a constant direction, it should still provide an order of magnitude estimate of the resonant PDI threshold in a non-monotonic plasma. For the non-resonant PDI, a similar estimate may be obtained by only considering propagation along the x -direction and setting $\ell(s_r) \approx l(x_r, \omega_1, \omega_2)$, such that (31) becomes $G \approx 2\gamma(x_r, k(x_r), \omega_1, \omega_2)l(x_r, \omega_1, \omega_2)/v_g(x_r, -k(x_r), \omega_2)$.

3. PDIs near the UHR

So far, PDIs involving gyrotron radiation with $\omega_0 \sim |\omega_{ce}|$ have been discussed in a rather general fashion; we now specialise to the case of PDIs near the UHR. As is known from the theory of cold electromagnetic plasma waves, X-mode radiation has a principal resonance ($k_0 \rightarrow \infty$, or $v_g(\mathbf{k}_0, \omega_0) \rightarrow 0$, for $\mathbf{k}_0 \perp \mathbf{B}$) at the UH frequency, $\omega_{\text{UH}}^2 = \omega_{ce}^2 + \omega_{pe}^2$, with a propagating X-mode only existing on the side where $\omega_0 < \omega_{\text{UH}}$. Under normal circumstances, X-mode radiation encountering the UHR is converted linearly into an electron Bernstein/warm UH wave [38], the dispersion relation of which we derive below. However, PDIs are also likely to occur near the UHR because $|E_0|$ (and hence μ_e) of the X-mode radiation becomes significantly enhanced compared with its normal value for gyrotron radiation, due to a low group velocity and full-wave effects [15] combined with the fact that linear Landau and cyclotron damping remains small, unless $\omega_{\text{UH}} \approx n|\omega_{ce}|$ for $n \in \mathbb{N}$ [38]. In this paper we focus on direct parametric decay of the X-mode radiation into electrostatic daughter waves before the linear mode conversion to warm UH waves takes place, as was done by [1–5]; this requires propagating daughter waves to exist in the region where $\omega_0 < \omega_{\text{UH}}$. For PDIs of the linearly converted warm UH waves see [17, 21, 22].

This work is, as previously mentioned, primarily motivated by the observation of strong anomalous scattering during some CTS experiments at the ASDEX Upgrade tokamak [6]; observations resembling the ones from ASDEX Upgrade have also been made during CTS experiments at the LHD stellarator [7, 8]. The CTS spectral power density obtained in one of these experiments (ASDEX Upgrade discharge 28286) is seen in figure 3. The figure shows peaks with frequency shifts of approximately 850 MHz relative to the gyrotron frequency ($\omega_0/(2\pi) = 104.93$ GHz) developing at $t = 2.100$ s and becoming well separated from the strong signal at small frequency shifts for $t \geq 2.500$ s. The frequency shift slightly exceeds the LH frequency of approximately 700 MHz at the UHR of the gyrotron radiation in the experiment (for reference, the plasma parameters are $N_e^{(0)} \approx 2.8 \times 10^{19} \text{ m}^{-3}$, $T_e \approx 300$ eV and $B \approx 3.35$ T at this location), and the occurrence of the peaks is additionally strongly correlated with a significant amount of power reaching the UHR in X-mode. The latter point is illustrated in figure 4 (the details of which are discussed below) through traces of the CTS probe rays, done using a code based on analytical approximations to the relativistic dispersion relation developed in [47, 48], at various times in the discharge: virtually no X-mode radiation reaches the UHR in the main plasma at the early time point, $t = 1.300$ s, while a smaller fraction of the X-mode beam may reach it at the intermediate time point, $t = 2.100$ s, and a significant fraction of the X-mode beam will reach it at the late time points, $t \geq 2.500$ s. Note, however, that the traced CTS probe ray does not reach the UHR in the main plasma before $t = 2.900$ s.

As seen in figure 4, the UHR is only accessible to X-mode radiation launched from its high-field side in

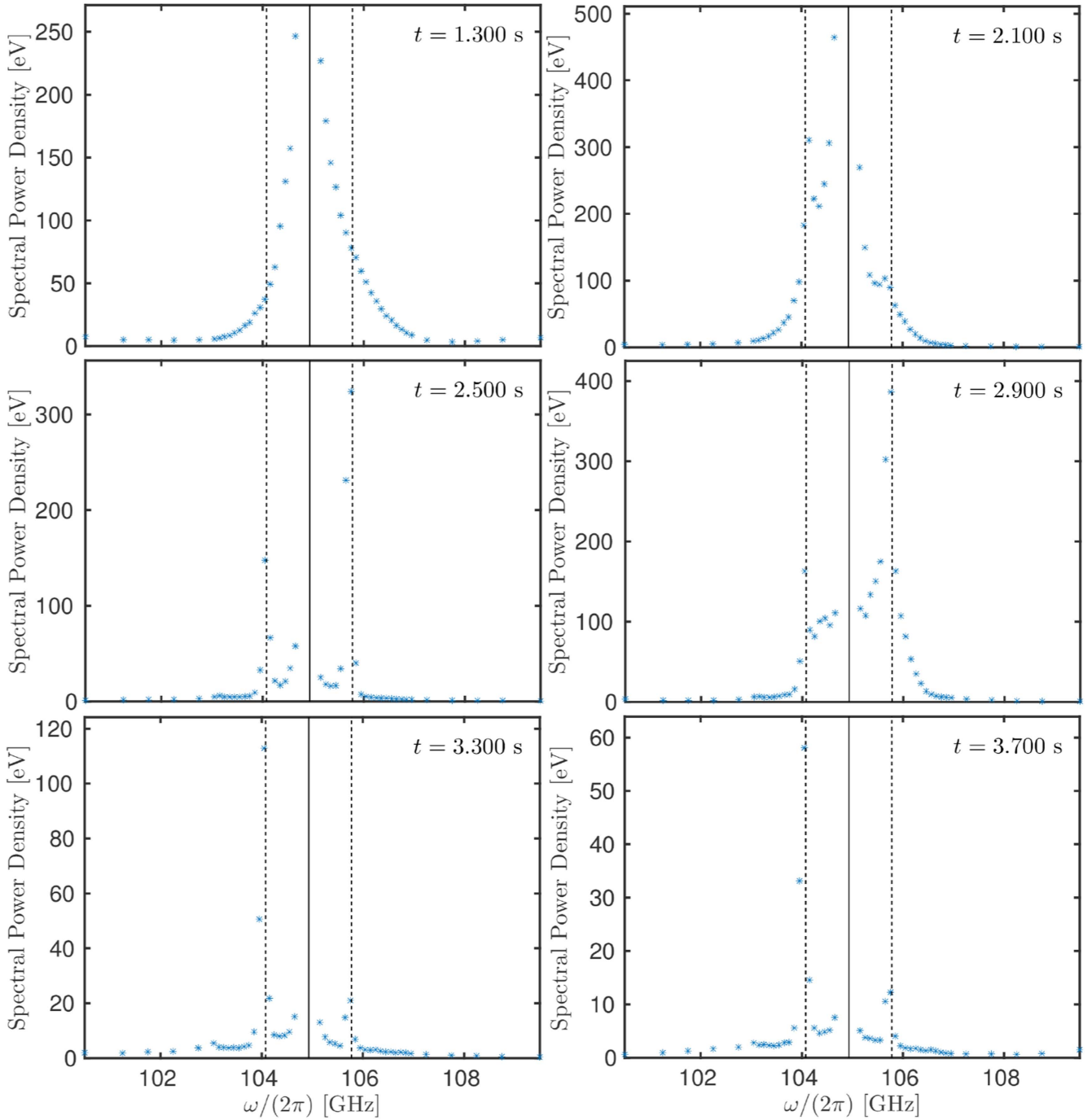


Figure 3. CTS spectral power density (in eV, as is customary [6]) around the gyrotron frequency $\omega_0/(2\pi) = 104.93$ GHz, marked by the full line, in ASDEX Upgrade discharge 28286. At the early time point, $t = 1.300$ s, no peaks are observed; at the intermediate time point, $t = 2.100$ s, peaks with frequency shifts of approximately 850 MHz, marked by dashed lines, start developing; at late time points, $t \geq 2.500$ s, these peaks become well-separated from the signal at small frequency shifts.

tokamak plasmas due to the location of the R cut-off. For CTS applications, access to the entire plasma volume is desired, so the 105 GHz gyrotron radiation is launched in O-mode from the low-field side. Thus, in order for power to reach the UHR, a reflection of the injected O-mode radiation from the high-field side wall, in which the reflected radiation is at least partially converted to X-mode, is necessary; a similar mechanism was invoked by [32] to explain generation of fast ions

during 1st harmonic O-mode ECRH, with a low-field side launch, at the TCA tokamak.

To understand the trajectories of the rays in figure 4, as well as the characteristics of the PDIs later on, we plot the development of the $N_e^{(0)}$ - and T_e -profiles obtained from integrated data analysis (IDA) [49] versus the normalised poloidal flux coordinate, ρ_{pol} ($\rho_{\text{pol}} = 0$ at the plasma centre and $\rho_{\text{pol}} = 1$ at the last closed flux surface, magnetic equilibria are calculated

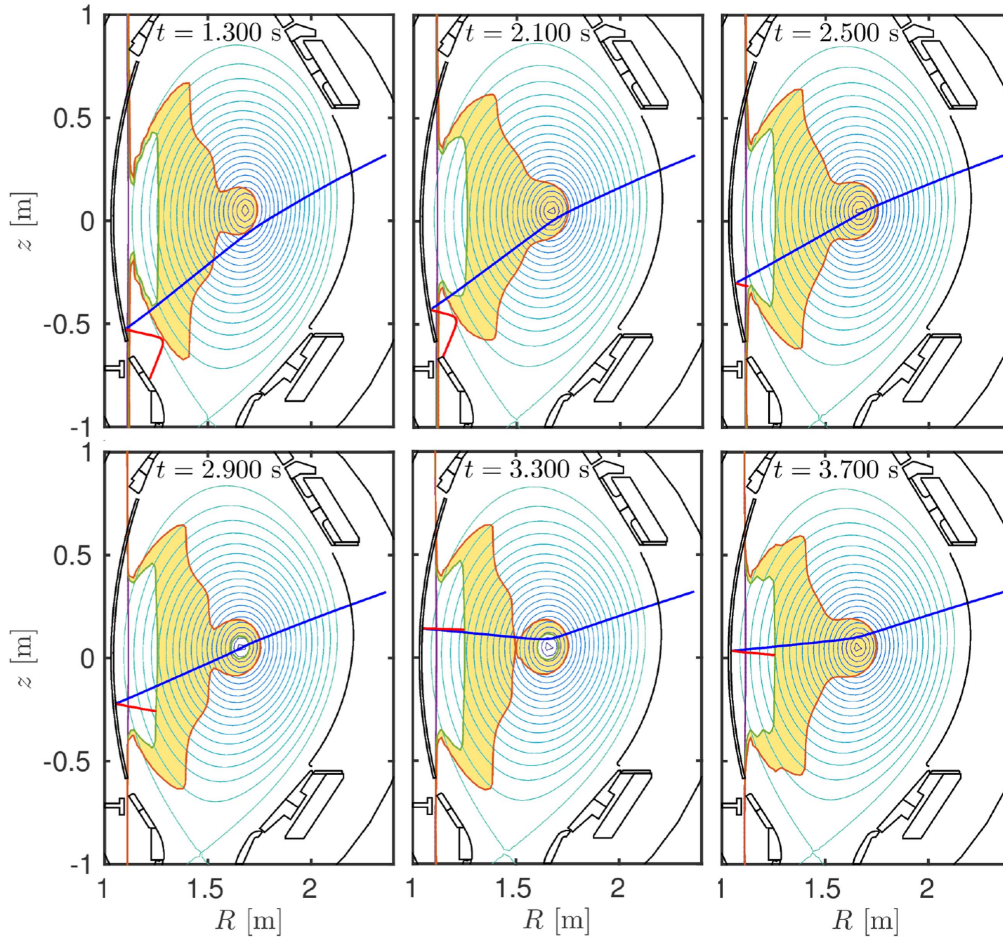


Figure 4. Traces of the central rays of the 105 GHz O-mode radiation injected from the low-field side (blue line) and the 105 GHz X-mode radiation reflected from the high-field side vessel wall (red line), projected into the (R, z) -plane of the cylindrical tokamak coordinate system, in ASDEX Upgrade discharge 28286 at $t = \{1.300, 2.100, 2.500, 2.900, 3.300, 3.700\}$ s. The green, purple, and orange lines indicate the locations of the UHR, the ECR, and the R cut-off, respectively; no propagating X-mode exists in the shaded areas; the background contours are closed magnetic flux surfaces indicating the position of the main plasma. At $t = 1.300$ s, virtually none of the reflected X-mode radiation reaches the UHR, while part of the reflected X-mode radiation may reach it at $t = 2.100$ s. For $t \geq 2.500$ s, most of the reflected X-mode radiation reaches the UHR, although the traced central beam ray does not reach it in the main plasma before $t = 2.900$ s. These observations are consistent with the 850 MHz shifted peaks in figure 3 being caused by a PDI occurring at the UHR. Rays have been traced using a code based on analytical approximations to the relativistic dispersion relation developed in [47, 48]. The $N_e^{(0)}$ - and T_e -profiles have been generated using IDA [49] and the magnetic ASDEX Upgrade equilibria obtained using the CLISTE code [50].

using the CLISTE code [50]), for $t = \{2.900, 3.300, 3.700\}$ s in figure 5. Evidently, $N_e^{(0)}$ is peaked around the plasma centre, resulting in the large refraction taking place here. However, the central peaking of $N_e^{(0)}$ is an extrapolation, as no measurements of the plasma parameters for $\rho_{\text{pol}} < 0.2$ were possible in the discharge. In order to address this issue, rays have also been traced for flat central $N_e^{(0)}$ - and T_e -profiles, marked by dotted lines in figure 5. These rays differ from the ones shown in figure 4 by suffering virtually no refraction at the plasma centre, but the PDI relevant conclusions, and the plasma parameters at the UHR (encountered at $\rho_{\text{pol}} \approx 0.8$), remain the same; the only difference is that the CTS probe ray encounters the UHR in the main plasma for $t \geq 2.500$ s with the flat profiles. To have a rough estimate of the experimental uncertainty of the PDI threshold and frequency shift, all subsequent calculations are

carried out for both the peaked and the flat profiles shown in figure 5; analyses are only performed for $t \geq 2.900$ s.

For PDIs to occur near the UHR by the mechanism described above, a non-negligible fraction of the reflected power, \mathcal{F} , should be coupled into the main plasma in X-mode and, additionally, absorption at the EC resonance (ECR) should not be excessive. These points are also addressed by the ray traces, since the evolution of the wave polarisation along the O-mode and X-mode rays, as well as during the high-field side wall reflection, determines \mathcal{F} , while the total optical thickness of the O-mode and X-mode rays, $\tau = -G$, determines the fraction of power transmitted through the ECR, $e^{-\tau}$. The total power reaching the UHR is approximately $P = \mathcal{F} e^{-\tau} P_0$, with P_0 being the gyrotron power. Figure 6 shows \mathcal{F} , $e^{-\tau}$ and $\mathcal{F} e^{-\tau}$ for the CTS probe rays reaching the UHR in the main plasma

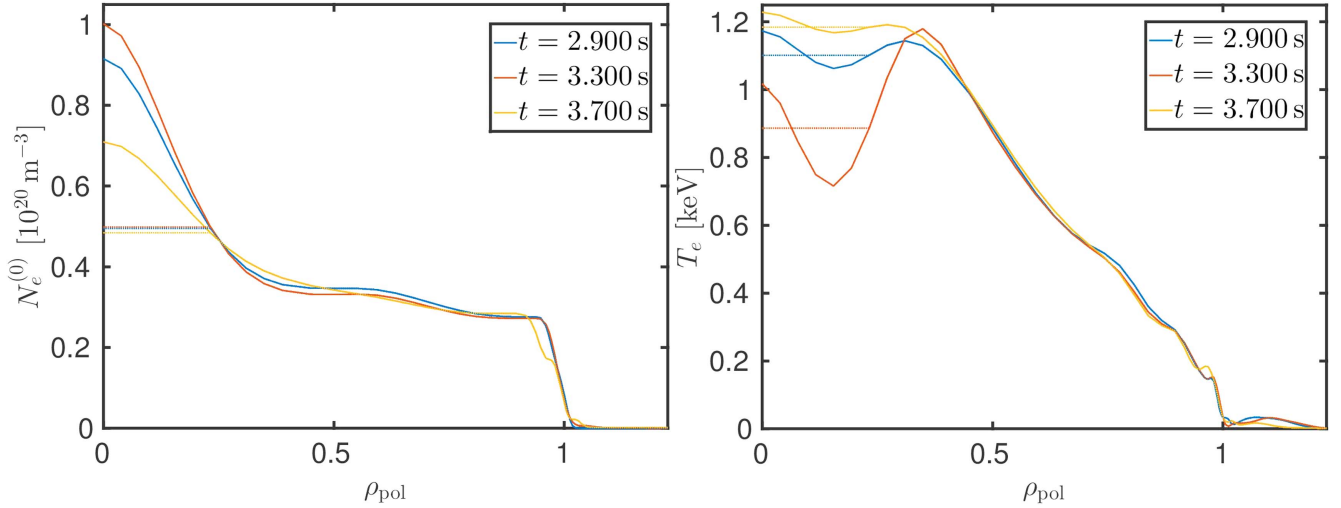


Figure 5. Development of $N_e^{(0)}$ and T_e versus the normalised poloidal flux coordinate, ρ_{pol} , in ASDEX Upgrade discharge 28286. The IDA profiles are marked by full lines, while the dotted lines represent the flat central profiles used to estimate the uncertainty resulting from the poorly diagnosed plasma centre.

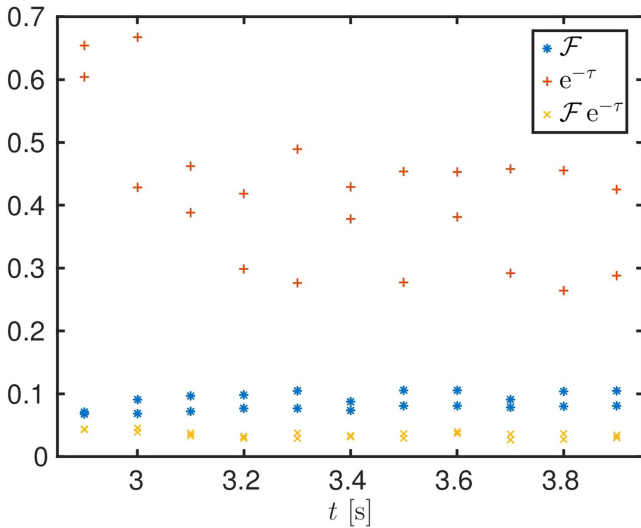


Figure 6. Fraction of reflected power coupled to the plasma in X-mode, \mathcal{F} , fraction of power transmitted by the plasma, $e^{-\tau}$, and fraction of power reaching the UHR in X-mode, $\mathcal{F}e^{-\tau}$, versus t in ASDEX Upgrade discharge 28286.

($t \geq 2.900$ s). \mathcal{F} is calculated as the square norm of the projection of the reflected ray polarisation vector along the X-mode polarisation vector at the ECR or the last closed flux surface, depending on which of these is encountered first; the high-field side wall is treated as a locally plane, perfectly reflecting mirror. As seen in figure 6, $\mathcal{F} \approx 0.1$ in all cases where the CTS probe ray reaches the UHR in the main plasma. τ is calculated using a relativistic model and is found to have moderate values, $\min(e^{-\tau}) = 0.265$, meaning that absorption at the ECR is non-excessive in all cases. Accounting for both τ and \mathcal{F} , the amount of gyrotron power reaching the UHR in X-mode is $P = \mathcal{F}e^{-\tau}P_0 \approx 0.04P_0$, corresponding to $P \approx 8$ kW for the

nominal gyrotron power, $P_0 = 200$ kW, in the experiment. This power level is of an order of magnitude where PDIs may be expected to occur near the UHR in a tokamak [3], allowing them to account for the CTS spectrum in figure 3. We note that both \mathcal{F} and $e^{-\tau}$ are quite sensitive functions of the toroidal gyrotron injection angle in the ASDEX Upgrade equilibria considered: when the gyrotron radiation is injected poloidally, virtually none of the reflected radiation is coupled to the plasma in X-mode, $\mathcal{F} \approx 0$, but the ECR is optically thin, $e^{-\tau} \sim 1$; as the toroidal gyrotron injection angle increases, \mathcal{F} grows while $e^{-\tau}$ decays, and when the numerical value of the toroidal gyrotron injection angle exceeds approximately 10° , the ECR becomes optically thick, $e^{-\tau} \approx 0$. The combination of these effects results in $\max(\mathcal{F}e^{-\tau}) \approx 0.04$ which coincides with the toroidal injection angle of approximately -5° used throughout the discharge. The above observations provide simple experimental prescriptions for suppressing PDIs at the UHR in 105 GHz O-mode CTS experiments at ASDEX Upgrade. However, it is noted that PDI suppression by a completely poloidal injection requires both the width of the gyrotron beam and its angular divergence to be very small, while PDI suppression by a large toroidal injection requires B to be large enough for the ECR to occur between the high-field side wall and the UHR, ideally inside the last closed flux surface; the latter prescription has successfully suppressed PDIs in 105 GHz O-mode CTS experiments at ASDEX Upgrade [6].

3.1. Electrostatic daughter waves at the UHR

To study PDIs near the UHR we derive dispersion relations for the electrostatic daughter waves likely to be involved in such instabilities. First, we note that, when $|(\text{Re}(\omega) - n\omega_{ce}) / (k_z v_{Te})| > 2$ (i.e. $\text{Re}(\omega) \not\approx n\omega_{ce}$, for all $n \in \mathbb{Z}$), $b_e = k_\perp^2 r_{Le}^2 \ll 1$, $k_z^2 / k_\perp^2 \ll 1$, and $\nu_e / \text{Re}(\omega) \ll 1$, the electron

$\chi_e(\mathbf{k}, \omega)$ in (9) may be approximated by [1]

$$\begin{aligned} \chi_e(\mathbf{k}, \omega) \approx & -\frac{\omega_{pe}^2}{\omega^2 - \omega_{ce}^2} - \frac{3\omega_{pe}^2\omega_{ce}^2 b_e}{(\omega^2 - \omega_{ce}^2)(\omega^2 - 4\omega_{ce}^2)} \\ & + \frac{\omega_{pe}^2}{\omega^2} \left[\frac{\omega_{ce}^2}{\omega^2 - \omega_{ce}^2} + i2\sqrt{\pi} \frac{\omega^3}{|k_z|^3 v_{Te}^3} e^{-\omega^2/(k_z^2 v_{Te}^2)} \right] \\ & \times \frac{k_z^2}{k_\perp^2} + i \frac{\omega_{pe}^2(\omega^2 + \omega_{ce}^2) \nu_e}{(\omega^2 - \omega_{ce}^2)^2 \omega}. \end{aligned} \quad (33)$$

For the high-frequency daughter waves, the ion response is negligible and the dispersion relation, $\text{Re}[\epsilon(-\mathbf{k}, \omega_2)] \approx 1 + \text{Re}[\chi_e(-\mathbf{k}, \omega_2)] = 0$, may be written as

$$\begin{aligned} 1 - \frac{\omega_{pe}^2}{\omega_2^2 - \omega_{ce}^2} - \frac{3\omega_{pe}^2\omega_{ce}^2 b_e}{(\omega_2^2 - \omega_{ce}^2)(\omega_2^2 - 4\omega_{ce}^2)} \\ + \frac{\omega_{pe}^2\omega_{ce}^2}{\omega_2^2(\omega_2^2 - \omega_{ce}^2)} \frac{k_z^2}{k_\perp^2} = 0. \end{aligned} \quad (34)$$

This is a cubic equation for ω_2^2 in terms of \mathbf{k} and the plasma parameters which can be solved using standard algebraic techniques. However, for the cases of interest the terms involving b_e and k_z^2/k_\perp^2 are small. Ignoring these, the order 0 dispersion relation becomes $\omega_2^2 \approx \omega_{UH}^2$, i.e. the dispersion relation gives a non-propagating oscillation at the UH frequency. Expanding (34) to order 1 in b_e and k_z^2/k_\perp^2 around $\omega_2 = \omega_{UH}$, we find

$$\omega_2^2 \approx \omega_{UH}^2 - \omega_{pe}^2 \left[\frac{b_e}{1 - \omega_{pe}^2/(3\omega_{ce}^2)} + \frac{\omega_{ce}^2}{\omega_{UH}^2} \frac{k_z^2}{k_\perp^2} \right]. \quad (35)$$

The above dispersion relation describes the previously mentioned limiting form of electron Bernstein waves known as warm UH waves, since ω_2 is close to ω_{UH} and depends on T_e through b_e , which are the principal high-frequency daughter waves in PDIs near the UHR. It is similar to the dispersion relation used by [1, 21, 22] to study PDIs near the UHR, and reduces to the one used by [4] for $k_z = 0$ and the one used by [2] for $\omega_{pe}^2 \ll \omega_{ce}^2$. The dispersion relation has a cut-off ($k = 0$) at $\omega_2 = \omega_{UH}$, and propagating waves only exist for $\omega_2 < \omega_{UH}$ when $\omega_{pe}^2 < 3\omega_{ce}^2$, while they exist for $\omega_2 > \omega_{UH}$ when $\omega_{pe}^2 > 3\omega_{ce}^2$ and $k_z = 0$. Thus, we see that a PDI in which the X-mode pump wave (with $\omega_0 < \omega_{UH}$) decays directly to two electrostatic daughter waves, as we are considering, will only be feasible when $\omega_{pe}^2 < 3\omega_{ce}^2$, limiting our theory to underdense and weakly overdense plasmas ($\omega_{pe}/|\omega_{ce}| < \sqrt{3}$),

consider PDIs for the linearly converted warm UH waves themselves which requires consideration of the backscattering type of instability [17]. The above dispersion relation is invalid when $\omega_{pe}^2 \approx 3\omega_{ce}^2$, where the UHR coincides with the 2nd harmonic ECR, $\omega_2 \approx \omega_{UH} \approx 2|\omega_{ce}|$, violating the assumptions used for deriving (35); in fact, PDIs may be inhibited in a narrow band around $\omega_{UH} = n|\omega_{ce}|$ for all $n \in \mathbb{N}$ due to bandgap effects, as observed in ionospheric modification experiments [23].

For reference we note that the group velocity of the warm UH waves, given by $\mathbf{v}_g(\mathbf{k}, \omega_2) = [\partial\omega_2^2(\mathbf{k})/\partial\mathbf{k}]/(2\omega_2)$, may be found by exploiting the azimuthal symmetry of (35) in \mathbf{k} -space,

$$\begin{aligned} \mathbf{v}_g(-\mathbf{k}, \omega_2) = \frac{\omega_{pe}^2}{k_\perp \omega_2} \left\{ \left[\frac{b_e}{1 - \omega_{pe}^2/(3\omega_{ce}^2)} - \frac{\omega_{ce}^2}{\omega_{UH}^2} \frac{k_z^2}{k_\perp^2} \right] \mathbf{e}_\perp \right. \\ \left. + \frac{\omega_{ce}^2}{\omega_{UH}^2} \frac{k_z}{k_\perp} \mathbf{e}_z \right\}, \end{aligned} \quad (36)$$

where $\mathbf{e}_\perp = \mathbf{k}_\perp/k_\perp$. The relatively small value of $v_g(-\mathbf{k}, \omega_2)$, especially for $k_z = 0$, is important for reducing the PDI threshold in inhomogeneous plasmas. Note also that, even though $k_z^2/k_\perp^2 \ll 1$, $\mathbf{v}_g(-\mathbf{k}, \omega_2)$ may have a significant z -component for $k_z \neq 0$. Finally, we calculate $\Gamma(-\mathbf{k}, \omega_2) \approx \text{Im}[\chi_e(-\mathbf{k}, \omega_2)]/\{\partial \text{Re}[\chi_e(-\mathbf{k}, \omega)]/\partial\omega\}|_{\omega=\omega_2}$ using the lowest order approximation, $\partial \text{Re}[\chi_e(\mathbf{k}, \omega)]/\partial\omega \approx 2\omega\omega_{pe}^2/(\omega^2 - \omega_{ce}^2)^2$, from (33),

$$\begin{aligned} \Gamma(-\mathbf{k}, \omega_2) \approx & \sqrt{\pi} \frac{(\omega_2^2 - \omega_{ce}^2)^2}{|k_z| k_\perp^2 v_{Te}^3} e^{-\omega_2^2/(k_z^2 v_{Te}^2)} \\ & + \frac{\omega_2^2 + \omega_{ce}^2}{2\omega_2^2} \nu_e \approx \frac{\omega_2^2 + \omega_{ce}^2}{2\omega_2^2} \nu_e; \end{aligned} \quad (37)$$

the last approximation follows from the fact that $\omega_2^2/(k_z^2 v_{Te}^2)$ is generally a large quantity, making the first (Landau damping) term extremely small and showing that warm UH waves are mainly damped by collisions; Landau damping is included due to its possible importance in damping the low-frequency daughter waves discussed below.

There is a larger number of possible low-frequency electrostatic daughter waves which may be excited by PDIs near the UHR, since the bulk of the frequency shift necessary to satisfy the selection rule is provided by the warm UH wave. However, because the low-frequency daughter waves should also be able to satisfy the \mathbf{k} -selection rules, we confine our attention to the cases where (33) is still a valid approximation for $\chi_e(\mathbf{k}, \omega)$, taking the limit $|\omega|^2 \ll \omega_{ce}^2$,

$$\chi_e(\mathbf{k}, \omega) \approx \frac{\omega_{pe}^2}{\omega_{ce}^2} - \frac{3\omega_{pe}^2}{4\omega_{ce}^2} b_e + \frac{\omega_{pe}^2}{\omega^2} \left[-1 + i2\sqrt{\pi} \frac{\omega^3}{|k_z|^3 v_{Te}^3} e^{-\omega^2/(k_z^2 v_{Te}^2)} \right] \frac{k_z^2}{k_\perp^2} + i \frac{\omega_{pe}^2 \nu_e}{\omega_{ce}^2 \omega}. \quad (38)$$

which are found in conventional tokamaks, as well as many stellarator experiments. When $\omega_{pe}^2 > 3\omega_{ce}^2$, as in spherical tokamaks or most ionospheric studies, it is necessary to

Note that this expression imposes a very strict condition on the smallness of k_z^2/k_\perp^2 (since generally $\omega_{pe}^2/|\omega|^2 \gg 1$) and that it does not satisfy the low-frequency quasi-neutrality condition,

$|\chi_e(\mathbf{k}, \omega_1)| \gg 1$, which is assumed by [35]. In general, $\chi_i(\mathbf{k}, \omega)$ should be determined from an expression like (9), but $\nu_i/\nu_e = O(\sqrt{m_e/m_i}) \ll 1$ [51], so we can ignore collisions completely for the ions. It is, however, not possible to expand $\chi_i(\mathbf{k}, \omega)$ in $b_i = r_{Li}^2 k_{\perp}^2$, as was done for $\chi_e(\mathbf{k}, \omega)$ in b_e , since $r_{Li}^2/r_{Le}^2 = m_i T_i / (Z_i^2 m_e T_e) \gg 1$, which implies that $b_i \gg b_e \ll 1$, not imposing any particular restriction on b_i . One can assume b_i to be small, as was done by [4], but generally it is necessary to evaluate (9), with $\nu_i \approx 0$ and $k_z^2/k_{\perp}^2 \ll 1$, including a large number of terms from the sum over n due to the potentially large value of b_i , in order to obtain $\chi_i(\mathbf{k}, \omega)$. If this is combined with $\chi_e(\mathbf{k}, \omega)$ from (38), the dispersion relation for pure ion Bernstein waves, which has a root between each integer value of ω_{ci} , is obtained. The present paper is mainly concerned with high-order pure ion Bernstein waves, leading to frequency shifts on the order of ω_{pi} (~ 1 GHz in the ASDEX Upgrade main plasma), where $\chi_i(\mathbf{k}, \omega)$ may be evaluated in the limit of $\text{Re}(\omega) \gg \omega_{ci}$ and $b_i \gg 1$; remember that $\omega_{pi}^2/\omega_{ci}^2 = [m_i/(Z_i m_e)] \omega_{pe}^2/\omega_{ce}^2$ in a simple plasma, so $\omega_{ci} \ll \omega_{pi}$ for $\omega_{pe} \sim |\omega_{ce}|$. Here, the basic behaviour can be obtained by considering the ions to be unmagnetised, since their trajectories are essentially straight lines on the relevant temporal and spatial scales (respectively, $1/\omega_1 \sim 1/\omega_{pi} \sim 200$ ps and $1/k_{\perp} \sim r_{Le}/\sqrt{b_e} \sim 30$ μm near the UHR in the considered ASDEX Upgrade discharge), although the details at integer values of ω_{ci} and interpretation of the Landau damping involve some subtleties [51, 52]. For unmagnetised ions we may insert $\chi_{\sigma}(\mathbf{k}, \omega)$ from (10) with $\nu_{\sigma} \approx 0$, and find

$$\begin{aligned}
 \chi_i(\mathbf{k}, \omega) &\approx \frac{2\omega_{pi}^2}{k^2 v_{Ti}^2} \left[1 + \frac{\omega}{k v_{Ti}} Z\left(\frac{\omega}{k v_{Ti}}\right) \right] \\
 &\approx -\frac{\omega_{pi}^2}{\omega^2} \left[1 + \frac{3k^2 v_{Ti}^2}{2\omega^2} - i2\sqrt{\pi} \frac{\omega^3}{k^3 v_{Ti}^3} e^{-\omega^2/(k^2 v_{Ti}^2)} \right] \\
 &\approx -\frac{\omega_{pi}^2}{\omega^2} \left[1 + \frac{3T_i}{Z_i T_e} \frac{|\omega_{ce}| \omega_{ci}}{\omega^2} b_e \right. \\
 &\quad \left. - i2\sqrt{\pi} \frac{\omega^3}{k_{\perp}^3 v_{Ti}^3} e^{-\omega^2/(k_{\perp}^2 v_{Ti}^2)} \right], \tag{39}
 \end{aligned}$$

where the first approximation follows from an asymptotic expansion of Z , valid for $\text{Re}(\omega)/(k v_{Te}) > \sqrt{2}$ [1], and the second approximation follows from setting $k \approx k_{\perp}$, which is permissible due to the requirement $k_z^2/k_{\perp}^2 \lesssim \omega_{pi}^2/\omega_{pe}^2 \ll 1$, imposed by the use of $\chi_e(\mathbf{k}, \omega)$ from (38) for $|\omega| \sim \omega_{pi}$. Note that $|\omega_{ce}| \omega_{ci} \sim \omega_{pi}^2$ for $\omega_{pe} \sim |\omega_{ce}|$, ensuring that the b_e -term in (39) is indeed of order $b_e \ll 1$, unless $\omega_{pe} \ll |\omega_{ce}|$ or $T_i \gg Z_i T_e$. We now obtain the dispersion relation of the low-frequency daughter waves in a simple plasma, $\text{Re}[\epsilon(\mathbf{k}, \omega_1)] = 1 + \text{Re}[\chi_i(\mathbf{k}, \omega_1)] + \text{Re}[\chi_e(\mathbf{k}, \omega_1)] = 0$, by inserting $\chi_e(\mathbf{k}, \omega)$ from (38) and $\chi_i(\mathbf{k}, \omega)$ from (39),

$$\begin{aligned}
 1 + \frac{\omega_{pe}^2}{\omega_{ce}^2} - \frac{\omega_{pi}^2}{\omega_1^2} - 3 \left(\frac{\omega_{pe}^2}{4\omega_{ce}^2} + \frac{T_i}{Z_i T_e} \frac{\omega_{pi}^2 |\omega_{ce}| \omega_{ci}}{\omega_1^4} \right) b_e \\
 - \frac{\omega_{pe}^2}{\omega_1^2} \frac{k_z^2}{k_{\perp}^2} = 0. \tag{40}
 \end{aligned}$$

This quadratic equation for ω_1^2 in terms of b_e and k_z^2/k_{\perp}^2 can be solved by the standard approach. However, just as for the high-frequency daughter waves, we note that the b_e - and k_z^2/k_{\perp}^2 -terms represent corrections, and that, ignoring these, the order 0 solution is $\omega_1^2 \approx \omega_{ce}^2 \omega_{pi}^2 / \omega_{UH}^2 = \omega_{LH}^2$, i.e. a non-propagating oscillation at the LH frequency, ω_{LH} , which is a resonance for cold electromagnetic plasma waves. Now, expanding (40) to order 1 in b_e and k_z^2/k_{\perp}^2 around $\omega_1 = \omega_{LH}$, also using the simple plasma identities $\omega_{pe}^2/\omega_{pi}^2 = m_i/(Z_i m_e)$ and $|\omega_{ce}| \omega_{ci} / \omega_{LH}^2 = \omega_{UH}^2 / \omega_{pe}^2$, the dispersion relation of the low-frequency daughter waves is found to be,

$$\omega_1^2 \approx \omega_{LH}^2 \left[1 + 3 \left(\frac{\omega_{pe}^2}{4\omega_{UH}^2} + \frac{T_i}{Z_i T_e} \frac{\omega_{UH}^2}{\omega_{pe}^2} \right) b_e + \frac{m_i}{Z_i m_e} \frac{k_z^2}{k_{\perp}^2} \right], \tag{41}$$

which describes so-called warm LH waves. The above dispersion relation was obtained in [1] and is similar to the one used by [2] for $\omega_{pe}^2 \ll \omega_{ce}^2$ and the electrostatic version given by [52] for $\omega_{pe}^2 \gg \omega_{ce}^2$. Evidently, the warm LH waves have a cut-off at $\omega_1 = \omega_{LH}$ and propagating waves only exist for $\omega_1 > \omega_{LH}$, meaning that the frequency shift of the high-frequency daughter waves for PDIs with warm LH low-frequency daughter waves should always exceed ω_{LH} . It is also clear that the above dispersion relation requires $k_z^2/k_{\perp}^2 \lesssim Z_i m_e / m_i \ll 1$, which is a strict requirement on the smallness of k_z^2/k_{\perp}^2 indeed. Following [1–3], we shall employ (41) when discussing both the resonant and the non-resonant PDIs. However, in the non-resonant case the mode leading to the largest γ , or the largest G , may deviate somewhat from the one given by the above dispersion relation, as the underlying assumption of $|\text{Im}[\epsilon(\mathbf{k}, \omega_1)]| \ll |\text{Re}[\epsilon(\mathbf{k}, \omega_1)]|$ is not generally satisfied here. This effect should not significantly change the results of the following analysis, and we further note that finding an unstable mode, even if it is not the most unstable one, will still imply the existence of a PDI, thus giving an upper bound of the PDI threshold. Nevertheless, a detailed study of the dispersion relation in the non-resonant case, and its consequences for the predicted ω_1 , may be of some interest for future work.

As was done for the warm UH waves, we compute the group velocity, $\mathbf{v}_g(\mathbf{k}, \omega_1) = [\partial \omega_1^2(\mathbf{k}) / \partial \mathbf{k}] / (2\omega_1)$, of the warm LH waves,

$$\begin{aligned}
 \mathbf{v}_g(\mathbf{k}, \omega_1) = \frac{\omega_{LH}^2}{k_{\perp} \omega_1} \left\{ \left[3 \left(\frac{\omega_{pe}^2}{4\omega_{UH}^2} + \frac{T_i}{Z_i T_e} \frac{\omega_{UH}^2}{\omega_{pe}^2} \right) b_e \right. \right. \\
 \left. \left. - \frac{m_i}{Z_i m_e} \frac{k_z^2}{k_{\perp}^2} \right] \mathbf{e}_{\perp} + \frac{m_i}{Z_i m_e} \frac{k_z}{k_{\perp}} \mathbf{e}_z \right\}. \tag{42}
 \end{aligned}$$

Similar to $\mathbf{v}_g(-\mathbf{k}, \omega_2)$, $\mathbf{v}_g(\mathbf{k}, \omega_1)$ is relatively small for $k_z = 0$, resulting in a low resonant PDI threshold in inhomogeneous plasmas, but acquires a significant z -component for $k_z \neq 0$, even when $k_z^2/k_{\perp}^2 \ll Z_i m_e / m_i$. Note also that $\mathbf{v}_g(\mathbf{k}, \omega_1)$ and $\mathbf{v}_g(-\mathbf{k}, \omega_2)$ are parallel for $k_z = 0$ and $\omega_{pe}^2 < 3\omega_{ce}^2$, making the back-scattering instability impossible in this case. We finally calculate $\Gamma(\mathbf{k}, \omega_1) = \text{Im}[\epsilon(\mathbf{k}, \omega_1)] / \{ \partial \text{Re}[\epsilon(\mathbf{k}, \omega)] / \partial \omega \}_{\omega=\omega_1}$, using

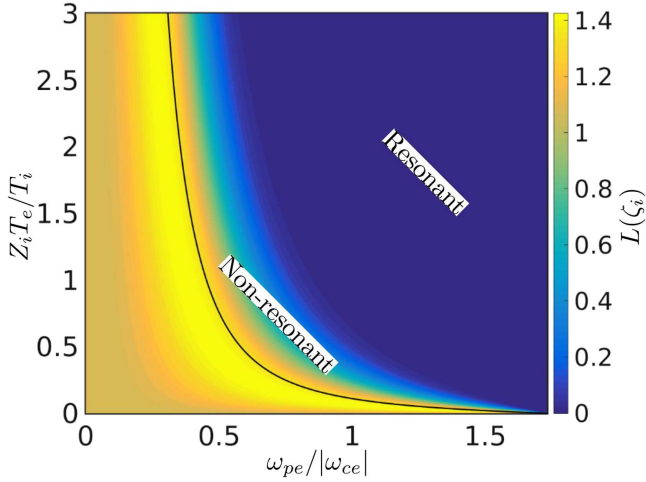


Figure 7. Contour plot of $L(\zeta_i)$ and the black line at which $\zeta_i^2 = 2$ versus $\omega_{pe}/|\omega_{ce}|$ and $Z_i T_e/T_i$, with ζ_i^2 from (46) for a deuterium-like plasma, $m_i/(Z_i m_e) = 3.67 \times 10^3$. Areas where the PDI is resonant and non-resonant are marked with text boxes. The analytical approximation breaks down below the $\zeta_i^2 = 2$ line. In the experiment $\omega_{pe}/|\omega_{ce}| \approx 0.5$ and $Z_i T_e/T_i \approx 1$, placing the PDI in the non-resonant region.

that $\partial \text{Re}[\epsilon(\mathbf{k}, \omega)]/\partial \omega \approx \partial \text{Re}[\chi_i(\mathbf{k}, \omega)]/\partial \omega \approx 2\omega_{pi}^2/\omega^3$,

$$\Gamma(\mathbf{k}, \omega) \approx \sqrt{\pi} \frac{\omega_1^2}{k_{\perp}^2 v_{Ti}^2} \left[\frac{\omega_1}{k_{\perp} v_{Ti}} e^{-\omega_1^2/(k_{\perp}^2 v_{Ti}^2)} + \frac{T_i}{Z_i T_e} \frac{\omega_1}{|k_z| v_{Te}} e^{-\omega_1^2/(k_z^2 v_{Te}^2)} \right] \omega_1 + \frac{\omega_{pe}^2}{2\omega_{ce}^2} \frac{\omega_1^2}{\omega_{pi}^2} \nu_e, \quad (43)$$

which shows that warm LH waves are subject to ion Landau damping (first term), electron Landau damping (second term), and electron collisional damping (third term).

3.2. Parametric decay into warm UH and warm LH waves

We now have all the ingredients necessary for studying PDIs in which the X-mode pump wave decays into a warm UH wave and a warm LH wave near the UHR. We restrict our attention to cases with $k_z = 0$ since a small, but finite, k_z^2/k_{\perp}^2 will rapidly increase convective losses parallel to \mathbf{B} without altering the propagation perpendicular to \mathbf{B} appreciably; a discussion including finite k_z within the dipole approximation is found in [1]; if the dipole approximation is abandoned, at least one of the daughter waves must have finite $|k_z| \sim |k_{0z}| \lesssim 3 \text{ cm}^{-1}$ ($k_z^2/k_{\perp}^2 \lesssim 10^{-4}$) to satisfy the selection rules in the ASDEX Upgrade discharge under consideration, but this should not significantly alter the results of the following analysis in the non-resonant case [2] or in the resonant case, if $k_z \approx k_{0z}$ for the warm UH wave here. Our goal is first to evaluate b_e from the selection rules, to determine the conditions under which the PDI is resonant and non-resonant, and the limits of validity for this analytical approach. In order to allow easier manipulation, we rewrite (41) and (35) as $\omega_1 = \omega_{LH} \sqrt{1 + A_1 b_e} \approx \omega_{LH} (1 + A_1 b_e/2)$ and $\omega_2^2 = \omega_{UH}^2 - \omega_{pe}^2 A_2 b_e$, with $A_1 = 3\{\omega_{pe}^2/(4\omega_{UH}^2) + [T_i/(Z_i T_e)]\omega_{UH}^2/\omega_{pe}^2\}$ and $A_2 = 1/[1 - \omega_{pe}^2/$

$(3\omega_{ce}^2)]$, respectively. Then, from the selection rules, $\omega_2^2 = (\omega_0 - \omega_1)^2 \approx (\omega_0 - \omega_{LH})^2 - A_1(\omega_0 - \omega_{LH})\omega_{LH}b_e$, and we find

$$b_e \approx \frac{\omega_{UH}^2 - (\omega_0 - \omega_{LH})^2}{A_2 \omega_{pe}^2 - A_1(\omega_0 - \omega_{LH})\omega_{LH}} \approx \frac{\omega_{UH}^2 - \omega_0^2 + 2\omega_0 \omega_{LH}}{A_2 \omega_{pe}^2 - A_1 \omega_0 \omega_{LH}}, \quad (44)$$

where the last approximation follows by neglecting the ω_{LH}^2 -terms, since $\omega_{LH} \ll \omega_0, \omega_{pe}$. Clearly, the assumption that $b_e \ll 1$ is only valid for $\omega_0^2 \approx \omega_{UH}^2$, i.e. near the UHR of the gyrotron, where (44) gives $b_e = O(\omega_0 \omega_{LH}/\omega_{pe}^2) \ll 1$; however, even here problems arise for $\omega_{pe}^2 \ll \omega_{ce}^2$, as $\omega_0 \gg \omega_{pe}$ and $A_1 \gg T_i/(Z_i T_e)$ in this case. To quantify the limits of validity of the above theory, as well as the conditions under which the resonant and non-resonant PDIs occur, we calculate,

$$\zeta_i^2 = \frac{\omega_1^2}{k_{\perp}^2 v_{Ti}^2} = \frac{Z_i T_e}{2T_i} \frac{\omega_1^2}{\omega_{ci} |\omega_{ce}| b_e} \approx \frac{Z_i T_e}{2T_i} \frac{\omega_{pe}^2}{\omega_{UH}^2} \left(\frac{A_2 \omega_{pe}^2 - A_1 \omega_0 \omega_{LH}}{\omega_{UH}^2 - \omega_0^2 + 2\omega_0 \omega_{LH}} + A_1 \right), \quad (45)$$

since this parameter determines the relative importance of the real and imaginary parts of the ion susceptibility, $\chi_i(\mathbf{k}, \omega) \approx (\omega_{pi}^2/\omega_1^2)[-1 - 3/(2\zeta_i^2) + iL(\zeta_i)]$ with $L(\zeta_i) = 2\sqrt{\pi} \zeta_i^3 e^{-\zeta_i^2}$, and the limit of the validity of this approximate form through the requirement $\zeta_i^2 > 2$; the non-resonant PDI occurs for $L(\zeta_i) \sim 1$, while the resonant PDI occurs for $L(\zeta_i) \ll 1$. A simple expression for ζ_i^2 in terms of the plasma parameters is obtained by setting $\omega_0 \approx \omega_{UH}$ in (45),

$$\zeta_i^2 \approx \frac{Z_i T_e}{4T_i} \frac{\omega_{pe}^2}{\omega_{UH}^2} \left(\frac{A_2 \omega_{pe}^2}{\omega_{UH} \omega_{LH}} + A_1 \right) \approx \frac{Z_i T_e}{4T_i} \sqrt{\frac{m_i}{Z_i m_e}} \frac{\omega_{pe}^3/|\omega_{ce}|^3}{(1 + \omega_{pe}^2/\omega_{ce}^2)[1 - \omega_{pe}^2/(3\omega_{ce}^2)]} + \frac{3}{4}; \quad (46)$$

the last approximation follows from the identity $\omega_{pe}^2/(\omega_{UH} \omega_{LH}) = \sqrt{m_i/(Z_i m_e)} \omega_{pe}/|\omega_{ce}|$ and neglect of the first term of $A_1 = 3\{\omega_{pe}^2/(4\omega_{UH}^2) + [T_i/(Z_i T_e)]\omega_{UH}^2/\omega_{pe}^2\}$ in comparison with $A_2 \omega_{pe}^2/(\omega_{UH} \omega_{LH})$, while the second term of A_1 is kept due to its importance at small $\omega_{pe}/|\omega_{ce}|$. A contour plot of $L(\zeta_i)$ and the line at which $\zeta_i^2 = 2$ for a deuterium-like plasma, $m_i/(Z_i m_e) = 3.67 \times 10^3$, versus $\omega_{pe}/|\omega_{ce}|$ and $Z_i T_e/T_i$ is seen in figure 7. From the figure, it is clear that the PDI will be non-resonant for moderate values of $\omega_{pe}/|\omega_{ce}|$ and $Z_i T_e/T_i$, resonant for large values, and that the analytical approximation breaks down for sufficiently small values. For $t \geq 2.900$ s in ASDEX Upgrade discharge 28286, the UHR is encountered at $\omega_{pe}/|\omega_{ce}| \approx 0.5$ by the CTS probe rays, and the plasma is further modelled as a pure deuterium plasma ($Z_i = 1$, $m_i/m_e = 3.67 \times 10^3$) with $T_i = T_e$, placing the expected PDI in the non-resonant region of figure 7.

Now that the basic questions related to the selection rules have been answered, we turn our attention to the problem of determining γ and the PDI threshold conditions for the non-resonant and resonant cases. Except when determining b_e and

ζ_i , the lowest order approximations ($\omega_1 \approx \omega_{\text{LH}}$ and $\omega_2 \approx \omega_{\text{UH}}$) are used and the b_e -terms neglected, resulting in the following approximate expressions,

$$\chi_i(\mathbf{k}, \omega_1) \approx \frac{\omega_{\text{UH}}^2}{\omega_{ce}^2} [-1 + iL(\zeta_i)],$$

$$1 + \chi_e(\mathbf{k}, \omega_1) \approx \frac{\omega_{\text{UH}}^2}{\omega_{ce}^2} (1 + iC_e), \quad (47)$$

$$\epsilon(\mathbf{k}, \omega_1) \approx i \frac{\omega_{\text{UH}}^2}{\omega_{ce}^2} [L(\zeta_i) + C_e], \quad \left. \frac{\partial \text{Re}[\epsilon(\mathbf{k}, \omega)]}{\partial \omega} \right|_{\omega=\omega_1}$$

$$\approx \frac{2\omega_{\text{UH}}^2}{\omega_{ce}^2 \omega_{\text{LH}}}, \quad \left. \frac{\partial \text{Re}[\epsilon(-\mathbf{k}, \omega)]}{\partial \omega} \right|_{\omega=\omega_2} \approx \frac{2\omega_{\text{UH}}}{\omega_{pe}^2},$$

where $C_e = (\omega_{pe}^2/\omega_{\text{UH}}^2)\nu_e/\omega_{\text{LH}} \ll 1$. Note that $|\epsilon(\mathbf{k}, \omega_1)|$ is indeed small in the resonant case, $L(\zeta_i) \ll 1$, and non-negligible in the non-resonant case, $L(\zeta_i) \sim 1$. An approximate version of μ_e^2 may also be obtained from (14) by noting that the X-mode is a quasi-electrostatic cold UH wave, and thus linearly polarised, near the UHR ($\omega_0 \approx \omega_{\text{UH}}$). From this it follows that all components of \mathbf{E}_0 have the same phase, and further taking $\mathbf{k} = k_{\perp} \mathbf{e}_x$, we find

$$\mu_e^2 \approx \frac{e^2 k_{\perp}^2}{m_e^2 (\omega_0^2 - \omega_{ce}^2)^2} \left(|E_{0x}|^2 + \frac{\omega_{ce}^2}{\omega_0^2} |E_{0y}|^2 \right)$$

$$\approx b_e \frac{\omega_{ce}^2}{\omega_{pe}^2} \left(\frac{\epsilon_0 |E_{0x}|^2}{N_e^{(0)} T_e} + \frac{\omega_{ce}^2}{\omega_{\text{UH}}^2} \frac{\epsilon_0 |E_{0y}|^2}{N_e^{(0)} T_e} \right), \quad (48)$$

which is similar to the μ_e^2 given by [2]. (48) shows that μ_e^2 is generally a small quantity of order $b_e \ll 1$, as assumed when deriving the parametric dispersion relation; exceptions occur when $\omega_{pe}^2 \ll \omega_{ce}^2$ or when the pump wave energy density ($\sim \epsilon_0 |E_0|^2$) is much larger than the thermal energy density ($\sim N_e^{(0)} T_e$), and the weak coupling approximation breaks down, at the UHR. The above expression is clearly maximised for $|E_{0x}| = |E_{0\perp}|$, i.e. $\mathbf{E}_{0\perp} \propto \mathbf{k}$, giving us the following μ_e^2 , useful for deriving the maximum γ ,

$$\mu_e^2 \approx b_e \frac{\omega_{ce}^2}{\omega_{pe}^2} \frac{\epsilon_0 |E_{0\perp}|^2}{N_e^{(0)} T_e}. \quad (49)$$

With (37), (47) and (49), we are now in a position to determine γ for the non-resonant PDI from (28),

$$\gamma \approx \frac{b_e}{8} \frac{1 + L(\zeta_i) C_e}{L(\zeta_i) + C_e} \frac{\epsilon_0 |E_{0\perp}|^2}{N_e^{(0)} T_e} \omega_{\text{UH}} - \frac{\omega_{\text{UH}}^2 + \omega_{ce}^2 \nu_e}{2\omega_{\text{UH}}^2}$$

$$\approx \frac{b_e}{8L(\zeta_i)} \frac{\epsilon_0 |E_{0\perp}|^2}{N_e^{(0)} T_e} \omega_{\text{UH}} - \frac{\omega_{\text{UH}}^2 + \omega_{ce}^2 \nu_e}{2\omega_{\text{UH}}^2}, \quad (50)$$

where $C_e \ll 1 \sim L(\zeta_i)$ has been used in the last approximation. From this we may easily determine the *non-resonant PDI threshold in a homogeneous plasma* ($\gamma > 0$),

$$|E_{0\perp}|^2 > \frac{4L(\zeta_i)}{b_e} \frac{(\omega_{\text{UH}}^2 + \omega_{ce}^2) \nu_e}{\omega_{\text{UH}}^3} \frac{N_e^{(0)} T_e}{\epsilon_0}, \quad (51)$$

which is the generalisation of the expression given by [3] to finite $\omega_{pe}/|\omega_{ce}|$ and $L(\zeta_i) \neq 1$ obtained in [1] (the non-

resonant γ , which is the one of relevance, is approximately 3 ns^{-1} near the UHR in the considered ASDEX Upgrade discharge).

Noting that $\Gamma(\mathbf{k}, \omega_1) \approx [L(\zeta_i)\omega_{\text{LH}} + (\omega_{pe}^2/\omega_{\text{UH}}^2)\nu_e]/2$, we can also determine γ for the resonant PDI from (26),

$$\gamma \approx \frac{1}{2} \left[\sqrt{\left(\frac{L(\zeta_i)}{2} \omega_{\text{LH}} - \frac{\omega_{ce}^2}{\omega_{\text{UH}}^2} \nu_e \right)^2 + \frac{b_e \epsilon_0 |E_{0\perp}|^2}{4 N_e^{(0)} T_e} \omega_{\text{UH}} \omega_{\text{LH}}} \right. \\ \left. - \frac{L(\zeta_i)}{2} \omega_{\text{LH}} - \nu_e \right] \quad (52)$$

and the corresponding *resonant PDI threshold in a homogeneous plasma*,

$$|E_{0\perp}|^2 > \frac{4[L(\zeta_i) + C_e] (\omega_{\text{UH}}^2 + \omega_{ce}^2) \nu_e N_e^{(0)} T_e}{b_e \omega_{\text{UH}}^3 \epsilon_0}, \quad (53)$$

which is very similar to that of the non-resonant PDI, but since we are now in the region of $L(\zeta_i) \ll 1$, its value is generally much smaller. For negligible damping, (52) becomes

$$\gamma \approx \frac{1}{4} \sqrt{\frac{b_e \epsilon_0 |E_{0\perp}|^2}{N_e^{(0)} T_e} \omega_{\text{UH}} \omega_{\text{LH}}}, \quad (54)$$

which is similar to the γ obtained by [4] for $\omega_{ci} \ll \omega_{pi}$, while being $\omega_{\text{UH}}^2/\omega_{pe}^2$ times that reported by [5, 27] within the weak coupling and dipole approximations, indicating that their approach reproduces a parametric dispersion relation similar to that of [18] here.

While the homogeneous PDI thresholds are of some interest, the actual thresholds are generally determined by inhomogeneities. For the resonant PDI well above the homogeneous threshold we can ignore damping and use γ from (54), while the magnitudes of the group velocities of the daughter waves for $\mathbf{k} \perp \mathbf{B}$ become $v_g(\mathbf{k}, \omega_1) \approx A_1 b_e \omega_{\text{LH}}/k_{\perp}$ and $v_g(-\mathbf{k}, \omega_2) \approx A_2 b_e \omega_{pe}^2/(\omega_{\text{UH}} k_{\perp})$, such that (32) gives

$$G \approx \frac{\pi}{8A_1 A_2} \frac{\omega_{\text{UH}}^2}{\omega_{pe}^2} \frac{l^2}{r_{Le}^2} \frac{\epsilon_0 |E_{0\perp}|^2}{N_e^{(0)} T_e},$$

$$|E_{0\perp}|^2 > 16A_1 A_2 \frac{\omega_{pe}^2}{\omega_{\text{UH}}^2} \frac{r_{Le}^2}{l^2} \frac{N_e^{(0)} T_e}{\epsilon_0}; \quad (55)$$

the threshold is determined by the condition $G > 2\pi$, and all quantities are to be evaluated at $x = x_r$. Before an exact threshold can be obtained from the above expression, we need to determine

$$\frac{1}{l^2} = \left| \left[\left. \frac{\partial k_x(x, \omega_1)}{\partial x} \right|_{x=x_r} - \left. \frac{\partial k_x(x, \omega_2)}{\partial x} \right|_{x=x_r} \right] \right|$$

$$= \frac{1}{2\sqrt{b_e} r_{Le}} \left| \left[\left. \frac{\partial b_e(x, \omega_1)}{\partial x} \right|_{x=x_r} - \left. \frac{\partial b_e(x, \omega_2)}{\partial x} \right|_{x=x_r} \right] \right|, \quad (56)$$

where the last equality follows from $k_x = k_{\perp} = \sqrt{b_e}/r_{Le}$ (for $\mathbf{k} = k_{\perp} \mathbf{e}_x$) and the fact that the selection rules are exactly satisfied at $x = x_r$. The x -derivatives of $b_e(x, \omega_1) = [\omega_1^2 - \omega_{\text{LH}}^2(x)]/[A_1(x)\omega_{\text{LH}}^2(x)]$ and $b_e(x, \omega_2) = [\omega_{\text{UH}}^2(x) -$

$\omega_2^2]/[A_2(x)\omega_{pe}^2(x)]$ may be evaluated, neglecting terms proportional to the small quantities $[\omega_1^2 - \omega_{LH}^2(x)]/[A_1(x)\omega_{LH}^2(x)]$ and $[\omega_{UH}^2(x) - \omega_2^2]/[A_2(x)\omega_{pe}^2(x)]$,

$$\begin{aligned} \frac{\partial b_e(x, \omega_1)}{\partial x} &\approx -\frac{1}{A_1(x)\omega_{LH}^2(x)} \frac{d\omega_{LH}^2(x)}{dx} \\ &= -\frac{1}{A_1(x)} \left[\frac{\omega_{ce}^2(x)}{\omega_{UH}^2(x)} \frac{1}{L_N(x)} + \frac{\omega_{pe}^2(x)}{\omega_{UH}^2(x)} \frac{2}{L_B(x)} \right], \\ \frac{\partial b_e(x, \omega_2)}{\partial x} &\approx \frac{1}{A_2(x)\omega_{pe}^2(x)} \frac{d\omega_{UH}^2(x)}{dx} \\ &= \frac{1}{A_2(x)} \left[\frac{1}{L_N(x)} + \frac{\omega_{ce}^2(x)}{\omega_{pe}^2(x)} \frac{2}{L_B(x)} \right]; \end{aligned} \quad (57)$$

$L_N(x) = N_e^{(0)}(x)/[dN_e^{(0)}(x)/dx] = N_i^{(0)}(x)/[dN_i^{(0)}(x)/dx]$ and $L_B = B(x)/[dB(x)/dx]$ are the density and magnetic field strength gradient scale lengths, respectively. Plugging these expressions into (56), we find

$$\begin{aligned} \frac{1}{l^2} &\approx \frac{1}{\sqrt{b_e}} \left| \left(\frac{\omega_{ce}^2}{A_1\omega_{UH}^2} + \frac{1}{A_2} \right) \frac{1}{2r_{Le}L_N} \right. \\ &\quad \left. + \left(\frac{\omega_{pe}^2}{A_1\omega_{UH}^2} + \frac{\omega_{ce}^2}{A_2\omega_{pe}^2} \right) \frac{1}{r_{Le}L_B} \right|, \end{aligned} \quad (58)$$

and thus the *resonant PDI threshold in an inhomogeneous plasma* is

$$\begin{aligned} |E_{0\perp}|^2 &> \frac{8}{\sqrt{b_e}} \frac{\omega_{pe}^2}{\omega_{UH}^2} \left| \left(\frac{A_2\omega_{ce}^2}{\omega_{UH}^2} + A_1 \right) \frac{r_{Le}}{L_N} \right. \\ &\quad \left. + \left(\frac{A_2\omega_{pe}^2}{\omega_{UH}^2} + \frac{A_1\omega_{ce}^2}{\omega_{pe}^2} \right) \frac{2r_{Le}}{L_B} \right| \frac{N_e^{(0)}T_e}{\epsilon_0}. \end{aligned} \quad (59)$$

For the non-resonant PDI well above the homogeneous threshold, we may neglect collisional damping and find $\gamma \approx \{b_e/[8L(\zeta_i)]\}[\epsilon_0|E_{0\perp}|^2/(N_e^{(0)}T_e)]\omega_{UH}$, while $v_g(-\mathbf{k}, \omega_2) \approx A_2b_e\omega_{pe}^2/(\omega_{UH}k_\perp)$ still holds, such that (31) yields

$$\begin{aligned} G &\approx \frac{k_\perp \ell}{4A_2L(\zeta_i)} \frac{\omega_{UH}^2 \epsilon_0 |E_{0\perp}|^2}{\omega_{pe}^2 N_e^{(0)}T_e}, \\ |E_{0\perp}|^2 &> \frac{8\pi A_2 L(\zeta_i)}{k_\perp \ell} \frac{\omega_{pe}^2 N_e^{(0)}T_e}{\omega_{UH}^2 \epsilon_0}, \end{aligned} \quad (60)$$

where the threshold is again determined by the condition $G > 2\pi$. This is the generalisation of the non-resonant inhomogeneous PDI thresholds given by [2, 3] obtained in [1]. By setting $\ell \approx l$, we obtain an explicit expression for the

non-resonant PDI threshold in an inhomogeneous plasma,

$$\begin{aligned} |E_{0\perp}|^2 &> \frac{8\pi L(\zeta_i)}{b_e^{3/4}} \frac{\omega_{pe}^2}{\omega_{UH}^2} \\ &\quad \times \sqrt{A_2 \left| \left(\frac{A_2\omega_{ce}^2}{A_1\omega_{UH}^2} + 1 \right) \frac{r_{Le}}{2L_N} + \left(\frac{A_2\omega_{pe}^2}{A_1\omega_{UH}^2} + \frac{\omega_{ce}^2}{\omega_{pe}^2} \right) \frac{r_{Le}}{L_B} \right|} \\ &\quad \times \frac{N_e^{(0)}T_e}{\epsilon_0}. \end{aligned} \quad (61)$$

Now that theoretical electric field PDI thresholds for decay of the cold X-mode pump wave into warm UH and LH daughter waves have been determined for both the resonant and non-resonant cases, we may determine the gyrotron power threshold near the UHR in the ASDEX Upgrade discharge considered earlier.

4. Investigation of PDIs near the UHR in ASDEX Upgrade

4.1. Field enhancement near the UHR

The main problem in going from the electric field thresholds to gyrotron power thresholds is to connect $|E_0|$ to P_0 for various gyrotron settings at various points in the plasma. Away from the UHR, this may be done relatively simply if we assume the beam to have a narrow Gaussian profile around the CTS probe ray. With this assumption, we can evaluate all wave propagation related quantities on the CTS probe ray, and \mathbf{E}_0 may be written as,

$$\mathbf{E}_0(\rho, s) = |E_0(0, s)| e^{-\rho^2/W^2(s)} \mathbf{e}_0(\mathbf{r}(s), \mathbf{k}_0(s), \omega_0), \quad (62)$$

where ρ is the shortest distance to the CTS probe ray, occurring at the point s along the CTS probe ray, while $W(s)$ and $\mathbf{e}_0(\mathbf{r}(s), \mathbf{k}_0(s), \omega_0)$ define the beam width and the geometric optics (X-mode) unit polarisation vector at the point on the CTS probe ray characterised by s , respectively. The relation between $|E_0(0, s)|$ and P_0 is found by first taking the wave energy at a given s to propagate at the group velocity of the corresponding point on the CTS probe ray, $\mathbf{v}_g(\mathbf{r}(s), \mathbf{k}_0(s), \omega_0)$. The total wave energy density, $U(\rho, s)$, is determined in a similar manner: $U(\rho, s) = \mathcal{M}(\mathbf{r}(s), \mathbf{k}_0(s), \omega_0)|E_0(\rho, s)|^2$, where $\mathcal{M}(\mathbf{r}, \mathbf{k}, \omega) = \mathbf{e}_0^*(\mathbf{r}, \mathbf{k}, \omega) \cdot [\partial \mathbf{M}(\mathbf{r}, \mathbf{k}, \omega)/\partial \omega] \cdot \mathbf{e}_0(\mathbf{r}, \mathbf{k}, \omega)$, with \mathbf{M} being the Maxwell operator from [51]. Now, the intensity of the beam is $I(\rho, s) = U(\rho, s)v_g(\mathbf{r}(s), \mathbf{k}_0(s), \omega_0) = \mathcal{M}(\mathbf{r}(s), \mathbf{k}_0(s), \omega_0)v_g(\mathbf{r}(s), \mathbf{k}_0(s), \omega_0)|E_0(0, s)|^2 e^{-2\rho^2/W^2(s)}$ and the total total power at a given s , $P(s) = \mathcal{F} e^{-\tau(s)} P_0$, is found by the integral $P(s) = 2\pi \int_0^\infty \rho I(\rho, s) d\rho$, assuming a large radius of curvature of the CTS probe ray compared with $W(s)$, from which

$$\begin{aligned} |E_0(0, s)| &= \sqrt{\frac{2\mathcal{F} e^{-\tau(s)} P_0}{\pi W^2(s) v_g(\mathbf{r}(s), \mathbf{k}_0(s), \omega_0) \mathcal{M}(\mathbf{r}(s), \mathbf{k}_0(s), \omega_0)}}. \end{aligned} \quad (63)$$

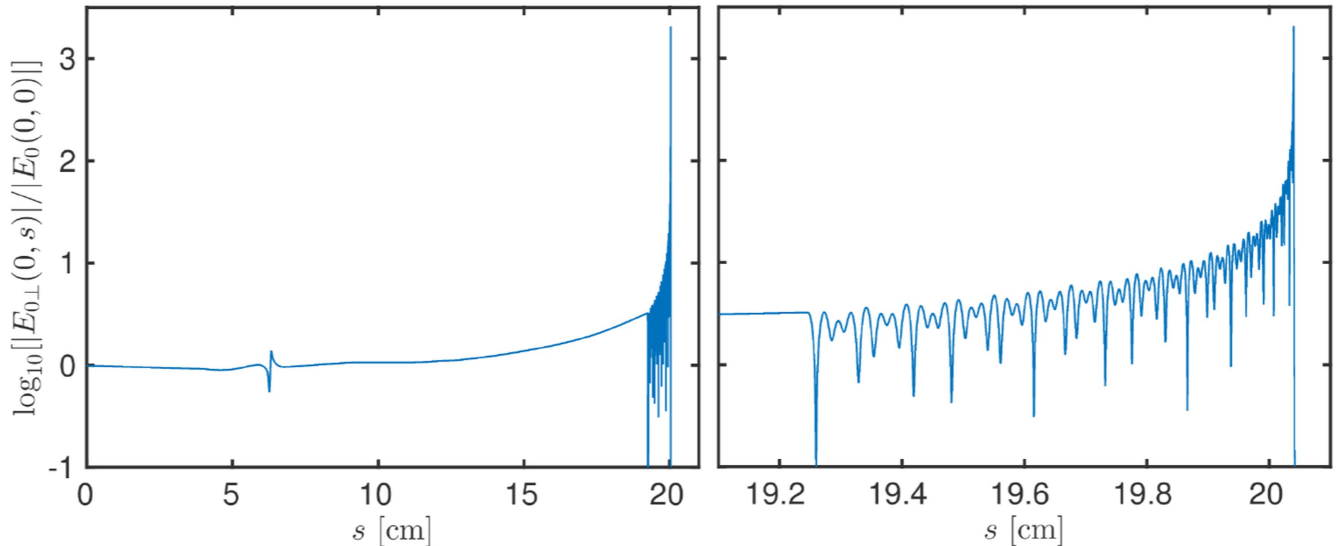


Figure 8. Logarithmic plots of the field enhancement along the ray of the reflected X-mode radiation for the peaked $N_e^{(0)}$ - and T_e -profiles at $t = 2.900$ s in ASDEX Upgrade discharge 28286.

For electromagnetic waves in a vacuum, $v_g = c$ and $\mathcal{M} = \epsilon_0/2$, (63) coincides with the well-known expression for a Gaussian beam; (63) also agrees with the result of [16] for propagation of a Gaussian beam parallel to the density gradient (and perpendicular to \mathbf{B}) in a plasma slab, using v_g and \mathcal{M} for cold X-mode radiation. $W(s)$ is undetermined by the above discussion, but since we are only interested in an estimate of \mathbf{E}_0 , we take it to be that of a free-space Gaussian beam, $W^2(s) = W_0^2 + 4c^2(s - s_0)^2/(\omega_0 W_0)^2$, with $W_0 = 2.29$ cm and $s_0 = 85.4$ cm (for $s = 0$ at the gyrotron launch point) characterising the beam waist and focal point of the ASDEX Upgrade gyrotrons, respectively; more accurate values of $W(s)$, as well as \mathbf{E}_0 itself, away from the UHR may be obtained using beam tracing codes such as TORBEAM [53] or WKBeam [54]. Note that the beam parameters are unchanged by the reflection from the high-field side wall, as it is modelled by a locally plane mirror.

(63) clearly shows field amplification at points with low group velocity, e.g. near the UHR, and $|E_0|$ is additionally seen to be proportional to $\sqrt{\mathcal{F} e^{-\tau(s)} P_0}/W(s)$, which is physically sensible. It does, however, just as clearly break down at the exact UHR, where $v_g \rightarrow 0$ and $|E_0(0, s)| \rightarrow \infty$, due to the failure of the geometric optics approximations at this point. Very close to the UHR we are thus forced to implement a full-wave solution in order to obtain meaningful results; this paper uses a simple 1D model, also used in [1], to estimate the field enhancement in the above region. The model, inspired by [15], is based on the cold plasma fluid equations, but includes collisional damping to limit $|E_0|$ at the UHR.

The procedure used for determining the field enhancement is as follows: first, the CTS probe ray is traced, from which \mathcal{F} , τ , and $\mathbf{E}_0(0, s)$ (away from the UHR) are calculated. At a point close to the UHR, $\mathbf{r}(s_f)$, the ray tracing is stopped and the plasma parameters used in the 1D full-wave treatment are extracted along a line parallel to $\mathbf{k}_0(s_f)$. Finally, $\mathbf{E}_0(0, s)$ is calculated close to the UHR by solving the 1D full-wave equations for an X-mode wave and equating the

amplitude to that obtained from ray tracing at $\mathbf{r}(s_f)$. Details of the implementation are found in [1]. Once the above quantities have been calculated, $\mathbf{E}_0(\rho, s)$ may be found from (62): $\mathbf{E}_0(\rho, s) = \mathbf{E}_0(0, s)e^{-\rho^2/W^2(s)}$.

It is clear that the above procedure contains a somewhat arbitrary step, namely the selection of the point at which the switch from ray tracing to the 1D full-wave solution is made and the length of the domain in which the 1D full-wave equations are solved. The choice of the transition point has some influence on the precise field profile near the UHR, but the exact domain length appears to be unimportant, so long as the UHR is present within the domain. The CTS probe ray may change direction rather abruptly at the transition between the ray tracing and the 1D full-wave regions, and no account can be made of the precise geometry and resulting refractive effects in the 1D full-wave model. Despite these shortcomings, the method is sufficient for obtaining the estimates in which we are interested. In the following, the transition between ray tracing and the 1D full-wave treatment is made at the same grid point of the X-mode ray (only changed for the peaked profile at $t = 3.600$ s) and the length of the 1D full-wave domain is 3 cm (except at $t = \{3.600, 3.700$ s) for the peaked profiles, where it is 2.5 cm). These parameters are chosen to ensure that the UHR is encountered and that the results are physically reasonable, i.e. avoiding artificial infinite field enhancements resulting from fast decay of the amplitude in the evanescent region and limited numerical accuracy.

Figure 8 contains logarithmic plots of $|E_{0\perp}(0, s)|/|E_0(0, 0)|$, calculated using the method described above, along the reflected X-mode ray at $t = 2.900$ s shown in figure 4 ($s = 0$ on the high-field side wall); these plots are illustrative of the field enhancement obtained in all cases. The left pane of figure 8 displays $|E_{0\perp}(0, s)|/|E_0(0, 0)|$ along the entire ray; apart from field enhancement near the UHR at $s \approx 20$ cm, it also shows the behaviour around the ECR at $s \approx 7$ cm. The right pane of figure 8 displays $|E_{0\perp}(0, s)|/|E_0(0, 0)|$ close to

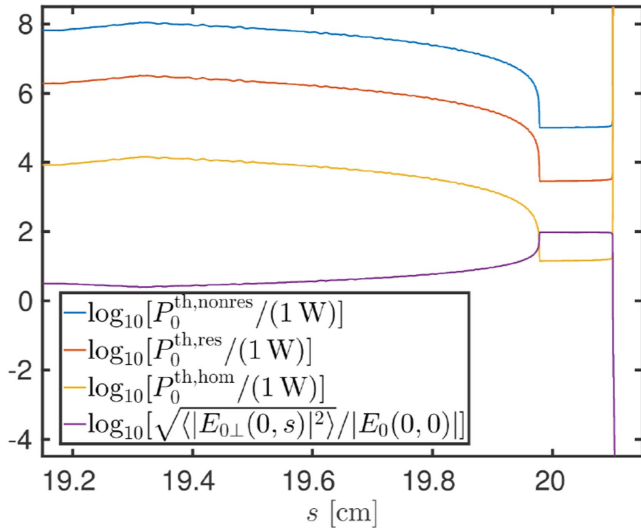


Figure 9. Logarithmic plots of the power thresholds and root mean square field enhancement along the ray of the reflected X-mode radiation for the peaked profile in ASDEX Upgrade discharge 28286 at $t = 2.900$ s.

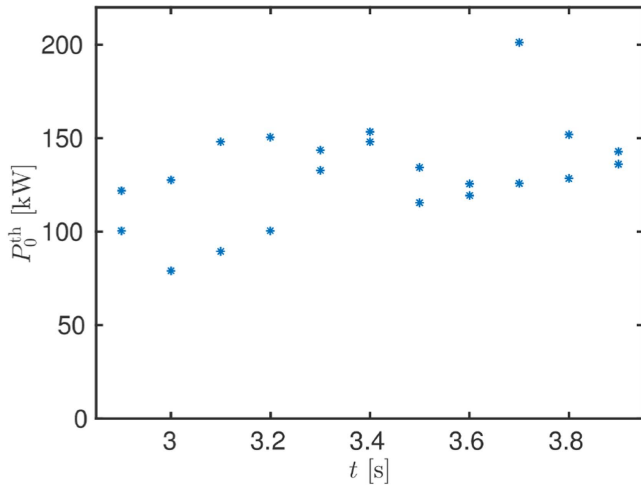


Figure 10. Gyrotron power threshold, P_0^{th} , versus t in ASDEX Upgrade discharge 28286. $P_0^{\text{th}} \sim 100$ kW in the shown part of the discharge and generally below the nominal gyrotron power, $P_0 = 200$ kW.

the UHR, and particularly shows the reduction of the pump wavelength (increase of k_0) as the UHR is approached, expected from cold plasma theory. A similar effect was not observed by [1] due to an error in the association of $|E_{0\perp}|$ with s in the 1D full-wave code used in that work. The transition between ray tracing and the 1D full-wave model is clearly visible in both panes, since the plane wave-like variation on the scale of the wavelength along the ray is factored out of \mathbf{E}_0 in the geometric optics approximation, while such a factorisation is generally not possible in the full-wave case and therefore not carried out; the amplitude of $|E_{0\perp}(0, s)|$ does, however, vary relatively smoothly across the transition, as it should. A very large field enhancement, $|E_{0\perp}(0, s)|/|E_0(0, 0)| \approx 2 \times 10^3$, is obtained at the UHR (just before the evanescence region) in all cases, pointing to this being the maximum field

enhancement allowed by collisions, which is confirmed by its reduction when the collision frequency increased keeping all other quantities constant.

4.2. PDI thresholds and frequency shifts

Now that we have a model for $|E_{0\perp}(0, s)|$ as a function of P_0 around the UHR, we proceed to determine the homogeneous and inhomogeneous thresholds for resonant and non-resonant PDIs using (51), (53), (59), and (61), with b_e and ζ_i given by (44) and (45), respectively. The calculation is only carried out along the CTS probe ray, as the lowest thresholds are expected to occur along it. Since (51) and (53) are essentially identical in the region $L(\zeta_i) \sim 1$, where equation (51) is valid, only the homogeneous threshold given by (53) is plotted, where ν_e is identified with the electron(-ion) Coulomb collision frequency in a simple plasma given by [51]. L_N and L_B are calculated from the variation along the CTS probe ray, taking the angle between \mathbf{k}_0 and \mathbf{B} into account, consistent with the treatment of the plasma parameter gradients in the 1D full-wave model [1]. The value of $|E_{0\perp}|$ used in (53), (59) and (61) also needs some consideration due to the rapid variation of $|E_{0\perp}|$ close to the UHR. We are modelling the PDI as occurring over a distance $l(s_r)$ around the point s_r at which the selection rules are exactly satisfied, and since $G \propto |E_{0\perp}|^2$ for both the resonant and non-resonant PDI in an inhomogeneous plasma, it is therefore appropriate use $|E_{0\perp}|^2$ averaged over an interval of length $l(s_r)$ around s_r , denoted by $\langle |E_{0\perp}|^2 \rangle$, in (59) and (61); $\langle |E_{0\perp}|^2 \rangle$ is also used in (53), as this threshold is mainly included to assess the importance of collisional damping on the PDI threshold. For simplicity, $\langle |E_{0\perp}|^2 \rangle$ is calculated in an interval $s \in [s_r - l(s_r)/2, s_r + l(s_r)/2]$ at each s_r along the CTS probe ray. Once $\langle |E_{0\perp}|^2 \rangle$ is known for a given P_0 , the gyrotron power threshold, P_0^{th} , is easily obtained using the fact that $\langle |E_{0\perp}|^2 \rangle \propto P_0$: $P_0^{\text{th}} = [\langle |E_{0\perp}|^{\text{th}} \rangle / \langle |E_{0\perp}|^2 \rangle] P_0$, with $\langle |E_{0\perp}|^{\text{th}} \rangle$ representing the right hand sides of (53) (homogeneous), (59) (inhomogeneous resonant) and (61) (inhomogeneous non-resonant); the resulting gyrotron power thresholds are denoted $P_0^{\text{th,hom}}$, $P_0^{\text{th,res}}$ and $P_0^{\text{th,nonres}}$, respectively.

Figure 9 shows logarithmic plots of $P_0^{\text{th,nonres}}$, $P_0^{\text{th,res}}$ and $P_0^{\text{th,hom}}$ in watt, as well as $\sqrt{\langle |E_{0\perp}(0, s)|^2 \rangle} / |E_0(0, 0)|$, close to the UHR at $t = 2.900$ s for the ray in figure 4; it is illustrative of all cases. Evidently, $P_0^{\text{th,hom}}$ is always much lower than $P_0^{\text{th,nonres}}$ and $P_0^{\text{th,res}}$, which is necessary for the neglect of collisions in the calculation of these. As expected from the discussion of figure 7, the PDI is non-resonant in the considered ASDEX Upgrade equilibrium, with $P_0^{\text{th,nonres}}$ being almost two orders of magnitude larger than $P_0^{\text{th,res}}$. Further, $P_0^{\text{th,nonres}}$, $P_0^{\text{th,res}}$ and $P_0^{\text{th,hom}}$ increase slightly, while $\sqrt{\langle |E_{0\perp}(0, s)|^2 \rangle} / |E_0(0, 0)|$ decreases slightly, at the transition from ray tracing to the 1D full-wave model due to the inclusion of wave lobes (compare with figure 8) and all quantities display a flat region around the point of maximum field enhancement at the UHR; the lengths of the above features indicate that $l \sim 1$ mm near the UHR. The minimum non-resonant gyrotron power threshold in figure 9 is $P_0^{\text{th}} \approx 100$ kW, which is on the order of the nominal experimental gyrotron power of 200 kW. We thus expect the PDI

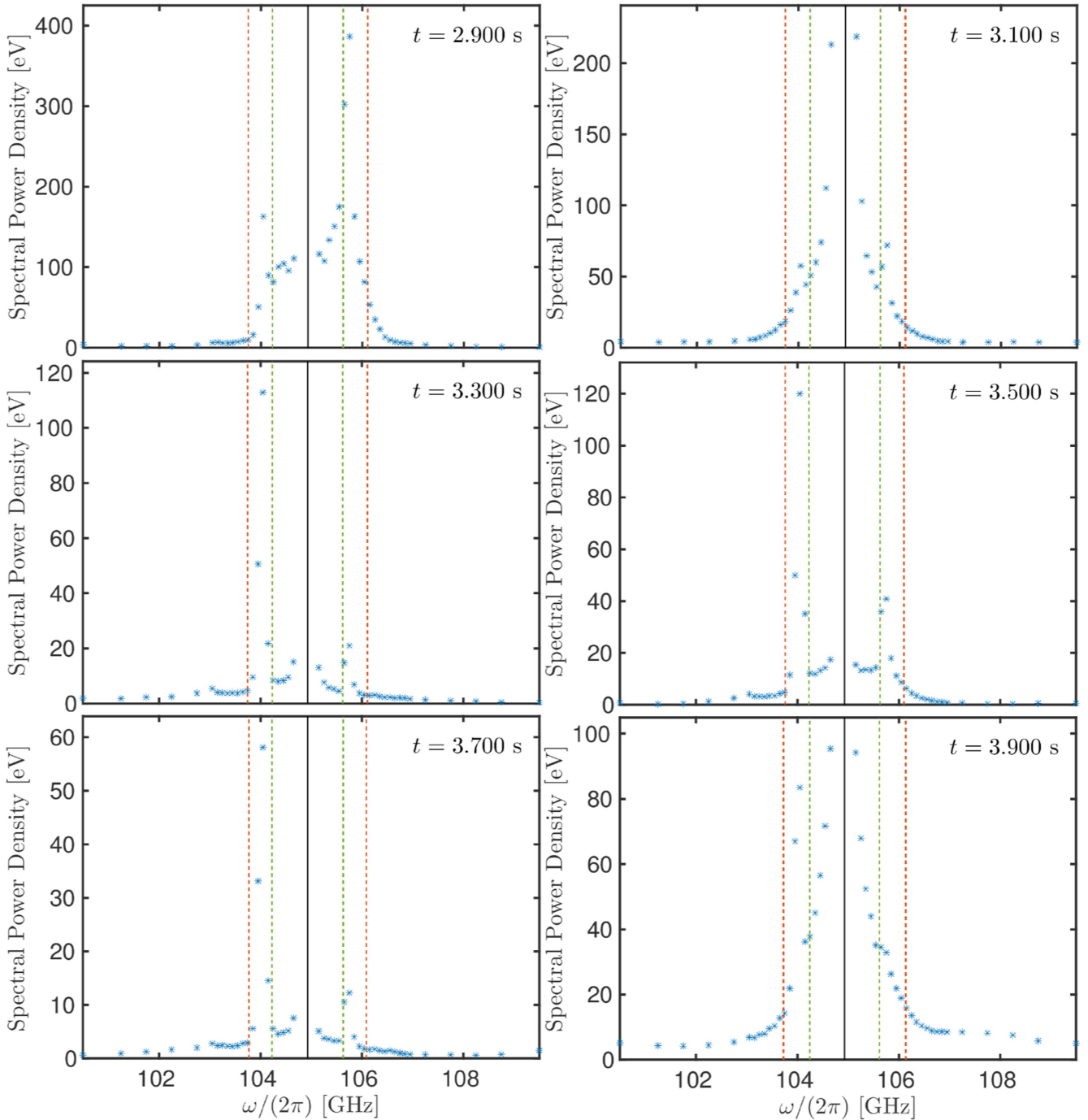


Figure 11. Predicted high-frequency daughter wave frequencies (orange dashed lines) and the gyrotron frequency shifted by the LH frequencies at the points of P_0^{th} (green dashed lines), along with the experimental CTS power spectra for $t \geq 2.900$ s in ASDEX Upgrade discharge 28286.

to occur for the peaked $N_e^{(0)}$ - and T_e -profiles at $t = 2.900$ s, allowing it to account for the peaks observed in figure 3 at this time point.

Figure 10 shows P_0^{th} , determined in a manner similar to that from figure 9, for $t \geq 2.900$ s. Clearly, $P_0^{\text{th}} \sim 100$ kW in all cases, and the presented theory thus predicts the occurrence of a PDI in the analysed part of the discharge where peaks are also observed in figure 3. In order to assess if it is reasonable to associate the observed peaks with the

mentioned PDI, we plot the predicted high-frequency daughter wave frequencies, $\omega_0 \pm \omega_1 = \omega_0 \pm \omega_{\text{LH}} \sqrt{1 + A_1 b_e}$, along with the observed CTS spectra, for $t \geq 2.900$ s in figure 11; the LH frequencies at the points of P_0^{th} are also plotted for reference. Evidently, the dipole PDI theory overestimates the peak frequency shift of approximately 850 MHz, giving values in the range (1.18 ± 0.03) GHz, while the simple estimate of the LH frequency underestimates it, giving values in the range

(695 ± 8) MHz. The dipole PDI theory does, however, provide an upper bound on the frequency shift of the peak, and the LH frequency a lower bound. The latter point may be understood from the fact that warm LH waves have $\omega_1 \geq \omega_{\text{LH}}$ according to their dispersion relation, (41), while the former may be understood if we assume the warm UH wave to be forward scattered by the pump wave, following a line of inquiry similar to that of [5], such that $k_1 = |k_2 - k_0|$ (and hence the relevant b_e) is maximised in the dipole limit, where $k_0 = 0$, assuming $k_2 > k_0$. The above considerations indicate that it is reasonable to associate the observed peaks with parametric decay of the (reflected) X-mode pump wave into a warm UH wave and a warm LH wave. Additionally, the upper and lower bounds on the frequency shift of the PDI peaks are important for the design of notch filters to protect millimetre-wave diagnostics against these. However, in order to determine the precise frequency shift of the peak top, a theory of the above PDI taking non-zero \mathbf{k}_0 , as well as possible deviations from the resonant warm LH wave dispersion relation, into account is necessary.

5. Conclusions and outlook

In this paper we have investigated parametric decay of an electromagnetic pump wave into two electrostatic daughter waves, particularly an X-mode pump wave decaying into a warm UH wave and a warm LH wave. This PDI has been shown to occur for $\omega_{pe} < \sqrt{3}|\omega_{ce}|$, and analytical $|E_{0\perp}|^2$ -thresholds have been derived for homogeneous and inhomogeneous plasmas in the resonant and non-resonant cases. The theory has been applied to CTS experiments at ASDEX Upgrade where 105 GHz O-mode radiation is injected from the low-field side, reflected by the high-field side wall, and part of the reflected radiation is coupled back into the plasma in X-mode, reaching the UHR where the above PDI may occur. The gyrotron power threshold of the above PDI is estimated to be ~ 100 kW, and is generally below the nominal gyrotron power of 200 kW used in the CTS experiment, indicating that the above PDI does indeed occur. This is further supported by the fact that the frequency shifts of the observed sidebands are reasonably close to the LH frequency and the value predicted by dipole PDI theory, which serve as lower and upper bounds of the frequency shifts, respectively. We note that the fraction of power reaching the UHR in X-mode in the experiment is a rather strong function of the toroidal gyrotron injection angle, peaking at approximately 0.04 close to the experimental value of -5° , and falling to virtually zero for poloidal injection and toroidal injection angles numerically greater than 10° ; both these regimes allow the PDI to be suppressed. PDI suppression at virtually poloidal injection is caused by a negligible fraction of reflected power being coupled to the plasma in X-mode, meaning that it should in principle always be possible to achieve PDI suppression by this method, but also that the method will only be applicable to narrow gyrotron beams of small angular divergence. PDI suppression at large toroidal injection angles relies on the ECR becoming optically thick,

which requires B to be large enough for the ECR to be located between the high-field side wall and the UHR, ideally inside the last closed flux surface. The latter method sets fewer restrictions on the gyrotron beam and has been successfully applied to suppress the PDI in 105 GHz O-mode CTS at ASDEX Upgrade; it does, however, restrict the B operation space. It is stressed that the PDI only occurs at the modest power levels of the reflected X-mode radiation (~ 10 kW) due to strong field enhancement close to the UHR which may be determined by a full-wave calculation.

There are several lines of inquiry which warrant further investigation. We have employed the dipole approximation, $\mathbf{k}_0 \approx \mathbf{0}$, in deriving the PDI growth rates, which appears to be the cause of the discrepancy between the predicted and observed PDI frequency shifts, and an investigation involving non-zero \mathbf{k}_0 is thus of interest; related to this, a treatment accounting for the deviation from the resonant LH dispersion relation (41) in the non-resonant case is also of interest. Further, it is of interest to repeat the PDI analysis for magnetised ions, with $\chi_\sigma(\mathbf{k}, \omega)$ from (9) and $\nu_\sigma \approx 0$, corresponding to general pure ion Bernstein low-frequency daughter waves. Another point of interest is to investigate the sidebands observed during CTS experiments at LHD [7, 8] in order to determine whether or not they may be explained by the theory employed to explain the sidebands during CTS experiments at ASDEX Upgrade. Additionally, confirmation of a gyrotron power threshold and the existence of warm LH daughter waves, along with ion heating generated by these [31–34], during CTS experiments at ASDEX Upgrade would provide further evidence for the theory; experiments of this type are planned for the 2017/2018 ASDEX Upgrade experimental campaign. The geometric optics and 1D full-wave models used to estimate \mathbf{E}_0 should also be compared with a full-wave solution taking the real geometry into account in order to assess their validity; such a full-wave solution would further allow us to investigate the cases in which the CTS probe ray does not reach to UHR in the main plasma, but where a significant fraction of the beam power may still do so. Finally, it would be of interest to perform fully nonlinear simulations of an X-mode beam encountering the UHR, e.g. using a particle-in-cell code like EPOCH [55], as done by [27] for a piecewise linear slab geometry, but employing a more realistic plasma profile in order to assess the actual frequency shift, growth rate and saturation level of the PDI in different experiments.

Acknowledgments

We thank Dr A Köhn for helpful discussions about field enhancement of X-mode radiation near the UHR. This work was supported by a research grant (15483) from VILLUM FONDEN. This work has been carried out within the framework of the EUROfusion Consortium and has received funding from the Euratom research and training programme 2014–2018 under grant agreement No. 633053. The views and opinions expressed herein do not necessarily reflect those of the European Commission.

ORCID iDs

M Salewski  <https://orcid.org/0000-0002-3699-679X>

References

- [1] Hansen S K 2016 Parametric decay and anomalous scattering from tokamak plasmas *Master's Thesis* Technical University of Denmark Kgs. Lyngby http://staff.dtu.dk/skni/~media/skni/SKH_Msc.ashx
- [2] Porkolab M 1982 Parametric decay instabilities in ECR heated plasmas *Proc. 2nd Workshop Hot Electron Ring Physics* vol 1 (San Diego) ed N A Uckan (Alexandria: National Technical Information Service) p 237
- [3] McDermott F S, Bekefi G, Hackett K E, Levine J S and Porkolab M 1982 *Phys. Fluids* **25** 1488
- [4] Tzoar N 1969 *Phys. Rev.* **178** 356
- [5] Dodin I Y and Arefiev A V 2017 *Phys. Plasmas* **24** 032119
- [6] Nielsen S K *et al* 2017 *Phys. Scr.* **92** 024001
- [7] Nishiura M *et al* (LHD Experiment Group) 2014 *Nucl. Fusion* **54** 023006
- [8] Kubo S *et al* (LHD experiment group) 2016 *J. Instrum.* **11** C06005
- [9] Silin V P 1965 *Sov. Phys.—JETP* **21** 1127
- [10] Aliev Y M, Silin V P and Watson C 1966 *Sov. Phys.—JETP* **23** 626
- [11] Amano T and Okamoto M 1969 *J. Phys. Soc. Japan* **26** 529
- [12] Piliya A D 1971 Decay instability in weakly inhomogeneous plasma *Proc. 10th Int. Conf. Phenomena in Ionized Gases (Oxford)* ed R N Franklin (Oxford: Donald Parsons & Co. Ltd) p 320
- [13] Rosenbluth M N 1972 *Phys. Rev. Lett.* **29** 565
- [14] Piliya A D 1973 *Sov. Phys.—JETP* **37** 629
- [15] White R B and Chen F F 1974 *Plasma Phys.* **16** 565
- [16] Gusakov E Z and Popov A Y 2016 *Phys. Plasmas* **23** 082503
- [17] Gusakov E Z and Surkov A V 2007 *Plasma Phys. Control. Fusion* **49** 631
- [18] Ott E, Hui B and Chu K R 1980 *Phys. Fluids* **23** 1031
- [19] Stefan V and Bers A 1984 *Phys. Fluids* **27** 175
- [20] Kasymov Z Z, Näslund E, Starodub A N and Stenflo L 1985 *Phys. Scr.* **31** 201
- [21] Sharma R P and Shukla P K 1983 *Phys. Fluids* **26** 87
- [22] Murtaza G and Shukla P K 1984 *J. Plasma Phys.* **31** 423
- [23] Leyser T B, Thidé B, Waldenvik M, Veszelei E, Frolov V L, Grach S M and Komrakov G P 1994 *J. Geophys. Res.* **99** 19555
- [24] Lin A T and Lin C-C 1981 *Phys. Rev. Lett.* **47** 98
- [25] Eliasson B and Shukla P K 2003 *Phys. Lett. A* **312** 91
- [26] Xiang N and Cary J R 2011 *Phys. Plasmas* **18** 122107
- [27] Arefiev A V, Dodin I Y, Köhn A, Du Toit E J, Holzhauser E, Shevchenko V F and Vann R G L 2017 *Nucl. Fusion* **57** 116024
- [28] Hiroe S and Ikegami H 1967 *Phys. Rev. Lett.* **19** 1414
- [29] Grek B and Porkolab M 1973 *Phys. Rev. Lett.* **30** 836
- [30] Okabayashi M, Chen K and Porkolab M 1973 *Phys. Rev. Lett.* **31** 1113
- [31] Bulyginsky D G, Gusev V K, Djachenko V V, Irzak M A, Kantor M Y, Larionov M M, Levin L S, Serebreny G A and Shustova N V 1984 ECR-heating of plasma in FT-1 tokamak and its influence on the ion component *Proc. 11th European Conf. Controlled Fusion and Plasma Physics* vol 1 (Aachen) (Mulhouse: European Physical Society) p 457
- [32] Pietrzyk Z A, Pochelon A, Behn R, Bondeson A, Dutch M, Goodman T P, Tran M Q and Whaley D R 1993 *Nucl. Fusion* **33** 197
- [33] Wilhelm R, Erckmann V, Janzen G, Kasperek W, Müller G, Räuchle E, Schüller P G, Schwörer K, Thumm M and the W VII-A Team 1984 *Plasma Phys. Control. Fusion* **26** 1433
- [34] Erckmann V, Janzen G, Kasperek W, Müller G, Räuchle E, Schüller P G, Schwörer K, Thumm K, Wilhelm R and the W VII-A Team 1985 Wave absorption and transport studies on ECR-heated stellarator plasmas in W VII-A *Proc. 10th Int. Conf. Plasma Physics and Controlled Nuclear Fusion Research* vol 2 (London) (Vienna: International Atomic Energy Agency) p 419
- [35] Porkolab M 1978 *Nucl. Fusion* **18** 367
- [36] Erckmann V and Gasparino U 1994 *Plasma Phys. Control. Fusion* **36** 1869
- [37] Laqua H P, Erckmann V, Hartfuß H J, Laqua H, W7-AS Team and ECRH Group 1997 *Phys. Rev. Lett.* **78** 3467
- [38] Laqua H P 2007 *Plasma Phys. Control. Fusion* **49** R1
- [39] Shevchenko V, Cunningham G, Gurchenko A, Gusakov E, Lloyd B, O'Brien M, Saveliev A, Surkov A, Volpe F and Walsh M 2007 *Fusion Sci. Technol.* **52** 202
- [40] Porkolab M 1974 *Phys. Fluids* **17** 1432
- [41] Opher M, Morales G J and Leboeuf J N 2002 *Phys. Rev. E* **66** 016407
- [42] Porkolab M and Cohen B I 1988 *Nucl. Fusion* **28** 239
- [43] Drake J F, Kaw P K, Lee Y C, Schmidt G, Liu C S and Rosenbluth M N 1974 *Phys. Fluids* **17** 778
- [44] Sagdeev R Z and Galeev A A 1969 *Nonlinear Plasma Theory* (New York: W. A. Benjamin, Inc.)
- [45] Weiland J and Wilhelmsson H 1977 *Coherent Non-Linear Interaction of Waves in Plasmas* (Oxford: Pergamon)
- [46] Berger R L, Chen L, Kaw P K and Perkins F W 1977 *Phys. Fluids* **20** 1864
- [47] Bindslev H 1991 *Plasma Phys. Control. Fusion* **33** 1775
- [48] Bindslev H 1992 *Plasma Phys. Control. Fusion* **34** 1601
- [49] Fischer R, Fuchs C J, Kurzan B, Suttrop W, Wolfrum E and The ASDEX Upgrade team 2010 *Fusion Sci. Technol.* **58** 675
- [50] McCarthy P J, Martin P and Schneider W 1999 The CLISTE interpretive equilibrium code *Technical Report IPP 5/85* Max-Planck-Institut für Plasmaphysik Garching bei München
- [51] Swanson D G 2003 *Plasma Waves* 2nd edn (Bristol: IOP Publishing)
- [52] Verdon A L, Cairns I H, Melrose D B and Robinson P A 2009 *Phys. Plasmas* **16** 052105
- [53] Poli E, Peeters A G and Pereverzev G V 2001 *Comput. Phys. Commun.* **136** 90
- [54] Weber H, Maj O and Poli E 2015 *EPJ Web Conf.* **87** 01002
- [55] Arber T D *et al* 2015 *Plasma Phys. Control. Fusion* **57** 113001

Power threshold and saturation of parametric decay instabilities near the upper hybrid resonance in plasmas

Cite as: Phys. Plasmas **26**, 062102 (2019); doi: [10.1063/1.5091659](https://doi.org/10.1063/1.5091659)

Submitted: 4 February 2019 · Accepted: 10 May 2019 ·

Published Online: 4 June 2019






View Online



Export Citation



CrossMark

S. K. Hansen,^{1,2,a)} S. K. Nielsen,² J. Stober,¹ J. Rasmussen,²  M. Salewski,²  M. Stejner,² 
and ASDEX Upgrade Team

AFFILIATIONS

¹Max-Planck-Institut für Plasmaphysik, D-85748 Garching b. München, Germany

²Department of Physics, Technical University of Denmark, DK-2800 Kgs. Lyngby, Denmark

^{a)}Electronic mail: Soeren.Kjer.Hansen@ipp.mpg.de

ABSTRACT

Parametric decay instabilities (PDIs) occur for large-amplitude waves in quadratically nonlinear media, where they provide a limit of validity of linear theories and allow efficient coupling between different, well-defined wave modes. We investigate PDIs near the upper hybrid resonance in plasmas by injection of high-power electron cyclotron (EC) waves at the ASDEX Upgrade tokamak. Our measurements of PDIs have an unprecedented frequency resolution, far below the ion cyclotron frequency, allowing the first observations of secondary and tertiary PDIs during the saturation phase in a controlled laboratory setting. Furthermore, we are for the first time able to systematically compare theoretical predictions of the EC wave power thresholds, which must be exceeded to excite such PDIs, with experimental observations, validating the theory. Our findings are relevant for EC wave heating and current drive in tokamaks and stellarators, including future fusion power plants, as well as in low-temperature laboratory and industrial plasmas, inertial confinement fusion, and ionospheric modification experiments.

Published under license by AIP Publishing. <https://doi.org/10.1063/1.5091659>

I. INTRODUCTION

In a parametric decay instability (PDI), a large-amplitude pump wave decays to two daughter waves once its amplitude exceeds a nonlinear threshold. PDIs are ubiquitous in quadratically nonlinear media, including optical crystals,¹ mechanical systems,² fluids,³ and plasmas.⁴ The PDI threshold indicates the limit of validity of linear theories and should consequently not be exceeded in applications relying on a linear medium response. On the other hand, the nonlinear response above the PDI threshold allows efficient coupling of the pump wave to different, well-defined daughter wave modes, which is crucial for applications such as telecommunications¹ and ionospheric modification experiments.^{5–11} It is thus of great importance to understand the PDI threshold, and the nonlinear response beyond it, to avoid the deleterious effects of an undesired nonlinear response and to exploit the nonlinear response for novel applications.

We consider PDIs occurring in connection with electron cyclotron resonance (ECR) heating of plasmas, which is widely applied for ionospheric modification experiments,^{5–11} as well as for generating and sustaining laboratory and industrial plasmas.^{12–14} A number of electromagnetic emission features in the electron cyclotron (EC)

frequency range have been attributed to particular PDIs occurring in connection with ECR heating. As the dispersion relations of the involved waves are known, this has allowed investigation of various properties of the ionosphere, such as the magnetic field,⁶ conditions for electron acceleration,⁷ the electron temperature,⁸ the ion composition,⁹ and pump-generated plasma layers.¹⁰ PDIs in the EC frequency range have also been observed in a number of laboratory plasmas, including low-temperature experiments,^{15–18} inertial confinement fusion experiments,⁴ and magnetic confinement fusion experiments both in tokamaks^{19–26} and in stellarators.^{27–31}

PDIs in laboratory plasmas have been used to demonstrate the occurrence of O-X-B heating,^{22,28,29} to provide direct heating,^{4,16–18,20,21,27,30} and can also deliver information about the plasma parameters^{15,19,23–26,31} but have generally been ignored when computing ECR heating and current drive characteristics.³² The occurrence of PDIs hampers, and may damage, laboratory EC wave diagnostics.^{23,24} Present theories even suggest that PDIs can lead to significantly different ECR heating and current drive characteristics than those expected from linear theories in some cases.³³ The detailed study of PDIs in the EC frequency range of a laboratory plasma presented here is thus of

significant interest, considering the increasing importance of ECR heating and current drive in present and future large-scale fusion experiments and the possibility of validating PDI models used for ionospheric modification experiments in laboratory plasmas, where the plasma parameters can be controlled and monitored to a much larger extent.

We specifically investigate PDIs occurring for X-mode polarized radiation near the upper hybrid resonance (UHR), where the pump wave frequency, f_0 , equals $f_{UH} = \sqrt{f_{pe}^2 + f_{ce}^2}$, and f_{pe} and f_{ce} are the electron plasma and cyclotron frequencies, respectively. Strong enhancement of the electric field of the X-mode pump wave near the UHR^{26,34} allows the thresholds of various PDIs to be exceeded. PDIs for X-mode radiation near the UHR are relevant for fundamental ECR heating both with the X-mode^{19–21,30,35} and the O-mode^{21,27} (O-mode can be converted to X-mode by reflections^{21,26,27}) for O-X-B heating,^{22,28,29,36–38} for collective Thomson scattering,^{24–26,31} and for ionospheric modification experiments;³⁹ similar PDIs also enter as secondary instabilities in the saturation phase of two-plasmon decay instabilities occurring for harmonic X-mode ECR heating^{23,33} and direct-drive inertial confinement fusion.^{4,40} Particular cases where such PDIs may occur in future experiments include ECR start-up at ITER, MAST-U, NSTX-U, and future fusion reactors,^{41–43} O-X-B heating at W7-X, and ionospheric modification experiments with significant O-X-conversion at the O-mode cutoff.

Energy conservation in the decay process imposes the selection rule that the daughter wave frequencies, $f_{1,2}$, should add up to the pump frequency, i.e., $f_1 + f_2 = f_0$. A number of theories have predicted the PDI near the UHR with the lowest threshold to be decay of the X-mode pump wave to a low-frequency lower hybrid (LH) wave and a high-frequency electron Bernstein wave (EBW);^{26,35–37,39} the LH wave frequency is $f_1 \sim f_{LH} \ll f_{pe}$, where f_{LH} is the cold LH frequency and the EBW frequency is $f_2 = f_0 - f_1 \approx f_{UH} - f_{LH}$. The occurrence of this instability is corroborated by experiments^{19–22,24–29,31} and simulations.^{38,44,45}

Here, we report an experiment from the ASDEX Upgrade (AUG) tokamak which allows the first systematic comparison between experimental observations and theoretical predictions²⁶ of the threshold of the above PDI. The unprecedented frequency resolution of the reported experiment additionally allows the first observations of the fine structure of spectra excited by PDIs near the UHR in a controlled laboratory setting. The fine structure consists of variations on the order of the ion cyclotron frequency, $f_{ci} \ll f_{LH}$, and is crucial for describing secondary and tertiary PDIs, involving coupling of the daughter waves excited by the primary instability or the pump wave itself to EBWs and ion Bernstein waves (IBWs), which eventually lead to saturation.

This paper is arranged as follows: Sec. II describes the experimental setup, Sec. III presents the experimental results, Sec. IV discusses the interpretation of the experimental results, and, finally, Sec. V provides our conclusions.

II. EXPERIMENTAL SETUP

A schematic of the experimental setup is shown in Fig. 1. In the experiment, 105 GHz O-mode radiation is injected from the low-field side of AUG at a toroidal angle of -4.8° , using a gyrotron from the system described in Ref. 46. The O-mode fraction of the scattered radiation near 105 GHz is picked up by a steerable radiometer on the low-field side, which includes a fast acquisition system⁴⁷ capable of

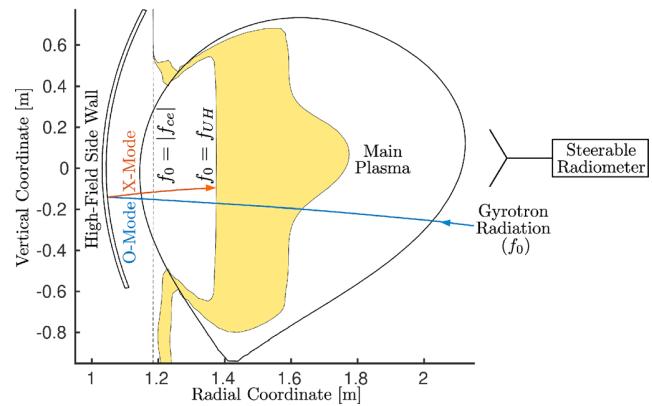


FIG. 1. Schematic of the experimental setup in AUG discharge 34575. No propagating X-mode exists in the shaded region.

resolving the fine structure of the PDI spectra. The ECR ($f_0 = |f_{ce}|$) of the 105 GHz radiation is located far on the high-field side and is optically thin for O-mode radiation. A significant fraction of the incident radiation can thus reflect off the high-field side wall and re-enter the plasma in the X-mode. When the ECR is not optically thick for the X-mode radiation, the electric field near the UHR may become sufficiently large to excite PDIs. The experimental setup is similar to the ones used for fundamental O-mode ECR heating,^{20,21,27} collective Thomson scattering,^{24–26,31} and EBW start-up,^{41–43} it also has much in common with the setups used for O-X-B heating^{22,28,29} and ionospheric modification experiments,^{5–11} the main difference being that O-X-conversion occurs at the O-mode cutoff ($f_0 = f_{pe}$) in these setups.

The analyzed experiment is an H-mode,⁴⁸ deuterium discharge during which the toroidal magnetic field, B_t , is swept from -2.66 T to -2.43 T over 3.5 s. For us, the most important effect of the sweep is the displacement of the ECR toward the high-field side, reducing its absorption by an order of magnitude. This is seen in Fig. 2; the spread in the data is due to uncertainties in the experimental equilibria.

To assess the development of the PDIs during the B_t -sweep, 200 evenly spaced 2 ms pulses are generated by the gyrotron. For a comparison of the experimental and theoretical²⁶ PDI thresholds, the gyrotron power, P_0 , is varied from 0 to 300 kW during each pulse. The variation of P_0 during a pulse is seen in Fig. 3. The scattered signal is recorded in 1 ms measurement pulses around the center of each gyrotron pulse. Power spectra are obtained by performing fast Fourier transforms on 655 ns windows of the recorded signal for all measurement pulses, giving a frequency resolution of 1.53 MHz, well below f_{ci} of deuterium in the experiment (~ 30 MHz).

III. EXPERIMENTAL RESULTS

The mean spectra recorded during three measurement pulses at different points in the B_t -sweep are seen in Fig. 4. All spectra are taken from the part of the B_t -sweep where PDI peaks are consistently visible and illustrate the qualitative development of these peaks. The gyrotron line is visible slightly below 105 GHz ($f_0 = 104.93$ GHz) in all spectra. The smaller peaks, separated by 0.7–1.1 GHz (slightly more than f_{LH} at the UHR) from the gyrotron peak, originate from the daughter waves excited by PDIs; the mechanisms through which they are generated are discussed in Sec. IV. As seen in Fig. 4, the PDI peaks start out as a

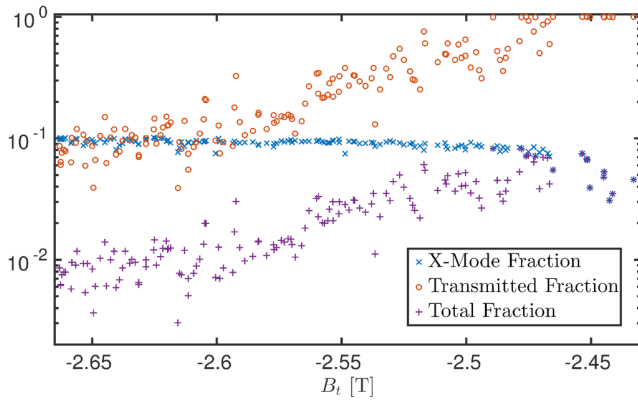


FIG. 2. Fraction of reflected power coupled to the plasma in X-mode (\times), fraction of injected power not absorbed at the ECR (\circ), and total fraction of injected power reaching the UHR in X-mode ($+$) vs B_t in AUG discharge 34575, based on the theory of Ref. 26.

few well-defined lines in pulse (a) and develop an increasingly complex structure, visible in pulses (b) and (c), as B_t is swept. The fine structure in pulses (b) and (c) indicates that secondary and tertiary PDIs occur during the saturation phase. In pulse (b), peaks separated by approximately 50 MHz (roughly $2f_{ci}$ at the UHR) occur around the primary peaks, indicating decay of the primary daughter waves to EBWs and second-order IBWs as the secondary PDI. In pulse (c), additional peaks separated by approximately 25 MHz (roughly f_{ci} at the UHR) appear throughout the frequency range covered by the radiometer, indicating decay of the pump wave to EBWs and arbitrary-order IBWs as the tertiary PDI. For reference, we plot the theoretical frequency of the most unstable up- and down-shifted primary daughter waves from Ref. 26, along with $f_0 \pm f_{LH}$, in Fig. 4. The theoretical frequency shift represents an upper bound on the true shift, while f_{LH} represents a lower bound. This may be explained by use of the dipole approximation in Ref. 26 and finite temperature effects, respectively.

To extract information about the P_0 -dependence of the PDI peaks, we calculate the spectral power, S , in the frequency ranges 103.8–104.2 GHz and 105.6–106.0 GHz for all spectra obtained during

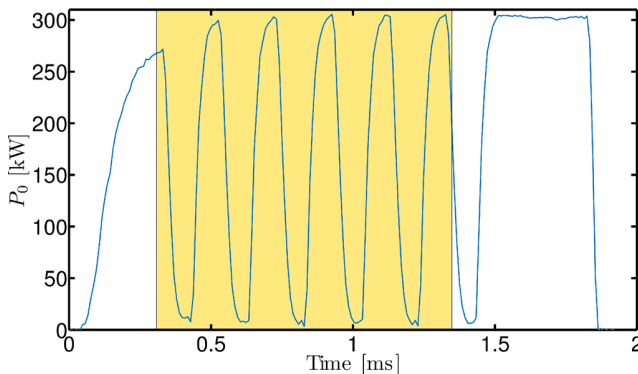


FIG. 3. Modulation of P_0 during a gyrotron pulse. The spectrum of the scattered radiation is measured using the steerable radiometer in the shaded interval during all gyrotron pulses.

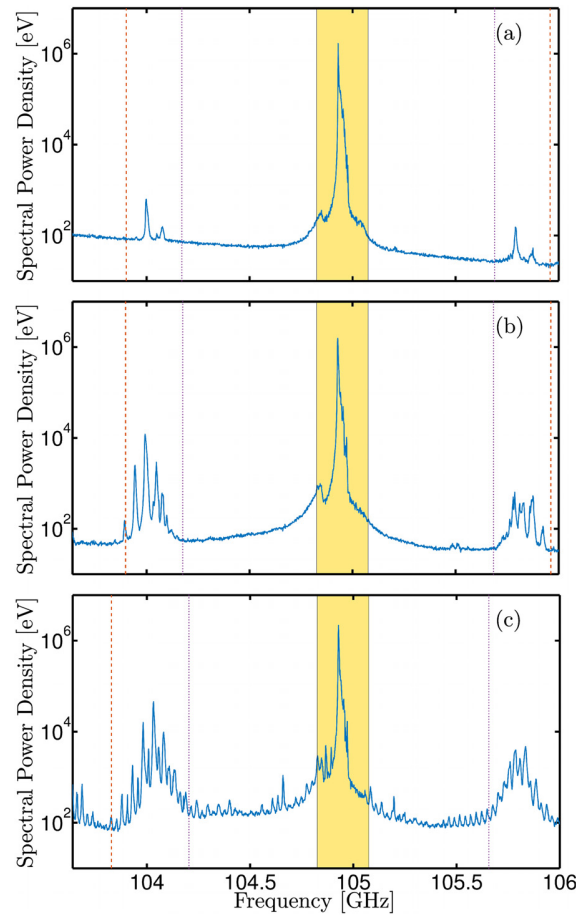


FIG. 4. Mean spectra recorded by the steerable radiometer in AUG discharge 34575 at $B_t = -2.53$ T (a), $B_t = -2.48$ T (b), and $B_t = -2.44$ T (c). The shaded areas indicate the stopband of the notch filter near f_0 , where the calibration is uncertain. The dashed lines indicate the most unstable modes according to Ref. 26; the dotted lines indicate $f_0 \pm f_{LH}$.

a measurement pulse. The frequency ranges are chosen such that they contain the primary PDI peaks, but not the gyrotron peak, and changing their precise limits does not change the subsequent conclusions if this remains the case. We derive $S(P_0)$ using P_0 -waveforms similar to that in Fig. 3. Figure 5 shows S vs P_0 for the measurement pulses whose mean spectra were shown in Fig. 4. Evidently, S depends nonlinearly on P_0 , as expected for PDI-generated peaks. In pulse (a), S only deviates appreciably from the background level for $P_0 > 250$ kW while in pulses (b) and (c), S increases roughly linearly with P_0 until 100 kW and 50 kW, respectively, but supra-linearly beyond these values. We note that S saturates for $P_0 > 200$ kW in pulse (b), while in pulse (c), some saturation occurs for $P_0 \in [100 \text{ kW}, 250 \text{ kW}]$, followed by more rapid growth for $P_0 > 250$ kW. This corroborates that the secondary instability involves the primary daughter waves, stabilizing S in the PDI region, while the tertiary instability involves the pump wave, opening additional channels through which power can flow into the PDI region, as stated above.

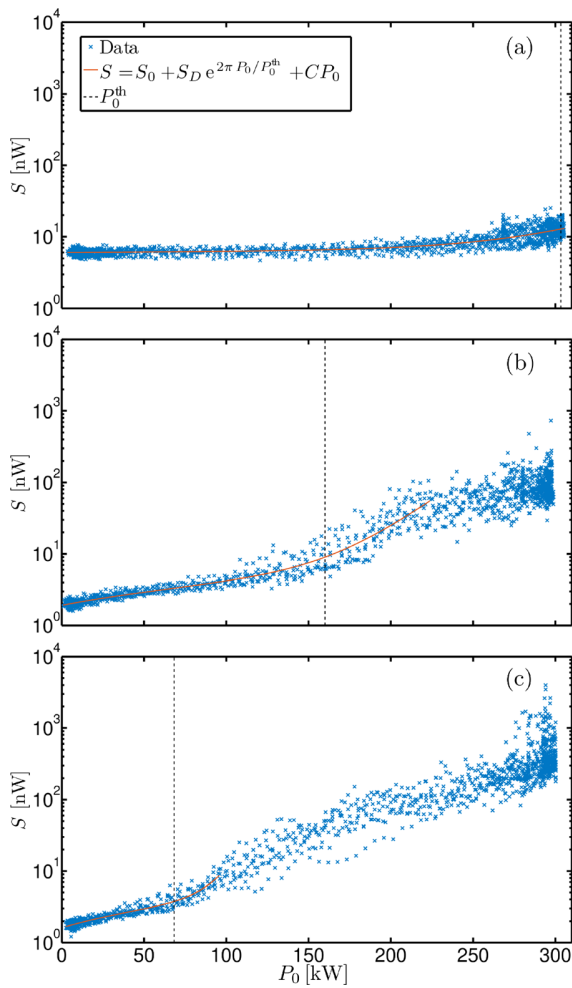


FIG. 5. S vs P_0 in AUG discharge 34575 at $B_t = -2.53$ T (a), $B_t = -2.48$ T (b), and $B_t = -2.44$ T (c). The experimental data (\times) are fitted using Eq. (1); the fits are marked by solid lines. The dashed lines indicate the fitted P_0^{th} -values.

To compare the experimental $S(P_0)$ with the dependence expected from Ref. 26, we introduce a physical model. First, S contains a thermal background contribution, S_0 , independent of P_0 . Second, S contains a P_0 -dependent contribution of the form $S_D e^{2\pi P_0/P_0^{\text{th}}}$ from the waves amplified by the primary PDI; S_D is the thermal background signal due to these waves, $e^{2\pi P_0/P_0^{\text{th}}}$ is the convective PDI amplification factor in the absence of collisions and saturation, and P_0^{th} is the convective PDI threshold defined in Refs. 49–51. Finally, S contains a contribution linear in P_0 , written as CP_0 , due to collective Thomson scattering of the gyrotron radiation^{24,52} and increased emission due to absorption at the ECR. Addition of the contributions yields

$$S = S_0 + S_D e^{2\pi P_0/P_0^{\text{th}}} + CP_0. \quad (1)$$

Least-square fits of the logarithm of the measured S to the logarithm of Eq. (1) are shown in Fig. 5. In the fits, we require all parameters to be non-negative and only include data up to a P_0 -value where

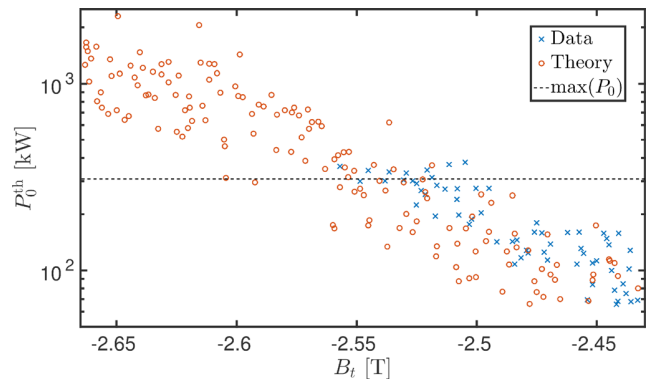


FIG. 6. Experimental (\times) and theoretical (\circ) P_0^{th} vs B_t in AUG discharge 34575. The dashed line marks $\max(P_0)$ in the experiment.

saturation sets in, as this effect is not included in the model. The cutoff power used is $1.4P_0^{\text{th}}$, provided that this value is smaller than $\max(P_0)$, and represents a rough experimental estimate of the gyrotron power threshold of the secondary instability.

To facilitate a comparison with theory,²⁶ the fitted P_0^{th} -values are indicated in Fig. 5. As expected, they are close to the points where the supra-linear increase in S with P_0 begins. Figure 6 shows the experimental values of P_0^{th} , obtained from fits similar to those in Fig. 5, and the theoretical predictions as functions of B_t . Note that we have only included fitted P_0^{th} -values from measurement pulses with a clear non-linear phase and that we have only included theoretical P_0^{th} -values for equilibria where the UHR was reached by the reflected X-mode ray. The theoretical P_0^{th} -values show a spread due to uncertainties in the experimental equilibria used for their calculation. The experimental P_0^{th} -values lie within this spread throughout the B_t -sweep, albeit with a small bias toward higher P_0^{th} -values. We also remark that PDI peaks are only observed for $|B_t| < 2.56$ T in the experiment, which coincides closely with the point where the theoretical P_0^{th} drops below $\max(P_0)$, as seen in Fig. 6.

IV. DISCUSSION

Having presented the main results of the experiment, we now discuss their interpretation in more detail. First of all, the waves excited by the PDIs under consideration are electrostatic in nature, meaning that they cannot be detected directly by the steerable radiometer used in the experiment. More specifically, the waves must somehow give rise to O-mode waves propagating toward the detector, owing to the cutoff region of the X-mode radiation (see Fig. 1) and the settings of the steerable radiometer polarizers.

For the primary PDI, a feasible mechanism is always provided by mixing of the injected waves with the low-frequency LH daughter waves excited by the PDI, which should lead to the observed down- and up-shifted peaks at the beat frequencies ($f_0 \mp f_1$). As long as the power of the injected waves remains large compared with that of the daughter waves, which should at least hold until saturation sets in, this signal will be proportional to the daughter wave power and thus provide a reliable measure of the PDI threshold. An alternative mechanism is provided by linear conversion of the high-frequency daughter waves to O-mode radiation. The efficiency of this mechanism is highly dependent on the direction of propagation of the high-frequency

daughter waves, as EBWs undergo linear conversion to X-mode waves at the UHR.²⁹ These X-mode waves may then be converted to O-mode waves by a wall reflection. On the other hand, EBWs going directly to the ECR will be almost completely absorbed for all reasonable conditions.²⁹ As the EBWs are backward propagating under the conditions in AUG ($f_{pe} < \sqrt{3}|f_{ce}|$),²⁶ high-frequency waves which are forwardscattered with respect to the pump wave vector will go directly to the ECR, while backscattered waves may undergo the conversion process described above. As the theory of Ref. 26 is based on the dipole approximation, which ignores the pump wave vector relative to those of the daughter waves, it does not provide direct information about the direction in which the high-frequency daughter waves propagate. However, the fact that the observed frequency shift of the daughter waves relative to the pump wave is smaller than what is expected theoretically (see Fig. 4) indicates forward scattering, as already noted in Ref. 26; this is also in agreement with recent numerical simulations.⁴⁵ Within the 1D-picture presented here, it thus seems that linear conversion of the high-frequency daughter waves to O-mode waves will not be efficient. This may additionally explain why the observed signal only rises two orders of magnitude above the linear background even at the highest power levels in the cases with the lowest ECR absorption.

For the secondary PDI, we postulated decay of the primary daughter waves into secondary EBWs and second-order IBWs, based on the observation of peaks separated by approximately $2f_{ci}$ around the primary PDI peaks. While we have not explicitly computed the threshold for this process, we have confirmed the possibility of satisfying the selection rules when the secondary EBW is forwardscattered with respect to the primary one; the details are given in the Appendix. The main mechanism through which O-mode radiation may be generated by this instability is mixing of the waves near the primary daughter frequencies ($f_0 \mp f_1$) with the second-order IBWs, generating waves at approximately $f_0 \mp f_1 \mp 2nf_{ci}$, where $n \in \mathbb{N}$. For the tertiary instability, similar mixing involving the injected waves and arbitrary-order IBWs is expected to explain the generation of O-mode radiation.

We note that there are still several points deserving further investigation. First, it would be of interest to extend the theory of Ref. 26 beyond the dipole approximation. This would allow us to obtain theoretical frequency shifts closer to the experimental values (see Fig. 4), as well as to investigate the directions of propagation of the daughter waves and the possibility of absolute PDIs, e.g., considered by Ref. 36, in greater detail. Second, the secondary and tertiary PDIs indicated by the experiment should be investigated theoretically. From this, we could obtain secondary and tertiary PDI thresholds for comparison with the experimental observations and construct a model describing the saturation phase of PDIs near the UHR. Finally, the experiment itself could be improved by investigating the low-frequency waves excited by the PDIs directly. Future experiments at AUG will be capable of this, using a B-dot probe⁵³ connected to the second channel of the fast acquisition system employed in the present Paper.⁴⁷

V. CONCLUSION

We have performed the first experimental investigation of PDIs near the UHR in a laboratory plasma capable of resolving the fine structure of the spectra excited by the PDIs and providing a comparison of the pump power necessary to excite the primary instability with the theory.

The recorded spectra showed initial development of PDI peaks separated by slightly more than f_{LH} from the pump peak, followed by development of peaks separated by $2f_{ci}$ from the primary PDI peaks, and finally development of peaks separated by f_{ci} throughout the frequency region covered by the radiometer. This indicates initial decay of the pump wave to EBWs and LH waves, followed by decay of the primary EBWs to other EBWs and second-order IBWs, and finally decay of the pump wave to EBWs and arbitrary-order IBWs.

By modulating the gyrotron power, we were able to obtain experimental PDI thresholds which corroborated the theoretical predictions from Ref. 26. These findings indicate that the possibility of PDIs occurring near the UHR during ECR start-up at ITER, MAST-U, NSTX-U, and future fusion reactors may be assessed using existing theories. The theory tested here is also applicable to O-X-B heating, planned for W7-X, and ionospheric modification experiments with significant O-X-conversion at the O-mode cutoff, provided that the plasma is only moderately overdense, $f_{pe} < \sqrt{3}|f_{ce}|$, at the UHR. For $f_{pe} > \sqrt{3}|f_{ce}|$, the theory of Ref. 36 is applicable.

ACKNOWLEDGMENTS

This work was supported by a research Grant (15483) from VILLUM FONDEN. This work has been carried out within the framework of the EUROfusion Consortium and has received funding from the Euratom research and training program 2014–2018 and 2019–2020 under Grant Agreement No. 633053. The views and opinions expressed herein do not necessarily reflect those of the European Commission.

APPENDIX: THE SECONDARY INSTABILITY

Here, we show the possibility of satisfying the selection rules for decay of a primary EBW daughter into secondary EBW and second-order IBW daughters near the UHR when $f_{pe} < \sqrt{3}|f_{ce}|$. We use the EBW dispersion relation from Ref. 26 for propagation perpendicular to the background magnetic field

$$f_2 = f_{UH} - \frac{f_{pe}^2}{2f_{UH}} \frac{r_{Le}^2 k_2^2}{1 - f_{pe}^2/(3f_{ce}^2)}, \quad f_2' = f_{UH} - \frac{f_{pe}^2}{2f_{UH}} \frac{r_{Le}^2 (k_2')^2}{1 - f_{pe}^2/(3f_{ce}^2)}, \quad (A1)$$

where f_2 and f_2' are the primary and secondary EBW frequencies, k_2 and k_2' are the primary and secondary EBW wave numbers, r_{Le} is the thermal electron Larmor radius defined in Ref. 26, and we have expanded the dispersion relation from Ref. 26 to first order in $r_{Le}^2 k_2^2 \ll 1$ and $r_{Le}^2 (k_2')^2 \ll 1$. Using the frequency selection rule of the primary PDI, $f_2 = f_0 - f_1 \approx f_{UH} - f_{LH}$, we obtain

$$|k_2| \approx \frac{\sqrt{2f_{LH}f_{UH} \left[1 - f_{pe}^2/(3f_{ce}^2) \right]}}{f_{pe} r_{Le}}, \quad (A2)$$

which does indeed satisfy $r_{Le}^2 k_2^2 \ll 1$ for the usual ordering ($f_{LH} \ll f_{pe} \leq f_{UH}$). The dispersion relation of the second-order IBW for propagation perpendicular to the background magnetic field in a simple plasma is given by Eq. (4.275) of Ref. 54,

$$f'_1 = 2f_{ci} \left[1 - \frac{3r_{Li}^2(k'_1)^2}{8(1 - 3v_A^2/c^2)} \right], \quad (A3)$$

where f'_1 is the IBW frequency, k'_1 is the IBW wave number, r_{Li} is the thermal ion Larmor radius, c is the vacuum speed of light, $v_A = c/\sqrt{1 + f_{pi}^2/f_{ci}^2} \ll c$ (since the ion plasma frequency, $f_{pi} > f_{LH} \gg f_{ci}$) is the Alfvén speed, and the expression is valid to first order in $r_{Li}^2(k'_1)^2 \ll 1$. Note that generally $r_{Li} \gg r_{Le}$, so $|k'_1|$ should be significantly smaller than $|k_2|$ and $|k'_2|$. Now, using the frequency selection rule of the secondary PDI, $f'_2 = f_2 - f'_1 \approx f_{UH} - f_{LH} - 2f_{ci}$, Eq. (A1) yields

$$|k'_2| \approx \frac{\sqrt{2(f_{LH} + 2f_{ci})f_{UH} \left[1 - \frac{f_{pe}^2}{(3f_{ce}^2)} \right]}}{f_{pe}r_{Le}} \approx |k_2| \left(1 + \frac{f_{ci}}{f_{LH}} \right); \quad (A4)$$

the last approximation follows by expansion to first order in $f_{ci}/f_{LH} \ll 1$. Taking \mathbf{k}_2 and \mathbf{k}'_2 to point in the same direction, the wave vector selection rule²⁶ of the secondary PDI gives

$$k'_1 = k_2 - k'_2 \approx -\frac{f_{ci}}{f_{LH}} k_2, \quad (A5)$$

with the negative sign indicating that \mathbf{k}'_1 points in the opposite direction of \mathbf{k}_2 and \mathbf{k}'_2 . Plugging Eq. (A2) into Eq. (A5), we find

$$\begin{aligned} r_{Li}^2(k'_1)^2 &\approx \frac{2f_{ci}^2 f_{UH} \left[1 - \frac{f_{pe}^2}{(3f_{ce}^2)} \right] r_{Li}^2}{f_{LH} f_{pe}^2 r_{Le}^2} \\ &= 2\sqrt{\frac{Z_i m_e}{m_i} \frac{T_i}{Z_i T_e} \frac{|f_{ce}| f_{UH}^2}{f_{pe}^3}} \left(1 - \frac{f_{pe}^2}{3f_{ce}^2} \right), \end{aligned} \quad (A6)$$

where Z_i is the ion charge number, m_e and m_i are the electron and ion masses, and T_e and T_i are the electron and ion temperatures. If f_{pe} and $|f_{ce}|$ have similar orders of magnitude, $r_{Li}^2(k'_1)^2 \sim \sqrt{Z_i m_e/m_i} |T_i/(Z_i T_e)| \ll 1$, as assumed in Eq. (A3). Particularly, typical conditions near the UHR of 105 GHz radiation in AUG discharge 34575 are $Z_i = 1$, $m_i/m_e = 3.67 \times 10^3$, electron density $\approx 3.1 \times 10^{19} \text{ m}^{-3}$, background magnetic field $\approx 3.3 \text{ T}$, and $T_e \approx T_i$, giving $r_{Le}^2 k_2^2 \approx 0.055$, $r_{Le}^2 (k'_2)^2 \approx 0.059$, and $r_{Li}^2 (k'_1)^2 \approx 0.24$. It is thus possible to satisfy the selection rules of the secondary PDI in the region of validity of the dispersion relations.

REFERENCES

¹X. Guo, C.-L. Zou, H. Jung, and H. X. Tang, *Phys. Rev. Lett.* **117**, 123902 (2016).
²F. Brau, H. Vandeparre, A. Sabbah, C. Poulard, A. Boudaoud, and P. Damman, *Nat. Phys.* **7**, 56 (2011).
³Q. Aubourg and N. Mordant, *Phys. Rev. Lett.* **114**, 144501 (2015).
⁴D. H. Froula, B. Yaakobi, S. X. Hu, P.-Y. Chang, R. S. Craxton, D. H. Edgell, R. Follett, D. T. Michel, J. F. Myatt, W. Seka, R. W. Short, A. Solodov, and C. Stoeckl, *Phys. Rev. Lett.* **108**, 165003 (2012).
⁵B. Thidé, H. Kopka, and P. Stubbe, *Phys. Rev. Lett.* **49**, 1561 (1982).
⁶T. B. Leyser, B. Thidé, H. Derblom, Å. Hedberg, B. Lundborg, P. Stubbe, and H. Kopka, *Phys. Rev. Lett.* **63**, 1145 (1989).
⁷T. B. Leyser, *Space Sci. Rev.* **98**, 223 (2001).
⁸P. A. Bernhardt, C. A. Selcher, R. H. Lehmborg, S. Rodriguez, J. Thomason, M. McCarrick, and G. Frazer, *Ann. Geophys.* **27**, 4409 (2009).

⁹P. A. Bernhardt, C. A. Selcher, R. H. Lehmborg, S. P. Rodriguez, J. F. Thomason, K. M. Groves, M. J. McCarrick, and G. J. Frazer, *Phys. Rev. Lett.* **104**, 165004 (2010).
¹⁰E. Sergeev, S. Grach, A. Shindin, E. Mishin, P. Bernhardt, S. Briczinski, B. Isham, M. Broughton, J. LaBelle, and B. Watkins, *Phys. Rev. Lett.* **110**, 065002 (2013).
¹¹C. J. Bryers, M. J. Kosch, A. Senior, M. T. Rietveld, and T. K. Yeoman, *J. Geophys. Res. Space Phys.* **118**, 7472, <https://doi.org/10.1002/2013JA019429> (2013).
¹²J. Asmussen, *J. Vac. Sci. Technol. A* **7**, 883 (1989).
¹³V. Erckmann and U. Gasparino, *Plasma Phys. Controlled Fusion* **36**, 1869 (1994).
¹⁴R. Geller, *Electron Cyclotron Resonance Ion Sources and ECR Plasmas* (IOP Publishing, Bristol, 1996).
¹⁵S. Hiroe and H. Ikegami, *Phys. Rev. Lett.* **19**, 1414 (1967).
¹⁶R. P. H. Chang, M. Porkolab, and B. Grek, *Phys. Rev. Lett.* **28**, 206 (1972).
¹⁷B. Grek and M. Porkolab, *Phys. Rev. Lett.* **30**, 836 (1973).
¹⁸M. Okabayashi, K. Chen, and M. Porkolab, *Phys. Rev. Lett.* **31**, 1113 (1973).
¹⁹F. S. McDermott, G. Bekefi, K. E. Hackett, J. S. Levine, and M. Porkolab, *Phys. Fluids* **25**, 1488 (1982).
²⁰D. G. Bulyginskii, V. V. D'yachenko, M. A. Irzak, M. M. Larionov, L. S. Levin, G. A. Serebrenyi, and N. V. Shustova, *Sov. J. Plasma Phys.* **12**, 77 (1986).
²¹Z. A. Pietrzyk, A. Pochelon, R. Behn, A. Bondeson, M. Dutch, T. P. Goodman, M. Q. Tran, and D. R. Whaley, *Nucl. Fusion* **33**, 197 (1993).
²²V. Shevchenko, G. Cunningham, A. Gurchenko, E. Gusakov, B. Lloyd, M. O'Brien, A. Saveliev, A. Surkov, F. Volpe, and M. Walsh, *Fusion Sci. Technol.* **52**, 202 (2007).
²³E. Westerhof, S. K. Nielsen, J. W. Oosterbeek, M. Salewski, M. R. De Baar, W. A. Bongers, A. Bürger, B. A. Hennen, S. B. Korsholm, F. Leipold, D. Moseev, M. Stejner, D. J. Thoen, and TEXTOR Team, *Phys. Rev. Lett.* **103**, 125001 (2009).
²⁴S. K. Nielsen, P. K. Michelsen, S. K. Hansen, S. B. Korsholm, F. Leipold, J. Rasmussen, M. Salewski, M. Schubert, M. Stejner, J. Stober, D. Wagner, and ASDEX Upgrade Team, *Phys. Scr.* **92**, 024001 (2017).
²⁵S. K. Hansen, S. K. Nielsen, M. Salewski, M. Stejner, J. Stober, and ASDEX Upgrade Team, *EPJ Web Conf.* **149**, 03020 (2017).
²⁶S. K. Hansen, S. K. Nielsen, M. Salewski, M. Stejner, J. Stober, and ASDEX Upgrade Team, *Plasma Phys. Controlled Fusion* **59**, 105006 (2017).
²⁷R. Wilhelm, V. Erckmann, G. Janzen, W. Kasperek, G. Müller, E. Rächle, P. G. Schüller, K. Schwörer, M. Thumm, and W VII-A Team, *Plasma Phys. Controlled Fusion* **26**, 1433 (1984).
²⁸H. P. Laqua, V. Erckmann, H. J. Hartfuß, H. Laqua, W7-AS Team, and ECRH Group, *Phys. Rev. Lett.* **78**, 3467 (1997).
²⁹H. P. Laqua, *Plasma Phys. Controlled Fusion* **49**, R1 (2007).
³⁰A. Köhn, G. Birkenmeier, A. Chusov, P. Diez, A. Feuer, U. Höfel, H. Höhnle, E. Holzhauser, W. Kasperek, S. Merli, M. Ramisch, J. Seifert, S. Wolf, and U. Stroth, *Plasma Phys. Controlled Fusion* **55**, 014010 (2013).
³¹S. Kubo, M. Nishiura, K. Tanaka, D. Moseev, S. Ogasawara, T. Shimojima, Y. Yoshimura, H. Igami, H. Takahashi, T. I. Tsujimura, R. Makino, and LHD Experiment Group, *J. Instrum.* **11**, C06005 (2016).
³²A. Fasoli, S. Brunner, W. A. Cooper, J. P. Graves, P. Ricci, O. Sauter, and L. Villard, *Nat. Phys.* **12**, 411 (2016).
³³E. Z. Gusakov and A. Y. Popov, *Phys. Plasmas* **23**, 082503 (2016).
³⁴R. B. White and F. F. Chen, *Plasma Phys.* **16**, 565 (1974).
³⁵M. Porkolab, in *Proceedings of 2nd Workshop Hot Electron Ring Physics (San Diego)*, edited by N. A. Uckan (National Technical Information Service, Alexandria, 1982), Vol. 1, p. 237.
³⁶E. Z. Gusakov and A. V. Surkov, *Plasma Phys. Controlled Fusion* **49**, 631 (2007).
³⁷I. Y. Dodin and A. V. Arefiev, *Phys. Plasmas* **24**, 032119 (2017).
³⁸A. V. Arefiev, I. Y. Dodin, A. Köhn, E. J. Du Toit, E. Holzhauser, V. F. Shevchenko, and R. G. L. Vann, *Nucl. Fusion* **57**, 116024 (2017).
³⁹N. I. Budko and V. V. Vaskov, *Geomagn. Aeron.* **34**, 350 (1994), see <http://eos.wdcb.ru/transl/gma/9403/pap15.ps>.
⁴⁰R. Yan, C. Ren, J. Li, A. V. Maximov, W. B. Mori, Z.-M. Sheng, and F. S. Tsung, *Phys. Rev. Lett.* **108**, 175002 (2012).
⁴¹V. Shevchenko, M. R. O'Brien, D. Taylor, A. N. Saveliev, and MAST Team, *Nucl. Fusion* **50**, 022004 (2010).

- ⁴²V. F. Shevchenko, Y. F. Baranov, T. Bigelow, J. B. Caughman, S. Diem, C. Dukes, P. Finburg, J. Hawes, C. Gurl, J. Griffiths, J. Mailloux, M. Peng, A. N. Saveliev, Y. Takase, H. Tanaka, and G. Taylor, *EPJ Web Conf.* **87**, 02007 (2015).
- ⁴³N. A. Lopez and F. M. Poli, *Plasma Phys. Controlled Fusion* **60**, 065007 (2018).
- ⁴⁴A. T. Lin and C.-C. Lin, *Phys. Rev. Lett.* **47**, 98 (1981).
- ⁴⁵M. G. Senstius, S. K. Nielsen, and R. G. L. Vann, *EPJ Web Conf.* **203**, 01010 (2019).
- ⁴⁶D. Wagner, G. Grünwald, F. Leuterer, A. Manini, F. Monaco, M. Munich, H. Schütz, J. Stober, H. Zohm, T. Franke, M. Thumm, G. Gantenbein, R. Heidinger, A. Meier, W. Kasperek, C. Lechte, A. Litvak, G. G. Denisov, A. V. Chirkov, E. M. Tai, L. G. Popov, V. O. Nichiporenko, V. E. Myasnikov, E. A. Solyanova, S. A. Malygin, F. Meo, and P. Woskov, *Nucl. Fusion* **48**, 054006 (2008).
- ⁴⁷M. Stejner, S. Nielsen, A. S. Jacobsen, S. B. Korsholm, F. Leipold, F. Meo, P. K. Michelsen, D. Moseev, J. Rasmussen, M. Salewski, M. Schubert, J. Stober, D. H. Wagner, and ASDEX Upgrade Team, *Rev. Sci. Instrum.* **85**, 093504 (2014).
- ⁴⁸J. Ongena, R. Koch, R. Wolf, and H. Zohm, *Nat. Phys.* **12**, 398 (2016).
- ⁴⁹A. D. Piliya, in *Proceedings of 10th International Conference on Phenomena in Ionized Gases (Oxford)*, edited by R. N. Franklin (Donald Parsons & Co. Ltd., Oxford, 1971) p. 320.
- ⁵⁰M. N. Rosenbluth, *Phys. Rev. Lett.* **29**, 565 (1972).
- ⁵¹A. D. Piliya, *Sov. Phys.-JETP* **37**, 629 (1973), http://www.jetp.ac.ru/cgi-bin/dn/e_037_04_0629.pdf.
- ⁵²H. Bindslev, *J. Atmos. Terr. Phys.* **58**, 983 (1996).
- ⁵³R. Ochoukov, V. Bobkov, C. Bruhn, R. D'Inca, H. Faugel, H. Fuenfgelder, R. McDermott, P. Schneider, G. Suarez-Lopez, J.-M. Noterdaeme, ASDEX Upgrade Team, and MST1 Team, *EPJ Web Conf.* **157**, 03038 (2017).
- ⁵⁴D. G. Swanson, *Plasma Waves*, 2nd ed. (IOP Publishing, Bristol, 2003).

Chapter 7

Conclusion

In this Thesis, we have investigated PDIs in the ECRH beams at ASDEX Upgrade, both theoretically and experimentally. We have provided a detailed introduction to the theory of PDIs, deriving some new expressions along with a number of known ones; it is our hope that this can serve as a more gentle introduction to the subject than pure journal articles for future researchers. On the experimental side, strong microwave signals generated by PDIs were found in scenarios involving the injection of 140 GHz X-mode radiation for ECRH and 105 GHz O-mode radiation for CTS. We have particularly obtained the first clear indication of PDIs during ELMs for second-harmonic 140 GHz X-mode ECRH, identified PDIs damaging ECE radiometers for third-harmonic 140 GHz X-mode ECRH, and carried out the first detailed comparison of experimental and theoretical PDI thresholds near the UHR in a controlled laboratory setting.

In the 140 GHz X-mode ECRH scenarios, the initial PDI involves decay of the injected X-mode pump wave to daughter EBWs and X-mode waves near half the pump frequency. This process takes place in the vicinity of the second-harmonic UHR of the pump wave and requires the excited daughter waves to be trapped in this region to reduce the power threshold of the initial PDI to a level attainable by the ECRH beams. Such trapping may occur if the electron density profile has a maximum near the second-harmonic UHR of the pump wave, e.g., during ELMs, rotating magnetic islands, edge density spikes, and near the plasma center.

At the standard magnetic field used for central second-harmonic ECRH at ASDEX Upgrade, $|B_t| = 2.5$ T, the second-harmonic UHR of 140 GHz radiation occurs at low electron densities, meaning that it will almost universally appear in the pedestal region for H-mode plasmas. This gives rise to microwave bursts in connection with ELMs, which may be detected by a radiometer observing an ECRH beam near the plasma edge. As observed by the CTS system, microwave bursts occur near half the ECRH frequency, as well as near the ECRH frequency itself; the latter bursts may be explained by a primary daughter wave decaying to a secondary daughter wave near its own frequency and a low-frequency daughter wave, followed by combination of the primary and secondary daughter waves to create a microwave near the pump frequency (cf. Fig. 1.4). The power threshold of the

bursts near the ECRH frequency are in rough agreement with the power threshold of the primary PDI from an analytical theory, which we have developed based on the results of [8, 10] with some modifications. Additionally, the duration of the microwave spikes observed near the ECRH frequency with the fast CTS system ($\sim 3 \mu\text{s}$) is in agreement with the passage time of the regions allowing daughter wave trapping through an ECRH beam according to a nonlinear MHD simulation of the ELM crash, performed using the JOREK code [154, 155]; the electron density and temperature profiles used in the theoretical calculation of the PDI threshold were also obtained from this simulation. We further note that quasi-continuous PDI-generated signals are observed just below the ECRH frequency while the plasma is still in L-mode. These signals are likely related to PDIs due to trapping in the non-monotonic density profiles associated with L-mode turbulence. Finally, quasi-continuous strong signals with a larger shift relative to the ECRH frequency also occur in the inter-ELM phases at low edge densities. These are likely related to PDIs in the density structures set up by inter-ELM modes. The PDI-related microwave signals observed in connection with ELMs, edge turbulence, and inter-ELM modes are generally not at a level which poses any danger to microwave diagnostics, and in order to reliably observe them, it is generally necessary for the view of a radiometer to overlap with an ECRH beam near the plasma edge. They do, however, present the possibility of creating a new type edge diagnostic, which would be able to measure the passage of ELM filaments, changes in the character of the edge turbulence, and inter-ELM modes in the localized region of an ECRH beam with high temporal resolution.

When the magnetic field is reduced, either to a level with the second-harmonic ECR on the high-field side ($|B_t| \approx 2.2 \text{ T}$) or to a level with a central third-harmonic ECR ($|B_t| \approx 1.8 \text{ T}$) for 140 GHz ECRH, the second-harmonic UHR may be present in the bulk plasma, although electron densities below $4.25 \times 10^{19} \text{ m}^{-3}$ are necessary even at $|B_t| = 1.8 \text{ T}$, meaning that this generally only occurs in L-mode plasmas or H-mode plasmas with fresh boronization/boron drop and density pump out from resonant magnetic perturbations. In these cases, PDIs with trapped daughter waves may occur in connection with rotating magnetic islands, edge density spikes, and near the plasma center. PDIs during rotating magnetic islands have been observed through quasi-periodic microwave bursts, whose rate of occurrence follow the rotation frequency of the magnetic island, near the ECRH frequency by the CTS system. Our results are similar to the original observations from TEXTOR [144, 156] and extend these to third-harmonic ECRH of X-mode plasmas. We do, however, note that the mere occurrence of a rotating magnetic island in the vicinity of a point at which the second-harmonic UHR surface is intersected by an ECRH beam is insufficient to guarantee that PDI-related microwave bursts will be observed. This is presumably due to the electron density bump associated with the magnetic island being too small to allow trapping of the daughter waves, although reliable electron density profiles in the islands will need to be obtained to confirm this hypothesis. More worryingly, the strong signals observed in connection with rotating magnetic islands near half the ECRH frequency were capable of permanently degrading an ECE mixer, necessitating a recalibration of the ECE system and reducing the sensitivity of the affected channels. A similar degradation of an ECE mixer was observed in connection with strong quasi-continuous signals,

attributed to PDIs occurring near the plasma center. These results point to a potential danger for third-harmonic X-mode ECRH at ITER, which will be used to allow H-mode access with relatively low (ECRH-dominated) heating power during the early operation phase. We particularly note that the ECE channels viewing the second-harmonic ECR in X-mode near the plasma edge in ITER will have frequencies close to half that used for central third-harmonic ECRH, just as in ASDEX Upgrade, due to the near $1/R$ -dependence of the magnetic field in a tokamak and the similar aspect ratios of ITER and ASDEX Upgrade. One scheme to prevent such degradation of the ECE mixers in ITER during third-harmonic ECRH would be to minimize the possibility of the ECE system picking up signals originating from ECRH beams, e.g., by focusing the ECRH power in sectors well removed from the ECE radiometers and orienting the closer beams away from the ECE views; the efficiency of such a scheme is indicated by the fact that ECE mixer degradation at ASDEX Upgrade was only observed after the commissioning of the ECRH3 system and seems to be particularly associated with operation of the gyrotron located closest to the ECE radiometers. The simple method of operating at high n_e in order to avoid the PDIs is not possible in the third-harmonic ECRH scenarios planned for ITER, which will have an ECRH frequency of 170 GHz, $|B_t| = 1.8$ T, and a plasma current of 5 MA [39], as the edge electron density required for the second-harmonic UHR to not occur in the bulk plasma ($7.1 \times 10^{19} \text{ m}^{-3}$) is well above the Greenwald edge density limit [50, 51] in these scenarios ($4.0 \times 10^{19} \text{ m}^{-3}$).

During injection of 105 GHz O-mode radiation for CTS, a primary PDI, involving decay of the electromagnetic pump wave to an EBW and a low-frequency LH wave near the UHR, may occur. While current theories [157] and low-temperature experiments [161] suggest that such a PDI, or a closely related one, may occur for the O-mode radiation itself in cases where the EBW is trapped, e.g., in connection with a magnetic island, the experimental evidence of such PDIs in tokamaks is less conclusive [158]; if such PDIs were shown to be important for (fundamental) O-mode ECRH in tokamaks, they would be of considerable concern for ITER. The PDIs at the UHR in ASDEX Upgrade, as well as other tokamaks and stellarators, seem to require conversion of a fraction of the O-mode radiation to X-mode radiation, or direct injection of X-mode radiation from the high-field side. When a sufficiently large amount of X-mode power (~ 10 kW in ASDEX Upgrade) reaches the UHR, the primary PDI will occur; the low PDI power threshold is a result of the enhancement of the electric field associated with the X-mode pump wave near the UHR. The 105 GHz ECR is located far on the high-field side for the standard magnetic field at ASDEX Upgrade, $|B_t| = 2.5$ T, reducing its optical thickness and consequently also the ECE background in the CTS spectra. This does, however, also allow a significant fraction of the injected O-mode radiation to reflect off the high-field side wall, be partially converted to X-mode and pass the ECR once more, after which it finally reaches the UHR where it may drive PDIs. The amount of X-mode power reaching the UHR may be varied by sweeping $|B_t|$, as this will change the optical thickness of the ECR. Combining such a sweep with ECRH power modulations on a much faster time scale made it possible to verify that the primary PDI power threshold derived theoretically for ASDEX Upgrade, taking the above conversion steps, as well as PDI physics, into account, by the Author [13] does

in fact agree with the experimentally observed PDI power threshold [14]. Additionally, the theoretical primary PDI threshold has recently been shown to agree with particle-in-cell simulations for ASDEX Upgrade-like parameters [17]. A shortcoming of the developed theory is its reliance on the dipole approximation, which limits its ability to predict the frequency of the daughter waves beyond upper and lower bounds. A point of further interest is the occurrence of secondary PDIs, involving decay of the primary EBW daughters to secondary EBW daughters and second-order IBWs, as well as tertiary PDIs involving decay of the pump wave to EBWs and arbitrary-order IBWs [14]. The continued investigation of PDIs for X-mode radiation near the UHR is of interest since they are expected to occur during O-X-B heating, planned for Wendelstein 7-X, and have already been used to indicate the occurrence of O-X-B heating at Wendstein 7-AS [166].

The above results indicate a number of topics deserving further study. First, the capabilities of an edge diagnostic based on the ELM-related PDIs have only been explored very tentatively and should be investigated in a wider range of scenarios, e.g., in small-ELM regimes and I-modes. Second, a more reliable setup for the island-related PDIs and better characterization of the island electron density profiles are highly desirable, as this would allow the conclusions regarding the occurrence and non-occurrence of such PDIs to be more firmly established and their consequences for future devices to be more reliably assessed. A more detailed investigation of PDIs in connection with edge density spikes and near the plasma center is also warranted. Finally, an extension of the theory used to describe the primary PDI near the UHR beyond the dipole approximation is desired, possibly by expanding the results of [143] to underdense plasmas, along with theoretical descriptions of the secondary and tertiary PDIs near the UHR.

Bibliography

- [1] Guo, X., Zou, C.-L., Jung, H. & Tang, H. X. On-chip strong coupling and efficient frequency conversion between telecom and visible optical modes. *Phys. Rev. Lett.* **117**, 123902 (2016).
- [2] Brau, F. *et al.* Multiple-length-scale elastic instability mimics parametric resonance of nonlinear oscillators. *Nature Phys.* **7**, 56 (2011).
- [3] Aubourg, Q. & Mordant, N. Nonlocal resonances in weak turbulence of gravity-capillary waves. *Phys. Rev. Lett.* **114**, 144501 (2015).
- [4] Thidé, B., Kopka, H. & Stubbe, P. Observations of stimulated scattering of a strong high-frequency radio wave in the ionosphere. *Phys. Rev. Lett.* **49**, 1561 (1982).
- [5] Bernhardt, P. A. *et al.* Stimulated Brillouin scatter in a magnetized ionospheric plasma. *Phys. Rev. Lett.* **104**, 165004 (2010).
- [6] Sergeev, E. *et al.* Artificial ionospheric layers during pump frequency stepping near the 4th gyroharmonic at HAARP. *Phys. Rev. Lett.* **110**, 065002 (2013).
- [7] Froula, D. H. *et al.* Saturation of the two-plasmon decay instability in long-scale-length plasmas relevant to direct-drive inertial confinement fusion. *Phys. Rev. Lett.* **108**, 165003 (2012).
- [8] Popov, A. Yu. & Gusakov, E. Z. Low-threshold absolute two-plasmon decay instability in the second harmonic electron cyclotron resonance heating experiments in toroidal devices. *Plasma Phys. Control. Fusion* **57**, 025022 (2015).
- [9] Gusakov, E. Z. & Popov, A. Yu. Theory of anomalous backscattering in second harmonic X-mode ECRH experiments. *Phys. Plasmas* **23**, 082503 (2016).
- [10] Gusakov, E. Z. & Popov, A. Yu. On a saturation mechanism of two-upper-hybrid-plasmon parametric decay instability in the second harmonic ECRH experiment. *Plasma Phys. Control. Fusion* **59**, 025005 (2017).
- [11] Gusakov, E. Z. & Popov, A. Yu. Theory of anomalous backscattering in second harmonic X-mode ECRH experiments. *JETP* **125**, 702 (2017).

- [12] Gusakov, E. Z. & Popov, A. Yu. Influence of the pump depletion on the anomalous absorption of the extraordinary wave in the second harmonic ECRH experiments. *Plasma Phys. Control. Fusion* **60**, 025001 (2018).
- [13] Hansen, S. K. *et al.* Parametric decay instability near the upper hybrid resonance in magnetically confined fusion plasmas. *Plasma Phys. Control. Fusion* **59**, 105006 (2017).
- [14] Hansen, S. K. *et al.* Power threshold and saturation of parametric decay instabilities near the upper hybrid resonance in plasmas. *Phys. Plasmas* **26**, 062102 (2019).
- [15] Nielsen, S. K. *et al.* Recent development of collective Thomson scattering for magnetically confined fusion plasmas. *Phys. Scr.* **92**, 024001 (2017).
- [16] Nielsen, A. H. *et al.* Numerical simulations of blobs with ion dynamics. *Plasma Phys. Control. Fusion* **59**, 025012 (2017).
- [17] Senstius, M. G., Nielsen, S. K., Vann, R. G. & Hansen, S. K. Particle-in-cell simulations of parametric decay instabilities at the upper hybrid layer of fusion plasmas to determine their primary threshold. *Plasma Phys. Control. Fusion* (accepted) (2019).
- [18] Hansen, S. K. *et al.* Parametric decay instability near the upper hybrid resonance and anomalous mm-wave scattering in tokamaks and stellarators. *EPJ Web Conf.* **149**, 03020 (2017).
- [19] Hansen, S. K. *et al.* Observation and modelling of the onset of parametric decay instabilities during gyrotron operation at ASDEX Upgrade. *EPJ Web Conf.* **203**, 02007 (2019).
- [20] Hansen, S. K. *et al.* Parametric decay instabilities during electron cyclotron resonance heating at ASDEX Upgrade. *Europhys. Conf. Abstracts* **43C**, P1.1075 (2019). URL <http://ocs.ciemat.es/EPS2019PAP/pdf/P1.1075.pdf>.
- [21] Nielsen, S. K. *et al.* Three-wave interaction during electron cyclotron resonance heating and current drive. In *Proc. 41st Int. Conf. Infrared, Millimeter, and Terahertz Waves (Copenhagen)* (IEEE, Piscataway, 2016).
- [22] Leipold, F. *et al.* Millimeter-wave receiver design for plasma diagnostics. In *Proc. 41st Int. Conf. Infrared, Millimeter, and Terahertz Waves (Copenhagen)* (IEEE, Piscataway, 2016).
- [23] Meyer, H. for the ASDEX Upgrade Team. Overview of physics studies on ASDEX Upgrade. *Nucl. Fusion* **59**, 112014 (2019).
- [24] Labit, B. *et al.* Dependence on plasma shape and plasma fueling for small edge-localized mode regimes in TCV and ASDEX Upgrade. *Nucl. Fusion* **59**, 086020 (2019).
- [25] Langmuir, I. Oscillations in ionized gases. *Proc. Natl. Acad. Sci. USA* **14**, 627 (1928).

- [26] Malmberg, J. H. & deGrassie, J. S. Properties of nonneutral plasma. *Phys. Rev. Lett.* **35**, 577 (1975).
- [27] Sarri, G. *et al.* Generation of neutral and high-density electron–positron pair plasmas in the laboratory. *Nature Commun.* **6**, 6747 (2014).
- [28] Debye, P. & Hückel, E. Zur Theorie der Elektrolyte. I. Gefrierpunktserniedrigung und verwandte Erscheinungen. *Physik. Zeitschr.* **24**, 185 (1923).
- [29] Grosso, G. & Pastori Parravicini, G. *Solid State Physics* (Academic Press, Amsterdam, 2000).
- [30] Fletcher, L. B. *et al.* Ultrabright X-ray laser scattering for dynamic warm dense matter physics. *Nature Photonics* **9**, 274 (2015).
- [31] de Broglie, L.-V. On the theory of quanta. *Ann. Phys. (Paris)* **3**, 22 (1925).
- [32] Freidberg, J. P. *Plasma Physics and Fusion Energy* (Cambridge University Press, Cambridge, 2007).
- [33] Jackson, J. D. Catalysis of nuclear reactions between hydrogen isotopes by μ^- mesons. *Phys. Rev.* **106**, 330 (1957).
- [34] Bethe, H. A. Energy production in stars. *Phys. Rev.* **55**, 434 (1939).
- [35] Hurricane, O. A. *et al.* Fuel gain exceeding unity in an inertially confined fusion implosion. *Nature* **506**, 343 (2014).
- [36] Ongena, J., Koch, R., Wolf, R. & Zohm, H. Magnetic-confinement fusion. *Nature Phys.* **12**, 398 (2016).
- [37] Pedersen, T. S. *et al.* First results from divertor operation in Wendelstein 7-X. *Plasma Phys. Control. Fusion* **61**, 014035 (2019).
- [38] Thomas, P. R. *et al.* Observation of alpha heating in JET DT plasmas. *Phys. Rev. Lett.* **80**, 5548 (1998).
- [39] ITER Organization. ITER research plan within the staged approach (level III – provisional version). Tech. Rep. ITR-18-003, ITER Organization, St. Paul-lez Durance (2018). URL <https://www.iter.org/technical-reports>.
- [40] The ASDEX Upgrade Team. URL https://www.aug.ipp.mpg.de/aug/local/aug_only/AUG_Aufbau/Drawing_Gallery/index.html (2011).
- [41] Wesson, J. *Tokamaks* (Oxford University Press, Oxford, 2004), 3rd edn.
- [42] Zohm, H. *Magnetohydrodynamic Stability of Tokamaks* (Wiley-VCH, Weinheim, 2015).

- [43] Wagner, F. *et al.* Regime of improved confinement and high beta in neutral-beam-heated divertor discharges of the ASDEX tokamak. *Phys. Rev. Lett.* **49**, 1408 (1982).
- [44] Viezzer, E. *et al.* High-accuracy characterization of the edge radial electric field at ASDEX Upgrade. *Nucl. Fusion* **53**, 053005 (2013).
- [45] Zohm, H. Edge localized modes (ELMs). *Plasma Phys. Control. Fusion* **38**, 105 (1996).
- [46] Suttrop, W. *et al.* First observation of edge localized modes mitigation with resonant and nonresonant magnetic perturbations in ASDEX Upgrade. *Phys. Rev. Lett.* **106**, 225004 (2011).
- [47] Kallenbach, A. *et al.* Non-boronized compared with boronized operation of ASDEX Upgrade with full-tungsten plasma facing components. *Nucl. Fusion* **49**, 045007 (2009).
- [48] Bortolon, A. *et al.* Real-time wall conditioning by controlled injection of boron and boron nitride powder in full tungsten wall ASDEX Upgrade. *Nucl. Mater. Energy* **19**, 384 (2019).
- [49] Leuthold, N. *et al.* Parameter dependence of ELM loss reduction by magnetic perturbations at low pedestal density and collisionality in ASDEX Upgrade. *Plasma Phys. Control. Fusion* **59**, 055004 (2017).
- [50] Greenwald, M. *et al.* A new look at density limits in tokamaks. *Nucl. Fusion* **28**, 2199 (1988).
- [51] Greenwald, M. Density limits in toroidal plasmas. *Plasma Phys. Control. Fusion* **44**, R27 (2002).
- [52] Lang, P. T. *et al.* High-efficiency plasma refuelling by pellet injection from the magnetic high-field side into ASDEX Upgrade. *Phys. Rev. Lett.* **79**, 1487 (1997).
- [53] Foster, C. A., Colchin, R. J., Milora, S. L., Kim, K. & Turnbull, R. J. Solid hydrogen pellet injection into the Ormak tokamak. *Nucl. Fusion* **17**, 1067 (1977).
- [54] Valovič, M. *et al.* Density control by pellets in plasmas with ELM mitigation by RMPs in the ASDEX Upgrade tokamak. *Plasma Phys. Control. Fusion* **60**, 085013 (2018).
- [55] Swanson, D. G. *Plasma Waves* (IOP Publishing, Bristol, 2003), 2nd edn.
- [56] Meyer, E. & Sessler, G. Schallausbreitung in Gasen bei hohen Frequenzen und sehr niedrigen Drucken. *Z. Phys.* **149**, 15 (1957).
- [57] Stubbe, P. & Sukhorukov, A. I. On the physics of Landau damping. *Phys. Plasmas* **6**, 2976 (1999).

- [58] Malmberg, J. H. & Wharton, C. B. Collisionless damping of electrostatic plasma waves. *Phys. Rev. Lett.* **13**, 184 (1964).
- [59] Bagrov, V. G. & Gitman, D. *The Dirac Equation and Its Solutions* (De Gruyter, Berlin, 2014).
- [60] Sukhorukov, A. I. & Stubbe, P. On the Bernstein–Landau paradox. *Phys. Plasmas* **4**, 2497 (1997).
- [61] Baldwin, D. E. & Rowlands, G. Plasma oscillations perpendicular to a weak magnetic field. *Phys. Fluids* **9**, 2444 (1966).
- [62] Bornatici, M. Theory of electron cyclotron absorption of magnetized plasmas. *Plasma Phys.* **24**, 629 (1982).
- [63] Bornatici, M., Cano, R., De Barbieri, O. & Engelmann, F. Electron cyclotron emission and absorption in fusion plasmas. *Nucl. Fusion* **23**, 1153 (1983).
- [64] Wagner, D. *et al.* Status of the new multi-frequency ECRH system for ASDEX Upgrade. *Nucl. Fusion* **48**, 054006 (2008).
- [65] Wagner, D. *et al.* Extension of the multi-frequency ECRH system at ASDEX Upgrade. *EPJ Web Conf.* **149**, 03004 (2017).
- [66] Kartikeyan, M. V., Borie, E. & Thumm, M. K. A. *Gyrotrons* (Springer, Berlin, 2004).
- [67] Tatsukawa, T. *et al.* ESR spectrometer with a wide frequency range using a gyrotron as a radiation power source. *Int. J. Infrared Millim. Waves* **16**, 293 (1995).
- [68] Bajaj, V. S. *et al.* 250 GHz CW gyrotron oscillator for dynamic nuclear polarization in biological solid state NMR. *J. Magn. Reson.* **189**, 251 (2007).
- [69] Stober, J. *et al.* Exploring fusion-reactor physics with high-power electron-cyclotron-resonance heating (ECRH) on ASDEX Upgrade (2019). Submitted to: *Plasma Phys. Control. Fusion*.
- [70] Hutchinson, I. H. *Principles of Plasma Diagnostics* (Cambridge University Press, Cambridge, 2002), 2nd edition edn.
- [71] Ochoukov, R. *et al.* Major upgrades of the high frequency B-dot probe diagnostic suite on ASDEX Upgrade. *EPJ Web Conf.* **157**, 03038 (2017).
- [72] Denk, S. S. *Study of Non-Thermal Electron Energy Distribution Functions by Modeling of Electron Cyclotron Emission from the Fusion Plasmas of the ASDEX Upgrade Tokamak*. Ph.D. thesis, Technische Universität München, Garching (2019).
- [73] Hartfuss, H. J., Geist, T. & Hirsch, M. Heterodyne methods in millimetre wave plasma diagnostics with applications to ECE, interferometry and reflectometry. *Plasma Phys. Control. Fusion* **39**, 1693 (1997).

- [74] Hicks, N. K. *et al.* Upgrades and real time NTM control application of the ECE radiometer on ASDEX Upgrade. In Lohr, J. (ed.) *Proc. 15th Joint Workshop ECE and ECRH (Yosemite)*, 238 (World Scientific, Singapore, 2009).
- [75] Igochine, V. *et al.* Tearing mode formation induced by internal crash events at different β_N . *Nucl. Fusion* **57**, 036015 (2017).
- [76] Fischer, R. *et al.* Integrated data analysis of profile diagnostics at ASDEX Upgrade. *Fusion Sci. Technol.* **58**, 675 (2010).
- [77] Froula, D. H., Glenzer, S. H., Luhmann, N. C. Jr. & Sheffield, J. *Plasma Scattering of Electromagnetic Radiation* (Academic Press, Amsterdam, 2011), 2nd edn.
- [78] Bindslev, H. A quantitative study of scattering from electromagnetic fluctuations in plasmas. *J. Atmos. Terr. Phys.* **58**, 983 (1996).
- [79] Furtula, V. *et al.* Design and performance of the collective Thomson scattering receiver at ASDEX Upgrade. *Rev. Sci. Instrum.* **83**, 013507 (2012).
- [80] Stejner, M. *et al.* Measuring main-ion temperatures in ASDEX Upgrade using scattering of ECRH radiation. In *Proc. 41st Int. Conf. Infrared, Millimeter, and Terahertz Waves (Copenhagen)* (IEEE, Piscataway, 2016).
- [81] Stejner, M. *et al.* Resolving the bulk ion region of millimeter-wave collective Thomson scattering spectra at ASDEX Upgrade. *Rev. Sci. Instrum.* **85**, 093504 (2014).
- [82] McCarthy, P. J., Martin, P. & Schneider, W. The CLISTE interpretive equilibrium code. Tech. Rep. IPP 5/85, Max-Planck-Institut für Plasmaphysik, Garching (1999).
- [83] Agarwal, G. S. *Quantum Optics* (Cambridge University Press, Cambridge, 2013).
- [84] Giustina, M. *et al.* Significant-loophole-free test of Bell's theorem with entangled photons. *Phys. Rev. Lett.* **115**, 250401 (2015).
- [85] The LIGO Scientific Collaboration. Enhanced sensitivity of the LIGO gravitational wave detector by using squeezed states of light. *Nature Photonics* **7**, 613 (2013).
- [86] Vahlbruch, H., Mehmet, M., Danzmann, K. & Schnabel, R. Detection of 15 dB squeezed states of light and their application for the absolute calibration of photoelectric quantum efficiency. *Phys. Rev. Lett.* **117**, 110801 (2016).
- [87] Mills, D. L. *Nonlinear Optics* (Springer, Berlin, 1998), 2nd edn.
- [88] Gusakov, E. Z. & Fedorov, V. I. Decay instability in an inhomogeneous plasma with trapped waves. *Sov. J. Plasma Phys.* **5**, 463 (1979).
- [89] Piliya, A. D. Decay instability in weakly inhomogeneous plasma. In Franklin, R. N. (ed.) *Proc. 10th Int. Conf. Phenomena in Ionized Gases (Oxford)*, 320 (Donald Parsons & Co. Ltd., Oxford, 1971).

- [90] Rosenbluth, M. N. Parametric instabilities in inhomogeneous media. *Phys. Rev. Lett.* **29**, 565 (1972).
- [91] Piliya, A. D. Nonstationary theory of decay instability in a weakly inhomogeneous plasma. *Sov. Phys.—JETP* **37**, 629 (1973).
- [92] Gusakov, E., Popov, A. & Tretinnikov, P. Possibility of anomalous emission at half-integer pump wave frequency harmonics in the X2 ECRH experiments. *Europhys. Conf. Abstracts* **43C**, P4.1076 (2019). URL <http://ocs.ciemat.es/EPS2019PAP/pdf/P4.1076.pdf>.
- [93] Gusakov, E. Z. & Popov, A. Yu. Possibility of strong anomalous absorption in the ECRH experiments. *Europhys. Conf. Abstracts* **43C**, P1.1079 (2019). URL <http://ocs.ciemat.es/EPS2019PAP/pdf/P1.1079.pdf>.
- [94] Altukhov, A. B. *et al.* Observation of the strong anomalous absorption of the X-mode pump in a plasma filament due to the two-plasmon decay. *EPL* **126**, 15002 (2019).
- [95] Lifshitz, E. M. & Pitaevskii, L. P. *Physical Kinetics*, vol. 10 of *Course of Theoretical Physics* (Butterworth Heineman, Oxford, 1981).
- [96] Jackson, J. D. *Classical Electrodynamics* (John Wiley & Sons, New York, 1999), 3rd edn.
- [97] Arfken, G. B. & Weber, H. J. *Mathematical Methods for Physicists* (Elsevier Academic Press, Amsterdam, 2005), 6th edn.
- [98] Erckmann, V. & Gasparino, U. Electron cyclotron resonance heating and current drive in toroidal fusion plasmas. *Plasma Phys. Control. Fusion* **36**, 1869 (1994).
- [99] Stix, T. H. *Waves in Plasmas* (AIP Press, New York, 1992).
- [100] Appleton, E. V. Wireless studies of the ionosphere. *J. Inst. Electr. Eng.* **71**, 642 (1932).
- [101] Braginskii, S. I. Transport processes in a plasma. *Rev. Plasma Phys.* **1**, 205 (1965).
- [102] Bhatnagar, P. L., Gross, E. P. & Krook, M. A model for collisions in gases. I. Small amplitude processes in charged and neutral one-component systems. *Phys. Rev.* **94**, 511 (1954).
- [103] Gross, E. P. & Krook, M. Model for collision processes in gases: Small-amplitude oscillations of charged two-component systems. *Phys. Rev.* **102**, 593 (1956).
- [104] Opher, M., Morales, G. J. & Leboeuf, J. N. Krook collisional models of the kinetic susceptibility of plasmas. *Phys. Rev. E* **66**, 016407 (2002).
- [105] Amano, T. & Okamoto, M. Parametric effects of an alternating field on inhomogeneous plasmas. *J. Phys. Soc. Jpn.* **26**, 529 (1969).

- [106] Porkolab, M. Parametric processes in magnetically confined CTR plasmas. *Nucl. Fusion* **18**, 367 (1978).
- [107] Bernhardt, P. A., Selcher, C. A. & Kowtha, S. Electron and ion Bernstein waves excited in the ionosphere by high power EM waves at the second harmonic of the electron cyclotron frequency. *Geophys. Res. Lett.* **38**, L19107 (2011).
- [108] Bernstein, I. B. Waves in a plasma in a magnetic field. *Phys. Rev.* **109**, 10 (1958).
- [109] Hansen, S. K. *Parametric Decay and Anomalous Scattering from Tokamak Plasmas*. Master's thesis, Technical University of Denmark, Kgs. Lyngby (2016).
- [110] Sharma, R. P. & Shukla, P. K. Nonlinear effects at the upper-hybrid layer. *Phys. Fluids* **26**, 87 (1983).
- [111] Leyser, T. B. *et al.* Downshifted maximum features in stimulated electromagnetic emission spectra. *J. Geophys. Res.* **99**, 19555 (1994).
- [112] Gusakov, E., Popov, A. & Sysoeva, E. Anomalous backscattering and absorption in second harmonic ECRH experiments due to low-threshold two UH plasmon decay instability in blobs. *EPJ Web Conf.* **157**, 03019 (2017).
- [113] Abramowitz, M. & Stegun, I. A. *Handbook of Mathematical Functions with Formulas, Graphs, and Mathematical Tables* (National Bureau of Standards, Washington, D. C., 1964), 9th edn.
- [114] Piliya, A. D. & Saveliev, A. N. High-order ion Bernstein waves in a non-uniform magnetic field. *Plasma Phys. Control. Fusion* **36**, 2059 (1994).
- [115] Landau, L. D. & Lifshitz, E. M. *The Classical Theory of Fields*, vol. 2 of *Course of Theoretical Physics* (Pergamon Press, Oxford, 1971), 3rd (revised) edn.
- [116] Mazzucato, E. *Electromagnetic Waves for Thermonuclear Fusion Research* (World Scientific, Singapore, 2014).
- [117] Einstein, A. Über einen die Erzeugung und Verwandlung des Lichtes betreffenden heuristischen Gesichtspunkt. *Ann. Phys. (Leipzig)* **322**, 132 (1905).
- [118] Weinberg, S. Eikonal method in magnetohydrodynamics. *Phys. Rev.* **126**, 1899 (1962).
- [119] Bernstein, I. B. Geometric optics in space – and time – varying plasmas. *Phys. Fluids* **18**, 320 (1975).
- [120] Bravo-Ortega, A. & Glasser, A. H. Theory and application of complex geometric optics in inhomogeneous magnetized plasmas. *Phys. Fluids B* **3**, 529 (1991).
- [121] Bindslev, H. Dielectric effects on Thomson scattering in a relativistic magnetized plasma. *Plasma Phys. Control. Fusion* **33**, 1775 (1991).

- [122] Bindslev, H. Relativistic effects in plasma reflectometry. *Plasma Phys. Control. Fusion* **34**, 1601 (1992).
- [123] Poli, E., Peeters, A. G. & Pereverzev, G. V. TORBEAM, a beam tracing code for electron-cyclotron waves in tokamak plasmas. *Comput. Phys. Commun.* **136**, 90 (2001).
- [124] Weber, H., Maj, O. & Poli, E. Scattering of diffracting beams of electron cyclotron waves by random density fluctuations in inhomogeneous plasmas. *EPJ Web Conf.* **87**, 01002 (2015).
- [125] Saleh, B. E. A. & Teich, M. C. *Fundamentals of Photonics* (Wiley-Interscience, New York, 2007), 2nd edn.
- [126] Berk, H. L. & Book, D. L. Plasma wave regeneration in inhomogeneous media. *Phys. Fluids* **12**, 649 (1969).
- [127] Berk, H. L. & Pfirsch, D. WKB method for systems of integral equations. *J. Math. Phys.* **21**, 2054 (1980).
- [128] Landau, L. D. & Lifshitz, E. M. *Quantum Mechanics: Non-Relativistic Theory*, vol. 3 of *Course of Theoretical Physics* (Pergamon Press, Oxford, 1965), 2nd (revised) edn.
- [129] White, R. B. & Chen, F. F. Amplification and absorption of electromagnetic waves in overdense plasmas. *Plasma Phys.* **16**, 565 (1974).
- [130] Berry, M. V. & Mount, K. E. Semiclassical approximations in wave mechanics. *Rep. Prog. Phys.* **35**, 315 (1972).
- [131] Lundborg, B. & Thidé, B. Standing wave pattern of HF radio waves in the ionospheric reflection region 1. General Formulas. *Radio Sci.* **20**, 947 (1985).
- [132] Lundborg, B. & Thidé, B. Standing wave pattern of HF radio waves in the ionospheric reflection region 2. Applications. *Radio Sci.* **21**, 486 (1986).
- [133] Lundborg, B. Analytic description of the electromagnetic wave field for effective refractive indices with an infinity. *Radio Sci.* **22**, 787 (1987).
- [134] Silin, V. P. Parametric resonance in a plasma. *Sov. Phys.—JETP* **21**, 1127 (1965).
- [135] Aliev, Yu. M., Silin, V. P. & Watson, C. Parametric resonance in a plasma in a magnetic field. *Sov. Phys.—JETP* **23**, 626 (1966).
- [136] Ott, E., Hui, B. & Chu, K. R. Theory of electron cyclotron heating of tokamak plasmas. *Phys. Fluids* **23**, 1031 (1980).
- [137] Porkolab, M. Parametric decay instabilities in ECR heated plasmas. In Uckan, N. A. (ed.) *Proc. 2nd Workshop Hot Electron Ring Physics (San Diego)*, vol. 1, 237 (National Technical Information Service, Alexandria, 1982). URL <https://www.osti.gov/biblio/5026952-H051yu/>.

- [138] Dodin, I. Y. & Arefiev, A. V. Parametric decay of plasma waves near the upper-hybrid resonance. *Phys. Plasmas* **24**, 032119 (2017).
- [139] Aamodt, R. E. & Russel, D. A. Alpha particle detection by scattering off of plasma fluctuations. *Nucl. Fusion* **32**, 745 (1992).
- [140] Bindslev, H. Three-wave mixing and Thomson scattering in plasmas. *Plasma Phys. Control. Fusion* **35**, 1615 (1993).
- [141] Bindslev, H. Low temperature model of non-linear wave mixing in plasmas. *Ukrainian J. Phys.* **40**, 457 (1995).
- [142] Rosenbluth, M. N., White, R. B. & Liu, C. S. Temporal evolution of a three-wave parametric instability. *Phys. Rev. Lett.* **31**, 1190 (1973).
- [143] Gusakov, E. Z. & Surkov, A. V. Induced backscattering in an inhomogeneous plasma at the upper hybrid resonance. *Plasma Phys. Control. Fusion* **49**, 631 (2007).
- [144] Westerhof, E. *et al.* Strong scattering of millimeter waves in tokamak plasmas with tearing modes. *Phys. Rev. Lett.* **103**, 125001 (2009).
- [145] Sensiust, M. G., Nielsen, S. K. & Vann, R. G. L. Particle-in-cell simulations of two plasmon decay in a non-monotonic density profile. *Europhys. Conf. Abstracts* **43C**, P4.1064 (2019). URL <http://ocs.ciemat.es/EPS2019PAP/pdf/P4.1064.pdf>.
- [146] Porte, L., Bartlett, D. V., Campbell, D. J. & Costley, A. E. First results with the upgraded ECE heterodyne radiometer on JET. *Europhys. Conf. Abstracts* **15C**, IV-357 (1991).
- [147] Taylor, G., Bush, C. E., Fredrickson, E. D., Park, H. K. & Ramsey, A. T. Intense electron cyclotron emission bursts during high power neutral beam heating on TFTR. *Nucl. Fusion* **32**, 1867 (1992).
- [148] Bartlett, D. V. *et al.* Observations of suprathermal electrons in the edge region of JET H-mode plasmas. *Europhys. Conf. Abstracts* **16C**, I-163 (1992).
- [149] Janos, A., Hastie, J., McGuire, K. & Fredrickson, E. Bursts of electron cyclotron emission during ELMs and high β disruptions in TFTR. *Plasma Phys. Control. Fusion* **38**, 1373 (1996).
- [150] Fuchs, Ch. & Austin, M. E. Measurements of edge-localized-mode induced electron cyclotron emission bursts in DIII-D. *Phys. Plasmas* **8**, 1594 (2001).
- [151] Freethy, S. J. *et al.* Electron kinetics inferred from observations of microwave bursts during edge localized modes in the Mega-Amp Spherical Tokamak. *Phys. Rev. Lett.* **114**, 125004 (2015).
- [152] Li, E., Austin, M. E., White, R. B. & Taylor, G. The build-up of energetic electrons triggering electron cyclotron emission bursts due to a magnetohydrodynamic mode at the edge of tokamaks. *Phys. Plasmas* **24**, 092509 (2017).

- [153] Willensdorfer, M. *et al.* Dynamics of ideal modes and subsequent ELM crashes in 3D tokamak geometry from external magnetic perturbations. *Plasma Phys. Control. Fusion* **61**, 014019 (2019).
- [154] Huysmans, G. T. A. & Czarny, O. MHD stability in X-point geometry: Simulation of ELMs. *Nucl. Fusion* **47**, 659 (2007).
- [155] Hoelzl, M. *et al.* Insights into type-I edge localized modes and edge localized mode control from JOREK non-linear magneto-hydrodynamic simulations. *Contrib. Plasma Phys.* **58**, 518 (2018).
- [156] Nielsen, S. K. *et al.* Experimental characterisation of anomalous strong scattering of mm-waves in TEXTOR plasmas with rotating islands. *Plasma Phys. Control. Fusion* **55**, 115003 (2013).
- [157] Gusakov, E. Z. & Popov, A. Yu. Parametric decay instability of an obliquely propagating ordinary wave in the electron cyclotron frequency range. *Phys. Plasmas* **25**, 012101 (2018).
- [158] Bruschi, A. *et al.* Side emissions during EC injection for PDI studies in FTU tokamak. *EPJ Web Conf.* **203**, 02005 (2019).
- [159] Kantor, M. Yu., Donné, A. J. H., Jaspers, R., van der Meiden, H. J. & TEXTOR Team. Thomson scattering system on the TEXTOR tokamak using a multi-pass laser beam configuration. *Plasma Phys. Control. Fusion* **51**, 055002 (2009).
- [160] Simonchik, L. V. *et al.* Decay of the X-mode into two upper-hybrid plasmons in the plasma filament. Experimental modeling and theoretical description. *EPJ Web Conf.* **149**, 03013 (2017).
- [161] Simonchik, L. *et al.* Experimental investigation of the ordinary wave anomalous absorption in the plasma filament. *Europhys. Conf. Abstracts* **43C**, P2.4012 (2019). URL <http://ocs.ciemat.es/EPS2019PAP/pdf/P2.4012.pdf>.
- [162] McDermott, F. S., Bekefi, G., Hackett, K. E., Levine, J. S. & Porkolab, M. Observation of the parametric decay instability during electron cyclotron resonance heating on the Versator II tokamak. *Phys. Fluids* **25**, 1488 (1982).
- [163] Bulyginskii, D. G. *et al.* Nonlinear phenomena during electron cyclotron resonance heating in the FT-1 tokamak. *Sov. J. Plasma Phys.* **12**, 77 (1986).
- [164] Pietrzyk, Z. A. *et al.* Electron cyclotron resonance heating on the TCA tokamak. *Nucl. Fusion* **33**, 197 (1993).
- [165] Wilhelm, R. *et al.* Electron cyclotron resonance heating and confinement in the W VII-A stellarator. *Plasma Phys. Control. Fusion* **26**, 1433 (1984).

- [166] Laqua, H. P. *et al.* Resonant and nonresonant electron cyclotron heating at densities above the plasma cutoff by O-X-B mode conversion at the W7-AS stellarator. *Phys. Rev. Lett.* **78**, 3467 (1997).
- [167] Laqua, H. P. Electron Bernstein wave heating and diagnostic. *Plasma Phys. Control. Fusion* **49**, R1 (2007).
- [168] Shevchenko, V. *et al.* Development of electron Bernstein wave research in MAST. *Fusion Sci. Technol.* **52**, 202 (2007).
- [169] Köhn, A. *et al.* Schemes of microwave heating of overdense plasmas in the stellarator TJ-K. *Plasma Phys. Control. Fusion* **55**, 014010 (2013).
- [170] Kubo, S. *et al.* Scattering volume in the collective Thomson scattering measurement using high power gyrotron in the LHD. *J. Instrum.* **11**, C06005 (2016).
- [171] Budko, N. I. & Vaskov, V. V. Powerful radio wave decay into upper hybrid or electron-cyclotron and lower hybrid plasma waves. *Geomagn. Aeron.* **34**, 350 (1994). URL <http://eos.wdcb.ru/transl/gma/9403/pap15.ps>.
- [172] Lin, A. T. & Lin, C.-C. Nonlinear penetration of upper-hybrid waves induced by parametric instabilities of a plasma in an inhomogeneous magnetic field. *Phys. Rev. Lett.* **47**, 98 (1981).
- [173] Arefiev, A. V. *et al.* Kinetic simulations of X-B and O-X-B mode conversion and its deterioration at high input powers. *Nucl. Fusion* **57**, 116024 (2017).
- [174] Senstius, M. G., Nielsen, S. K. & Vann, R. G. L. Particle-in-cell simulations of parametric decay instabilities near the upper hybrid layer. *EPJ Web Conf.* **203**, 01010 (2019).